Design of Thermal Systems Using Topology Optimization

Haertel, Jan Hendrik Klaas

Publication date:
2018

Document Version
Publisher's PDF, also known as Version of record

Technical University of Denmark

Design of Thermal Systems Using Topology Optimization

Jan Hendrik Klaas Haertel
Department of Energy Conversion and Storage

Ph.D. Thesis, December 2017

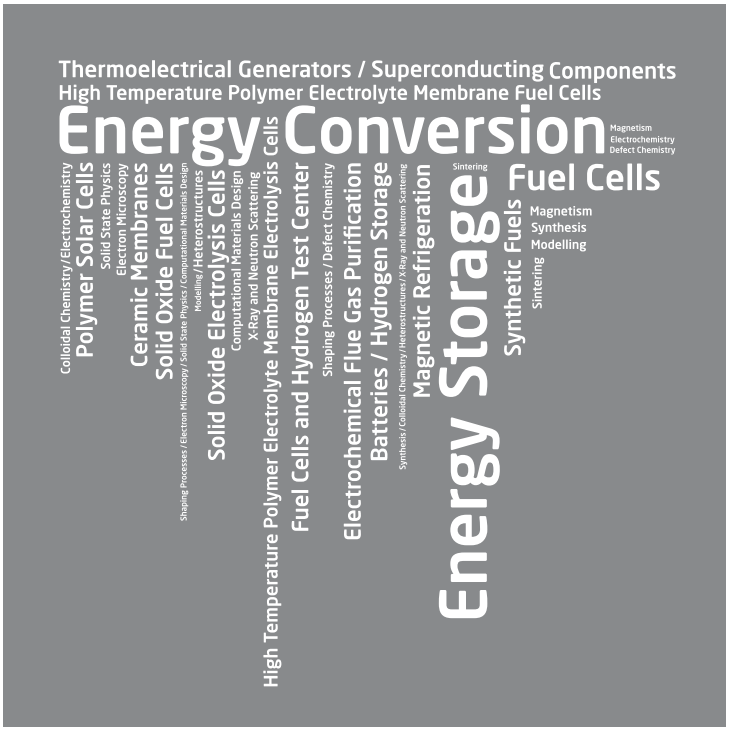

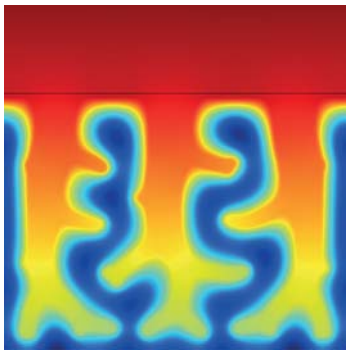

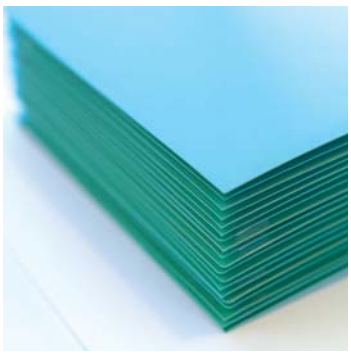

DTU Energy
Department of Energy Conversion and Storage

Abstract

The goal of this thesis is to apply topology optimization to the design of different thermal systems such as heat sinks and heat exchangers in order to improve the thermal performance of these systems compared to conventional designs. The design of thermal systems is a complex task that has traditionally relied on experience, intuition, and trial and error approaches. Topology optimization, in contrast, allows for a systematic optimization of such systems and the identification of unintuitive and unexpected geometries. Both numerical optimizations and, to a lesser extent, experimental validations of optimized designs are presented within this thesis. The main contribution of the thesis is the development of several numerical optimization models that are applied to different design challenges within thermal engineering.

Topology optimization is applied in an industrial project to design the heat rejection system of a robotic downhole oil well intervention tool and an optimized prototype is built that can operate in environments of 200 °C instead of 175 °C, opening a new market for the company. A similar model is used in a different project to optimize the heat sink of a commercial tablet. The design of 3D printed dry-cooled power plant condensers using a simplified thermofluid topology optimization model is presented in another study. A benchmarking of the optimized geometries against a conventional heat exchanger design is conducted and the topology optimized designs show a superior performance. A thermofluid topology optimization heat sink model is applied to the design of forced convection air-cooled heat sinks. Two topology optimized designs are exemplarily benchmarked against a size optimized parallel fin heat sink and an up to 13% lower thermal resistance is found to be realized by the topology optimization. The design of cross-flow heat exchangers using thermofluid topology optimization is presented in another work. This novel approach can explicitly solve the Navier Stokes equations and capture the heat transfer in both fluids at a low computational cost.

Lastly, the fabrication and experimental validation of different topology optimized heat transfer devices is summarized. The developed robotic downhole tool prototype is successfully tested in the laboratory under conditions similar to those in boreholes. Two optimized commercial tablet heat sinks are manufactured, mounted in the device, and experimentally compared to an unoptimized heat sink. Moreover, the fabrication and experimental benchmarking of 3D optimized natural convection heat sinks against conventional heat sink designs is presented. Investment casting using 3D stereolithography printed patterns is used to fabricate different heat sink designs and this technology is demonstrated to be promising for the fabrication of topology optimized metal parts.

Resumé (Danish abstract)

Formålet med denne afhandling er at anvende topologioptimering til designet af forskellige termiske systemer såsom varmeafledere og varmevekslere, for at forbedre den termiske ydeevne af disse systemer sammenlignet med konventionelle designs. Design af termiske systemer er en kompleks opgave, der traditionelt er baseret på erfaring, intuition og "trial-and-error" tilgange. Topologioptimering giver derimod mulighed for systematisk optimering af sådanne systemer og identifikation af utilsigtede og uventede geometrier. Både numeriske optimeringer og til en vis grad eksperimentelle valideringer af optimerede designs præsenteres i denne afhandling. Hovedbidraget fra denne afhandling er udviklingen af flere numeriske optimeringsmodeller, der kan anvendes til forskellige designudfordringer inden for termoteknik.

Topologioptimering anvendes i et industriprojekt til design af et varmeafledningssystem til et kabelbaserede oliebrønd-robot-værktøj. En optimeret prototype, der kan fungere ved 200 °C i stedet for 175 °C, er bygget, og dette åbner et nyt marked for virksomheden. En lignende topologioptimeringsmodel bruges i et andet projekt til design af varmeafledere til en kommerciel tablet. Design af 3D-printede tørkølede kraftværkkondensatorer ved anvendelse af topologioptimering er præsenteret i et andet studie. En sammenligning af et konventionelt parallelkanal varmevekslerdesign og topologi-optimerede-varmevekslere er udført, og de topologioptimerede designs præsterer bedst. En termofluid-topologioptimering varmeafleder model anvendes til konstruktionen af en varmeafleder med tvungenkonvektion-luftkøling. To topologioptimerede designs er eksempelvis sammenlignet med en parallel fin varmeafleder, og op til 13% lavere termisk modstand opnås ved topologioptimering. Designet af tværstrømsvarmevekslere ved anvendelse af termofluid topologioptimering er præsenteret i et andet projekt. Denne nye tilgang kan eksplicit beskrive varmeoverførslen i begge væsker ved lave beregningsomkostninger.

Endelig opsummeres fremstillingen og eksperimentel validering af forskellige topologioptimerede varmeoverføringsenheder. Den udviklede olie-brønd-robotværktøj-prototype testes med succes i laboratoriet under forhold, der ligner dem i borehuller. To optimerede tablet-varmeafledere fremstilles, monteres i enheden og eksperimentelt sammenlignes med en ikke-optimeret varmeafleder. Desuden præsenteres fremstilling og sammenligning af 3D optimerede naturlig-konvektion-varmeafledere og konventionelt designede varmeafledere. Investeringsstøbning ved hjælp af 3D stereolithografisk trykte mønstre bruges til at fremstille forskellige varmeafledere, og denne teknologi er lovende demonstreret til fremstilling af topologioptimerede metaldele.

Preface

This PhD project has been funded by the TOpTEn project sponsored through the Sapere Aude Program of the Danish Council for Independent Research (DFF 4005-00320). Moreover, I would like to thank the Direktør Professor H.I. Hannovers Legat for a travel grant which partially supported my 4.5 months external research stay at the University of Wisconsin – Madison.

First of all, I wish to sincerely thank my supervisors Kurt Engelbrecht, Boyan Lazarov, and Ole Sigmund for the guidance, support, and stimulating discussions during these three years. I have learnt a lot from each one of you and it has been a pleasure to work with you. In particular, I would like to express my deep gratitude towards my main supervisor Kurt who has always been a great support and ready to help while also giving me the freedom and trust to pursue my ideas independently. Moreover, I wish to sincerely thank Greg Nellis who supervised me during my external research stay in the Mechanical Engineering Department at UW - Madison.

Furthermore, I would like to thank Stefano Soprani, Tian Lei, Alberto Damonte, Alessandro Manzo, and David Martinez for the close and enjoyable collaboration in different research projects.

Thank you, Sanford Klein for the stimulating discussions during my time in Madison, Rasmus Bjørk for the help with regards to running COMSOL/MATLAB on the cluster, Niels Aage, Casper Andreasen, and Joe Alexandersen for the help with regards to the topology optimization implementation in COMSOL, Andrea Insinga for the help with different problems in MATLAB and LaTeX, and Katrine Elsøe for revising the Danish abstract of this thesis.

I also wish to thank my colleagues in the EFM section, especially Kristina Navickaité and Stefano Dall'Ollio, and in the TopOpt group for the collegial atmosphere and for always being willing to provide help. Also, I would like to thank Nini Pryds for the advice he has provided during my PhD studies and our secretary Anita Voss for the much appreciated help with various administrative issues. Moreover, thanks to the members of the Solar Energy Lab at UW – Madison, especially Ahmad, for the collegial work atmosphere during my stay in the group.

A special thanks to my friends in DTU Energy, especially Alessia, Alex, Daniel, Hendrik, Katrine, Kosova, Kristina, Megha, Salvo, and Stéven, as well as Michael and Tony in DTU Elektro, for the time spent together and all the serious and silly discussions in these three years. Also, a special thanks to my old friends in Germany, particularly Artur, Clemens, and Sven, for having stayed in close contact despite the physical distance.

Finally, I wish to express my deep gratitude towards my parents, Gabi and Klaus, and my siblings, Anna and Kai, for the continuous support during my PhD studies and my entire life.

List of Publications

The following journal articles, conference papers and extended conference abstract are part of this thesis:

P1 S. Soprani, J. H. K. Haertel, B. S. Lazarov, O. Sigmund and K. Engelbrecht, "Topology Optimization of an Actively Cooled Electronics Section for Downhole Tools", *Proceedings of the COMSOL Conference 2015*, 2015

P2 S. Soprani, J. H. K. Haertel, B. S. Lazarov, O. Sigmund and K. Engelbrecht, "A design approach for integrating thermoelectric devices using topology optimization", *Applied Energy*, vol. 176, pp. 49-64, 2016.

P3 J. H. K. Haertel and G. F. Nellis, "A Fully Developed Flow Thermofluid Model for Topology Optimization of 3D-Printed Air-Cooled Heat Exchangers", *Applied Thermal Engineering*, vol. 119, pp. 10-24, 2017.

P4 J. H. K. Haertel, K. Engelbrecht, B. S. Lazarov and O. Sigmund, "Topology Optimization of Thermal Heat Sinks", *Proceedings of the COMSOL Conference 2015*, 2015.

P5 J. H. K. Haertel, K. Engelbrecht, B. S. Lazarov and O. Sigmund, "Topology Optimization of a Pseudo 3D Thermofluid Heat Sink Model", *International Journal of Heat and Mass Transfer*, vol. 121C, pp. 1073-1088, 2018.

P6 T. Lei, J. Alexandersen, B. S. Lazarov, F. Wang, J. H. K. Haertel, O. Sigmund and K. Engelbrecht, "Investment casting and experimental test of heat sinks designed by topology optimization", [Under review in *International Journal of Heat and Mass Transfer*].

P7 J. H. K. Haertel, K. Engelbrecht, B. S. Lazarov and O. Sigmund, "Cross-flow heat exchanger design using thermofluid topology optimization", Extended abstract, *10th International Conference on Computational Heat, Mass and Momentum Transfer (ICCHM^{2}T 2017)*, 2017.

Contents

Chapter 1

Introduction

1.1 Motivation

The continuous downscaling of semi-conductor electronics in devices such as smartphones and laptops which goes along with increasing power rates that need to be dissipated poses significant challenges to the cooling design of these systems (Garimella et al., 2008). Efficient heat management of electronics is moreover desirable as it allows operation at higher performance for longer periods of time (Vassighi and Sachdev, 2006). Also the performance of various other technical devices as for example heat exchangers and thermoelectric generators depends critically on effective heat transfer. Improved thermal design can reduce the device's energy consumption during operation which also reduces the operational costs; e.g. less pumping power needed for an optimized heat exchanger that transfers the same amount of heat at a lower pressure drop. Another possible objective of thermal design optimization is to increase the efficiency per heat exchanger mass or volume which can save material and result in more compact and cost-effective devices, hence yielding a competitive advantage for the manufacturer.

The design of thermal systems is a complex task that has traditionally relied on the engineers' experience and intuition, insights from experiments as well as numerical studies, and trial-and-error approaches. In contrast, topology optimization (TO) allows for an automated and systematic optimization of thermal systems and the identification of complex and unintuitive optimized structures. The latter becomes even more important with the increasing maturing of additive manufacturing technologies that offer unprecedented design freedom. The aim of this thesis is to extend the state of the art of thermofluid topology optimization using a commercial finite element software. Different optimization models are developed in order to open new application areas for topology optimization in the field of thermal engineering. Solving coupled thermofluid problems is computationally expensive and the main challenge of the works presented in this thesis is to simplify the considered design problems to optimization models which can be solved on a powerful desktop computer and in the used commercial simulation software framework. This allows these optimization models to be applied by a broader range of users than dedicated large-scale optimization models which require longer development time and access to high performance computing tools.

1.2 Introduction to Topology Optimization

Size, shape, and topology optimization deal with improving a structure with regards to a desired objective, e.g. stiffness or temperature while satisfying a given set of constraints, e.g. the amount of material used or the system pressure drop. In size optimization, the design variables can be for example the thickness or width of members of a predefined structure. In shape optimization, the shape of a structure is described by a predefined parametrization

which contains the design variables. Both size and shape optimizations are limited in the set of possible optimization outcomes as a priori assumptions about the design need to be made. Topology optimization can be seen as a generalization of shape optimization as also topological[1] changes can occur during the optimization process. Moreover, it has the distinct advantage that no initial design parametrization is needed which can save development time and allows, as stated above, to identify complex and unexpected optimized geometries.

Topology optimization was originally introduced almost three decades ago by Bendsøe and Kikuchi (Bendsøe and Kikuchi, 1988) using "the homogenization approach to topology optimization". Over the time, different topology optimization approaches have been developed which include density (Bendsøe, 1989; Zhou and Rozvany, 1991; Mlejnek, 1992), level set (Wang et al., 2003; Allaire et al., 2004), topological derivative (Sokolowski and Zochowski, 1999), evolutionary approaches (Xie and Steven, 1993), and others. Density-based topology optimization is the only technique used in the works included in this thesis and the reader is referred to a review paper by Sigmund and Maute (Sigmund and Maute, 2013) for an overview and comparison of the different approaches. Topology optimization is concerned with distributing material within a specified region, referred to as the design domain, to find the optimal layout of a structure within this region. In density-based topology optimization the material distribution problem is represented by a density field which can take the value of 0, corresponding to void, and 1, corresponding to solid, in each point of the design domain, hence allowing for a flexible representation of arbitrary topologies. This binary optimization problem is relaxed to continuous values between 0 and 1 in order to make use of efficient gradient-based optimization methods as sensitivity information in topology optimization can be obtained at low computational cost. The optimization consists of a repeated evaluation of the discretized physics problem, computation of the sensitivities, and design update until convergence to a final optimized design is reached. A comparison of size optimization, shape optimization, and topology optimization based on a structural mechanics problem is shown in Fig. 1.1.

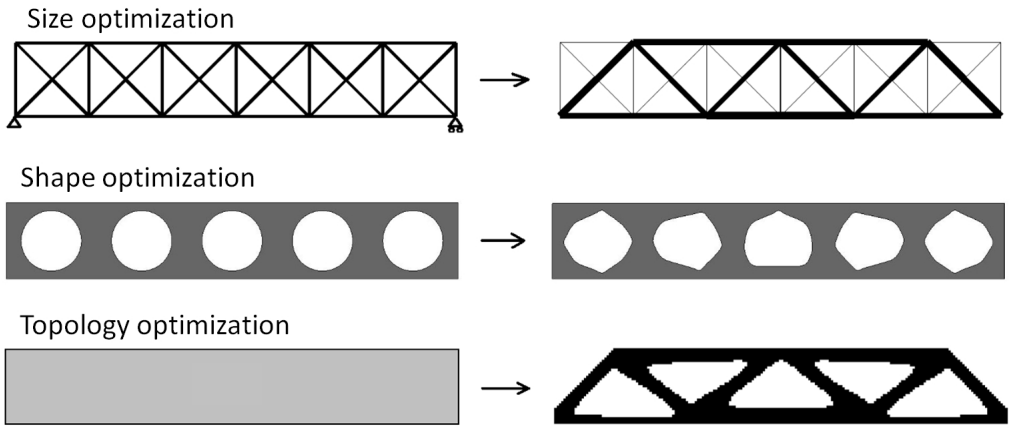

Fig. 1.1: Comparison of size optimization, shape optimization, and topology optimization based on a structural mechanics problem (Bendsoe and Sigmund, 2003).

[1]The topology defines the way in which constituent parts are interrelated or arranged. A given topology is conserved under continuous deformation such as bending or stretching, but not merging or detaching.

A comprehensive treatment of topology optimization theory, methods, and applications is found in the monograph by Bendsøe and Sigmund (Bendsoe and Sigmund, 2003). Topology optimization originated and matured within structural mechanics but has since then been applied to a wide range of fields such as acoustics (Dühring et al., 2008), photonics (Jensen and Sigmund, 2011), heat transfer (Sigmund, 2001), and others. Topology optimization applied to the design of thermal systems is an active area of research. Early applications of topology optimization to heat transfer problems deal with 2D heat conduction problems with convective heat transfer to an ambient fluid in the out-of-plane direction under the assumption of a constant heat transfer coefficient as for example presented in (Sigmund, 2001). The design dependent convective boundary to the ambient fluid needs to be captured when treating 2D conduction problems with convective heat transfer within the modeled plane. This can be achieved by using an interpolation scheme (Yin and Ananthasuresh, 2002; Bruns, 2007; Iga et al., 2009), by applying level set based topology optimization to track the boundary (Ahn and Cho, 2010), or by comparing the density of adjacent elements in the finite element mesh (Joo et al., 2017). A constant heat transfer coefficient is assumed in (Yin and Ananthasuresh, 2002; Bruns, 2007; Ahn and Cho, 2010) whereas (Iga et al., 2009) and (Joo et al., 2017) use a surrogate model for the heat transfer coefficient to capture the dependence of the local convective heat transfer on the geometry of the optimized structure to some degree. More recently published works present also 3D optimization models with diffusive heat transport in the solid and design dependent convective boundaries with a constant heat transfer coefficient using density-based (Dede et al., 2015; Zhou et al., 2016) and level set (Coffin and Maute, 2016a) topology optimization. An optimized heat sink design is fabricated using additive layer manufacturing and subsequently experimentally evaluated in the work by Dede and coworkers (Dede et al., 2015). Pizzolato et al. (Pizzolato et al., 2017) apply density-based topology optimization to the design of conducting fins in a phase change material (PCM) storage tank modeling the solidification of the PCM as transient thermal diffusion problem both in 2D and 3D. The work presented in paper **P2** (and preliminary results in paper **P1**) deals with the thermal integration of a thermoelectric cooler in a robotic downhole intervention tool using topology optimization to distribute conducting and insulating material in a 3D domain. An existing industrial design challenge is addressed in this study and, for the first time, topology optimization is applied to the thermal design of a thermoelectric system, including a detailed model of the thermoelectric (Peltier) cooler. Furthermore, the fabrication and experimental validation of the optimized prototype is presented. The work shown in section 4.2 and 6.3 deals with the heat rejection enhancement of a commercial tablet (Damonte, 2017; Manzo, 2017). Two topology optimized heat sink designs are generated based on a 2D steady state thermal diffusion model. The designs are fabricated, mounted in the tablet, and experimentally benchmarked against an unoptimized heat sink.

The studies on topology optimization presented above simplify the heat transfer to the ambient fluid by assuming a constant heat transfer coefficient or a surrogate model for it. This limiting assumption can be avoided when using conjugate heat transfer, or thermofluid, topology optimization models that also explicitly consider the heat transfer in the fluid during the optimization. Fluid flow topology optimization was first treated in the seminal paper by Borrvall and Petersson (Borrvall and Petersson, 2003) for Stokes flow and later extended by others to the Navier-Stokes equations (Gersborg-Hansen et al., 2005; Olesen et al., 2006). Flow through solid areas is penalized in these works by a friction term based on lubrication theory. In later works as e.g. (Andreasen et al., 2009) for a transport problem, a Brinkman friction

term, which represents the force exerted on a fluid flowing through an ideal porous medium, is used to control the flow during the optimization. Alternatively, level-set based topology optimization has been applied to fluid topology optimization as for example presented in (Zhou and Li, 2008; Challis and Guest, 2009; Kreissl and Maute, 2012). Later works have also treated turbulent flow problems applying the Spallart-Almaras turbulence model to the design of 2D ducts (Kontoleontos et al., 2013; Yoon, 2016; Papoutsis-Kiachagias and Giannakoglou, 2016) and also 3D industrial applications (Papoutsis-Kiachagias and Giannakoglou, 2016), i.e. the optimization of an air-conditioning duct in a passenger car and the optimization of a plenum chamber of a race car. Very recently, Dilgen et al. (Dilgen et al., 2017) presented topology optimization of 2D and 3D turbulent flow problems using different turbulence closure models. Topology optimization of transient flow problems has been treated in (Deng et al., 2011; Kreissl et al., 2011; Deng et al., 2013) using a finite element framework and (Nørgaard et al., 2016) using the lattice Boltzmann method.

First more academic applications of topology optimization to 2D forced convection conjugate heat transfer problems are given in (Dede, 2009; Yoon, 2010). 2D topology optimization of water-cooled microchannel heat sinks is presented in (Dede, 2012) solving the Navier-Stokes equations and (Koga et al., 2013) assuming Stokes flow where (Koga et al., 2013) fabricate and experimentally evaluate an optimized heat sink prototype. Matsumori et al. (Matsumori et al., 2013) apply topology optimization to a 2D thermofluid heat exchanger model under the assumption of the same thermal conductivity in the solid and fluid. Similar but more general models, as conductivity differences between solid and fluid are considered, are treated in (Yaji et al., 2016) that apply 2D lattice Boltzmann modeling and (Yaji et al., 2015) who use a level set topology optimization approach to generate optimized designs in 2D and 3D. A thermofluid model for topology optimization under tangential thermal gradients is presented (Qian and Dede, 2015). The abovementioned works on thermofluid topology optimization of heat sinks, except for (Yaji et al., 2015) that also conduct 3D optimizations, rely on 2D optimization models. This approach was extended by (McConnell and Pingen, 2012) and later **P4** to a pseudo 3D model with a heat sink base plate thermally interacting with a thermofluid design layer that represents the heat sink fins and fluid flow.

The main contribution of **P5** is to validate the underlying assumptions of the pseudo 3D heat sink model and to demonstrate its capabilities in different studies as only some exemplifying results are provided in the conference papers (McConnell and Pingen, 2012) and **P4**. Novelties presented in **P5** are the comparison of heat transfer resistance minimized fins to pressure drop minimized fins and the analysis of the influence of thermal hotspots in the heat sink base plate on the topology optimization. Also the application of symmetry boundary conditions to generate designs periodic to the flow direction and the benchmarking of topology optimized designs against size optimized parallel fin designs had thus far only been presented in the fully developed flow heat exchanger model treated in **P3**. The 2D optimization model presented in **P3** differs from the works above as the fluid flow is not within the modeled plane but perpendicular to it. Moreover, the abovementioned thermofluid topology optimization works treat rather academic heat sink or heat exchanger problems whereas the optimizations in **P3** are conducted for specific "real world" operating conditions associated with dry-cooled power plant condensers, even though the optimization is accomplished using some simplifying assumptions. Furthermore, a systematic benchmarking of the topology optimized designs against a size optimization model is provided which had been a novelty for thermal topology optimization. The cross-flow heat

exchanger topology optimization model presented in section 5.3 is a combination of the in-plane 2D Navier-Stokes flow modeled in **P5** and the out-of-plane fully developed flow modeled in **P3**. This interpolation between two flows perpendicular to each other is a novelty in topology optimization. Moreover, a boundary identification method (Clausen et al., 2015) is for the first time applied to fluid flow topology optimization to represent the heat exchanger material between the different flows.

All thermofluid topology optimization models mentioned above assume viscous flow in the fluid problem whereas a thermofluid Darcy potential flow model is used in (Zhao et al., 2018) to approximate turbulent flow in a cooling channel design problem. Turbulent flow thermofluid topology optimization has thus far to the author's best knowledge only been presented in (Kontoleontos et al., 2013) using a Spalart-Allmaras turbulence model; however, the temperature distribution in the solid is neglected in the work.

Natural convection topology optimization problems have only more recently been treated due to the complex coupling of the thermal and fluid problem. The field was pioneered by Alexandersen et al. (Alexandersen et al., 2014) presenting 2D density-based topology optimization of heat sinks and micropumps. A steady-state laminar flow is assumed and the coupling of the thermal and fluid problem is modeled using the Boussinesq approximation. The natural convection heat sink model was later extended to 3D (Alexandersen et al., 2015) and large-scale 3D (Alexandersen et al., 2016). Level set-based topology optimization applied to 3D and 2D transient natural convection problems is treated in (Coffin and Maute, 2016b). Also the designs presented in **P6** rely on the large-scale 3D model presented in (Alexandersen et al., 2016); however, the focus of **P6** lies on the fabrication and experimental validation of the optimized heat sinks. For the first time, investment casting using 3D stereolithography printed patterns is used to fabricate 3D metal heat transfer devices designed by topology optimization. Moreover, the fabricated heat sinks are compared experimentally to pin-fin heat sinks and it is shown that the topology optimized heat sinks perform best at the conditions designed for in all analyzed cases. The reader is referred to the review paper by Dbouk (Dbouk, 2016) for an in-depth summary of works on topology optimization applied to the design of thermal systems.

The main contributions of this thesis are summarized in the following:

- Paper **P2** demonstrates the applicability of topology optimization as a design tool for efficient thermal integration of a thermoelectric module into a system with specific design constraints. A 3D thermal diffusion topology optimization model including a detailed model of a thermoelectric cooler is developed and used for this purpose.

- Paper **P3** presents a novel fully developed flow thermofluid topology optimization model where the fluid flow is perpendicular to the 2D modeled design domain. The model is applied to the design of dry-cooled power plant condensers considering specific operating conditions associated with such devices. Moreover, a systematic benchmarking against a conventional heat exchanger geometry is conducted showing superior performance of the topology optimized designs.

- In paper **P5**, detailed studies on a thermofluid pseudo 3D heat sink model are presented and the underlying assumptions of this modeling approach are validated. Furthermore, thermal resistance minimized heat sink fins are compared to pressure drop minimized fins and the effect of thermal hot spots in the base plate on the topology optimization is studied.

- In section 5.3 of this thesis and the extended conference abstract **P7**, a novel cross-flow heat exchanger topology optimization model is presented which explicitly considers the heat transfer in two fluids flowing perpendicular to each other. A boundary identification method is used to represent the heat exchanger material which separates the two 2D modeled flows.

Chapter 2

Topology optimization implementation

2.1 General design problem

As stated in section 1.2, a continuous design field (density field), γ, taking values between 0 and 1 in each point of the design domain, Ω_d, is introduced in density-based topology optimization to represent the material distribution problem that minimizes an objective functional, F, subject to given constraint functionals, G_j. This optimization problem can be stated mathematically as follows:

$$\begin{aligned} \min_{\gamma}: \quad & F = F(\gamma, \mathbf{s}(\gamma)) \\ \text{s.t.:} \quad & \mathcal{R}(\gamma, \mathbf{s}(\gamma)) = \mathbf{0} \\ & G_1(\gamma) = \int_{\Omega_d} \gamma \; dV - f \, V_{\Omega_d} \leq 0 \\ & G_i(\gamma, \mathbf{s}(\gamma)) \leq 0, \qquad\qquad i = 2, ..., M+1 \\ & 0 \leq \gamma(\mathbf{x}) \leq 1, \qquad\qquad \forall \, \mathbf{x} \in \Omega_d \end{aligned} \tag{2.1}$$

where $\mathbf{s}$ is the state vector of the considered physics problem, $\mathcal{R}$ is the residual of the discretized physics problem, G_1 is a volume constraint that limits the amount of material distributed in the design domain with volume V_{Ω_d} to the prescribed volume fraction f, and G_i correspond to M extra constraints that may be included in the design problem.

2.2 Interpolation functions

Different interpolation functions are used in density-based topology optimization to interpolate between design density and material properties. In many problems it is necessary that intermediate densities are sufficiently penalized by the interpolation function to ensure convergence to a final black and white design. This can be achieved using for example the SIMP (Solid Isotropic Material with Penalization) or power law approach which was first introduced by Bendsøe (Bendsøe, 1989) and is defined as:

$$I_{SIMP} = \gamma^p \tag{2.2}$$

where p is the penalization exponent which can be set to a value greater than 1 to penalize intermediate densities. An alternative interpolation function that has among others the advantage over the SIMP interpolation of a non-zero first derivative at $\gamma = 0$, is a RAMP-style

interpolation introduced by Stolpe and Svanberg (Stolpe and Svanberg, 2001a). A slightly modified version of this interpolation is presented in (Alexandersen et al., 2014) and given by:

$$I_j(\gamma) = \frac{\gamma\,(C_j(1+b_j)-1)+1}{C_j\,(1+b_j\,\gamma)} \tag{2.3}$$

where b_j is the interpolation convexity parameter and C_j is defined by the ratio of material properties of the two phases between which is interpolated. For the Brinkman friction term used in topology optimization of fluids, an interpolation function as stated in (Alexandersen et al., 2014) and introduced in the seminal paper by Borrvall and Petersson (Borrvall and Petersson, 2003) can be used:

$$I_\alpha(\gamma) = \frac{1-\gamma}{1+b_\alpha\,\gamma} \tag{2.4}$$

where b_α is a parameter determining the convexity of the interpolation.

2.3 Adjoint sensitivity analysis

The sensitivities of the objective and given constraint functionals with respect to the design variables need to be determined in order to use efficient gradient-based optimization methods. Topology optimization is characterized by a large number of design variables and typically few constraint functionals. For these kind of problems, the adjoint method (Michaleris et al., 1994; Giles and Pierce, 2000) can provide the design sensitivities very efficiently. The adjoint problem is given by:

$$\left(\frac{\partial \mathcal{R}}{\partial \mathbf{s}}\right)^T \lambda = \left(\frac{\partial \Phi}{\partial \mathbf{s}}\right)^T \tag{2.5}$$

where λ is the vector of the adjoint varibles and $\Phi(\gamma, \mathbf{s}(\gamma))$ is either the objective functional or a given constraint functional that depends on the design and state variables. The design sensitivities can be computed as:

$$\frac{d\Phi}{d\gamma} = \frac{\partial \Phi}{\partial \gamma} - \lambda^T \frac{\partial \mathcal{R}}{\partial \gamma} \tag{2.6}$$

where $\frac{d}{d\gamma}$ indicates the total derivative and $\frac{\partial}{\partial \gamma}$ the partial derivative with regards to the design variables. The partial derivatives of Φ and $\mathcal{R}$ with respect to the design variables can be derived analytically. It is important to emphasize that the adjoint problem (2.5) is linear also in case of the state problem being nonlinear. It should moreover be noted that the transpose of the tangent system matrix of the original state problem, $\left(\frac{\partial \mathcal{R}}{\partial \mathbf{s}}\right)^T$, can be re-used when solving the adjoint problem for one or more constraint functionals in addition to the objective functional.

2.4 Density filter and projection

Density filtering is used in topology optimization to ensure mesh independence of the solution[1] and is, moreover, needed in thermofluid topology optimization to avoid problems with ill-posedness of the optimization problem (Sigmund and Petersson, 1998). A Helmholtz-type

[1] Mesh-dependency means that qualitatively different designs are obtained for different mesh-sizes. Ideally, mesh-refinement should allow for a more detailed resolution of the physics and better description of the boundary region but result in the same optimized structure.

partial differential equation (PDE) filter (Lazarov and Sigmund, 2011) is an easy-to-implement density filter:

$$-r_{filter}^2 \nabla^2 \tilde{\gamma} + \tilde{\gamma} = \gamma \qquad \text{in } \Omega_d \tag{2.7}$$

where $\tilde{\gamma}$ is the filtered design field and r_{filter} is the filter parameter. To reduce the gray area between solid and fluid which is inherently introduced by the filtering process, a smoothed heaviside projection (Wang et al., 2011) can be applied on the filtered design field:

$$\bar{\tilde{\gamma}} = \frac{\tanh(\beta\,\eta) + \tanh(\beta\,(\tilde{\gamma} - \eta))}{\tanh(\beta\,\eta) + \tanh(\beta\,(1 - \eta))} \tag{2.8}$$

where $\bar{\tilde{\gamma}}$ is the projected design field, β is a parameter controlling the projection steepness, and η is the projection threshold parameter. It should be noted that the projected design field becomes the physical meaningful one in the interpolation functions (2.2, 2.3, 2.4).

2.5 Topology optimization process

The flow of computations for gradient-based topology optimization using the finite element method (FEM) is shown in Fig. 2.1. The optimization is initialized by providing an initial design or initial guess. This choice can be important as for example thermofluid topology optimization often results in quite non-convex optimization problems where the risk of converging to only locally optimal topologies may be high. Based on the initial design, a finite element analysis of the (multi) physics problem of interest is conducted. If e.g. thermal diffusion or thermofluid problems are considered, the FEM analysis yields the temperature field and, in case of thermofluid problems, also the velocity- and pressure field. The sensitivities of the objective functional and given constraint functionals are then determined using the adjoint method as briefly described in section 2.3. Based on this information, an optimization method is used to conduct the design update. Topology optimization problems are nonlinear optimization problems with a large number of design variables and can be solved with various numerical optimization methods. The Method of Moving Asymptotes (MMA) (Svanberg, 1987) which was specifically developed for structural optimization applications and its globally convergent version GCMMA (Svanberg, 2002) are well established within the density-based topology optimization community due to their versatility and applicability to large-scale problems (Bendsoe and Sigmund, 2003; Deaton and Grandhi, 2014). But also general optimziation methods as for example Sequential Quadratic Programming (Boggs and Tolle, 1995) and primal-dual interior point methods (Forsgren and Gill, 1998) can be applied to topology optimization. Interested readers are referred to (Rojas-Labanda and Stolpe, 2015) that provides a benchmarking of different optimization solvers applied to finite element based structural topology optimization problems. Once the updated design is computed, the optimization is checked for convergence based on a suitable criterion or the optimization is stopped when a specified number of optimization iterations are reached. The cycle from FEM analysis to design update is repeated in case the convergence criterion or maximum number of optimization iterations is not yet reached.

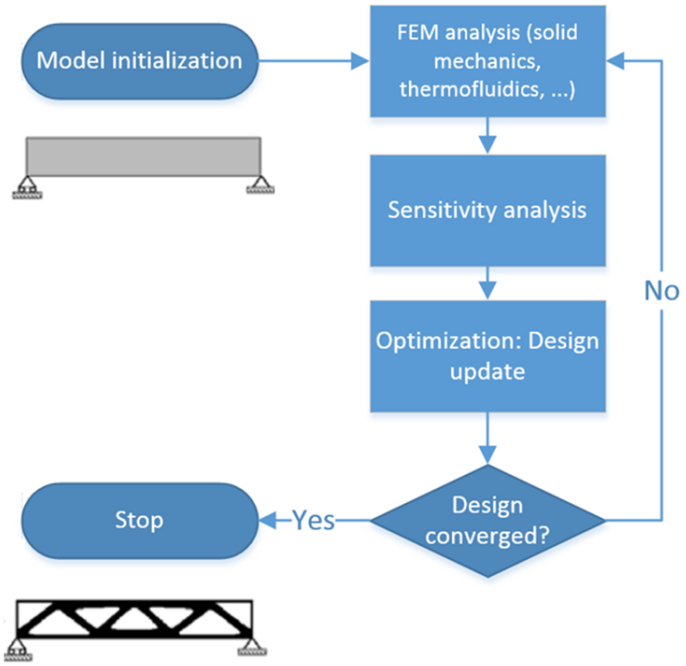

Fig. 2.1: The flow of computations for gradient-based topology optimization using the finite element method.

2.6 Governing equations of thermal and thermofluid topology optimization

In this section, it is briefly described in a general way how the topology optimization method is coupled with the governing equations of heat transfer problems. Note that all optimizations presented in this thesis are applied to steady state problems. See the different papers attached to this thesis and section 5.3 for the specific respective modeling approach since the thermal diffusion, thermal convection-diffusion, and Navier Stokes equations are only stated in a general way in the following.

2.6.1 Heat transfer modeling

The thermal diffusion equation is given by:

$$-\nabla \cdot (k_s \, \nabla T_s) = \dot{q}_{source} \tag{2.9}$$

where k_s is the solid thermal conductivity, T_s is the temperature field in the solid, and $\dot{q}_{source}$ can be a volumetric heat source or heat sink. If two materials with different thermal conductivities are distributed by the topology optimization, the solid thermal conductivity is a function of the density field within the design domain. Hence, equation (2.9) becomes:

$$-\nabla \cdot (k_s(\gamma) \, \nabla T_s) = \dot{q}_{source} \qquad \text{in } \Omega_d \tag{2.10}$$

The thermal convection-diffusion equation is defined as:

$$\rho_f \, c_f \, \mathbf{u} \, \nabla T_f - \nabla \cdot (k_f \, \nabla T_f) = \dot{q}_{source} \tag{2.11}$$

where ρ_f is the fluid density, c_f is the specific fluid heat capacity, $\mathbf{u}$ is the fluid velocity vector, and T_f is the fluid temperature field. Within the design domain, the topology otpimziation interpolates between heat transfer in the solid and in the fluid. Thus, equation (2.11) becomes:

$$\gamma \, \rho_f \, c_f \, \mathbf{u} \, \nabla T - \nabla \cdot (k(\gamma) \, \nabla T) = \dot{q}_{source} \qquad \text{in } \Omega_d \tag{2.12}$$

where T is the unified temperature field for solid and fluid. Note that the advective energy transport term is multiplied with the design variable to ensure that no advective energy transport occurs in solid regions. This penalization of the advection term is added since slight fluid leakage through solid regions is to some degree unavoidable in density-based topology optimization.

2.6.2 Fluid dynamics modeling

In all thermofluid models presented in this thesis, a steady state, laminar, and incompressible flow is assumed. The continuity equation and Navier-Stokes equation for an incompressible fluid are defined as:

$$\rho_f \, (\nabla \cdot \mathbf{u}) = 0 \tag{2.13}$$

$$\rho_f \cdot (\mathbf{u} \cdot \nabla) \, \mathbf{u} = -\nabla p + \mu_f \, (\nabla^2 \mathbf{u}) \tag{2.14}$$

where p is the pressure field and μ_f is the dynamic viscosity of the fluid. In fluid flow topology optimization a Brinkman friction term, which corresponds to the force exerted on a fluid flowing through an ideal porous medium, is used to control the flow within the design domain (Borrvall and Petersson, 2003). Adding this velocity dependent momentum sink to the Navier Stokes equation yields:

$$\rho_f \cdot (\mathbf{u} \cdot \nabla) \, \mathbf{u} = -\nabla p + \mu_f \, (\nabla^2 \mathbf{u}) - \overline{\alpha} \, \mathbf{u} \, I_\alpha(\gamma) \qquad \text{in } \Omega_d \tag{2.15}$$

where $\overline{\alpha}$ is the maximum inverse permeability of the porous medium and $I_\alpha(\gamma)$ is the interpolation function stated in section 2.2. The maximum inverse permeability is given by:

$$\overline{\alpha} = \mu_f / (Da \, L_c^2) \tag{2.16}$$

where Da is the Darcy number and L_c a characteristic length of the problem, e.g. the design domain width. The value of the Darcy number is chosen such that the fluid flow through solid domains is negligible. However, too large values of the Darcy number can cause numerical problems and issues with convergence to poor local optima.

Chapter 3

Computational implementation

All topology optimization models presented in this thesis, apart from the optimization model used in paper **P6**, are implemented in the commercial finite element software COMSOL Multiphysics (COM). Note that the description in this chapter only refers to the models used in the papers **P1**-**P5** and section 5.3 as the optimizations presented in paper **P6** were conducted by Joe Alexandersen using a different modeling framework[1]. Using COMSOL has several advantages for setting up multiphysics topology optimization models. It allows for a fast and easy implementation of different coupled physics problems, boundary conditions, and model geometries. Furthermore, it has a built-in library with temperature dependent material properties. Another advantage of using COMSOL for topology optimization applications is its *optimization module* which automatically solves the adjoint problem to provide sensitivities for the objective and constraint functionals. The main limitation of COMSOL is its limited scalability which presently makes the solution of thermofluid 3D or transient 2D models computationally prohibitive. Dedicated models as presented in (Alexandersen et al., 2016) for large-scale 3D heat sink design are currently needed for such optimizations; however, implementing such models requires more development time than modeling in COMSOL and, moreover, access to high performance computing resources. Topology optimization of real-world application 3D thermal diffusion models is possible within COMSOL as shown in paper **P2**, as the governing equations are linear and hence less demanding to solve in a TO implementation. Another drawback of COMSOL is the limited possibility to control and access numerical and optimization parameters which, in case problems occur during the optimization, limits the options of troubleshooting and fixing these problems.

COMSOL's *heat transfer module* is used in all models to solve the respective thermal problem and COMSOL's *CFD module* is used to solve the Navier Stokes equations in the thermofluid models presented in P4, P5, and section 5.3. The simplified Navier-Stokes fully developed flow equation solved in the model presented in paper **P3** and section 5.3 is implemented in the *coefficient form PDE interface* which is also used in all models to solve the filter-PDE 2.7. Meshes comprised of triangular elements are used in all 2D optimization models and tetrahedral elements are used in the 3D optimization model presented in the papers **P1** and **P2**. The parallel sparse direct solver PARDISO (Schenk and Gärtner, 2004) that is available in COMSOL is used to solve the system of discretized finite element equations. Segregated solver steps are used for the fluid problem, if existent in the model, thermal problem, and filter PDE. All optimizations are conducted using COMSOL's *optimization module* using the Globally Convergent version of the Method of Moving Asymptotes (GCMMA) (Svanberg, 2002). COMSOL automatically provides the sensitivities for the optimization and constraint functionals as stated

[1]The 3D natural convection heat sink designs presented in paper **P6** were generated by Joe Alexandersen using a large-scale in-house thermofluid topology optimization model (Alexandersen et al., 2016) implemented in PETSc (Balay et al., 2016) based on the topology optimization framework described in (Aage et al., 2015).

above. COMSOL is interfaced with MATLAB to allow for automated parameter value changes during the optimization. This is necessary because a continuation approach (Sigmund and Petersson, 1998; Stolpe and Svanberg, 2001b) is applied to the convexity parameters of the different used interpolation functions and the projection steepness parameter. A continuation approach is applied to ensure a more convex optimization problem in the beginning and to consequently gradually increase the penalization of intermediate densities as well as to increase the sharpness of the solid-fluid interface. The optimizations are run on a computer cluster even though they can also be conducted on a powerful desktop computer; however, at a longer computation time. To conduct the optimizations on a computer cluster, MATLAB is run, which then starts the COMSOL server to conduct the optimizations where the parameter changes during the continuation approach are controlled using a MATLAB script.

Chapter 4

Thermal diffusion topology optimization models

4.1 Thermal integration of thermoelectric devices

Paper **P2** and the preliminary results presented in the conference paper **P1** demonstrate how density-based topology optimization can be applied to the thermal design of a thermoelectric system. Effective thermal integration reduces the temperature difference between the thermoelectric module and its thermal reservoirs which increases the overall system efficiency. The specific design challenge considered in this work is the integration of a thermoelectric cooler (TEC) into a robotic downhole oil well intervention tool that operates in environments up to 200 °C. The design of this cooling system was Stefano Soprani's PhD project (Soprani et al., 2016) which was conducted as an industrial PhD project carried out at the company Welltec A/S while Stefano Soprani was enrolled at DTU. A detailed 3D model of the downhole tool had already been implemented by Stefano Soprani in COMSOL and I helped him to couple this model with a topology optimization approach.

The heat management strategy presented in this study is needed to prevent overheating issues when the borehole temperature exceeds the maximum temperature rating of the robotic tool's electronics which is 175 °C. To reject the heat dissipated by the electronics to the hotter well fluid, a thermoelectric cooler is used which can create a heat flux from its cold side to its hot side when an electric current is applied. A representation of the modeled downhole tool including a zoom on the TEC device is shown in Fig. 4.1. The downhole tool has a metallic housing of which the geometry is non-optimizable as its dimensions are defined by the well bore. There are two different electronic components in the tool: the high temperature sensitive (HTS) electronics which are likely to fail at temperatures above 175 °C and the high temperature non-sensitive (HTNS) electronics that can operate at temperatures above 200 °C. Both electronics dissipate heat where the majority of the heat is generated in the HTNS electronics. The HTS electronics are thermally connected to the thermoelectric cooler so that it can absorb the cooling load and maintain the sensitive electronics at a safe temperature. Within the domain of the optimizable chassis, which is shown as slightly transparent light blue in Fig. 4.1, aluminum and insulating material can be distributed freely in order to enable an efficient heat rejection form the TEC's hot side to the well fluid and, at the same time, thermally protect the HTS electronics from the hot surroundings and the heat dissipated by the HTNS electronics. The thermal diffusion equation is solved within the design domain and the thermal conductivity is interpolated between aluminum and insulating material using the SIMP interpolation (equation (2.2)) to represent the material distribution problem. A simplified homogeneous model is used to represent the TEC of which the geometry is fixed and not subject to the optimization. The

heat transfer from the metal housing to the well fluid is not explicitly modeled but represented by Newton's law of cooling, i.e. a specified heat transfer coefficient.

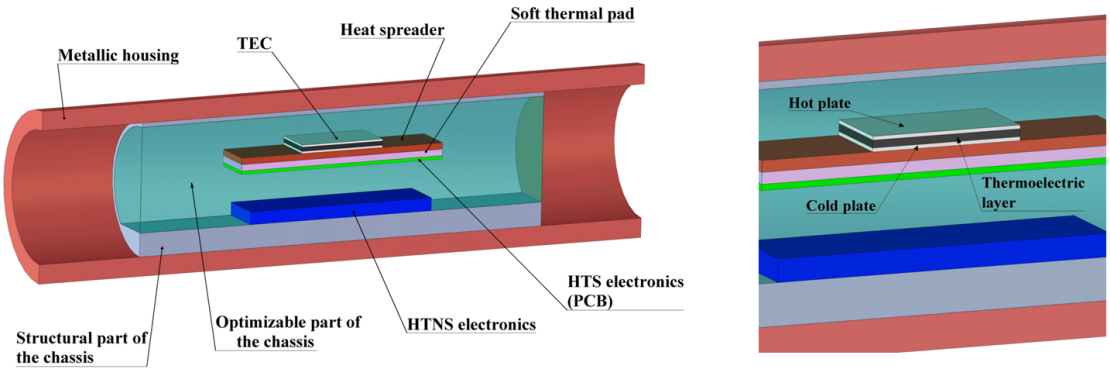

Fig. 4.1: Representation of the longitudinal section of the downhole tool (left) and particular of the thermoelectric cooler (right).

The optimization objective is to minimize the average temperature of the HTS electronics. Optimizations are conducted for different values of TEC feed current and well fluid heat transfer coefficient in order to study the system's performance in different well fluid convection regimes. An exemplifying optimized design and the corresponding temperature distribution are shown in Fig. 4.2 for a TEC feed current of 2 A and a convection coefficient of 100 W/(m^2 K). An aluminum pad connects the hot plate of the TEC to the structural chassis and provides a thermal path to reject the excessive heat radially. The rest of the optimized domain is filled with insulating material to protect the HTS electronics from the hot surroundings. Similar designs are obtained for other combinations of low TEC feed currents and high well fluid convection coefficients. When the well fluid convection coefficient is lowered and the TEC feed current increased, a broader heat sink is generated that spreads the heat not only radially but also along the longitudinal direction of the tool. For the combination of lowest analyzed convection coefficient and highest analyzed TEC feed current, the joule heating in the TEC is higher than the capability of the well fluid to remove the heat through convection. In this case, an active cooling is infeasible so that the HTS electronics heat up above the well fluid temperature and a direct cooling path is formed between the HTS electronics and the structural chassis. To get a better overview of the general design trends with regards to the boundary conditions, the fraction of aluminum placed in the optimizable domain is studied for all simulated cases. It is found that the amount of employed aluminum decreases with increasing convection coefficient and increases with increasing feed current. To choose a design concept that will be robust at different convective regimes in the well, it is important to assess the performance of the optimized designs also at conditions they were not optimized for. A high sensitivity of the optimization process to the TEC feed current is found whereas the convection coefficient only has a minor influence on the optimized designs. Based on the abovementioned studies, an optimized prototype of the actively cooled downhole tool is designed. An optimal TEC feed current which minimizes the HTS electronics average temperature and depends on the convection coefficient is determined for this prototype. The manufacturing, assembly, and experimental testing of the prototype are briefly summarized in section 6.1.

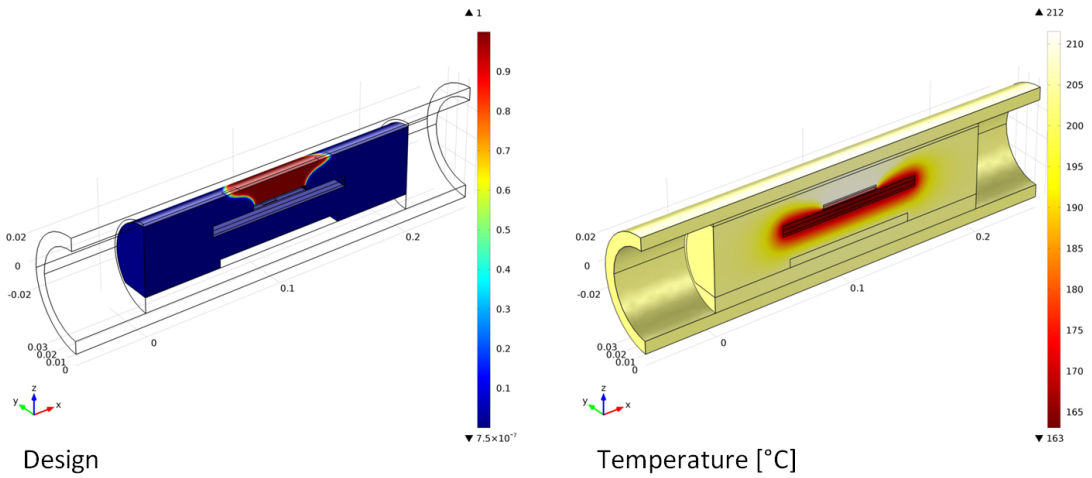

Fig. 4.2: Left: Optimized downhole tool for a TEC feed current of 2 A and a convection coefficient of 100 W/(m^2 K) where red corresponds to aluminum and blue to insulation material. Right: Corresponding temperature distribution within the tool.

4.2 Design optimization of a commercial tablet's heat sink

An optimization model based on the thermal diffusion equation, similar to the model described in section 4.1, was used in a master thesis project to optimize the design of a commercial tablet's heat sink. The master students Alberto Damonte, studying at the Polytechnic University of Milan, and Alessandro Manzo, studying at the Polytechnic University of Turin, collaborated in this thesis project and I co-supervised them. A journal paper, with me as a co-author, is under preparation but it is currently in a draft state and the reader is referred to the master theses (Damonte, 2017; Manzo, 2017) for detailed information on the project. In the following, a brief outline of the modeling and optimization results will be given and a brief outline of the fabrication and experimental validation of optimized heat sinks is given in section 6.3.

A view on the back side of the tablet with back cover and battery removed is shown in Fig. 4.3. Moreover, a zoom on the tablet section where most of the heat is dissipated, which includes the tablet's CPU, is provided. A simplified 2D model of the tablet is implemented in COMSOL which solves the thermal diffusion equation and the heat transfer to the ambient air is modeled under the assumption of a constant convection coefficient. The modeling of the heat generation within the tablet is tuned in the model based on experimental measurements using thermocouples and based on measurements with an infrared thermal imaging camera. The topology optimization method is used to design the tablet's heat sink in order to minimize the average temperature of the design domain and the area around the tablet's CPU. The optimization is conducted both with a "classical" topology optimization formulation and a robust formulation (Wang et al., 2011). In both cases, a volume constraint on the maximum amount of heat sink material is used. Optimized designs, both for the "classical" and robust formulation, are depicted in Fig. 4.4 where the same volume constraint value is used in both cases. The smaller white rectangle represents the area of the tablet CPU where the heat generation is modeled and it can be seen that, in both cases, the heat sink branches from

this area in order to efficiently dissipate the heat. The heat sink that is generated without using a robust formulation extends further away from the area of heat generation and has more branches than the heat sink designed using a robust formulation. Moreover, it can be seen that there is grey area, which is meaningless from a manufacturing point of view, in the design that is generated without robust formulation whereas a sharp heat sink material-void transition is realized in the robust design.

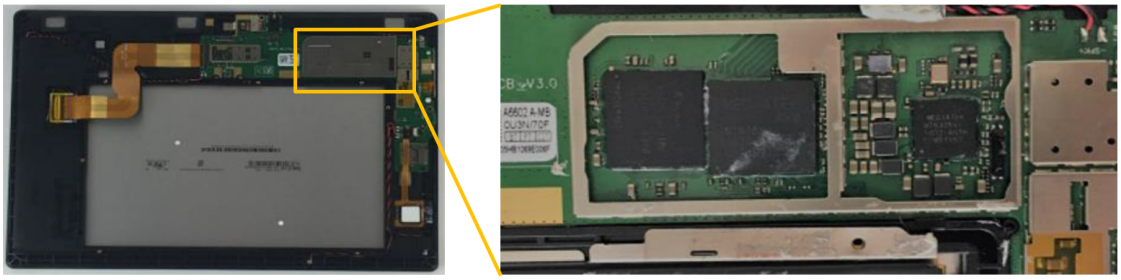

Fig. 4.3: Left: Back side of the tablet with back cover and battery removed. Right: Zoom on the tablet section where most heat is generated which includes the tablet's CPU (Damonte, 2017).

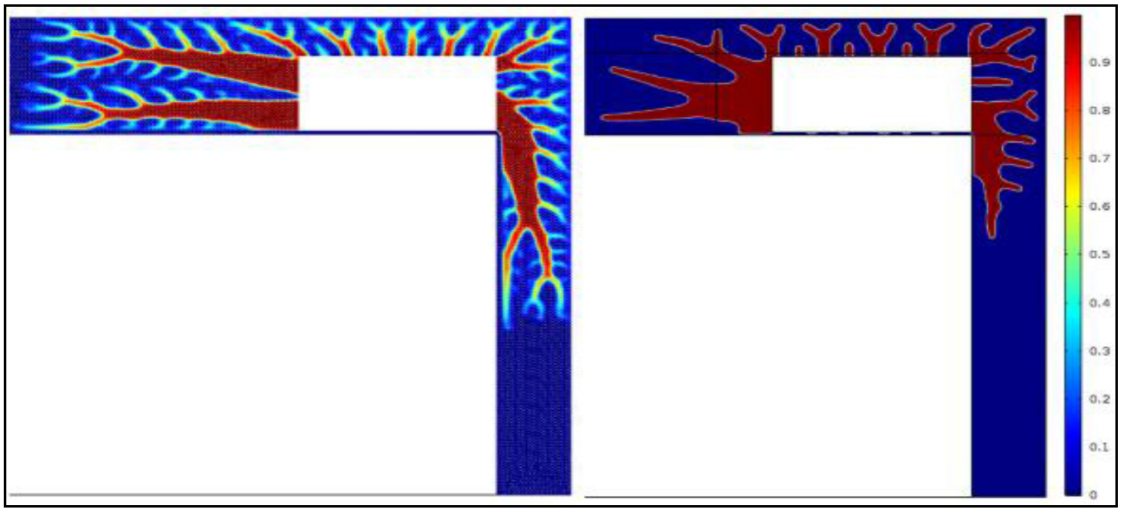

Fig. 4.4: Topology optimized tablet heat sinks without using a robust formulation (left) and with robust formulation to ensure a minimum feature size (right). Red corresponds to heat sink material and blue to void (air) (Damonte, 2017).

Chapter 5

Thermofluid topology optimization models

5.1 A fully developed flow heat exchanger model

The work presented in paper **P3** was conducted during my external stay in the Mechanical Engineering Department at the University of Wisconsin - Madison where I worked within a larger research project that was concerned with designing, fabricating, and experimentally characterizing 3D printed dry-cooled power plant condensers. Economical dry-cooling technologies that do not reduce the power plant efficiency are critically needed as power plants are currently the single largest users of fresh water in the United States (Macknick et al., 2011) which is increasingly becoming an issue in several regions of the country. One 3D printing method considered is fused layer modeling (FLM) which can be used to fabricate complex surfaces from a relatively inexpensive polymer using inexpensive equipment. The major drawback of using polymers as heat exchanger material is their low thermal conductivity; however, this drawback can be overcome by using fillers such as metal filaments to increase the effective conductivity of the resulting composite. It was my task to apply topology optimization to the design of such polymer composite heat exchangers where the specific challenge was to provide a model that is computationally not too expensive for the COMSOL modeling framework and which is stable for the expected Reynolds numbers in the higher range of laminar flow conditions. When using a thermofluid optimization model relying on solving the Navier Stokes equations for the fluid problem as presented in section 5.2 and the papers **P4** and **P5**, stability issues were observed during the optimization for the specific operating conditions of the analyzed heat exchangers. Therefore, a simplified thermofluid fully developed flow model was developed, as it results in a linear Navier Stokes equation which is stable for arbitrary Reynolds numbers in the laminar flow regime. The fully developed flow model is computationally cheaper than a model based on solving the full Navier Stokes equations but still the heat transfer in the fluid is explicitly captured in the optimization model which is not the case in the thermal diffusion models treated in chapter 4. Even though the fully developed flow approach results in a simplified linear Navier Stokes equation, the computational demand is increased compared to pure thermal diffusion models and, hence, only 2D models are studied. However, using a 3D optimization model would only yield a limited benefit as the fully developed flow approach inherently leads to a 2D fluid problem and 2D design space.

The considered heat exchanger is configured in a cross-flow arrangement which is typical for gas-to-liquid heat exchangers. The heat exchanger's macrostructure consists of a large number of unit cells and both the macrostructure and a unit cell are depicted in Fig. 5.1. Within the unit cell, there is substantial design freedom with regards to heat transfer enhancing structures on the air-side. In the applied 2D modeling approach, the unit cell cross section perpendicular

to the air-flow is considered as shown in Fig. 5.2. Colored in grey are the walls separating the water and air flow at the top and bottom of the unit cell as well as the side walls of the unit cell which are required for mechanical stability of the macro-structure. Within the blue inner area, the distribution of material can be freely chosen in order to shape the air channels using heat transfer enhancing structures. To further reduce the computational resources required, only a part of the unit cell's cross section is modeled, as shown in Fig. 5.2. By exploiting symmetry on the left, right, and bottom of the modeled domain, a periodic design representative of the entire unit cell can be obtained by optimizing a relatively small fraction of the cell. Note that the water-side heat transfer is not explicitly modeled in this approach and instead a water temperature is prescribed as the boundary condition on the outer side of the wall. The air flow is modeled under the assumption of a steady state, laminar, and incompressible flow and the fully developed internal flow Navier Stokes equation including a Brinkman friction term is solved for the fluid problem. Within the design domain, the thermal conductivity in the thermal convection-diffusion equation is interpolated between a higher conductivity in the fins and the lower thermal conductivity of air. In this modeling approach, the air-side pressure drop and temperature increase over the heat exchanger are prescribed and values similar to actual operating conditions anticipated in dry-cooled condensers are chosen. See paper **P3** for a detailed description of the modeling including the prescribed boundary conditions.

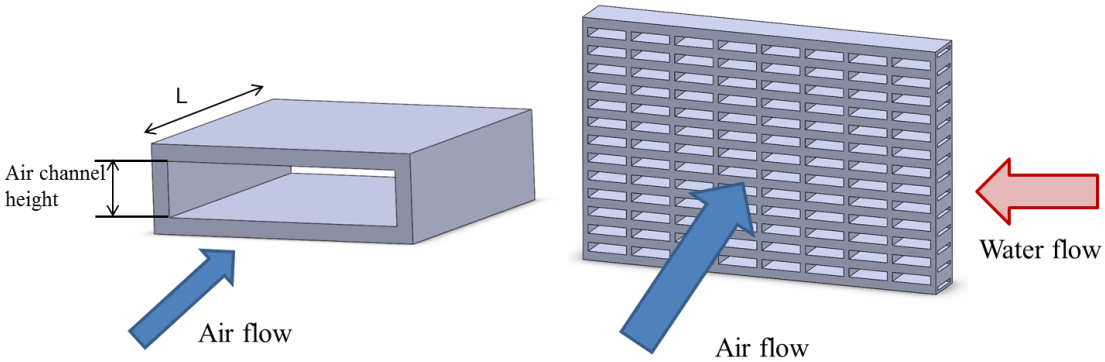

Fig. 5.1: Air-side heat exchanger unit cell (left) shown without heat transfer enhancing structures and macrostructure (right) consisting of a large array of unit cells.

The optimization objective is to maximize the heat transfer rate between water and air and the difference between the air bulk temperature and the prescribed water temperature is set as a constraint. This approach corresponds to maximizing the heat exchanger conductance, which is the inverse of the total thermal resistance between water and air, for a fixed value of air-to-water temperature difference. The optimization model is used to generate optimized structures for different air channel heights and effective polymer composite conductivities ranging between 0.1 W/(m K), which is in the order of unfilled polymers, and 300 W/(m K), which is in the range of metallic materials. An exemplifying optimized design for a polymer composite conductivity of 5 W/(m K) and an air channel height of 6 mm as well as the corresponding air velocity and temperature are shown in Fig. 5.3. The optimized design consists of three fins connected to the wall that separates the water and the air flow. The three fins are roughly of the same size and have smaller secondary branches. The fluid channels tend to become slightly larger closer

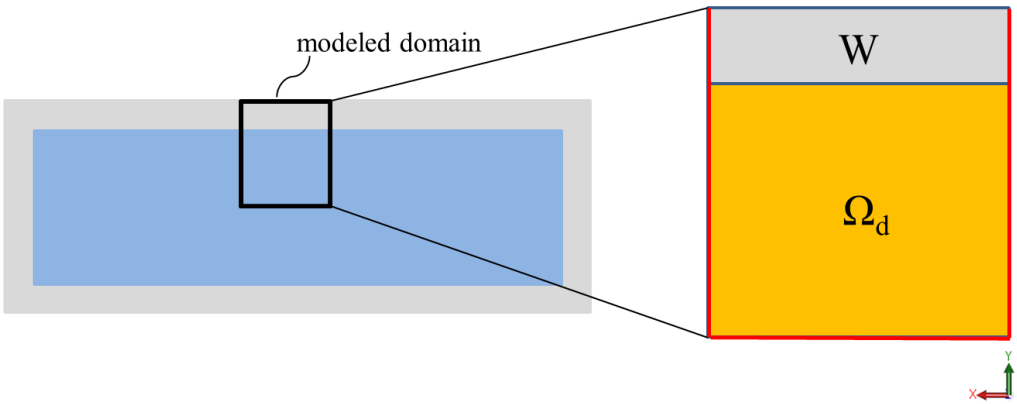

Fig. 5.2: Illustration of the frontal view on the heat exchanger unit cell (left) and zoomed in view on the domain modeled for the optimization (right). The domains d (design domain) and W (wall) as well as symmetry boundary conditions (red lines) are indicated.

to the top boundary of the design domain. Consequently, the fluid flow is increasing closer to the hot water boundary which allows the heat transfer between the water and the air flow to take place with minimal heat transfer resistance in the polymer. The temperature distribution shown in Fig. 5.3 (c) shows the cool air channels in the design and the warmer heat exchanger material. It can be seen how the dendritic structures conduct the heat relatively evenly in all parts of the design domain.

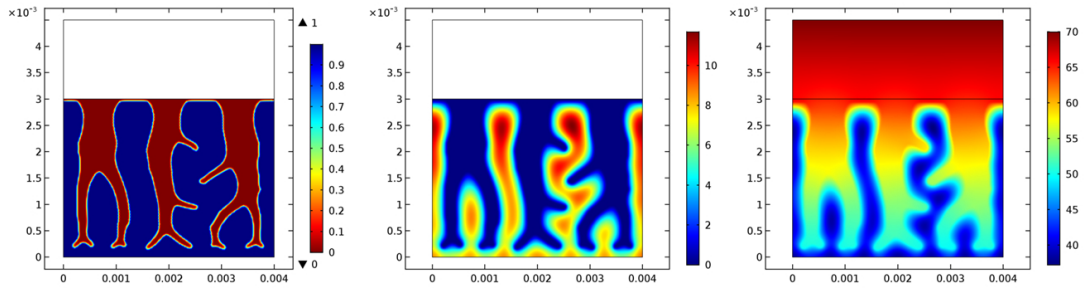

(a) Design (b) Velocity [m/s] (c) Temperature [°C]

Fig. 5.3: Optimized design for a polymer composite conductivity of 5 W/(m K) and an air channel height of 6 mm where red corresponds to fin material and blue to air passages. Moreover, the corresponding air velocity and temperature field.

The effect of varying the composite conductivity for a constant air channel height, and vice versa, on the optimized designs is discussed qualitatively. The resulting Reynolds numbers in the optimized designs are determined and it is found that the laminar flow assumption used in the optimization model seems to be well justified. Moreover, parametric studies are conducted to study the influence of the composite conductivity and the air channel height on the heat exchanger conductance per volume and the heat exchanger conductance per mass. Both parameters have a significant influence on the heat exchanger conductance and the results

for conductance per volume and conductance per mass are qualitatively relatively similar. As anticipated, the heat exchanger conductance increases with increasing composite conductivity. It is shown that an optimal air channel height, or unit cell height, exists for a given composite conductivity and that this optimal height increases with increasing composite conductivity. Furthermore, a brief study regarding the influence of the air-side operating parameters pressure drop and temperature increase over the heat exchanger on the optimized designs and on the heat exchanger conductance is presented. In the analyzed case, halving the pressure drop results in a decrease of conductance per volume of around 18% compared to the reference case and doubling the pressure drop yields a conductance per volume increase of 25%. Halving and doubling the air-side temperature increase has a comparable effect on the heat exchanger conductance.

A systematic benchmarking against a size-optimized slot channel model is conducted to compare the topology optimized designs to a simpler but established heat exchanger geometry. The slot channel model consists of vertical slots for air flow and the slot width is adjusted for a given number of slots to maximize the heat exchanger conductance subject to the same air flow bulk temperature constraint that is applied to the topology optimization model. The optimal air channel height, optimal number of fins, and optimal fin width are determined for different composite thermal conductivities. The respective size optimized slot channel designs are compared to the topology optimized designs for different composite conductivities and similarities and differences are discussed. The main difference is that the topology optimized designs have fewer fins which are thicker and have finer secondary and in some cases tertiary branches. The topology optimized fins are assumed to be more suited for additive manufacturing since they are characterized by a lower aspect ratio, i.e. length over widths of fins. To analyze the aspect of manufacturability more quantitatively, a comparison of the aspect ratios of the topology optimized designs to the aspect ratios of the slot channel designs for the respective same composite conductivity is conducted. Both an unconstrained slot channel model and a slot channel model with a minimum fin width of 0.3 mm are considered since the unconstrained model yields fairly low fin widths for higher conductivities. Aspect ratios of the same order are found for the topology optimized designs and the constrained slot channel designs. For lower composite conductivities, the aspect ratios of the unconstrained slot channel model are also in the same order. However, for higher conductivities, the aspect ratios of the unconstrained slot channel model are significantly higher than those of the other two models. Lastly, the improvement of conductance per heat exchanger volume afforded by the topology optimized designs compared to the slot channel designs is studied, again for the unconstrained slot channel model and the model with a 0.3 mm minimum fin width constraint. In all cases, the topology optimized designs yield a higher conductance than the slot channel designs and the improvement afforded by the topology optimization increases with increasing thermal conductivity. For a composite conductivity of 300 W/(m K), a 36% higher conductance is realized by the topology optimization compared to the unconstrained slot channel model and a 71% higher conductance is achieved compared to the constrained slot channel model. Hence, this work demonstrates to some degree the potential of topology optimization for designing additively manufactured heat transfer devices. Note that the fully developed flow model is also used in the cross-flow heat exchanger model presented in section 5.3; however, in combination with a full Navier Stokes modeling of the second fluid.

5.2 A pseudo 3D heat sink model

Paper **P5** (preliminary results were presented in the conference paper **P4**) deals with the topology optimization of forced convection heat sinks which are used in a wide range of applications. The specific design challenge chosen in this study is the optimization of air-cooled heat sinks for microelectronics cooling. The main modeling difference compared to the fully developed flow model presented in paper **P3** is that the fluid flow is modeled in 2D within the design domain plane so that the full Navier Stokes equations are solved. This results in a nonlinear multiphysics problem that is harder to solve numerically than the simplified fully developed flow model. The computational load is increased due to the nonlinearity of the full Navier Stokes equations and since the fluid problem consists of three state variables, the x and y component of the fluid velocity and the pressure, instead of a single state variable, the z-component of the fluid velocity used in the fully developed flow model. Another issue with the nonlinearity of the Navier Stokes equation is the decreasing numerical stability during the optimization with increasing Reynolds number. This aspect limits the presented studies to low to moderate Reynolds numbers which is further discussed in **P5**.

A pseudo 3D heat sink optimization model is used in this work which consists of a thermally coupled 2D thermofluid design layer and 2D base plate with thermal conduction. This approach allows for increased modeling details compared to pure 2D optimization models as e.g. presented in (Dede, 2009; Matsumori et al., 2013) since, for example, thermal hotspots in the base plate can be captured by the model. Still, the computational burden is significantly decreased compared to full 3D optimization models (Alexandersen et al., 2016); however, at the cost of using simplifying assumptions and restricting the design freedom to two dimensions. The pseudo 3D heat sink modeling concept is shown in Fig. 5.4. On the left, a 3D sketch of a forced convection heat sink with pin fins and heat generation in the base plate is depicted. The right side shows the simplified pseudo 3D model comprised of the 2D modeled thermofluid design layer and the 2D modeled conductive base plate. Each point of the design domain, which is indicated in green, can either represent fin material or fluid passage which allows for a flexible optimization of the number of fins, the fin spacing relative to each other, and the fin cross-sections. Two different design layer geometries corresponding to *model a* and *model b* are considered in paper **P5**. In *model a*, symmetry conditions are applied at the top and bottom of the modeled domain (the air-flow is from the left to the right) such that the optimized design represents a part of a larger heat sink structure which is periodic perpendicular to the flow direction. The fluid problem is modeled under the assumption of an incompressible, laminar, and steady state flow. The continuity equation and the Navier Stokes equations including a Brinkman friction term are solved. For the thermal problem, the thermal diffusion problem in the base plate and the thermal convection-diffusion equation in the thermofluid design layer are solved. Within the design domain, the thermal conductivity in the thermal convection-diffusion equation is interpolated between a higher conductivity in the fins and the lower thermal conductivity of air. See paper P5 for a detailed description of the thermofluid modeling and the modeling of the heat transfer between heat sink base plate and thermofluid design layer.

The optimization objective is to minimize the heat sink thermal resistance for a prescribed pressure drop over the heat sink and fixed uniform heat production rate in the base plate. As an example, an optimized design for a pressure drop of 3 Pa over the heat sink and the corresponding air velocity magnitude, temperature field in the thermofluid layer, and temperature field in the base plate are depicted in Fig. 5.5. There are four fins within the design domain

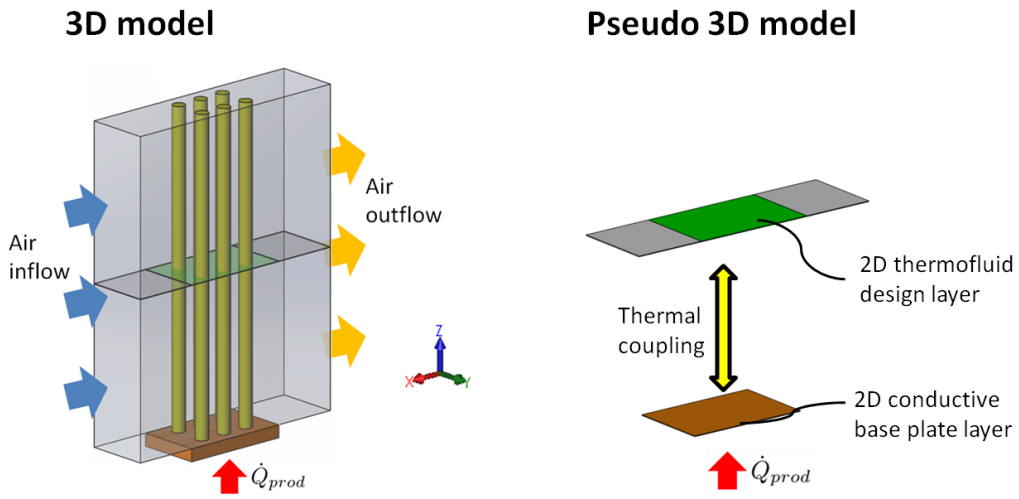

Fig. 5.4: Left: 3D sketch of a forced convection heat sink as treated in this work including base plate (brown), fins (yellow) and modeled domain for air flow (grey). Exemplarily, pin fins are depicted in yellow. Right: Simplified pseudo 3D model consisting of a 2D thermofluid design layer where green corresponds to the design domain and grey to non-optimizable fluid area as well as the 2D modeled base plate (brown). The thermofluid design layer is also shown in the 3D model for illustrative purposes.

where the bottom left and top right fin are halved by the symmetry boundary. It is moreover notable that the fins have to some degree streamlined shapes and that the fins are arranged almost diagonally within the design domain. The streamlined fin shapes decrease the overall system pressure drop and the diagonal arrangement increases the contact distance between the fluid and the solid by forcing the fluid to take a slightly diagonal path across the heat sink. Furthermore, it can be seen that the maximum temperature in the fins is around 42 °C and the base plate temperature is fairly uniform around 45.7 °C.

Optimizations are conducted for pressure drops between 0.5 and 7 Pa to study the influence of increasing convection rates on the optimized designs. For 0.5 Pa, a design with two fins within the design domain is generated and for the other cases, topologies similar to the one shown in Fig. 5.5 are obtained where the length and thickness of the fins increases with increasing pressure drop. One of the main contributions of paper **P5** is to validate the applied pseudo 3D modeling approach. A pseudo 3D validation model is used to assess, among others, the accuracy of the solid fluid representation using a density field with Brinkman penalization by replacing this modeling approach with an explicit separate modeling of solid and fluid domains. In this validation model, the thermofluid design layer and base plate are still modeled two-dimensionally. Furthermore, a full 3D validation model with explicit representation of the solid-fluid boundaries and a body-fitted mesh is used to quantify the influence of the assumptions inherent to the pseudo 3D modeling approach. These are the simplification of the 3D thermofluid problem to the 2D thermofluid design layer and the assumptions made to model the heat transfer coupling between base plate and thermofluid layer. These effects are captured explicitly in the 3D model. Validation simulations using both validation models are conducted

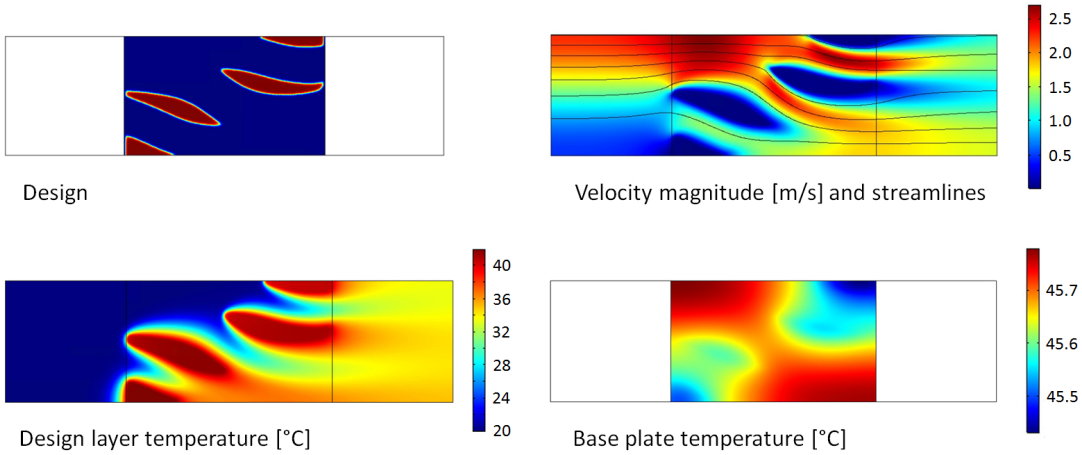

Fig. 5.5: Optimized *model a* design obtained for a pressure drop over the heat sink of 3 Pa where red corresponds to solid and blue to fluid. Additionally, the corresponding velocity field, temperature field in the thermofluid design layer, and temperature field in the metal base plate are shown.

over the entire analyzed pressure drop range and a good agreement between the models in terms of thermal resistance and pressure drop prediction are found. Furthermore, different reasons for the deviations that are observed between the models are discussed. A cross-check based on the pseudo 3D validation model is conducted and each design performs best at the pressure drop for which it was optimized.

The fins obtained from the thermal resistance minimization optimizations are to some degree streamlined as mentioned above. For this reason, it is interesting to compare thermal resistance minimized fin designs with pressure drop minimized fin designs. This is done using the same initial design of a single fin in the middle of the design domain and the optimizations are conducted for different constraints on the maximum fin volume. Differences between the fin shapes are discussed and the pressure drop minimized fin designs are compared to results from comparable studies in the literature. Moreover, the thermal resistance and pressure drop of the designs obtained by pressure drop minimization and thermal resistance minimization are compared. As expected, the pressure drop minimized fins have a lower pressure drop over the heat sink but a higher thermal resistance than the thermal resistance minimized fins and the differences between the designs increase with decreasing volume constraint value. In all optimizations described above, a uniform heat generation rate is assumed in the base plate which leads to relatively uniform base plate temperatures as can be exemplarily seen in Fig. 5.5. Therefore, an exemplifying optimization is conducted for a model with non-uniform heat generation in the base plate which results in thermal hotspots. A qualitatively different topology than in the case of a uniform heat generation rate is obtained and the non-uniform heat generation design has a slightly lower thermal resistance than the design for uniform heat generation which demonstrates the usefulness of including the thermal diffusion problem in the base plate in the optimization model. The cross-check mentioned above is important since poor local optima within the generated designs can be identified. However, it is limited in the sense that the designs are only compared within the optimized set and, therefore, it is of interest to

benchmark the performance of the topology optimized designs against a conventional heat sink geometry . In this work, a size optimized parallel fin design with uniform fin width is chosen as the reference geometry. The benchmarking is conducted for one exemplifying case with uniform heat generation in the base plate and one case with non-uniform heat generation. In the first case, the topology optimized design has a 9.8% lower thermal resistance and in the case of non-uniform heat generation, the topology optimized design has a 13.6% lower thermal resistance. This provides some confirmation for the added value of topology optimization compared to geometrically less flexible optimization methods. As mentioned above, also a second design layer geometry, *model b*, is considered. This more academic model is non-periodic and has a smaller inlet and outlet width than design domain width. It is included in this work to generate more complex topologies and to demonstrate a case where the number of fins in the optimized designs varies for different pressure drops over the heat sink. Designs optimized for different pressure drops are presented and discussed and a cross-check of the designs based on a pseudo 3D body-fitted mesh validation model is conducted where each design performs best at the pressure drop for which it is optimized.

5.3 A cross-flow heat exchanger model

This section presents a more academic thermofluid cross-flow heat exchanger topology optimization model that explicitly considers the heat transfer in both fluids. An interface identification method (Clausen et al., 2015) is used to represent the solid heat exchanger material that separates both fluid flows in a flexible way during the optimization. This section differs from the other sections of this thesis in the sense that it is more detailed and comprises a more detailed modeling description since it is based on preliminary work that has so far only been published as the extended conference abstract **P7**. Also paper **P3** presents an optimization model that is applied to the design of a cross-flow heat exchanger; however, only the air-side heat transfer is modeled and the water-side is not explicitly considered to simplify the model. This simplification is justified by the fact that the dominant heat transfer resistance in the considered gas-to-liquid heat exchanger is on the gas-side. In this section, a more detailed model for cross-flow heat exchanger design is presented in which the heat transfer in both fluids is explicitly considered. The specific application presented in this section is an air-to-air heat exchanger. It should be noted that the model presented here is preliminary work and several aspects, which will be discussed within this section, need to be further investigated in future studies. The main limitation of the presented model is that only fluids with the same thermal conductivity can be considered. In the near future, a journal paper is planned to be written on a more general version of this model which can consider two fluids with different thermal conductivities.

5.3.1 General description of the heat exchanger model

The optimization of a shell and tube cross-flow heat exchanger, as exemplarily depicted in Fig. 5.6 (left), is considered in this study. Heat is transferred between a fluid that flows within the heat exchanger shell, *fluid 1*, and a second fluid, *fluid 2* which flows within the pipes inside the heat exchanger shell. Due to the large number of optimization iterations that are needed in topology optimization to reach convergence to a final design, only a small cuboidal part of the cross-flow heat exchanger is considered, as depicted in Fig. 5.6, in order to reduce the computational burden. The computational complexity of the thermofluid problem is further reduced by only considering a 2D cross-section of the cuboid which is indicated in orange in Fig. 5.6. In this modeling approach, *fluid 1* flows within the 2D modeled domain and *fluid 2* flows within the pipes perpendicular to the 2D modeled domain. A thermally and fluid dynamically fully developed internal flow is assumed for *fluid 2* which is similar to the modeling approach presented in paper **P3**. The 2D representation of the cross-flow heat exchanger is further abstracted in the presented modeling approach and a scheme of this more abstract model is shown in Fig. 5.7. At each point within the design domain, which is indicated in orange, either *fluid 1* can flow within the xy-plane or *fluid 2* can flow perpendicular to the xy-plane. The domains marked in gray are not part of the design domain and there is only in-plane *fluid 1* flow. The topology optimization can freely determine within the design domain where passages for *fluid 1* and where passages for the cross-flowing *fluid 2* should be. For this purpose, a density-field is introduced which takes the value 0 in areas where *fluid 2* flows perpendicular to the modeled domain and 1 in areas where *fluid 1* flows within the modeled plane. In this way, the number of passages for *fluid 2* and the cross-sections of these passages can be determined by the topology optimization. Symmetry boundary conditions are applied at the sides of the modeled domain in order to obtain a structure that is periodic perpendicular to both flow

directions.

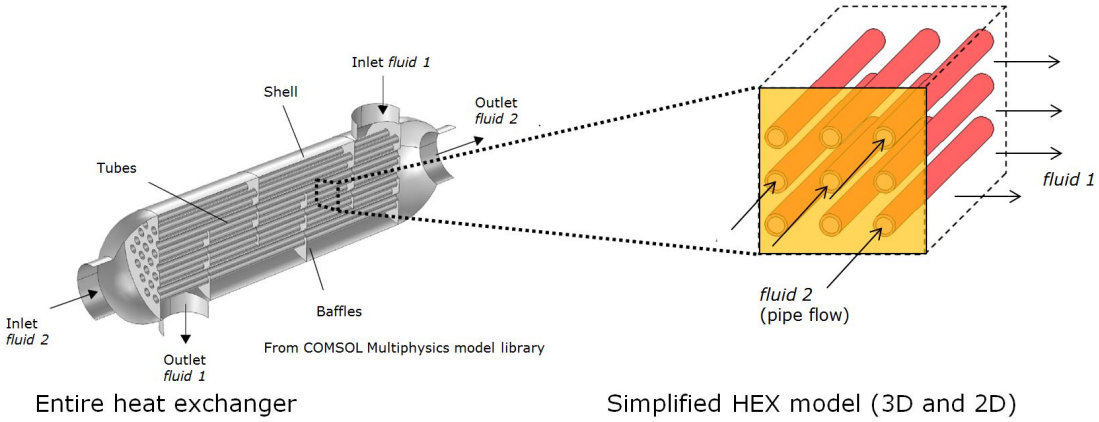

Fig. 5.6: Left: Exemplifying depiction of a cross-flow heat exchanger (HEX) as treated in this study. Right: Simplified representation in 3D and 2D of the cross-flow heat exchanger.

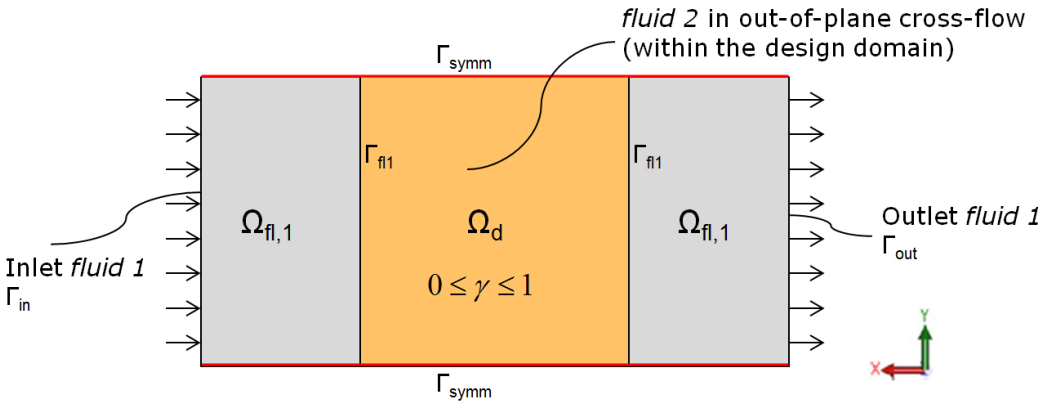

Fig. 5.7: Simplified and further abstracted cross-flow heat exchanger model as used in this study. The design domain, Ω_d, is indicated in orange and non-optimizable *fluid 1* area, $\Omega_{fl,1}$, is indicated in grey. Moreover, the different boundaries Γ_i are indicated.

5.3.2 Applied interface representation method

As stated in the previous section, the design domain contains both passages for *fluid 1* and *fluid 2* which is represented by the density field or design field. The design field can only represent areas of either *fluid 1* or *fluid 2* but also the solid heat exchanger material that separates the two fluids needs to be represented flexibly during the optimization. This is exemplarily shown in Fig. 5.8 (left) for a single circular pipe within which *fluid 2* (gray) is flowing in the out-of-plane direction and *fluid 1* (white) flows within the xy-plane around the pipe. The solid heat exchanger pipe material is indicated in black. An interface identification method as

presented in (Clausen et al., 2015) is used in this work to identify the interface through the gradient of the design field. This method is explained in the following. Note that for reasons of simplicity of writing, the filtered and projected design field, $\bar{\tilde{\gamma}}$, is within this section referred to as φ. The process of obtaining an interface with defined thickness from the design field gradient is shown in Fig. 5.8 (right). The filtered and projected design field, φ, is filtered once more in order to obtain a smooth gradient between areas of *fluid 1* and *fluid 2*. The same PDE filter as for the filtering of the design field, γ, is used (equation 2.7). However, a different filter parameter is applied to decouple the length scale of the interface thickness from the length scale of the original density filtering. The thickness of the interface follows from the value of the filter parameter that is used when filtering φ, $r_{filter,\,\varphi}$. Note that the interface thickness is not the same as the filter parameter. A proportionality constant which defines the relation between these two parameters can probably be derived analytically as it is done for the structural mechanics problem presented in (Clausen et al., 2015). However, this is omitted in this preliminary work which serves mainly to demonstrate the general applicability of the interface identification method to this cross-flow heat exchanger design problem. The normalized Euclidean norm of the spatial gradient of the second smoothed field, $\tilde{\varphi}$, is computed in the following way:

$$\|\nabla\tilde{\varphi}\|_{\varepsilon} = \varepsilon\,\|\nabla\tilde{\varphi}\| \tag{5.1}$$

where the normalization factor ε is defined as the maximum possible gradient norm of the second smoothed field, φ. From this follows that:

$$0 \leq \|\nabla\tilde{\varphi}\|_{\varepsilon} \leq 1 \quad ,\forall\,\varphi \tag{5.2}$$

Clausen et al. (Clausen et al., 2015) derive the value of ε analytically to be:

$$\varepsilon = \frac{r_{filter,\,\varphi}}{\sqrt{3}} \tag{5.3}$$

for the case of only applying Neumann boundary conditions to the filter PDE (equation (2.7)). In this work, both Neumann and Dirichlet boundary conditions are used so that using equation (5.3) results in an insufficiently scaled field. Therefore, the following heuristically chosen value of the normalization factor is used in this preliminary work:

$$\varepsilon = 2\,r_{filter,\,\varphi} \tag{5.4}$$

It is important to note that this value of ε is only an approximation and either, if possible, an analytical expression should be derived for this value for the case of also considering Dirichlet boundary conditions or only Neumann boundary conditions should be used for the filtering of the projected design field, if possible. These aspects need to be addressed in subsequent work. The physically meaningful projected normalized design field gradient, $\overline{\|\nabla\tilde{\varphi}\|_{\varepsilon}}$, is obtained using a smoothed heaviside projection (equation (2.8)) which is also used for the projection of the filtered design field. Note that different projection steepness and threshold parameters, β_{φ} and η_{φ}, are used in this projection compared to the parameters of the projection of the filtered design field which will be referred to as β_{γ} and η_{γ} within this section.

5.3.3 Thermofluid modeling of the cross-flow heat exchanger

Throughout this study, an incompressible, steady-state, and laminar flow is assumed.

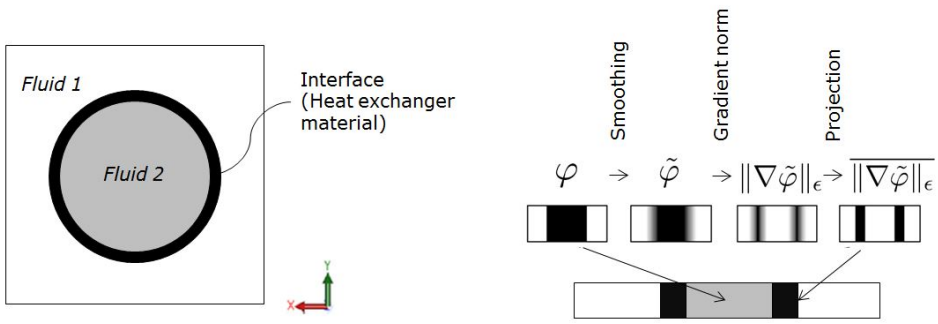

Fig. 5.8: Left: 2D representation of the interface identification problem in the context of the presented model. Right: 1D representation of the interface identification process as presented in (Clausen et al., 2015).

.

5.3.3.1 Fluid dynamics modeling of *fluid 1*

The continuity equation (equation (2.13)) and the following Navier Stokes equations are solved for *fluid 1* which flows within the xy-plane:

$$\rho_{fl,1} \cdot (\mathbf{u} \cdot \nabla)\, \mathbf{u} = -\nabla p + \mu_{fl,1}\, (\nabla^2 \mathbf{u}) + \mathbf{F}_{\alpha,1}(\varphi, \overline{\|\nabla\tilde{\varphi}\|_\varepsilon}) \qquad \text{in } \Omega_{fl,1} \cup \Omega_d \tag{5.5}$$

where $\rho_{fl,1}$ and $\mu_{fluid,1}$ are the density and dynamic viscosity of *fluid 1* and $F_{\alpha,1}$ is the Brinkman friction term for *fluid 1*. The Brinkman friction term needs to prevent *fluid 1* from flowing through both the solid heat exchanger material areas and areas of *fluid 2* and is therefore dependent on both the projected design field, φ, and its projected gradient norm, $\overline{\|\nabla\tilde{\varphi}\|_\varepsilon}$. The Brinkman friction term for *fluid 1* is defined as:

$$\mathbf{F}_{\alpha,1} = \mathbf{0} \qquad \text{in } \Omega_{fl,1} \tag{5.6}$$

$$\mathbf{F}_{\alpha,1}(\varphi, \overline{\|\nabla\tilde{\varphi}\|_\varepsilon}) = -\overline{\alpha}_{fl,1}\, I_{\alpha,1}(\varphi, \overline{\|\nabla\tilde{\varphi}\|_\varepsilon})\, \mathbf{u} \qquad \text{in } \Omega_d \tag{5.7}$$

where $\overline{\alpha}_{fl,1}$ is the maximum inverse permeability for *fluid 1* and $I_{\alpha,1}(\varphi, \overline{\|\nabla\tilde{\varphi}\|_\varepsilon})$ is the interpolation function of the Brinkman term used for *fluid 1*. The interpolation functions used in this model are stated in subsection 5.3.4.1. The maximum inverse permeability for *fluid 1* is computed according to equation (2.16) where the width of the modeled domain is used as characteristic length, L_c.

The pressure drop between *fluid 1* inlet and outlet, $\Delta p_{fl,1}$, is prescribed and symmetry boundary conditions are used at the top and bottom of the modeled domain which are given by the following two equations:

$$\mathbf{u} \cdot \mathbf{n} = 0 \qquad \text{on } \Gamma_{symm} \tag{5.8}$$

$$\mathbf{K} - (\mathbf{K} \cdot \mathbf{n})\, \mathbf{n} = \mathbf{0} \qquad \text{on } \Gamma_{symm} \tag{5.9}$$

where $\mathbf{n}$ is the vector normal to the respective boundary and $\mathbf{K}$ is defined as:

$$\mathbf{K} = [\mu_{fl,1}\, (\nabla\mathbf{u} + (\nabla\mathbf{u})^T)]\, \mathbf{n} \tag{5.10}$$

5.3.3.2 Fluid dynamics modeling of *fluid 2*

In an approach that is similar to the modeling presented in paper **P3**, a fully developed internal flow in the z-direction is assumed for *fluid 2* which leads to the following simplified Navier Stokes equation:

$$\mu_{fl,2}\,(\nabla^2 w) = \frac{\Delta p_{fl,2}}{\Delta z} + F_{\alpha,2}(\varphi, \overline{\|\nabla\tilde{\varphi}\|_\varepsilon}) \qquad \text{in } \Omega_d \tag{5.11}$$

where $\mu_{fl,2}$ is the dynamic viscosity of *fluid 2*, w is the *fluid 2* velocity in the z-direction, $\frac{\Delta p_{fl,2}}{\Delta z}$ is the driving pressure gradient for *fluid 2*, and $F_{\alpha,2}$ is the Brinkman friction term for *fluid 2*. This Brinkman term also depends on φ and its projected gradient norm in order to ensure that *fluid 2* does not flow within areas of the solid heat exchanger material or areas of *fluid 1*. The Brinkman term for *fluid 2* is given by:

$$F_{\alpha,2}(\varphi, \overline{\|\nabla\tilde{\varphi}\|_\varepsilon}) = -\overline{\alpha}_{fl,2}\, I_{\alpha,2}(\varphi, \overline{\|\nabla\tilde{\varphi}\|_\varepsilon})\, w \qquad \text{in } \Omega_d \tag{5.12}$$

where $\overline{\alpha}_{fl,2}$ is the maximum inverse permeability used for *fluid 2*. The inverse permeability is defined in this case by:

$$\overline{\alpha}_{fl,2} = \frac{10}{\mu_{fl,2}}\,\frac{\Delta p_{fl,2}}{\Delta z} \tag{5.13}$$

Symmetry boundary conditions are applied at the top and bottom boundary of the design domain:

$$-\,\mathbf{n}\,\cdot\,(-\nabla w) = 0 \qquad \text{on } \Gamma_{symm} \tag{5.14}$$

A no-slip boundary condition is imposed on the remaining boundaries of the design domain:

$$w = 0 \qquad \text{on } \Gamma_{fl1} \tag{5.15}$$

5.3.3.3 Heat transfer modeling

The thermal problem is described by a single steady state convection-diffusion equation which interpolates between the heat transfer in both fluids. This equation is given by:

$$\rho_{fl,1}\, c_{fl,1}\, \nabla T\, \varphi\, \mathbf{u} - \nabla\cdot(k(\varphi, \overline{\|\nabla\tilde{\varphi}\|_\varepsilon})\,\nabla T) = -\rho_{fl,2}\, c_{fl,2}\frac{\Delta T_{HEX,fl,2}}{\Delta z}\,(1-\varphi)\, w \tag{5.16}$$

where $c_{fl,1}$ and $c_{fl,2}$ are the respective specific heat capacity of *fluid 1* and *fluid 2*, k is the thermal conductivity, T is the temperature field which defines the temperature in both fluids, $\rho_{fl,2}$ is the density of *fluid 2*, and $\frac{\Delta T_{HEX,fl,2}}{\Delta z}$ is the thermal gradient in the z-direction within *fluid 2*. It can be seen that the projected design field, φ, interpolates between the convection-diffusion equation for *fluid 1* and the convection-diffusion equation for thermally and fluid dynamically fully developed internal laminar flow in the z-direction which is used for *fluid 2*. The thermal conductivity, k, depends on both φ and $\overline{\|\nabla\tilde{\varphi}\|_\varepsilon}$ to allow for an interpolation between the conductivities of *fluid 1*, *fluid 2*, and the solid heat exchanger material. However, in this preliminary work, the thermal conductivities are assumed to be the same in both fluids which simplifies the definition of k to:

$$k(\varphi, \overline{\|\nabla\tilde{\varphi}\|_\varepsilon}) = k(\overline{\|\nabla\tilde{\varphi}\|_\varepsilon}) = k_{fl,1,2}\, I_k(\overline{\|\nabla\tilde{\varphi}\|_\varepsilon}) \tag{5.17}$$

where $k_{fl,1,2}$ is the thermal conductivity of both fluids.

The inlet temperature of *fluid 1* is set to a fixed value:

$$T = T_{fl,1,in} \qquad \text{on } \Gamma_{in} \tag{5.18}$$

where $T_{fl,1,in}$ is the prescribed inlet temperature. The outlet and symmetry boundary condition for the temperature field is given by:

$$\mathbf{n} \cdot \nabla T = 0 \qquad \text{on } \Gamma_{out} \cup \Gamma_{symm} \tag{5.19}$$

5.3.4 Practical implementation

5.3.4.1 Interpolation functions

The interpolation function of the Brinkman term used for *fluid 1* ($j = 1$) and *fluid 2* ($j = 2$) is defined in a similar way and given by:

$$I_{\alpha,j}(\varphi, \overline{\|\nabla\tilde{\varphi}\|_\varepsilon}) = I_{\alpha,\varphi,j}(\varphi) + (1 - I_{\alpha,\varphi,j}(\varphi))\, I_{\alpha,\overline{\|\nabla\tilde{\varphi}\|_\varepsilon},j}(\overline{\|\nabla\tilde{\varphi}\|_\varepsilon}) \qquad j = 1,2 \tag{5.20}$$

where $I_{\alpha,\varphi,j}(\varphi)$ is an interpolation function which is only dependent on the projected design variable field and $I_{\alpha,\overline{\|\nabla\tilde{\varphi}\|_\varepsilon},j}(\overline{\|\nabla\tilde{\varphi}\|_\varepsilon})$ is an interpolation function that is only dependent on the projected gradient norm of φ. For $I_{\alpha,\varphi,1}$ a function as stated in (Alexandersen et al., 2014) and originally presented in (Borrvall and Petersson, 2003) is used:

$$I_{\alpha,\varphi,1}(\varphi) = \frac{1-\varphi}{1 + b_{\alpha,1}\,\varphi} \tag{5.21}$$

where $b_{\alpha,1}$ is an interpolation convexity parameter. The interpolation $I_{\alpha,\varphi,2}$ is chosen to be linear as it is also presented for the fully developed flow model described in paper **P3**. Hence, the function is given by:

$$I_{\alpha,\varphi,2}(\varphi) = \varphi \tag{5.22}$$

The interpolation $I_{\alpha,\overline{\|\nabla\tilde{\varphi}\|_\varepsilon},j}$ is chosen to be linear for both fluids and given by:

$$I_{\alpha,\overline{\|\nabla\tilde{\varphi}\|_\varepsilon},j} = \overline{\|\nabla\tilde{\varphi}\|_\varepsilon} \qquad j = 1,2 \tag{5.23}$$

Also the convex interpolation which is stated in equation (5.21) was tested for $I_{\alpha,\overline{\|\nabla\tilde{\varphi}\|_\varepsilon},j}$ but in that case blurred *fluid 1*-*fluid 2* interfaces were observed in the optimized designs during preliminary optimizations. However, it should be investigated in future work if a convex interpolation can be used for certain convexity parameter values or in combination with a continuation strategy.

A RAMP-style interpolation as stated in (Alexandersen et al., 2014) and originally presented in (Stolpe and Svanberg, 2001a) is used for the interpolation of the thermal conductivity, I_k:

$$I_k(\overline{\|\nabla\tilde{\varphi}\|_\varepsilon}) = \frac{(1 - \overline{\|\nabla\tilde{\varphi}\|_\varepsilon})\,(C_k(1+b_k) - 1) + 1}{C_k\,(1 + b_k\,(1 - \overline{\|\nabla\tilde{\varphi}\|_\varepsilon}))} \tag{5.24}$$

where

$$C_k = \frac{k_{fl,1,2}}{k_s} \tag{5.25}$$

where k_s is the thermal conductivity of the solid heat exchanger material.

5.3.4.2 Optimization formulation

The optimization objective is to maximize the transferred heat between *fluid 1* and *fluid 2* subject to a constraint on the maximum temperature difference between the inlet temperature of *fluid 1*, $T_{fl,1,in}$, and the velocity weighted average temperature of *fluid 2* (i.e. the *fluid 2* bulk temperature, $T_{fl,2,bulk}$). This approach is similar to the optimization formulation used in paper **P3**; however, in that work only the heat transfer in the fluid which is flowing in the out-of-plane direction is modeled. The *fluid 2* bulk temperature is computed in the following way:

$$T_{fl,2,bulk} = \frac{\int_{\Omega_d} (1-\varphi)\, w\, T\, d_{\Omega_d}}{A_{\Omega_{fl,2}}\, w_{average,fl,2}} \tag{5.26}$$

where $A_{\Omega_{fl,2}}$ is the *fluid 2* flow area of the design domain and $w_{average,fl,2}$ is the average value of w within this area. Note that as an approximation, $T_{fl,2,bulk}$, $A_{\Omega_{fl,2}}$, and $w_{average,fl,2}$ are computed without considering the solid interface area, i.e. it is only evaluated whether a given part of the design domain is passage for *fluid 1* or passage for *fluid 2* as determined by the projected design field, φ. A formulation that includes both the projected design field and $\overline{\|\nabla\tilde{\varphi}\|_\varepsilon}$ should be derived for these computations in future works.

The heat that is transferred between *fluid 1* and *fluid 2* is both defined by the total amount of heat transported by *fluid 2* and by the enthalpy difference between Γ_{in} and Γ_{out} in *fluid 1*. In this work, the transferred heat is computed based on the energy transport in *fluid 2*; however, it should be investigated in future work if a formulation based on the enthalpy change in *fluid 1* leads to a more stable or more efficient optimization.

5.3.4.3 Computational implementation

In the following, the computational implementation of the cross-flow heat exchanger model is briefly described. The model is implemented in COMSOL Multiphysics (COM) and the implementation is done in a similar way as described in chapter 3 in a generic way for the optimization models which are used in this thesis. In the presented implementation, no continuation strategy (Sigmund and Petersson, 1998; Stolpe and Svanberg, 2001b) is used, i.e. the same optimization parameters are used for all optimization iterations. These parameters are stated in Table 5.1. Note that it is planned to test different continuation strategies in subsequent work in order to reduce the risk of converging to poor local optima and to increase the stability of the optimization.

Table 5.1: Constant numerical and optimization parameters of the cross-flow heat exchanger model.

Parameter	Value	Parameter	Value
$b_{\alpha,1}$ [-]	7.5	Da [-]	10^{-5}
b_k [-]	20	max. element size in Ω_d [mm]	1.9×10^{-2}
β_γ [-]	7.5	max. element size in $\Omega_{fl,1}$ [mm]	5.5×10^{-2}
β_φ [-]	12.5	r_γ [mm]	2.9×10^{-2}
η_γ [-]	0.5	r_φ [mm]	4.8×10^{-2}
η_φ [-]	0.5		

5.3.5 Preliminary results

Both *fluid 1* and *fluid 2* are assumed to have the thermophysical properties of air. Other constant model parameters are stated in Table 5.2. Note, that the thermal conductivity of the solid heat exchanger material is set to a value of 1 W/(m K) which is a significantly lower conductivity than that of metallic heat exchanger materials. However, a thermal conductivity of that order can be found in polymer heat exchangers (T'Joen et al., 2009). This low thermal conductivity is chosen within this work to improve the numerical stability during the optimization and to facilitate the choice of the convexity parameter value of the conductivity interpolation, b_k. Future studies with higher solid thermal conductivities are planned.

Table 5.2: Constant model parameters of the cross-flow heat exchanger model.

Parameter	Value	Parameter	Value
k_s [W/(m K)]	1	$T_{fl,1,in}$ [°C]	100
$\Delta T_{HEX,fl,2}$ [°C]	16	min. $T_{fl,2,bulk}$ [°C]	80

Within the presented work, a uniform initial design field of value 0.5 is used. As an example, an optimized design for $\Delta p_{fl,1} = 5$ Pa and $\Delta p_{fl,2} = 12$ Pa is shown in Fig. 5.9. The distance between the *fluid 1* inlet and the left boundary is 1 mm, the design domain length is 1.5 mm, and the distance between the right boundary of the design domain and the *fluid 1* outlet is 1 mm. The width of the modeled domain is 1.5 mm and the channel height, Δz, is 8 mm. There are three passages for *fluid 2* which are to some extent streamlined except for a blunt feature where the respective fluid passage reaches the boundary of the design domain. The top and bottom *fluid 2* passages are both halved by the symmetry boundary. A maximum *fluid 1* velocity of around 2.4 m/s and a maximum *fluid 2* velocity of around 4.8 m/s are observed. It can be seen how the Brinkman penalization effectively prevents *fluid 1* from flowing through the interface area and *fluid 2* passages. Also *fluid 2* is effectively prevented by the Brinkman penalization from flowing through the interface area or through *fluid 1* passages. The temperature field shows how *fluid 1* is being cooled down while flowing around the passages of the colder *fluid 2*. Figure 5.10 shows the projected design field, φ, and the corresponding projected design field gradient, $\overline{\|\nabla\tilde{\varphi}\|_\varepsilon}$, of the optimized design depicted in Fig. 5.9. It can be seen that the projected design field gradient provides a clear representation of the *fluid 1*-*fluid 2* interface, which corresponds to the solid heat exchanger material. In general, a uniform thickness of the interface is realized; however, it should be noted that the interface is slightly larger at both $\Gamma_{fl,1}$ boundaries. The increased thickness is probably due to the Dirichlet boundary condition used in the second filter step at the $\Gamma_{fl,1}$ boundary and it needs to be investigated in future research how an entirely uniform interface thickness can be guaranteed. This may be possible by only using Neumann boundary conditions in the second filtering step but this needs to be validated in future research.

Optimized designs for two different heat exchanger geometries and different pressure drops are depicted in Fig. 5.11. The modeled geometry of design (a) and (c) is the same as the geometry shown in Fig. 5.9. The modeled domain of design (b) and (d) has a width of 2.5 mm, the distance from the *fluid 1* inlet and outlet to the design domain is in both cases 1 mm, and the design domain length is 1 mm. The same *fluid 1* pressure drop is set for design (a) and (c) but for design (a), $\Delta p_{fl,2}$ is 12 Pa, and for design (c), $\Delta p_{fl,2}$ is 3.2 Pa. Comparing design (a) and (c), it can be seen that the same topology with three passages for *fluid 2* is

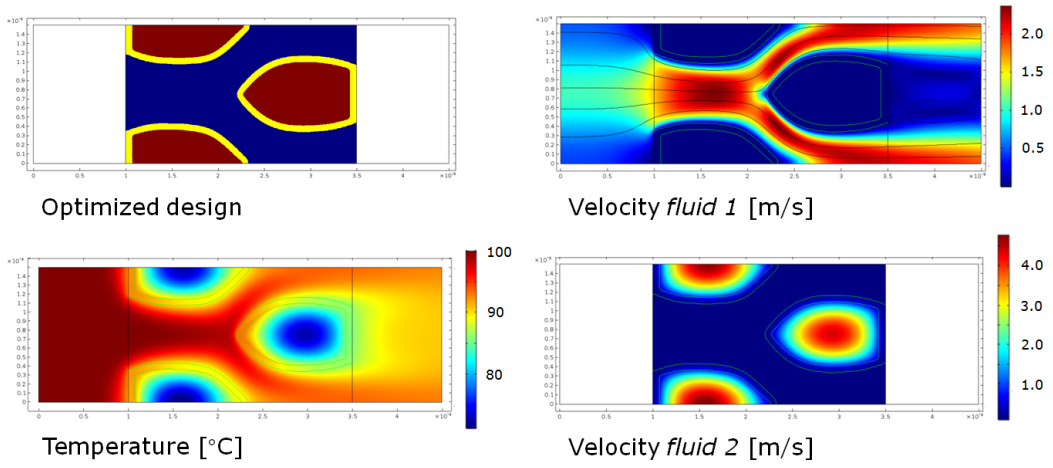

Fig. 5.9: Exemplifying optimized design where *fluid 1* passages are indicated in blue, *fluid 2* passages are indicated in red, and the solid heat exchanger material is indicated in yellow. Moreover, the corresponding respective *fluid 1* and *fluid 2* velocity field and the temperature field is shown.

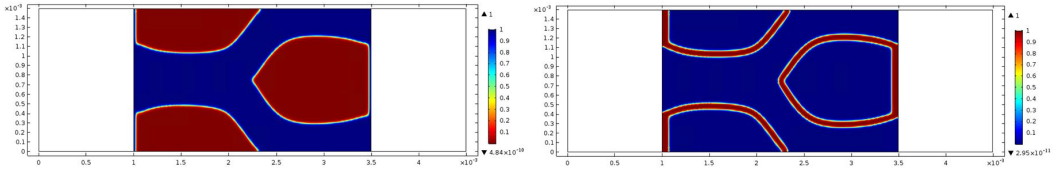

Fig. 5.10: Left: Projected design field, φ, of the optimized design shown in Fig. 5.9 where *fluid 1* passages are indicated in blue and *fluid 2* passages are indicated in red. Right: Corresponding projected design field gradient, $\overline{\|\nabla\tilde{\varphi}\|_\varepsilon}$.

formed. However, the total cross-section of *fluid 1* passage is in design (c) reduced compared to design (a) and the total *fluid 2* cross-section is increased. This makes sense since the $\Delta p_{fl,2}$ is decreased in design (c) compared to $\Delta p_{fl,1}$. The larger *fluid 2* cross-sections allow to still maintain a relatively large *fluid 2* volume flow even though the pressure drop in that fluid is lower. Also for design (b) and (d), similar topologies are generated with three passages for *fluid 2* where the top and bottom passage is halved by the symmetry boundary. The reduced ratio of $\Delta p_{fl,2}$ to $\Delta p_{fl,1}$ in design (d) compared to design (b) is also in this case reflected in a reduced ratio of total *fluid 1* cross-section to total *fluid 2* cross-section. All designs exhibit a clear 0/1 field without areas of intermediate density, meaning that the optimized designs represent practical geometries.

5.3.6 Conclusions and outlook

A more academic thermofluid model for the design of cross-flow heat exchangers is presented in this section. An interface identification method is used to represent the solid heat exchanger

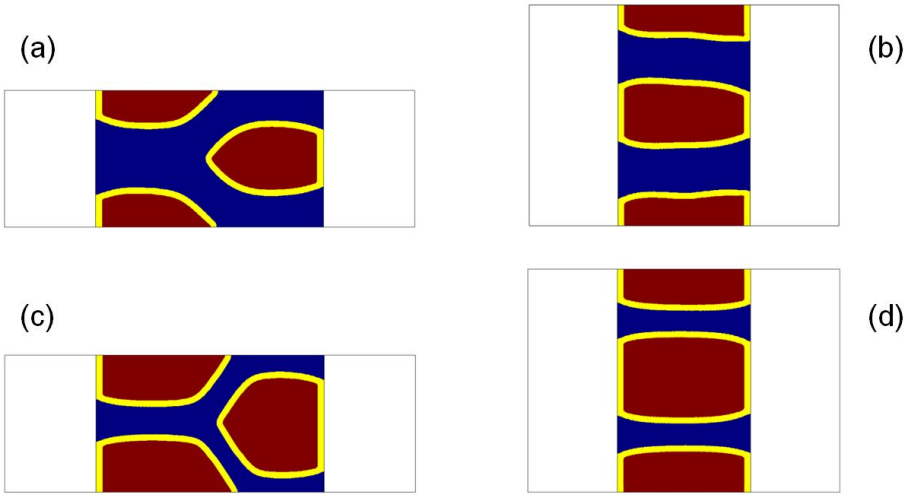

Fig. 5.11: Optimized designs for different heat exchanger geometries and different values of $\Delta p_{fl,2}$. *Fluid 1* passages are indicated in blue, *fluid 2* passages are indicated in red, and the solid heat exchanger material is indicated in yellow. The designs (a) and (b) correspond to $\Delta p_{fl,2} = 12$ Pa and the designs (c) and (d) correspond to a pressure drops $\Delta p_{fl,2} = 3.2$ Pa. The *fluid 1* pressure drop is in all cases 5 Pa

material which separates the two fluids that flow perpendicular to each other. The presented preliminary work demonstrates the applicability of the optimization model to design cross-flow heat exchangers; however, there are different aspects that should be further investigated in future studies which are discussed briefly below. The current model can only consider two fluids with the same thermal conductivity. A more general conductivity interpolation should be developed, which can represent different thermal conductivities in *fluid 1*, *fluid 2*, and the solid heat exchanger material. Dirichlet boundary conditions are used in the PDE-filter applied to the projected design field which causes issues with the normalization of the design gradient and the uniformity of the interface thickness. These aspects need to be further investigated in future work. The modeling is conducted under a laminar flow assumption. This assumption should be validated in the final designs for both *fluid 1* and *fluid 2*. The current optimization objective is formulated based on the energy that it transported by *fluid 2*. It should be investigated if a formulation based on the enthalpy change in *fluid 1* leads to a more stable or more efficient optimization. Continuation strategies for the interpolation convexity parameters and the projection steepness parameters should be tested in order to increase the stability of the optimization and to decrease the risk of converging to poor local optima. Moreover, different initial designs should be tested as the optimization problem is quite non-convex. It should be aimed at developing an optimization model with more realistic material properties and operating conditions. This includes larger model dimensions, higher pressure drops, and a higher solid heat exchanger material thermal conductivity. Furthermore, the modeling approach should be validated with 3D simulations where the different interfaces are explicitly represented and a body-fitted mesh is used. Also, the fabrication and experimental validation of optimized designs should be investigated.

Chapter 6

Experimental validation of topology optimized designs

It is important to not only present numerical optimization results but also to fabricate prototypes based on these results and to validate the performance of the topology optimized structures experimentally. Even though there is a large body of literature on topology optimization applied to heat transfer problems, only very few works have addressed the experimental validation of topology optimized designs in the context of heat transfer (Koga et al., 2013; Dede et al., 2015).

6.1 Prototyping and testing of the optimized downhole tool

As already mentioned in section 4.1, an optimized prototype of the of the actively cooled downhole tool is designed based on the topology optimization studies that were conducted. An illustration of the final design is shown in Fig. 6.1. Note that some assembly constraints needed to be taken into account when designing the final system: It can for example be seen that the thermoelectric cooler is clamped between the heat spreader and the aluminum pad using two plastic screws. Based on this design, a prototype is manufactured and assembled. The prototype is tested in an experimental setup using an oven which provides a dry and ventilated hot environment at defined temperatures. Experiments are conducted for different operating conditions using different TEC feed currents. The experimentally measured temperatures of the TEC hot plate and the high temperature sensitive electronics are compared to simulation predictions and a good agreement between experiment and model is found. Moreover, it is demonstrated that the thermoelectric cooler can maintain the thermal load at more than 33 K below the oil well temperature, which allows the sensitive components to operate in an oil well above 200 °C. See paper **P2** and (Soprani et al., 2016) for further information.

6.2 Investment casting and experimental test of heat sinks designed by topology optimization

Paper **P7** presents the application of investment casting using 3D stereolithography printed patterns to the fabrication of topology optimized natural convection heat sinks and experimental validations of the structures. The work will only be briefly summarized in this thesis as I was only to a minor degree involved in the project. Stereolithography (SLA) assisted investment casting (IC) is a promising alternative to metal 3D additive manufacturing (AM) since it allows

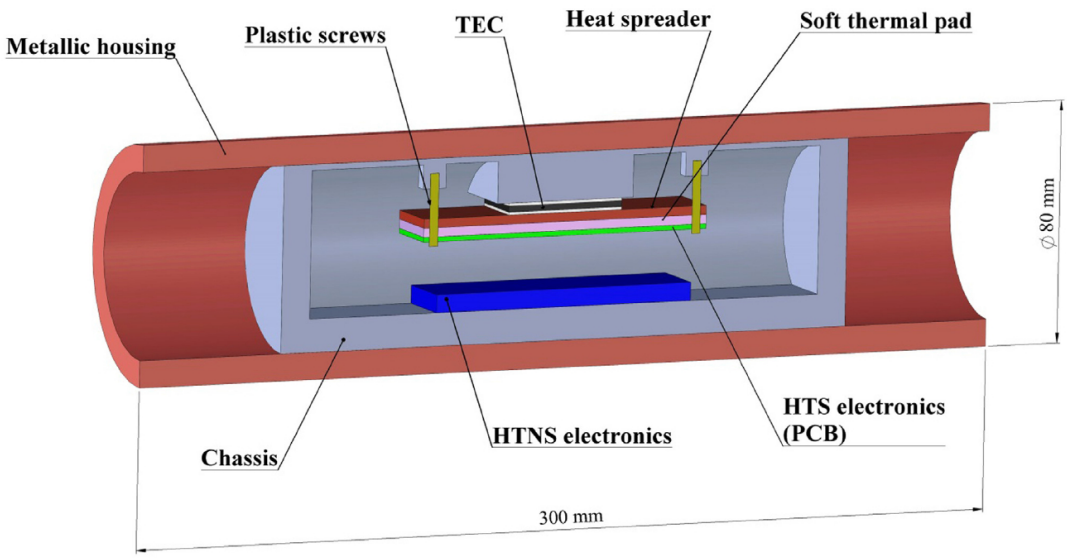

Fig. 6.1: Illustration of the longitudinal section of the final downhole tool design.

for manufacturing complex metal parts with high accuracy and at a lower cost compared to metal 3D printing. Moreover, investment casting can be done using a wide range of highly conductive metals that are commonly used in heat transfer devices whereas 3D metal additive manufacturing is limited to a few steels, aluminum and titanium alloys that have thermal conductivities of less than 200 W/(m K). The optimized natural convection heat sink designs that are studied in this work were generated by Joe Alexandersen using a large-scale in-house topology optimization model (Alexandersen et al., 2016). Three topology optimized heat sinks and five conventionally designed reference pin-fin heat sinks are cast based on Britannia metal which is a tin-based alloy. The obtained metal topology optimized heat sinks and three reference pin-fin heat sinks are depicted in Fig. 6.2. Note that the dark surfaces are resulting from a graphite spray which was applied to the heat sinks in order to be able to capture good thermographs of them using an infrared thermal imaging camera. The geometries "horiz1" and "horiz2" are optimized for an orientation where the heating surface (and the bottom plate of the heat sink) is perpendicular to the horizontal direction. The design domains are chosen as, respectively, 1/4 and 1/8 of the full heat sink domain. The design "vert" is obtained for an orientation where the heat sink base plate is aligned horizontally and the design domain is 1/4 of the full heat sink domain. It can be seen that these different boundary conditions lead to significant differences between the optimized geometries. The pin-fin reference heat sinks are designed such that they have the same overall size as the topology optimized designs and the metal volume is controlled to be close to the average value of the topology optimized heat sinks' volume.

The topology optimized heat sinks are experimentally compared to the pin-fin heat sinks and it is found that the topology optimized designs always yield a lower thermal resistance at the working conditions for which they are designed, which is also confirmed by validation simulations in COMSOL. Further simulation-based studies with regards to the flow pattern

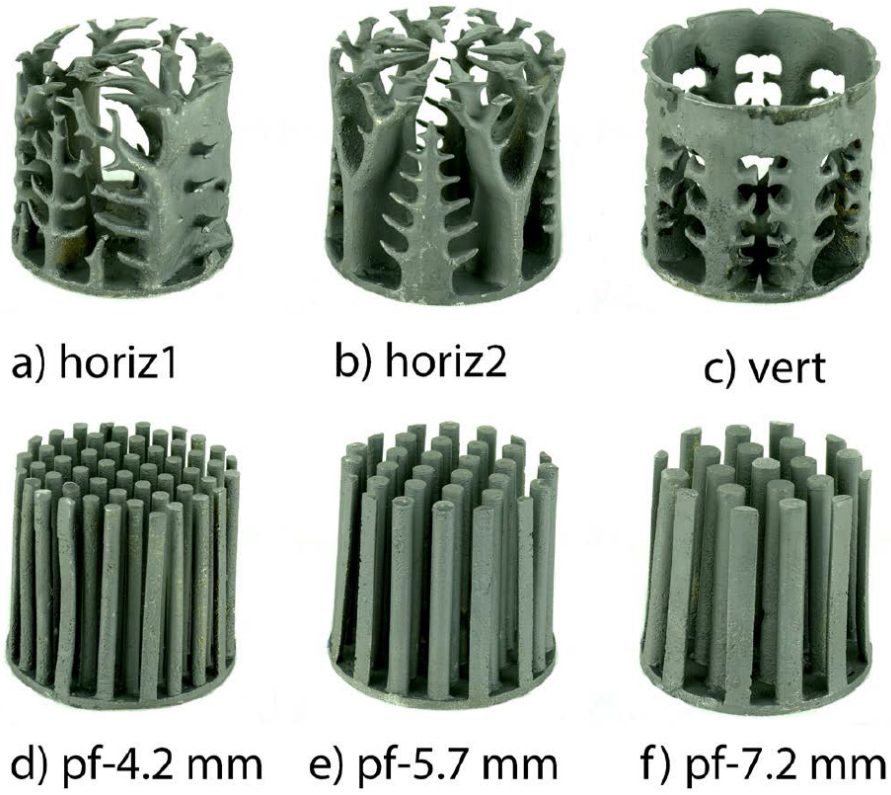

Fig. 6.2: Topology optimized heat sinks and reference heat sinks fabricated by stereolithography assisted investment casting.

around the heat sinks, the temperature profile, and the local heat transfer coefficient on the heat sink surface are presented. Additionally, measured thermographs of the heat sinks are presented and compared to the simulation predictions. Moreover, the impact of the heat sink orientation and the impact of radiation on the performance of the different heat sinks are studied.

6.3 Experimental benchmarking of the optimized tablet heat sinks

The two optimized tablet heat sinks shown in Fig. 4.4, one design obtained without using a robust topology optimization formulation (the "classical" design) and one design obtained using a robust formulation, are fabricated by laser cutting of an Aluminum plate. Some minor post-processing of the optimized designs needed to be conducted in order to obtain manufacturable heat sink contours. This was especially the case for the "classical" design since it exhibits some areas with intermediate densities at the solid-void interface. Moreover, an unoptimized heat sink of comparable surface area, and consequently mass, is fabricated in order to compare the

performance of the optimized heat sinks to a conventional design. The resulting fabricated heat sinks are shown in Fig. 6.3. The manufactured heat sinks are mounted in the tablet and evaluated experimentally. An average temperature of the area around the CPU of 45.7 °C, 47.3 °C, and 48.5 °C is respectively measured for the "classical" design, the robust design, and the reference design. This shows that the topology optimized designs yield an improved performance, even though the temperature difference to the reference design is not so dramatic. This observed trend in terms of realized average temperature is reproduced in 3D natural convection validation simulations of the designs using an explicit representation of the solid-void interface. The reader is again referred to the master theses (Damonte, 2017; Manzo, 2017) for further information regarding the different aspects mentioned in this section.

Fig. 6.3: "Classical" heat sink design (left), robust heat sink design (middle), and reference heat sink (right)(Damonte, 2017).

Chapter 7

Conclusions and outlook

7.1 Conclusions

This thesis presents how density-based topology optimization can be applied to different design challenges within thermal engineering. Numerical optimization models, based on 2D and 3D thermal diffusion modeling as well as 2D thermofluid modeling, are developed for several problems such as heat sink and heat exchanger design. Furthermore, the fabrication and experimental validation of different devices is presented.

A detailed 3D thermal diffusion model of a robotic oil well downhole intervention tool is used to optimize the thermal integration of a thermoelectric cooler into this system. Based on the presented optimization studies, a prototype of the downhole tool is designed which can operate in environments of 200 °C instead of 175 °C. A similar 2D thermal diffusion model is used in another study to generate optimized heat sinks for a commercial tablet. The application of topology optimization to the design of 3D printed dry-cooled power plant condensers is presented in another work. A simplified 2D thermofluid fully developed flow heat exchanger model is developed and used to optimize the air-side heat exchanger surface. The topology optimized designs are compared to a conventional slot channel heat exchanger geometry and it is found that the topology optimized designs show a superior performance which provides some confirmation for the usefulness of topology optimization to exploit the design freedom that additive manufacturing techniques provide. A pseudo 3D thermofluid heat sink model is applied to the design of forced convection air-cooled heat sinks. The pseudo 3D optimization model is validated with full 3D validation simulations and a good agreement between the models is found. Pressure drop minimizations are compared to thermal resistance minimizations and the influence of thermal hotspots in the base plate on the optimization is studied in an exemplifying case. Furthermore, two topology optimized designs are benchmarked against a size optimized parallel fin heat sink and the thermal resistance of the topology optimized designs is found to be up to 13% lower. A 2D thermofluid model for cross-flow heat exchanger design is presented which explicitly considers the heat transfer in both fluids. The Navier Stokes equations are solved for one fluid flowing within the modeled plane and a fully developed flow is assumed for the second fluid that is flowing perpendicular to the plane. A boundary identification method is used to flexibly represent the solid heat exchanger material that separates the two fluids. The model is applied to the optimization of an air-to-air heat exchanger and preliminary results are presented and discussed.

A prototype of the oil well downhole intervention tool is manufactured and successfully tested in an experimental setup, demonstrating the ability of the Peltier cooler coupled to the heat sink to maintain sensitive components at a lower temperature than the fluid in the well. Two topology optimized tablet heat sinks are fabricated, mounted in the tablet, and experimentally benchmarked against an unoptimized heat sink where the topology optimized

heat sinks are found to reject the heat more effectively. In another study, investment casting using 3D stereolithography printed patterns is applied to the fabrication of topology optimized natural convection heat sinks. This manufacturing technique is demonstrated to be promising for fabricating topology optimized metal parts as designs can be produced at relatively low cost and with high accuracy. Optimized heat sinks are experimentally benchmarked against conventionally designed heat sinks and it is found that the topology optimized designs realize the most effective heat dissipation when tested under the conditions for which they are optimized.

7.2 Outlook

The general aim of future research on thermal and thermofluid topology optimization should be to extend the range of industrially relevant problems to which topology optimization can be applied, to demonstrate the added value of using topology optimization compared to conventional design methods, and to manufacture and experimentally validate optimized designs. Different more specific suggestions for future research on topology optimization in the context of thermal engineering are given below:

- Most works on thermofluid topology optimization are currently limited to lower and medium Reynolds numbers as also discussed in section 5.2 and the papers **P3** and **P5**. More research regarding methods for treatment of higher Reynolds numbers problems is needed to broaden the range of problems to which topology optimization can be applied. Promising approaches are RANS modeling (Kontoleontos et al., 2013; Yoon, 2016; Papoutsis-Kiachagias and Giannakoglou, 2016; Dilgen et al., 2017) and transient modeling (Deng et al., 2011; Kreissl et al., 2011; Deng et al., 2013; Nørgaard et al., 2016); however, both methods lead to significantly increased computational cost compared to steady state laminar flow modeling. Transient optimization models can further increase the applicability range of topology optimization as inherently time-dependent problems such as the design of thermal regenerators can be treated.

- Future studies should include a meaningful benchmarking of presented topology optimized designs against conventionally designed structures to demonstrate and quantify the advantage of using topology optimization to design that specific system. To conduct such benchmarking is moreover important as thermofluid topology optimization problems are in many cases highly nonlinear and non-convex, as compared to structural problems, so that optimizations can easily converge to poor local optima as discussed in section 5.2.

- As outlined in chapter 6, only a limited number of works ((Dede et al., 2015; Damonte, 2017; Manzo, 2017; Koga et al., 2013), **P2**, and **P6**) have so far presented the manufacturing and experimental validation of topology optimized structures. Future research in this area is needed, especially in connection with benchmarking studies against reference designs, to provide sound confirmation for the advantages of using topology optimization to design thermal systems.

- Thus far, no large-scale 3D topology optimization models, as presented in (Alexandersen et al., 2016) for natural convection problems, have been applied to forced convection thermofluid problems. There are many technical systems with forced convection that exhibit pronounced 3D phenomena for which the application of 3D optimization models

would be very interesting. Such problems can only, if at all, be approximated with 2D optimization models and optimal designs are in many cases expected to exhibit three dimensionally varying features which cannot be designed using 2D models.

- Multiple thermofluid layers could be added to the pseudo 3D heat sink model presented in the papers **P4** and **P5** to be able to capture more pronounced 3D effects in the optimization model as also discussed in paper **P5**.

- Structures that are periodic perpendicular to the flow direction are generated with the pseudo 3D heat sink optimization model which allows to obtain larger optimized structures by only optimizing a small domain and, hence, significantly reducing the computational burden. The next step is to generate structures that are also periodic within the flow direction. This is less trivial than treating periodicity perpendicular to the flow direction but there exist thermofluid models for treating periodicity in the flow direction, see e.g. (Buckinx, 2017), and it would be very interesting to combine such models with a topology optimization approach.

- The cross-flow heat exchanger model presented in section 5.3 is planned to be generalized to allow the thermal conductivity to differ between the two fluids. Moreover, the conductivity of the heat exchanger material and the operating conditions of the heat exchanger should be chosen such that a more realistic problem is represented. Full 3D validation simulations of optimized geometries are planned to be conducted in order to assess the physical validity of the presented 2D optimization model. In future works, the presented interface identification method could be coupled with a large-scale 3D model to allow for the 3D optimization of thermal systems with two spatially separated fluid flows.

- The heat transfer enhancing structures presented in paper **P3** exhibit fairly thin features for higher composite conductivities which might be hard or impossible to fabricate. Robust topology optimization approaches (Wang et al., 2011; Lazarov et al., 2016) could be applied to this problem and comparable problems in order to ensure a minimum length scale on the solid structure. Moreover, it would be very interesting to apply robust optimization approaches to design structures that are robust with regards to varying operating conditions, e.g. different heat flux magnitudes that are to be dissipated from a heat sink, or with regards to manufacturing uncertainties.

Bibliography

Comsol multiphysics 5.2.

N. Aage, E. Andreassen, and B. S. Lazarov. Topology optimization using petsc: An easy-to-use, fully parallel, open source topology optimization framework. *Structural and Multidisciplinary Optimization*, 51(3):565–572, 2015.

S.-H. Ahn and S. Cho. Level set–based topological shape optimization of heat conduction problems considering design-dependent convection boundary. *Numerical Heat Transfer, Part B: Fundamentals*, 58(5):304–322, 2010. doi: 10.1080/10407790.2010.522869.

J. Alexandersen, N. Aage, C. S. Andreasen, and O. Sigmund. Topology optimisation for natural convection problems. *International Journal for Numerical Methods in Fluids*, 76(10):699–721, 2014. doi: 10.1002/fld.3954.

J. Alexandersen, O. Sigmund, and N. Aage. Topology optimisation of passive coolers for light-emitting diode lamps. In *Proceedings of the 11th World Congress of Structural and Multidisciplinary Optimisation*, 2015.

J. Alexandersen, O. Sigmund, and N. Aage. Large scale three-dimensional topology optimisation of heat sinks cooled by natural convection. *International Journal of Heat and Mass Transfer*, 100:876–891, 2016. doi: 10.1016/j.ijheatmasstransfer.2016.05.013.

G. Allaire, F. Jouve, and A.-M. Toader. Structural optimization using sensitivity analysis and a level-set method. *Journal of computational physics*, 194(1):363–393, 2004.

C. S. Andreasen, A. R. Gersborg, and O. Sigmund. Topology optimization of microfluidic mixers. *International Journal for Numerical Methods in Fluids*, 61(5):498–513, 2009.

S. Balay, S. Abhyankar, M. Adams, P. Brune, K. Buschelman, L. Dalcin, W. Gropp, B. Smith, D. Karpeyev, D. Kaushik, et al. Petsc users manual revision 3.7. Technical report, Argonne National Lab.(ANL), Argonne, IL (United States), 2016. URL `http://www.mcs.anl.gov/petsc/`.

M. P. Bendsøe. Optimal shape design as a material distribution problem. *Structural optimization*, 1(4):193–202, 1989.

M. P. Bendsøe and N. Kikuchi. Generating optimal topologies in structural design using a homogenization method. *Computer methods in applied mechanics and engineering*, 71(2): 197–224, 1988.

M. P. Bendsoe and O. Sigmund. *Topology Optimization: Theory, Methods, and Applications*. Springer, 2003. doi: 10.1007/978-3-662-05086-6.

P. T. Boggs and J. W. Tolle. Sequential quadratic programming. *Acta numerica*, 4:1–51, 1995.

T. Borrvall and J. Petersson. Topology optimization of fluids in Stokes flow. *International journal for numerical methods in fluids*, 41(1):77–107, 2003. doi: 10.1002/fld.426.

T. E. Bruns. Topology optimization of convection-dominated, steady-state heat transfer problems. *International Journal of Heat and Mass Transfer*, 50(15):2859–2873, 2007. doi: 10.1016/j.ijheatmasstransfer.2007.01.039.

G. Buckinx. *Macro-Scale Flow and Heat Transfer in Systems with Periodic Solid Structures*. PhD thesis, KU Leuven, 2017.

V. J. Challis and J. K. Guest. Level set topology optimization of fluids in Stokes flow. *International journal for numerical methods in engineering*, 79(10):1284–1308, 2009.

A. Clausen, N. Aage, and O. Sigmund. Topology optimization of coated structures and material interface problems. *Computer Methods in Applied Mechanics and Engineering*, 290:524–541, 2015.

P. Coffin and K. Maute. Level set topology optimization of cooling and heating devices using a simplified convection model. *Structural and multidisciplinary optimization*, 53(5):985–1003, 2016a. doi: 10.1007/s00158-015-1343-8.

P. Coffin and K. Maute. A level-set method for steady-state and transient natural convection problems. *Structural and Multidisciplinary Optimization*, 53(5):1047–1067, 2016b. doi: 10.1007/s00158-015-1377-y.

A. Damonte. Design and Validation of a Heat Sink for Consumer Eelectronics Using Topology Optimization. Master's thesis, Politecnico di Milano, 2017.

T. Dbouk. A review about the engineering design of optimal heat transfer systems using topology optimization. *Applied Thermal Engineering*, 112:841–854, 2016. doi: 10.1016/j.applthermaleng.2016.10.134.

J. D. Deaton and R. V. Grandhi. A survey of structural and multidisciplinary continuum topology optimization: post 2000. *Structural and Multidisciplinary Optimization*, 49(1):1–38, 2014. doi: 10.1007/s00158-013-0956-z.

E. M. Dede. Multiphysics topology optimization of heat transfer and fluid flow systems. In *Proceedings of the COMSOL Users Conference*, 2009.

E. M. Dede. Optimization and design of a multipass branching microchannel heat sink for electronics cooling. *Journal of Electronic Packaging*, 134(4):041001, 2012. doi: 10.1115/1.4007159.

E. M. Dede, S. N. Joshi, and F. Zhou. Topology optimization, additive layer manufacturing, and experimental testing of an air-cooled heat sink. *Journal of Mechanical Design*, 137(11):111702, 2015. doi: 10.1115/1.4030989.

Y. Deng, Z. Liu, P. Zhang, Y. Liu, and Y. Wu. Topology optimization of unsteady incompressible Navier–Stokes flows. *Journal of Computational Physics*, 230(17):6688–6708, 2011.

Y. Deng, Z. Liu, and Y. Wu. Topology optimization of steady and unsteady incompressible Navier–Stokes flows driven by body forces. *Structural and Multidisciplinary Optimization*, 47(4):555–570, 2013.

C. B. Dilgen, S. B. Dilgen, D. R. Fuhrman, O. Sigmund, and B. S. Lazarov. Topology optimization of turbulent flows. *Computer Methods in Applied Mechanics and Engineering*, 2017.

M. B. Dühring, J. S. Jensen, and O. Sigmund. Acoustic design by topology optimization. *Journal of sound and vibration*, 317(3):557–575, 2008.

A. Forsgren and P. E. Gill. Primal-dual interior methods for nonconvex nonlinear programming. *SIAM Journal on Optimization*, 8(4):1132–1152, 1998.

S. V. Garimella, A. S. Fleischer, J. Y. Murthy, A. Keshavarzi, R. Prasher, C. Patel, S. H. Bhavnani, R. Venkatasubramanian, R. Mahajan, Y. Joshi, et al. Thermal challenges in next-generation electronic systems. *Components and Packaging Technologies, IEEE Transactions on*, 31(4):801–815, 2008. doi: 10.1109/TCAPT.2008.2001197.

A. Gersborg-Hansen, O. Sigmund, and R. B. Haber. Topology optimization of channel flow problems. *Structural and Multidisciplinary Optimization*, 30(3):181–192, 2005.

M. B. Giles and N. A. Pierce. An introduction to the adjoint approach to design. *Flow, turbulence and combustion*, 65(3-4):393–415, 2000.

A. Iga, S. Nishiwaki, K. Izui, and M. Yoshimura. Topology optimization for thermal conductors considering design-dependent effects, including heat conduction and convection. *International Journal of Heat and Mass Transfer*, 52(11):2721–2732, 2009. doi: 10.1016/j.ijheatmasstransfer.2008.12.013.

J. S. Jensen and O. Sigmund. Topology optimization for nano-photonics. *Laser & Photonics Reviews*, 5(2):308–321, 2011. doi: 10.1002/lpor.201000014.

Y. Joo, I. Lee, and S. J. Kim. Topology optimization of heat sinks in natural convection considering the effect of shape-dependent heat transfer coefficient. *International Journal of Heat and Mass Transfer*, 109:123–133, 2017. doi: 10.1016/j.ijheatmasstransfer.2017.01.099.

A. A. Koga, E. C. C. Lopes, H. F. V. Nova, C. R. de Lima, and E. C. N. Silva. Development of heat sink device by using topology optimization. *International Journal of Heat and Mass Transfer*, 64:759–772, 2013. doi: 10.1016/j.ijheatmasstransfer.2013.05.007.

E. Kontoleontos, E. Papoutsis-Kiachagias, A. Zymaris, D. Papadimitriou, and K. Giannakoglou. Adjoint-based constrained topology optimization for viscous flows, including heat transfer. *Engineering Optimization*, 45(8):941–961, 2013. doi: 10.1080/0305215x.2012.717074.

S. Kreissl and K. Maute. Levelset based fluid topology optimization using the extended finite element method. *Structural and Multidisciplinary Optimization*, 46(3):311–326, 2012.

S. Kreissl, G. Pingen, and K. Maute. Topology optimization for unsteady flow. *International Journal for Numerical Methods in Engineering*, 87(13):1229–1253, 2011.

B. S. Lazarov and O. Sigmund. Filters in topology optimization based on Helmholtz-type differential equations. *International Journal for Numerical Methods in Engineering*, 86(6): 765–781, 2011. doi: 10.1002/nme.3072.

B. S. Lazarov, F. Wang, and O. Sigmund. Length scale and manufacturability in density-based topology optimization. *Archive of Applied Mechanics*, 86(1-2):189–218, 2016. doi: 10.1007/s00419-015-1106-4.

J. Macknick, R. Newmark, G. Heath, and K. C. Hallett. A review of operational water consumption and withdrawal factors for electricity generating technologies. Technical report, mar 2011.

A. Manzo. Enhancing the Thermal Design of an Electronic Device using Topology Optimization. Master's thesis, Politecnico di Torino, 2017.

T. Matsumori, T. Kondoh, A. Kawamoto, and T. Nomura. Topology optimization for fluid–thermal interaction problems under constant input power. *Structural and Multidisciplinary Optimization*, 47(4):571–581, 2013. doi: 10.1007/s00158-013-0887-8.

C. McConnell and G. Pingen. Multi-layer, pseudo 3d thermal topology optimization of heat sinks. In *Volume 7: Fluids and Heat Transfer, Parts A, B, C, and D*. ASME International, nov 2012. doi: 10.1115/imece2012-93093.

P. Michaleris, D. A. Tortorelli, and C. A. Vidal. Tangent operators and design sensitivity formulations for transient non-linear coupled problems with applications to elastoplasticity. *International Journal for Numerical Methods in Engineering*, 37(14):2471–2499, 1994.

H. Mlejnek. Some aspects of the genesis of structures. *Structural Optimization*, 5(1-2):64–69, 1992.

S. Nørgaard, O. Sigmund, and B. Lazarov. Topology optimization of unsteady flow problems using the lattice Boltzmann method. *Journal of Computational Physics*, 307:291–307, 2016.

L. H. Olesen, F. Okkels, and H. Bruus. A high-level programming-language implementation of topology optimization applied to steady-state Navier–Stokes flow. *International Journal for Numerical Methods in Engineering*, 65(7):975–1001, 2006.

E. Papoutsis-Kiachagias and K. Giannakoglou. Continuous adjoint methods for turbulent flows, applied to shape and topology optimization: industrial applications. *Archives of Computational Methods in Engineering*, 23(2):255–299, 2016.

A. Pizzolato, A. Sharma, K. Maute, A. Sciacovelli, and V. Verda. Topology optimization for heat transfer enhancement in Latent Heat Thermal Energy Storage. *International Journal of Heat and Mass Transfer*, 113:875–888, 2017. doi: 10.1016/j.ijheatmasstransfer.2017.05.098.

X. Qian and E. M. Dede. Topology optimization of a coupled thermal-fluid system under a tangential thermal gradient constraint. *Structural and Multidisciplinary Optimization*, 2015. doi: 10.1007/s00158-016-1421-6.

S. Rojas-Labanda and M. Stolpe. Benchmarking optimization solvers for structural topology optimization. *Structural and Multidisciplinary Optimization*, pages 1–21, 2015.

O. Schenk and K. Gärtner. Solving unsymmetric sparse systems of linear equations with pardiso. *Future Generation Computer Systems*, 20(3):475–487, 2004. doi: 10.1016/s0167-739x(03)00188-2.

O. Sigmund. Design of multiphysics actuators using topology optimization–Part i: One-material structures. *Computer methods in applied mechanics and engineering*, 190(49):6577–6604, 2001. doi: 10.1016/s0045-7825(01)00251-1.

O. Sigmund and K. Maute. Topology optimization approaches. *Structural and Multidisciplinary Optimization*, 48(6):1031–1055, 2013.

O. Sigmund and J. Petersson. Numerical instabilities in topology optimization: a survey on procedures dealing with checkerboards, mesh-dependencies and local minima. *Structural optimization*, 16(1):68–75, 1998. doi: 10.1007/bf01214002.

J. Sokolowski and A. Zochowski. On the topological derivative in shape optimization. *SIAM journal on control and optimization*, 37(4):1251–1272, 1999.

S. Soprani, K. Engelbrecht, C. Bahl, and C. Nesgaard. *Active cooling of a down hole well tractor*. PhD thesis, Technical University of Denmark, 2016.

M. Stolpe and K. Svanberg. An alternative interpolation scheme for minimum compliance topology optimization. *Structural and Multidisciplinary Optimization*, 22(2):116–124, 2001a. doi: 10.1007/s001580100129.

M. Stolpe and K. Svanberg. On the trajectories of penalization methods for topology optimization. *Structural and Multidisciplinary Optimization*, 21(2):128–139, 2001b. doi: 10.1007/s001580050177.

K. Svanberg. The method of moving asymptotes - a new method for structural optimization. *International journal for numerical methods in engineering*, 24(2):359–373, 1987.

K. Svanberg. A class of globally convergent optimization methods based on conservative convex separable approximations. *SIAM journal on optimization*, 12(2):555–573, 2002. doi: 10.1137/s1052623499362822.

C. T'Joen, Y. Park, Q. Wang, A. Sommers, X. Han, and A. Jacobi. A review on polymer heat exchangers for HVAC&R applications. *international journal of refrigeration*, 32(5):763–779, 2009. doi: 10.1016/j.ijrefrig.2008.11.008.

A. Vassighi and M. Sachdev. *Thermal and power management of integrated circuits*. Springer Science & Business Media, 2006. doi: 10.1007/0-387-29749-9.

F. Wang, B. S. Lazarov, and O. Sigmund. On projection methods, convergence and robust formulations in topology optimization. *Structural and Multidisciplinary Optimization*, 43(6):767–784, 2011. doi: 10.1007/s00158-010-0602-y.

M. Y. Wang, X. Wang, and D. Guo. A level set method for structural topology optimization. *Computer methods in applied mechanics and engineering*, 192(1):227–246, 2003.

Y. M. Xie and G. P. Steven. A simple evolutionary procedure for structural optimization. *Computers & structures*, 49(5):885–896, 1993.

K. Yaji, T. Yamada, S. Kubo, K. Izui, and S. Nishiwaki. A topology optimization method for a coupled thermal–fluid problem using level set boundary expressions. *International Journal of Heat and Mass Transfer*, 81:878–888, 2015. doi: 10.1016/j.ijheatmasstransfer.2014.11.005.

K. Yaji, T. Yamada, M. Yoshino, T. Matsumoto, K. Izui, and S. Nishiwaki. Topology optimization in thermal-fluid flow using the lattice Boltzmann method. *Journal of Computational Physics*, 307:355–377, 2016. doi: 10.1016/j.jcp.2015.12.008.

L. Yin and G. K. Ananthasuresh. A novel topology design scheme for the multi-physics problems of electro-thermally actuated compliant micromechanisms. *Sensors and Actuators A: Physical*, 97:599–609, 2002. doi: 10.1007/978-3-642-59497-7_59.

G. H. Yoon. Topological design of heat dissipating structure with forced convective heat transfer. *Journal of Mechanical Science and Technology*, 24(6):1225–1233, 2010. doi: 10.1007/s12206-010-0328-1.

G. H. Yoon. Topology optimization for turbulent flow with Spalart–Allmaras model. *Computer Methods in Applied Mechanics and Engineering*, 303:288–311, 2016.

X. Zhao, M. Zhou, O. Sigmund, and C. S. Andreasen. A poor mans approach to topology optimization of cooling channels based on a Darcy flow model. *International Journal of Heat and Mass Transfer*, 116:1108–1123, 2018.

M. Zhou and G. I. N. Rozvany. The COC algorithm, Part ii: topological, geometrical and generalized shape optimization. *Computer Methods in Applied Mechanics and Engineering*, 89(1):309–336, 1991.

M. Zhou, J. Alexandersen, O. Sigmund, and C. B. Pedersen. Industrial application of topology optimization for combined conductive and convective heat transfer problems. *Structural and Multidisciplinary Optimization*, 54(4):1045–1060, 2016. doi: 10.1007/s00158-016-1433-2.

S. Zhou and Q. Li. A variational level set method for the topology optimization of steady-state Navier–Stokes flow. *Journal of Computational Physics*, 227(24):10178–10195, 2008.

Appendix

Appendix A

Appendix

A.1 P1 - Topology Optimization of an Actively Cooled Electronics Section for Downhole Tools

S. Soprani, J. H. K. Haertel, B. S. Lazarov, O. Sigmund and K. Engelbrecht

***Proceedings of the COMSOL Conference 2015*, 2015**

Topology Optimization of an Actively Cooled Electronics Section for Downhole Tools

S. Soprani*[1], J. H. K. Haertel[1], B. S. Lazarov[2], O. Sigmund[2], K. Engelbrecht[1],
[1] Department of Energy Conversion and Storage - Technical University of Denmark, [2]Department of Mechanical Engineering - Technical University of Denmark.
* Frederiksborgvej 399 - Building 778, 4000 Roskilde, Denmark, stefs@dtu.dk

Abstract: Active cooling systems represent a possible solution to the electronics overheating that occurs in wireline downhole tools operating in high temperature oil and gas wells. A Peltier cooler was chosen to maintain the downhole electronics to a tolerable temperature, but its integration into the downhole electronics unit proved to be challenging, because of the space constraints and the proximity of the cooling zone (electronics) to the heat sink (well fluid). The topology optimization approach was therefore chosen to optimize the thermal design of the actively cooled electronics section and the SIMP (Solid Isotropic Material with Penalization) method was implemented in COMSOL Multiphysics. Several optimized designs were obtained for different operating conditions and their sensitivity to the change in the boundary conditions was evaluated. A final design for the electronics unit was selected, according to the topology optimization results and assembly constraints, and compared to the optimized cases.

Keywords: Topology optimization, SIMP, Electronics cooling.

1. Introduction

Well interventions are remedial operations that are performed in oil and gas wells in order to restore or increase the production. The *electric wireline* well intervention technique relies on the usage of a cabling technology that connects the downhole tools to the surface equipment and, thanks to the integration of electronic components into the downhole devices, allows the operator to remotely control the tool during the operation. However, the application of the wireline technique in high temperature wells, where the temperature can range between 150 °C and 200 °C, is often restricted by the electronics temperature limit, which is currently set to 175 °C for the majority of the employed components available on the market.

Active cooling systems represent a possible solution to the electronics overheating [1] as they could extend the application of the wireline tools to a wider range of high temperature wells. The high-temperature sensitive electronics would be maintained below the well temperature, while the well fluid would be used as a heat sink for the cooler excessive heat. A thermoelectric cooler (TEC) was chosen to fulfill this task [2], because of its compactness and lack of moving parts; on the other hand its low efficiency (COP) might generate issues due to excessive heat rejection at the hot end in the case of low convection regimes in the oil well.. It is therefore very important to define an effective thermal design of the electronics unit that provides a good thermal path to reject the excessive heat to the well, protects the cooled electronics from the hot surroundings and minimizes the heat leakages. The limited availability of space in the downhole tool and the proximity between the cooling load and the heat sink make this task challenging.

The topology optimization approach was adopted in order to define an optimized distribution of the thermal conductive material and thermal insulation, so the high-temperature sensitive components' temperature could be minimized. The geometry of the electronics unit was modelled in COMSOL Multiphysics and the topology optimization SIMP (Solid Isotropic Material with Penalization) method [3] was implemented. A density filter was applied in order to avoid mesh-dependent solutions, and coupled with a projection function, in order to obtain a better resolution of the design variable distribution that defines the optimized distribution of thermally conductive material and thermal insulation.

2. System integration overview

The downhole tool electronics unit (Figure 1) is composed of two main structural components: a 200 mm long cylindrical *chassis* (O.D. 60 mm), on which the electronic components are installed,

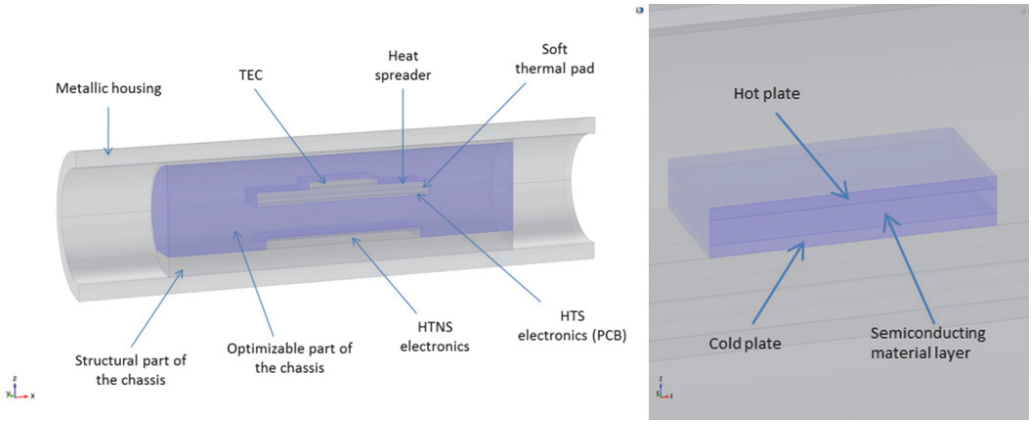

Figure 1. COMSOL Multiphysics representation of the longitudinal section of the downhole tool (left side) and particular of the TEC device with the two plates and the semiconducting material layer highlighted in blue (right side).

and a 300 mm long metallic *housing* (O.D. 80 mm, I.D. 60 mm), which encloses the chassis and the electronics, protecting and sealing them from the outer well fluid at high pressure. The chassis, in turn, is divided into a "*structural*" part made of aluminum, that provides mechanical stability to the system, and an "*optimizable*" part, that will be the object of the topology optimization.

Furthermore, the electronic components can be distinguished into *high temperature-non sensitive (HTNS)* and *high temperature-sensitive (HTS)* components. The first dissipate 5 W, are mounted directly on the chassis and are passively cooled; the latter dissipate 1 W, are installed on a printed circuit board (PCB) and are actively cooled with the TEC. The TEC cold plate is thermally coupled with the HTS electronics through a copper *heat spreader* and a *soft thermal pad*. On the other side, the TEC hot plate needs to be thermally connected to the well fluid through a heat sink that the topology optimization solver is asked to optimize. The design of the system aims at maintaining the HTS electronics below 175 °C, when operating in a 200 °C well environment.

3. Governing equations

The heat transfer within the system is mainly driven by heat conduction, so the heat transfer PDE (Eq. 1) was implemented in the COMSOL model through the Heat Transfer module.

$$\nabla(-k\nabla T) = Q_{source} \tag{1}$$

Where k ($Wm^{-1}K^{-1}$) is the material thermal conductivity, T (K) is the temperature and Q_{source} (Wm^{-3}) is a volumetric heat source.

A modified heat transfer equation, that accounted for the thermoelectric effect, was implemented in the TEC semiconductor domain, in between the TEC hot and cold plates, through the Coefficient Form PDE module.

$$\nabla(\boldsymbol{J}ST - k\nabla T) = Q_{JouleHeating} \tag{2}$$

Where $\boldsymbol{J}$ (Am^{-2}) is the electric current density vector, S (VK^{-1}) is the material Seebeck coefficient, $Q_{JouleHeating}$ (Wm^{-3}) is the heat source associated to the Joule effect. The layer between the TEC hot and cold plates (Figure 1), in reality, is composed of leg pairs of semiconductor material (Bi_2Te_3) separated by air; in order to reduce the geometry complexity this layer was modelled as isotropic and homogeneous, and its properties were weighted based on the volumes of Bi_2Te_3 and air (Eq. 3, 4, 5). Equations from Gordon et al. [4] were used to characterize the behavior of Bi_2Te_3, while the COMSOL material library was used for the air properties. The equations were combined through linear coefficients in order to match a commercial Peltier cooler performance that was evaluated in terms of hot and cold plate temperatures at different cooling loads and operating temperatures.

$$S = S_1(-2.025e-9T^2 + 1.42e-6T + \\ -4.49e-5) \tag{3}$$

$$k = k_1(2.91e-5T^2 - 0.019T + 4.81) + \\ +k_2\, k_{air}(T) \tag{4}$$

$$\sigma = \sigma_1(4.35e.8T - 2.754e - 6)^{-1} \quad (5)$$

$$Q_{JouleHeating} = 0.268\,\sigma^{-1}\,\boldsymbol{J}\cdot\boldsymbol{J} \quad (6)$$

Where $k_{air}(T)$ ($Wm^{-1}K^{-1}$) is the thermal conductivity of air as a function of temperature from the COMSOL material library; S_1 = 0.349, k_1 = 0.215, k_2=0.732 and σ_1 = 0.309 are linear coefficients. At the two ends of the electronics unit, an adiabatic boundary condition was set. A convective heat flux, simulating the well fluid interaction with the housing surface, was imposed by setting the external well fluid temperature T_{fl} and heat transfer convective coefficient h. The partial differential equations (1) and (2) were then interfaced through a Dirichlet boundary condition that matched the temperatures at the interface. Heat sources were set in the HTNS electronics domain (5W) and at the interface between the PCB and the soft thermal pad (1 W), to simulate the electronics power dissipation. According to empirical estimations, thermal contact resistances were simulated by setting a thin resistive layer at the interface between the structural chassis and the housing (R_{th1} = 1.1e-3 m^2KW^{-1}), between the HTNS electronics and the structural chassis (R_{th2} = 2.5e-5 m^2KW^{-1}), and between the TEC plates and the structural chassis/heat spreader (R_{th3} = 2.5e-5 m^2KW^{-1}). R_{th1} was estimated through the comparison between simulation results and experimental data from thermal tests on the structural chassis. R_{th2} and R_{th3} instead, simulated a 0.1 mm thick layer of thermal grease, with a thermal conductivity of 4 $Wm^{-1}K^{-1}$. Another relevant boundary condition was set for the TEC feed current I_{feed} and used to characterize the cooler operating state.

4. Topology optimization implementation

The topology optimization problem can be stated as follows:

$$minimize: \quad f_{obj}(T, \rho_{design}) = \frac{1}{A_{PCB}}\int_{\Omega_{PCB}} T\, d\Omega_{PCB} \quad (7)$$

$$constraints: \quad 0 \le \rho_{design} \le 1 \quad (8)$$

$$0 \le \int_{\Omega} \rho_{design} d\Omega \le \gamma V_{\Omega} \quad (9)$$

$$0 \le \gamma \le 1 \quad (10)$$

$$\boldsymbol{r}(T, \rho_{design}) = \boldsymbol{0} \quad (11)$$

Where f_{obj} is the objective function to be minimized, defined as the integral average of the temperature distribution along the PCB surface Ω_{PCB}; A_{PCB} is the PCB area surface (m^2), ρ_{design} is the design variable that can range between 0 (thermal insulation) and 1 (aluminum), and whose distribution needs to be optimized; γ is the fraction of the optimizable domain V_{Ω} that sets the constraint on the maximum volume that can be occupied by aluminum; $\boldsymbol{r}(T, \rho_{design})$ is the residual of the discretized system of the state equations reported in section 3.

The topology optimization problem was implemented in COMSOL through the Optimization module: ρ_{design} was defined and bounded as a *control variable field*, while the volume constraint was set with an *integral inequality constraint*. A density filter [5] was applied to the design variable, in order to make the solution independent from the mesh size (Eq. 12), and implemented in COMSOL through the Coefficient Form PDE module:

$$-r^2\nabla^2\tilde{\rho} + \tilde{\rho} = \rho_{design} \quad (12)$$

Where r is a filter parameter and is equal to 1.5 times the maximum mesh element length in the optimizable domain. $\tilde{\rho}$ was then projected in order to obtain a sharper transition zone between aluminum and insulator in the optimized topology [6]; Eq. 13 was used.

$$\bar{\tilde{\rho}} = \frac{tanh(\beta\eta) + tanh(\beta(\tilde{\rho} - \eta))}{tanh(\beta\eta) + tanh(\beta(1 - \eta))} \quad (13)$$

η = 0.5 ensured a good convergence of the solution; β was ramped from 1 to 8, using the continuation approach, as suggested by Wang et al. [7]. The thermal properties of the optimizable domain were then calculated through the projected design variable, with an interpolation function that defined the thermal conductivity.

$$k_{\Omega} = k_{ins} + (k_{Al} - k_{ins})\bar{\tilde{\rho}}^{p} \quad (14)$$

Where k_{Ω} ($Wm^{-1}K^{-1}$) is the domain effective thermal conductivity, k_{ins} = 0.17 $Wm^{-1}K^{-1}$ and k_{Al}= 138 $Wm^{-1}K^{-1}$ are respectively the thermal conductivities of the thermal insulation and of the considered aluminum alloy, and p = 3 [7] is the penalization coefficient.

The problem was solved through the optimization solver MMA (Method of Moving Asymptotes), embedded in COMSOL.

5. Results

The model was simulated for a well temperature of 200 °C and different conditions of well fluid convection regimes h and TEC feed current I_{feed}, so the design could be optimized for different operating conditions.

The system was optimized for I_{feed} of 1, 2, 3 and 4 A, according to the modelled commercial cooler specifications, and for h of 25, 50, 100 and 500 $Wm^{-2}K^{-1}$, in order to reproduce low, medium-low and medium well fluid convection regimes. h = 25 $Wm^{-2}K^{-1}$ is defined as the worst case design condition, while for h > 500 $Wm^{-2}K^{-1}$ the design of the unit is expected not to be critical anymore. The optimization of the system balanced the use of aluminum and thermal insulation in different ways at different boundary conditions; a tradeoff between thermal protection of the cooled electronics and heat rejection of the excessive heat was always reached and two main design concepts were individuated.

Low TEC feed currents and high values of convective coefficients led to an optimized design (*Design 1*) where an aluminum pad connects the cooler hot plate to the structural chassis, so the excessive heat can be rejected radially through the housing to the well (Figure 2). Low I_{feed} (low ohmic losses across the cooler) and high h values make the heat rejection process not critical, so the thermal protection of the cooled electronics is prioritized and the use of aluminum is limited to provide a radial heat sink. The length of the aluminum pad increases when the feed current grows or the heat transfer convective coefficient decreases.

High TEC feed currents and low values of convective coefficients, on the other side, led to a design (*Design 2*) where the heat rejection becomes more problematic than in the previous case. An aluminum layer is now attached to the structural chassis (Figure 3). This layer does not only provide a radial path for the excessive heat to be rejected to the well, but also spreads it along the longitudinal direction of the tool; a better distribution of the heat enhances the heat exchange with the well fluid and minimizes the heat backflow to the cooled electronics. Thermal insulation still protects the cooled electronics from the HTNS components and the hot surroundings. The thickness of the layer increases with I_{feed} and when h decreases.

The balance between materials can be evaluated, for different boundary conditions, through the ratio of used aluminum over the optimizable volume (Figure 4).

$$R = \frac{1}{V_\Omega} \int_\Omega \bar{\tilde{\rho}} \, d\Omega \tag{15}$$

Where R is the aluminum usage ratio and V_Ω is the optimizable domain volume (m^3). In order to have a good overview of the system behavior, the sensitivity of the optimized designs to operations at different boundary conditions was assessed. The performance of the system was evaluated in terms of temperature at which the HTS electronics could be maintained.

The electronics section was initially optimized for a certain value of feed current and well fluid convective coefficient; the resulting

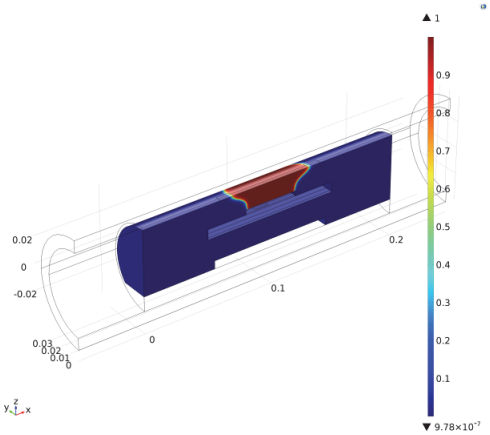

Figure 2. $\bar{\tilde{\rho}}$ distribution for the *Design 1* concept. System optimized for I_{feed} = 1 A and h = 100 $Wm^{-2}K^{-1}$.

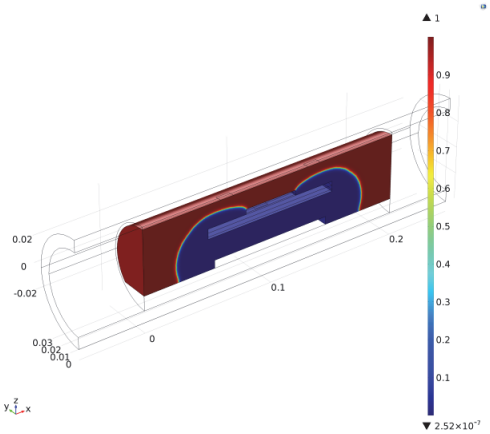

Figure 3. $\bar{\tilde{\rho}}$ distribution for the *Design 2* concept. System optimized for I_{feed} = 4 A and h = 50 $Wm^{-2}K^{-1}$.

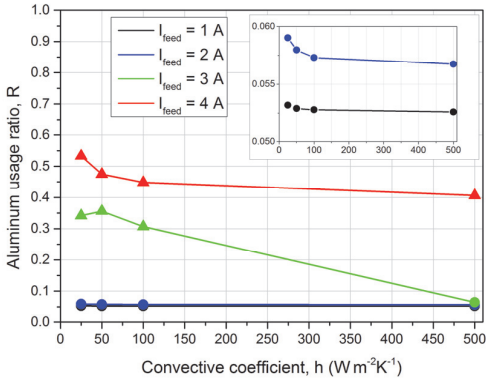

Figure 4. *R* vs. well fluid convective coefficient, for different TEC feed currents. Different symbols refer to the different optimized design concepts.
● = Design 1, ▲ = Design 2.

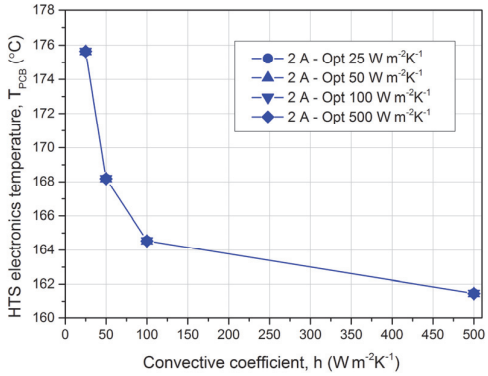

Figure 5. HTS electronics temperature vs. well fluid convective coefficient for four different systems, optimized for I_{feed} = 2 A and h = 25, 50, 100 and 500 $Wm^{-2}K^{-1}$.

design was then simulated, maintaining the TEC feed current constant, at different values of well fluid convective coefficients. Figure 5 reports the performance of the optimized designs versus the well fluid convective coefficient: each of the five illustrated curves refers to a system optimized for I_{feed} = 2 A and a different value of h. It can be noticed the five curves overlap and the performance of the systems is very similar, despite they were optimized for different h values. A maximum temperature mismatch of 0.05 °C between the curves was found. The same behavior was obtained with the optimizations with the other feed currents. For I_{feed} = 1 A the maximum mismatch between the curves is equal to 0.005 °C, for I_{feed} = 3 A is equal to 0.88 °C and for I_{feed} = 4 A is equal to 0.88 °C. We can conclude the optimization of the electronics unit, at a given feed current is not significantly sensitive to the well fluid convective coefficients in the considered range; in other words, the performance of the optimized systems, at a given feed current, is not significantly sensitive to the length/thickness of the optimized aluminum pad/layer and can be considered robust.

The same approach was used to evaluate the sensitivity of the optimized designs to the TEC feed current, at a given convective coefficient. The electronics section was first optimized for a certain value of feed current and well fluid convection; the resulting design was then simulated, maintaining the convection regime constant, at different values of operating current. Figure 6 shows the optimization process is more sensitive to the feed current as the mismatch between the curves can go up to several degrees Celsius. An optimal feed current I_{opt} that minimizes the HTS electronics temperature can be individuated. It can be defined as the TEC feed current at which the marginal gain in absorbed heat flux, due to an infinitesimal increase of the TEC feed current, becomes lower than the heat flux that leaks through the insulation. I_{opt} is slightly different for each optimized design, but mainly depends on h and on the well fluid capability of absorbing the excessive heat. I_{opt} is equal to ~1.9 A for h = 25 $Wm^{-2}K^{-1}$, to ~2.3 A for h = 50 $Wm^{-2}K^{-1}$, to ~2.6 A for h = 100 $Wm^{-2}K^{-1}$ and to ~2.9 A for h = 500 $Wm^{-2}K^{-1}$. The designs that best operate around the optimal current are the ones optimized for 2 A and 3 A.

The topology optimization results, together with the knowledge of the practical assembly constraints, were used to define the final design for the actively cooled downhole electronics unit (Figure 7). *Design 1* proved to be as well performing as *Design 2* around the optimal current, but with a lower employment of aluminum and therefore with a lower weight. The aluminum pad that provided the thermal path from the cooler hot plate to the structural chassis proved to be crucial. An aluminum pad, 41x41 mm was therefore implemented in the final design, illustrated in Figure 7. No aluminum layer was included, except for 2 walls, 10 mm thick, at each end of the chassis. They provide mechanical stability, an additional

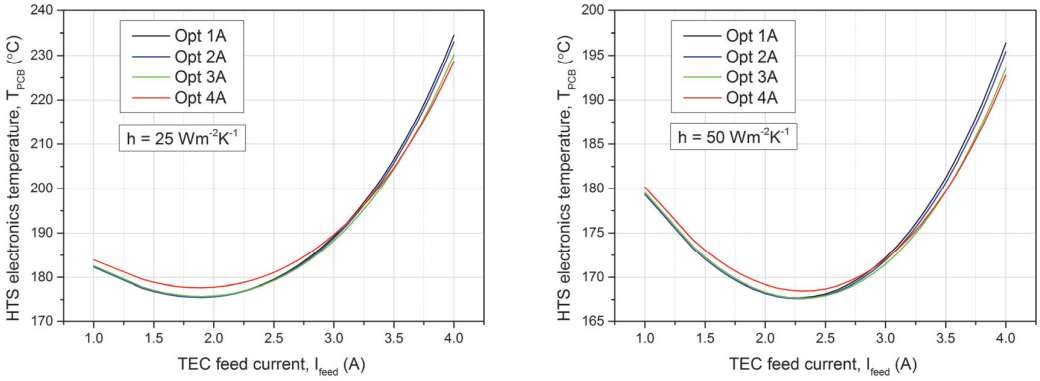

Figure 6. HTS electronics temperature vs. TEC feed current for four different systems, optimized for I_{feed} = 1, 2, 3 and 4 A, and h = 25 $Wm^{-2}K^{-1}$ (left side) and 50 $Wm^{-2}K^{-1}$ (right side).

thermal path for the heat to better spread in case of low heat rejection rate, and are suitable for the installation of pins for the assembly of the system. The chassis would be in fact split in a bottom half, were the HTNS electronics are installed, and a top half, where the cooling system is installed. The two halves would then be coupled and held in place by four pins (not reported in Figure 7). Two smaller pads, 8x8 mm, with threaded holes, were also designed in the top part of the chassis in order to clamp the cooler in between the heat spreader and the chassis itself, through a plastic screw system. The rest of the domain is filled with thermal insulation.

Simulations proved the chosen design operates very closely to the optimized systems performance (Table 1). The difference in HTS electronics temperature is very small when operating at 1 or 2 A, as the chosen design is very similar to the *Design 1* concept: the electronics is maintained maximum 0.09 K above the HTS electronics temperature in the optimized case. When operating at 3 and 4 A the mismatch becomes higher, since the *Design 2* concept would work better at high feed currents. However, the HTS components are always maintained less than 1 K above the optimized case for operations at 3 A. The mismatches are larger than 1 K for I_{feed} = 4 A, but can be

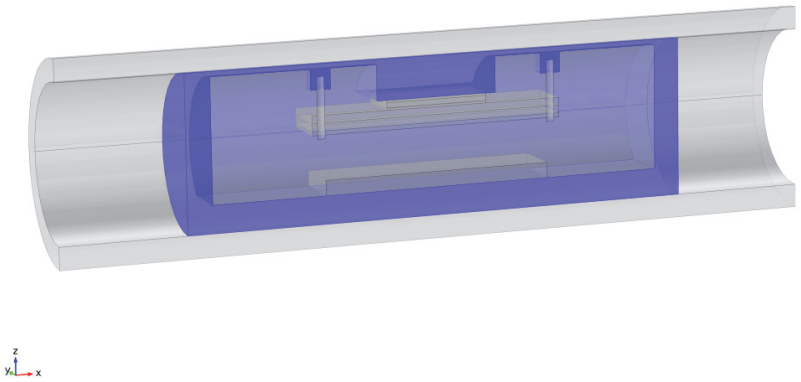

Figure 7. COMSOL Multiphysics illustration of the longitudinal section of the final design. The designed aluminum chassis is highlighted in blue.

considered irrelevant; a feed current of 4 A is far from the observed optimal feed currents and the system would always aim to operate close to the optimal conditions, between 2 and 3 A.

Table 1. Comparison between the performance of the optimized systems (Opt) and final chosen design (Design). $\Delta T = T_{HTS,design} - T_{HTS,Opt}$.

h $(Wm^{-2}K^{-1})$	*Opt - 1A* T_{HTS} (°C)	*Design - 1A* T_{HTS} (°C)	ΔT (K)
25	182.31	181.95	0.10
50	179.32	178.97	0.11
100	177.83	177.47	0.11
500	176.56	176.21	0.11
h $(Wm^{-2}K^{-1})$	*Opt - 2A* T_{HTS} (°C)	*Design - 2A* T_{HTS} (°C)	ΔT (K)
25	175.63	175.68	0.05
50	168.18	168.23	0.05
100	164.54	164.57	0.04
500	161.46	161.48	0.03
h $(Wm^{-2}K^{-1})$	*Opt - 3A* T_{HTS} (°C)	*Design - 3A* T_{HTS} (°C)	ΔT (K)
25	188.22	188.93	0.71
50	171.48	171.87	0.39
100	163.68	163.90	0.22
500	157.12	157.35	0.23
h $(Wm^{-2}K^{-1})$	*Opt - 4A* T_{HTS} (°C)	*Design - 4A* T_{HTS} (°C)	ΔT (K)
25	228.62	233.59	4.97
50	192.79	195.71	2.92
100	177.25	179.29	2.04
500	165.23	166.37	1.14

6. Conclusions

The distribution of thermally conductive material and thermal insulation was optimized within an actively cooled electronics unit for downhole tools. The heat transfer mechanisms were modelled in COMSOL Multiphysics and the topology optimization SIMP method was implemented. Diverse design concepts were obtained for different boundary conditions. The analysis of the resulting designs supported the development of a final unit, whose performance was compared to the optimized cases. An acceptable deviation between them was assessed and the importance of controlling the operating conditions close to the optimal TEC feed current was underlined.

7. Acknowledgments

S. Soprani and K. Engelbrecht would like to show their gratitude to the Danish Ministry of Technology and Innovation and to Welltec A/S for partially funding this work. The authors would also like to acknowledge the TopTEN project, sponsored through the Sapere Aude Program of the Danish Council for Independent Research (DFF–4005-00320), for supporting this study.

8. References

[1] A.G. Flores. Active Cooling for Electronics in a Wireline Oil-Exploration Tool, *Ph.D. thesis*, M.I.T., USA (1996).

[2] S. Soprani, K. Engelbrecht, A.J. Nørgaard. Active Cooling and Thermal Management of a Downhole Tool Electronics Section, *Proceedings of the 24th IIR International Congress of Refrigeration*, Yokohama, Japan (2015).

[3] E.M. Dede, J. Lee, T. Nomura. Multiphysics simulation: electromechanical system applications and optimization, *Springer London* (2014).

[4] J.M. Gordon, K.C. Ngc, H.T. Chuac, A. Chakrabortyc, The electro-adsorption chiller: a miniaturized cooling cycle with applications to micro-electronics, *International Journal of Refrigeration,* 25 (8): 1025–1033 (2002).

[5] B. S. Lazarov, O. Sigmund. Filters in Topology Optimization Based on Helmholtz-Type Differential Equations, *International Journal for Numerical Methods in Engineering*, 86 (6): 765-781 (2011).

[6] F. Wang, B. S. Lazarov, O. Sigmund. On Projection Methods, Convergence and Robust Formulations in Topology Optimization, *Structural and Multidisciplinary Optimization*, 43 (6): 767-784 (2011).

[7] O. Sigmund, K. Maute. Topology Optimization Approaches, *Structural and Multidisciplinary Optimization*, 48 (6): 1031-1055 (2013).

A.2 P2 - A design approach for integrating thermoelectric devices using topology optimization

S. Soprani, J. H. K. Haertel, B. S. Lazarov, O. Sigmund and K. Engelbrecht

***Applied Energy*, vol. 176, pp. 49-64, 2016.**

Applied Energy 176 (2016) 49–64

Contents lists available at ScienceDirect

Applied Energy

journal homepage: www.elsevier.com/locate/apenergy

A design approach for integrating thermoelectric devices using topology optimization

S. Soprani [a,*], J.H.K. Haertel [a], B.S. Lazarov [b], O. Sigmund [b], K. Engelbrecht [a]

[a] Department of Energy Conversion and Storage, Technical University of Denmark, Denmark
[b] Department of Mechanical Engineering, Technical University of Denmark, Denmark

HIGHLIGHTS

- The integration of a thermoelectric (TE) cooler into a robotic tool is optimized.
- Topology optimization is suggested as design tool for TE integrated systems.
- A 3D optimization technique using temperature dependent TE properties is presented.
- The sensitivity of the optimization process to the boundary conditions is studied.
- A working prototype is constructed and compared to the model results.

ARTICLE INFO

Article history:
Received 5 February 2016
Received in revised form 29 April 2016
Accepted 2 May 2016

Keywords:
Topology optimization
Thermoelectric devices
Thermoelectric cooling
System integration
Thermal management
Downhole electronics cooling

ABSTRACT

Efficient operation of thermoelectric devices strongly relies on the thermal integration into the energy conversion system in which they operate. Effective thermal integration reduces the temperature differences between the thermoelectric module and its thermal reservoirs, allowing the system to operate more efficiently. This work proposes and experimentally demonstrates a topology optimization approach as a design tool for efficient integration of thermoelectric modules into systems with specific design constraints. The approach allows thermal layout optimization of thermoelectric systems for different operating conditions and objective functions, such as temperature span, efficiency, and power recovery rate. As a specific application, the integration of a thermoelectric cooler into the electronics section of a downhole oil well intervention tool is investigated, with the objective of minimizing the temperature of the cooled electronics. Several challenges are addressed: ensuring effective heat transfer from the load, minimizing the thermal resistances within the integrated system, maximizing the thermal protection of the cooled zone, and enhancing the conduction of the rejected heat to the oil well. The design method incorporates temperature dependent properties of the thermoelectric device and other materials. The 3D topology optimization model developed in this work was used to design a thermoelectric system, complete with insulation and heat sink, that was produced and tested. Good agreement between experimental results and model forecasts was obtained and the system was able to maintain the load at more than 33 K below the oil well temperature. Results of this study support topology optimization as a powerful design tool for thermal design of thermoelectric systems.

1. Introduction

Over the past decades, thermoelectric devices (TEDs) have become competitive solutions for waste energy recovery, heat pumping, and cooling applications [1–5]. Advantages of TEDs include compactness, gas-free solid-state operation, lack of moving parts, and long life-span. However, a lower energy conversion efficiency compared to other well established technologies [6] can limit their application. In order to increase energy conversion efficiency, optimization of thermoelectric devices is an active research topic, both in terms of the thermoelectric materials employed [7–10], and the architecture of devices [11–16]. Additionally, efficient TED operation strongly relies on the integration into the overall energy conversion system [17–21]. Effective heat transfer at the cold and hot plates, minimization of thermal resistances within the system, and reduction of heat leakages each

* Corresponding author at: Frederiksborgvej 399, Building 778, 4000 Roskilde, Denmark.
E-mail address: stefs@dtu.dk (S. Soprani).

http://dx.doi.org/10.1016/j.apenergy.2016.05.024
0306-2619/

improves overall efficiency. These features depend on the thermal layout of the integrated system and should be taken into account during the design phase to maximize effectiveness.

Here, we present a novel automated method, using topology optimization, to design thermal interfaces and insulation solutions for a TED to be integrated in a system with design constraints. Topology optimization has not previously been applied to thermoelectric systems, but this technique has great potential as a powerful design tool, as it can be used to optimize the topology of heat sinks, heat exchangers, and to define optimized distributions of thermally conducting and insulating material based on a set of design constraints. We show that the method can be implemented using commercial software, is robust, and is suitable for TED applications that must be packaged in a defined space. The method can be used to optimize a thermoelectric system for a variety of objective functions, such as efficiency, power recovery rate, and temperature span. Contrary to size and shape optimization approaches, topology optimization requires no initial design concept or a priori parametrization [22,23]. This flexibility is especially important in the early design phase, as it saves development time and can yield unintuitive optimized structures. Density-based topology optimization methods are particularly promising, since they consider the systematic distribution of material within a design domain, while aiming to optimize a certain objective function.

Topology optimization was first developed and established for structural mechanics applications and was subsequently applied to various other disciplines [24,25]. Prior studies on heat transfer using topology optimization have mainly focused on pure 2D heat conduction problems [22,26,27] as well as heat conduction with convective heat transfer to an ambient fluid [28–32]. Later works have included the explicit modeling of the fluid flow within the optimization domain in thermo-fluid models with forced convection in 2D [33–38] and 3D [39]. More recent applications of the approach have extended models to consider 2D topology optimization of natural convection [40] and radiation as the dominant heat transfer mechanism [41]. The design, manufacturing and subsequent experimental testing of optimized forced-convection heat sinks have also been presented [42–44].

Building on previous studies, this work addresses an existing industrial challenge and applies topology optimization to a thermoelectric system for the first time. Here, it is used to design the thermal integration of a thermoelectric cooler (TEC) in a downhole tool for oil well interventions. The space constraints imposed by the application and the clearly defined thermal boundary conditions make this an attractive case for topology optimization [45]. In the studied application, the TEC maintains a specific group of electronics at a temperature below the outside well temperature to prevent overheating issues that occur when the borehole exceeds the maximum temperature rating of the electronics (175 °C). Topology optimization is used to optimize the distribution of the insulating material, which thermally protects the cooled electronics, and of the conducting material, which aids in rejecting heat from the TEC to the well. The objective of the optimization is to minimize the temperature of the cooled electronics. A more detailed discussion regarding well interventions, active cooling, and thermal management of downhole electronics, is given in Refs. [46–51].

A model of the thermoelectric device was developed for this application, implemented in a 3D finite element model of the system, and coupled with the optimization algorithm. Temperature dependent properties of the TEC were implemented in order to capture the effects of the real material properties during the optimization process. The topology optimization model was used to optimize the design of the system for different operating conditions and to define the optimal working conditions of the TEC. The improvements in performance for the optimized systems were assessed and used to define a final design of the electronics unit, which is also practical from a manufacturing and assembly standpoint. The defined setup was then manufactured and experimentally tested at different operating conditions, and the results compared to the model predictions.

2. Description of the system

This chapter briefly introduces the electronics unit system, its main components and the overall thermal management principle. A 3D model of the longitudinal section of the system is illustrated in Fig. 1.

The analyzed downhole electronics unit is composed of the following parts:

- *Metallic cylindrical housing:* a hollow cylinder that shields and seals the inner components from the harsh well environment.
- *Chassis:* a rigid metallic support used for final assembly, on which the electronics are mounted and slid into the housing. It is divided in a structural part, which mechanically supports the system; and an optimizable part, which surrounds the components within the structural chassis and is the object of the topology optimization.
- *Electronic components:* they can be split into high temperature-sensitive (HTS) and high temperature-non-sensitive (HTNS) components. The former are likely to fail when their operating temperature exceeds 175 °C, the latter can even operate above 200 °C. The HTS electronics are mounted on a printed circuit board (PCB) and are characterized by a power dissipation rate of 1 W; the HTNS electronics are mounted directly on the chassis and dissipate an estimated 5 W.

Additional components, used for the integration of the active cooling system into the tool, are:

- *Thermoelectric cooler:* the cooling system is connected to an electric power source and transfers a heat flux from the cold to the hot plate, when an electric current is applied. The TEC cold plate needs to be thermally coupled to the HTS electronics, while the hot plate requires a thermal link to the hot reservoir, represented by the well environment.
- *Metallic heat spreader:* a rigid plate attached to the TEC cold plate that, together with the thermal pad, constitutes the thermal interface between the PCB and the cooler.
- *Soft thermal pad:* a soft silicone sheet, which is inserted between the PCB and the copper plate to create a thermal path between the irregular surface of the PCB and the heat spreader.

The heat management strategy aims at maintaining the HTS electronics at 175 °C or below when the tool is operating in a 200 °C environment. It is based on the passive cooling of the HTNS components, which can withstand high temperatures, and the active cooling of the HTS components through the Peltier module. The PCB is therefore thermally coupled, through the heat spreader and the thermal pad, with the cold plate of the Peltier module so the cooling load can be absorbed by the cooler. The TEC hot plate, in turn, needs to be thermally connected to the chassis; in this way, the excessive heat can flow through the housing and be rejected to the well fluid that laps the outer surface of the housing, through convective heat transfer. A tight mechanical contact is ensured between the structural chassis and the housing, to reduce the contact thermal resistance.

It is important to note that the thermal connection between the TEC hot plate and the chassis, as well as the distribution of

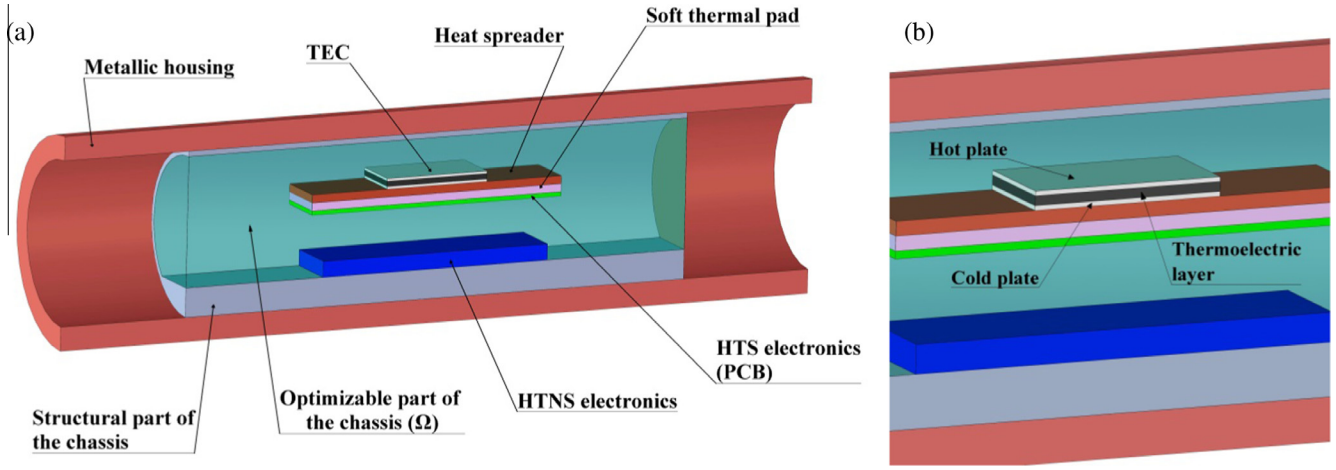

Fig. 1. Representation of the longitudinal section of the downhole tool (1a); the domain of the optimizable chassis is represented as partially transparent and colored in light blue. Particular of the TEC device (1b). (For interpretation of the references to color in this figure legend, the reader is referred to the web version of this article.)

insulating material, will be the result of the topology optimization process. The optimization is expected to define an optimized distribution of thermally conducting material and thermal insulation inside the unit, so the refrigerated electronics are properly protected from the hot surroundings and the excessive heat is effectively rejected to the well fluid. These two phenomena both act towards the minimization of the HTS electronics temperature, which is the objective of the optimization. While the optimization is focused on the thermal integration of the TEC, the topology of the TEC module itself is not the object of the optimization. The finite-element model of the TEC is implemented to simulate the performance of a commercial high-temperature module to be integrated into the downhole tool. The freedom to optimize the electronics unit is limited by three factors: the tool needs to fit a specific well piping size, so its dimensions are constrained to the values reported in Table 1; the position and the design of the components inside the system are constrained by the application; the structural part of the chassis cannot be optimized because of its mechanical function.

3. Finite element model

3.1. Governing equations

The geometry shown in Fig. 1 was implemented in the finite element software COMSOL Multiphysics [52] and divided in domains, each of them characterized by different material properties and governing equations. In order to simulate the heat transfer within the system, mainly driven by heat conduction, the heat transfer PDE (Eq. (1)) was solved in all the domains, except for the thermoelectric material layer.

$$\nabla(-k\nabla T) = Q_{source} \tag{1}$$

where k is the material thermal conductivity, T is the temperature, and Q_{source} is a volumetric heat source. Eq. (1) was not applied to the thermoelectric material domain, as the heat transport related to the thermoelectric effect also needed to be taken into account. A modified heat transfer PDE (Eq. (2)) was used instead.

$$\nabla(\boldsymbol{J}S'T - k'\nabla T) = Q'_{JouleHeating} \tag{2}$$

where $\boldsymbol{J}$ is the electric current density vector, S' is the material Seebeck coefficient, and $Q'_{JouleHeating}$ is the heat source associated with the Joule heating effect.

3.2. Boundary conditions

The boundary conditions were set in order to simulate the operating and external conditions that could occur in a well during a downhole intervention. A convective heat flux was set on the outer surface of the housing, to reproduce the interaction between the well fluid and the tool.

$$-\boldsymbol{n}\cdot(-k\nabla T) = h(T - T_{ext}) \tag{3}$$

Furthermore, the tool electronics unit would be assembled in the middle of a tool string, composed of several sections, and the heat transfer with the well is expected to mainly occur radially. For this reason, adiabatic boundaries were set at the two ends of the cylindrical setup.

$$-\boldsymbol{n}\cdot(-k\nabla T) = 0 \tag{4}$$

where $\boldsymbol{n}$ is the surface normal vector, T_{ext} is the well fluid temperature and h is the heat transfer convection coefficient. Concerning

Table 1
List of the components with their dimensions and properties.

Component	Length (mm)	I.D. (mm)	O.D. (mm)	Thermal conductivity (W m^{-1} K^{-1})
Metallic housing	300	62	80	150
Structural chassis	200	58	62	138
Optimizable chassis	200	–	58	Eq. (16)
Component	**Length (mm)**	**Depth (mm)**	**Height (mm)**	**Thermal conductivity (W m^{-1} K^{-1})**
TEC plates	40	40	0.95 each	27
TEC thermoelectric layer	40	40	2.0	Eq. (8)
Heat spreader	100	40	3.0	400
Soft thermal pad	100	40	3.0	12
HTNS electronics	90	42	6.0	130
HTS electronics (PCB)	100	40	1.6	0.3

the interface between the thermoelectric material domain, where Eq. (2) is solved, and the rest of the geometry, where Eq. (1) is solved, a Dirichlet boundary condition was defined to provide consistency to the temperature distribution. Heat sources were set in the HTNS electronics domain (5 W), and at the interface between the PCB and the soft thermal pad (1 W), to simulate the power dissipation of both electronics modules. Thermal resistances, $R_{th1,2}$ = 2.5e−5 m^2 K W^{-1}, were modeled at the interface between the HTNS electronics and the structural chassis, and on the outer boundaries of the TEC hot/cold plates; they simulated the contribution of a 0.1 mm thick layer of thermal grease, with a thermal conductivity of 4 W m^{-1} K^{-1}. An additional thermal resistance, R_{th3} = 1.1e3 m^2 K W^{-1}, was set at the interface between the structural chassis and the housing in order to simulate the contact resistance given by the assembly. The value of this thermal resistance was estimated through the comparison between simulation results and experimental data from thermal tests on an analogue setup.

The operating conditions of the cooler were characterized by the TEC feed current I_{feed}, which represents the electric current which is supplied to the module and is given to the model as an input. The correlation between this parameter and the current density vector $\boldsymbol{J}$ (see Eq. (2)) is explained in more detail in the next section.

3.3. TEC model

A particular focus was put on the modeling of the thermoelectric cooler. Its main components are two aluminum oxide plates, between which leg pairs of semiconducting material (p–n junctions) are mounted, electrically connected in series, and separated by air. Reproducing the detailed geometry of the module would have drastically increased the complexity and the computational time of the 3D topology optimization model. Therefore a simplified model of the TEC was developed: the intermediate semiconductor layer was modeled as homogeneous and isotropic, and equivalent material properties were weighted on the properties of Bi_2Te_3 and air. In this way, the cooling effect driven by a given TEC feed current could be approximated to the real case, while the geometry could be significantly simplified.

As a consequence of the homogenization process, the electric and thermal transport phenomena could not be differentiated within the Bi_2Te_3 and air domains, and the inhomogeneous temperature gradient across the module could not be reproduced. However, this approximation was considered acceptable as it preserves the average heat fluxes that drive heat transfer in the integrated system.

Fig. 2 illustrates the steps that were used to develop the homogeneous model and that are explained in the following subsections.

3.3.1. Effective current density

In the *real device*, the thermoelectric leg pairs are fed in series. The current density through the legs $\boldsymbol{J}$ can be expressed, in good approximation, as the 3D vector [0, 0, $\pm J_z$]. The only non-zero contribution is along the z-axis, perpendicular to the TEC plates, and can be equal to $-J_z$ or $+J_z$. The scalar current density can be defined as:

$$J_z = \frac{I_{feed}}{A_{leg}} \tag{5}$$

where J_z is the scalar current density along the z-axis, I_{feed} is the TEC feed current and A_{leg} is the cross sectional area of the single thermoelectric leg.

In the *intermediate modeling step*, the thermoelectric legs are all doped p-type and are fed in parallel. The current density vector is now equal to [0, 0, $+J_z$]. Given the parallel configuration, and in order to maintain the same thermoelectric effect in each leg as the *real device*, the TEC feed current becomes N times bigger, where N is the number of thermoelectric legs installed in the module.

In the *homogeneous model*, there is no distinction between thermoelectric legs and air. The homogeneous layer is supplied by a

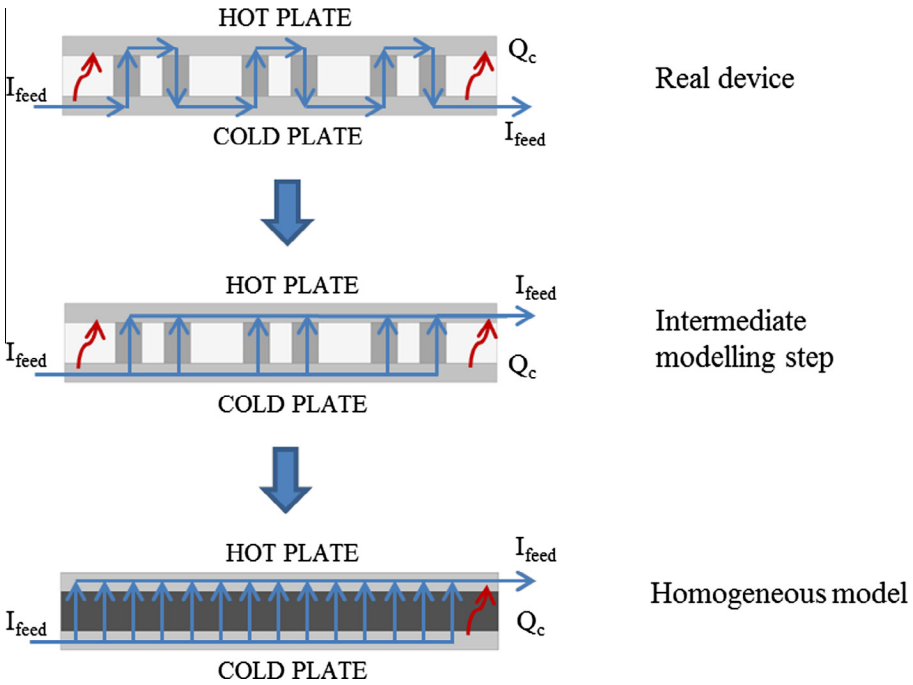

Fig. 2. Illustration of the simplification process for the TEC model. The longitudinal section and the working principle of the *real device* and of the *homogeneous model* are included. For the sake of a better understanding, an intermediate step of the model development, called *intermediate modelling step*, is also included.

uniform electric current equal to $N{\cdot}I_{feed}$, in the positive z-axis direction. A different current density needs to be defined:

$$J'_z = \frac{NI_{feed}}{A_{tot}} = \frac{NI_{feed}}{A_{tot}} \cdot \frac{NA_{leg}}{NA_{leg}} = \frac{I_{feed}}{A_{leg}} \cdot \frac{A_{\mathrm{BiTe}}}{A_{tot}} = J_z x_{\mathrm{BiTe}} \tag{6}$$

where J'_z is the equivalent scalar current density for the homogeneous model, A_{tot} is the total cross sectional area of the thermoelectric module, A_{BiTe} is equal to N times A_{leg} and represents the cross sectional area occupied by the thermoelectric legs in the *real device*, and x_{BiTe} is the ratio between A_{BiTe} and A_{tot}. x_{BiTe} is also equal to the volume ratio between bismuth telluride and the total volume of the intermediate layer.

3.3.2. Effective Seebeck coefficient

Given the TEC PDE for the homogeneous layer in Eq. (2), we want to maintain the same thermoelectric cooling effect $\boldsymbol{J}'S$ as the *real device*. First, it is assumed that the Seebeck coefficient of the layer does not change with the homogenization process. However, the current density has changed and it can be imposed:

$$J'_z S = J_z S' \rightarrow S' = S x_{\mathrm{BiTe}} \tag{7}$$

More intuitively, one could think that the thermoelectric cooling effect is now generated with the same scalar current density J_z as the *real device*, but only by a portion of the layer (x_{BiTe}), ideally occupied by the Bi_2Te_3 legs. Although the cooling effect is maintained to be the same, the homogeneous approximation spreads it equally along the whole layer.

3.3.3. Effective thermal conductivity of the layer

The heat transfer within the intermediate layer occurs mainly from a cooler plate to the other, while the temperature gradient along the direction parallel to the plates is expected to be negligible. It is therefore assumed that the effective thermal resistance of the layer is equal to the parallel coupling of the thermal resistances, of air and Bi_2Te_3, between the hot and cold plate.

$$k' = k_{air}\frac{A_{air}}{A_{tot}} + k_{\mathrm{BiTe}}\frac{A_{\mathrm{BiTe}}}{A_{tot}} = k_{air}(1 - x_{\mathrm{BiTe}}) + k_{\mathrm{BiTe}} x_{\mathrm{BiTe}} \tag{8}$$

where k' is the thermoelectric layer equivalent thermal conductivity for the homogeneous model, and t is the thermoelectric layer thickness.

3.3.4. Effective electrical conductivity of the layer

In analogy with the effective thermal conductivity calculation, and neglecting the air electrical conductivity:

$$\sigma' = \sigma_{\mathrm{BiTe}} x_{\mathrm{BiTe}} + \sigma_{air} x_{air} = \sigma_{\mathrm{BiTe}} x_{\mathrm{BiTe}} \tag{9}$$

where σ' is the thermoelectric layer equivalent electric conductivity for the homogeneous model. Consequently the Joule heating term can be calculated as:

$$Q'_{JouleHeating} = \frac{x_{\mathrm{Bi_2Te_3}}}{\sigma_{\mathrm{Bi_2Te_3}}} \boldsymbol{J}\cdot\boldsymbol{J} = \frac{J_z^2}{\sigma_{\mathrm{Bi_2Te_3}}} x_{\mathrm{Bi_2Te_3}} \tag{10}$$

Again, the original Joule losses are maintained, but are spread uniformly along the layer because of the homogeneous approximation.

A suitable high-temperature commercial cooler was disassembled and analyzed, so the main geometric features could be measured. They are summarized in Table 2.

The properties of Bismuth Telluride S_{BiTe}, k_{BiTe} and σ_{BiTe} from [53] were implemented as non-linear functions of temperature. In order to better match the performance of the high-temperature commercial cooler, a linear coefficient was multiplied to the expressions of the Bi_2Te_3 Seebeck coefficient, thermal conductivity, and electrical conductivity. The linear coefficients are the result of a best fit analysis based on experimental data and are respectively equal to $S_1 = 1.30$, $k_1 = 0.80$, and $\sigma_1 = 1.15$.

Table 2
Geometric features of the modelled thermoelectric cooler.

Parameter	Description	Value
h_{TEC}	Total height of the module	3.90 mm
l_{TEC}	Edge length of the module	40.0 mm
$h_{Al_2O_3}$	Height of the hot/cold plate	0.95 mm
N	Number of thermoelectric legs	254
$h_{Bi_2Te_3}$	Height of the single thermoelectric leg	2.00 mm
$l_{Bi_2Te_3}$	Edge length of the single thermoelectric leg	1.30 mm
A_{leg}	Cross sectional area of a thermoelectric leg	1.69e−6 m^2
$x_{Bi_2Te_3}$	Volume fraction of semiconductor materials	0.27

3.4. Topology optimization and SIMP method

The topology optimization approach was used to assess which distribution of aluminum/thermal insulation inside the electronics unit minimized the temperature of the HTS electronics. Filling the electronics unit with only thermal insulation would maximize the thermal protection of the cooling zone from heat leakages, but would not provide an effective thermal path for the rejected heat to flow to the well environment. The Peltier module would therefore not be able to work within the cooling design conditions. Filling the electronics unit with aluminum, instead, would enhance the heat rejection process, but would not protect the cooling zone from heat leakages, making the cooling process ineffective. A tradeoff needs to be reached and the Solid Isotropic Material with Penalization (SIMP) method allowed looking for an optimized solution.

The main goal of the SIMP method, as part of the density-based topology optimization approaches, is to achieve a binary design within the optimizable domain, where the design variable can be equal to 0, representing thermal insulation, or to 1, representing aluminum. The topology optimization problem can be stated as follows:

$$minimize: f_{obj}(T, \rho_{design}) = \frac{1}{A_{PCB}} \int_{\Omega_{PCB}} T d\Omega_{PCB} \tag{11}$$

$$subject\ to: 0 \leqslant \rho_{design} \leqslant 1 \tag{12}$$

$$\boldsymbol{r}(T, \rho_{design}) = 0 \tag{13}$$

where f_{obj} is the objective function to minimize, equal to the integral average of the temperature distribution along the PCB surface Ω_{PCB}; A_{PCB} is the PCB area surface; ρ_{design} is the design variable that can range between 0 (thermal insulation) and 1 (aluminum), and the distribution of which needs to be optimized; $\boldsymbol{r}$ (T, ρ_{design}) is the residual of the state governing equations within the discretized system.

A PDE-based density filter [54] was used to smooth the interfaces between aluminum and insulator and to introduce a minimum length scale into the design. The PDE-based filter was used because it can be implemented in the optimization model with little additional effort and it offers a computationally efficient method of density filtering. The PDE that was used for filtering is stated in Eq. (14).

$$-r^2\nabla^2\tilde{\rho} + \tilde{\rho} = \rho_{design} \tag{14}$$

where $\tilde{\rho}$ is the filtered density field and r is a filter parameter, defined as 1.5 times the maximum element size and equal to 3e−3 m. Since density filtering inherently introduces a band of intermediate densities between aluminum and insulator, the

filtered design variable field $\tilde{\rho}$ was then projected towards 0 and 1 to obtain a crisp design. For this purpose a smoothed threshold projection [55] was used.

$$\bar{\tilde{\rho}}_i = \frac{\tanh(\beta\eta) + \tanh(\beta(\tilde{\rho}_i - \eta)}{\tanh(\beta\eta) + \tanh(\beta(1-\eta))} \quad (15)$$

where $\tilde{\rho}_i$ is the projected density field, η is the projection threshold, equal to 0.5, and β defines the steepness of the projection.

When applying the topology optimization SIMP method, it is not possible to theoretically guarantee the convergence to a global optimum. Nevertheless, it is possible to tune the optimization parameters through the continuation method to ensure that the solution is close to the global optimum [56]. In this study, using a steep projection at the beginning of the optimization could result in convergence to local minima. Therefore, a continuation approach [55] was used to ramp β, which means that the optimization was started with an almost linear projection ($\beta = 1$) and β was subsequently gradually increased to steepen the projection function. Thus, one could ensure that the optimization problem is convexified at the beginning of the optimization, while ending up with a crisp design.

The difference of thermal conductivity between aluminum and thermal insulation was accounted by an interpolation function k_{SIMP} that defined the effective thermal conductivity of the optimizable chassis.

$$k_{SIMP} = k_{ins} + (k_{Al} - k_{ins})\bar{\tilde{\rho}}^p \quad (16)$$

where k_{SIMP} is the effective thermal conductivity, $k_{ins} = 0.17\ \mathrm{W\,m^{-1}\,K^{-1}}$ and $k_{Al} = 138\ \mathrm{W\,m^{-1}\,K^{-1}}$ are respectively the thermal conductivities of the insulator and of the aluminum, $\bar{\tilde{\rho}}$ is the projected design variable, and p is the penalization coefficient. When performing topology optimization for continuous design variables, intermediate regions (areas where the design variable assumes intermediate values between 0 and 1) can appear in the final distribution; these transition zones are not physically meaningful for the analyzed problem and need to be reduced as much as possible. Classically, a penalization coefficient $p = 3$ is used in topology optimization in combination with an active volume constraint [30] to make intermediate regions unattractive with respect to the optimization problem, and to drive the control variable towards either 0 or 1. In this work, no active volume constraint was used, nevertheless a faster convergence was found for $p = 3$, compared to a linear interpolation ($p = 1$). Therefore $p = 3$ was used for the simulations. The globally convergent version of the Method of Moving Asymptotes (GCMMA) [57] was finally used to solve the optimization problem; this algorithm is implemented in COMSOL Multiphysics [52] with the solver name *MMA*.

In this study, the structural and design constraints limited the optimization possibilities to the chassis domain only and did not require or allow the optimization of other components (e.g. metallic housing, heat spreader, TEC). However, the topology optimization approach can be used to simultaneously optimize multiple geometrical features by implementing additional interpolation functions for different optimizable domains. This process would increase the non-linearity of the optimization problem, consequentially increasing the computation cost and the risk of converging to local minima. Thus, in these cases, a more careful solution of the problem through the continuation method should be adopted.

4. Results

4.1. Definition of the optimized design concepts

The model was used to optimize the topology of the electronics unit for different boundary conditions of TEC feed current and well fluid convective heat transfer coefficient. The system was optimized for TEC feed currents $I_{feed} = 1$, 2, 3 and 4 A, where the maximum feed current stated by the analyzed commercial TEC supplier is 6 A; and for convective heat transfer coefficients $h = 10$, 25, 50, 100 and 500 $\mathrm{W\,m^{-2}\,K^{-1}}$, in order to reproduce very low, low, and medium well fluid convection regimes. The well temperature T_{ext} was set to 200 °C, as the maximum temperature at which the system is expected to operate.

The optimized structure was found to be a function of the boundary conditions. Various boundary conditions led to different tradeoffs between thermal protection of the cooled electronics and excessive heat rejection from the cooler to the well. The model proved to optimize the unit according to three different design configurations: *Design* 1, where the thermal insulation of the cooled electronics is prioritized; *Design* 2, where the conduction of the excessive heat towards the well is equally important as the thermal protection; and *Design* 3, where the excessive heat rejection is crucial for the operation of the system. A more detailed illustration of the three design concepts is given in the following paragraphs.

Low feed currents and high well fluid convection coefficients led to an optimized system (*Design* 1 concept), where only an aluminum pad links the cooler hot plate to the structural chassis and provides a thermal path for the excessive heat to be dissipated radially. The remaining volume of the unit is filled with thermal insulation (Fig. 3a–d). In this case the thermal protection of the electronics is prioritized, as the heat rejection from the cooler to the well is not challenging. Low currents generate small Joule losses across the cooler and the high convection coefficients provide an effective heat rejection towards the well. The length of the aluminum plate increases when the TEC feed current grows and when the external convection coefficient decreases, so the heat can be better spread through the structural chassis and housing, towards the well.

When the feed current is increased and the well fluid convection coefficient lowered, the optimized system (*Design* 2 concept) aims at better spreading the excessive heat, coming from the cooler hot plate, around the structural chassis and housing. A better distribution of the heat enhances, in fact, the heat exchange with the well, limits the temperature gradients due to the thermal resistances, and reduces the heat backflow to the cooled electronics. This is done by adding an aluminum layer, around the structural chassis, that spreads the heat not only radially, but also along the longitudinal direction of the tool (Fig. 3e and f). A thermally insulating layer still protects the cooled components from the hot surroundings. The thickness of the aluminum layer grows when the feed current, and the Joule losses, increase or when the well fluid convection coefficient decreases.

A third type of optimized design (*Design* 3 concept) appeared for $I_{feed} = 4$ A and $h = 10\ \mathrm{W\,m^{-2}\,K^{-1}}$, which respectively correspond to the highest feed current and the lowest convection coefficient that were simulated. In this case the power dissipation rate, due to Joule heating, proves to be much higher than the capability of the well fluid to remove heat through the convective mechanism. The generated heat flux increases the HTS electronics temperature above the well temperature, making active cooling infeasible at these operating conditions. The optimization process hence strongly prioritizes the heat rejection by creating a thermal path between the PCB and the well fluid, while two thin insulating layers protect the electronics from the cooler hot plate and from the HTNS electronics (Fig. 3g and h).

The balance between thermal protection of the cooled electronics and rejection of the excessive heat is reached differently for each set of boundary conditions and with different aluminum-thermal insulation ratios. Computing the volume percentage of employed aluminum, over the total optimizable volume, helps to

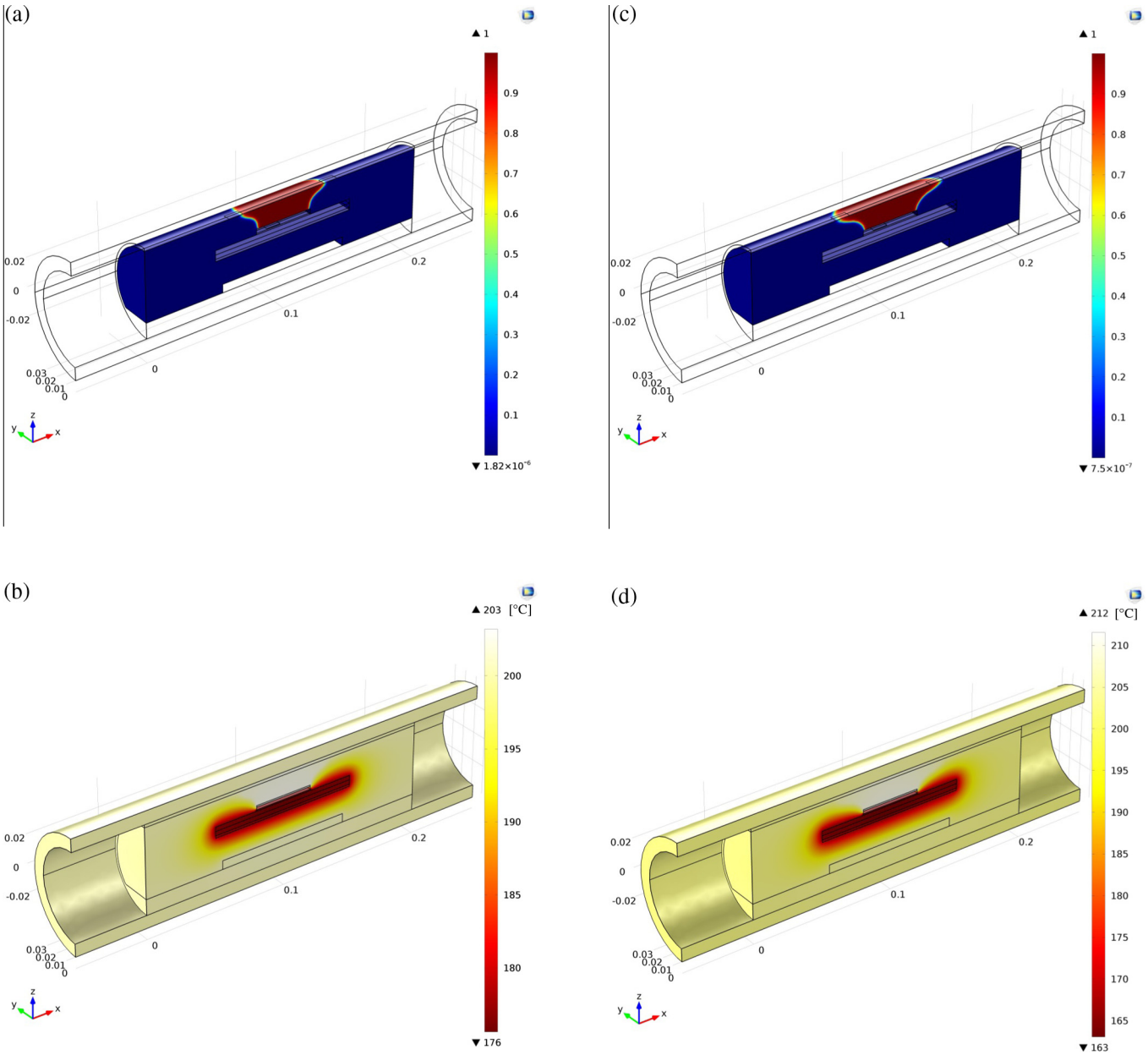

Fig. 3. Density field and resulting temperature distribution of the optimized *Design* 1 concept at I_{feed} = 1 A/h = 500 W m^{-2} K^{-1} (a and b), and at I_{feed} = 2 A/h = 100 W m^{-2} K^{-1} (c and d); of the optimized *Design* 2 concept at I_{feed} = 3 A/h = 50 W m^{-2} K^{-1} (e and f), and of the optimized *Design* 3 concept at I_{feed} = 4 A/h = 10 W m^{-2} K^{-1} (g and h). The density fields illustrate the different distributions of aluminum (red) and thermal insulation (blue), for the four optimized systems. (For interpretation of the references to color in this figure legend, the reader is referred to the web version of this article.)

Fig. 3 (*continued*)

have a clearer picture of the optimized designs trend with the boundary conditions. That can be calculated with the following expression:

$$R = \frac{1}{V_\Omega}\int_\Omega \bar{\tilde{\rho}}\, d\Omega \tag{17}$$

where V_Ω is the volume of the optimizable domain and $\bar{\tilde{\rho}}$ is the projected design variable.

The amount of employed aluminum decreases with the convection coefficient and increases with the feed current (Fig. 4); more in general, more aluminum is employed when a better heat rejection to the well is needed.

4.2. Comparison of the optimized designs

Defining the categories of the optimized topologies is only the first step towards the selection of a final design for the actively cooled electronics unit. The performance of the optimized designs, at conditions they were not optimized for, is also an important feature to take into account. Furthermore, a cross-validation between the resulting topologies can be used to check for convergence to local minima. It can be detected if an optimized design does not show the best performance at the boundary condition it was optimized for.

A first sensitivity analysis was carried out to evaluate how the performance of an optimized system would change at different well fluid convection regimes. The electronics section was first optimized for a certain value of feed current and well fluid convection; the optimized design was then simulated at different values of convection coefficient, maintaining the TEC feed current constant. The resulting performances were compared as illustrated

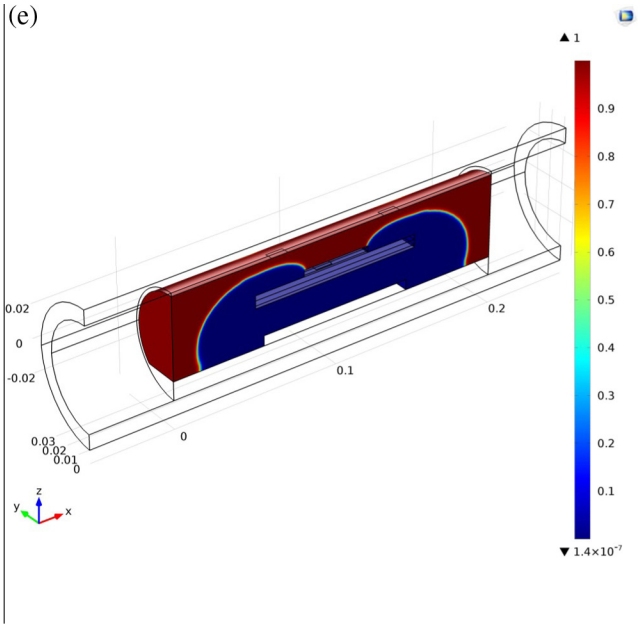

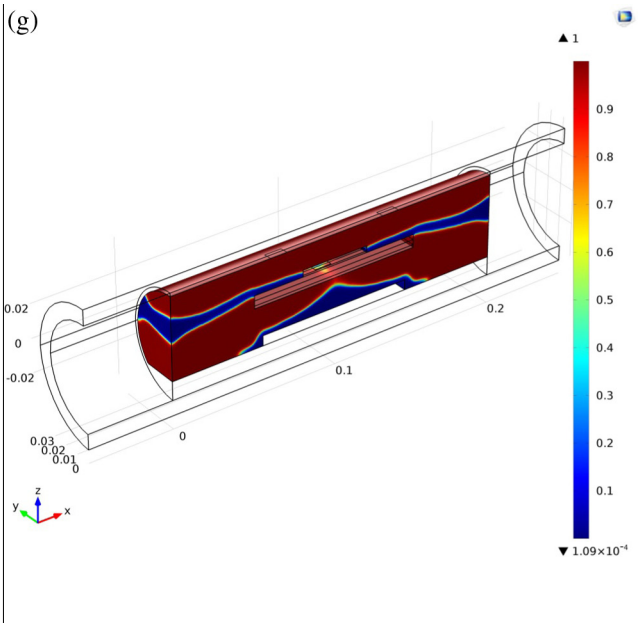

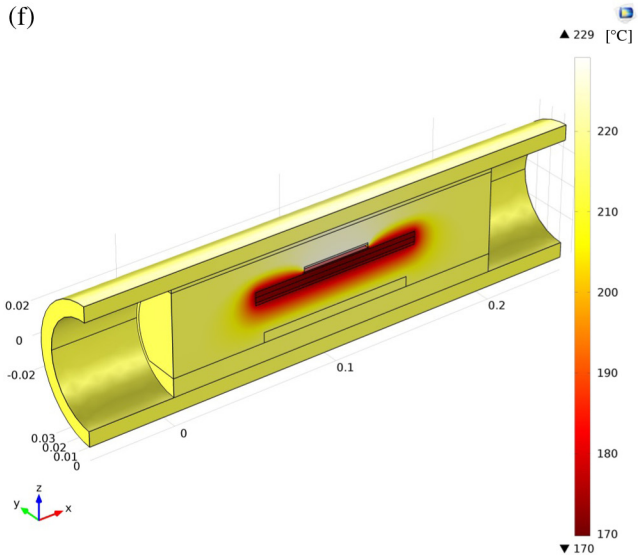

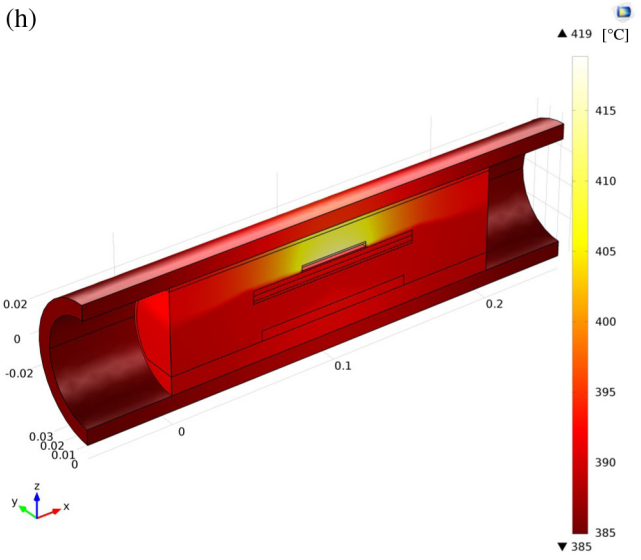

Fig. 3 (*continued*)

Fig. 3 (*continued*)

in Fig. 5. The performance of the system was evaluated in terms of HTS electronics average temperature, computed through the objective function reported in Eq. (11).

Fig. 5a reports the performance trend with h of the systems optimized for $h = 10\ \mathrm{W\ m^{-2}\ K^{-1}}$ and $I_{feed} = 1$, 2, and 3 A. As forecast, the HTS electronics is maintained colder at higher h values, when the heat rejection to the well is enhanced. Furthermore, higher feed currents are able to keep the electronics colder only if the well fluid is able to absorb the additional excessive heat, generated by the higher Joule losses. The lowest T_{HTS}, at a certain convection regime, is given by the system that was optimized for it.

Unexpectedly, it was found that the systems optimized for the same feed current operate very closely to each other, independently on the value of h they were optimized for. The performance trends of the systems optimized for $I_{feed} = 1$, 2 and 3 A, and $h > 10\ \mathrm{W\ m^{-2}\ K^{-1}}$, would in fact overlap with the corresponding three curves illustrated in Fig 5a. A maximum mismatch of only 0.05 °C, 0.01 °C, and 1.47 °C was found between the performance trends of the systems optimized for $I_{feed} = 1$, 2, and 3 A, respectively. This analysis proved that the optimization process is not significantly sensitive to the considered well fluid convection range. In other words, the length of the aluminum pad, which characterizes the *Design* 1 concept, as well as the thickness of the aluminum layer, which characterizes the *Design* 2 concept, do not significantly affect the performance of the optimized systems between 1 A and 3 A.

On the contrary, not all the topologies optimized for 4 A have a similar behavior. As Fig. 5b shows, the system optimized for 4 A and $10\ \mathrm{W\ m^{-2}\ K^{-1}}$ (*Design* 3 concept) maintains the electronics at a significantly lower temperature at low convection coefficients, compared to the one optimized for 4 A and $25\ \mathrm{W\ m^{-2}\ K^{-1}}$. However, above $25\ \mathrm{W\ m^{-2}\ K^{-1}}$ the system optimized for 4 A and $25\ \mathrm{W\ m^{-2}\ K^{-1}}$ (*Design* 2 concept) is able to maintain the HTS electronics down to a 37 °C lower temperature. In analogy with the previous cases, the other designs optimized for 4 A and $h > 25\ \mathrm{W\ m^{-2}\ K^{-1}}$ were found to operate similarly to the case

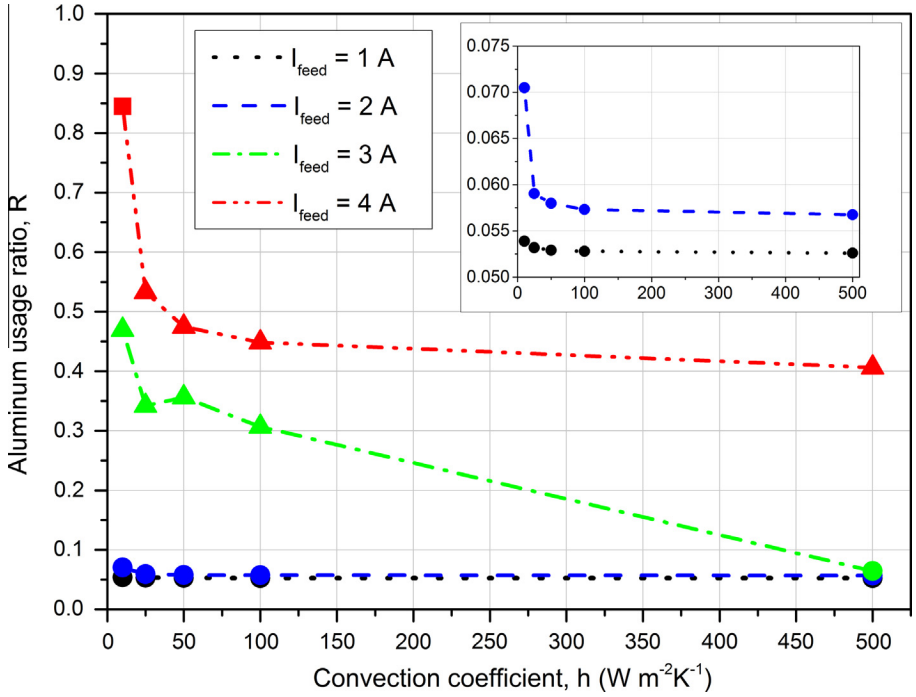

Fig. 4. *R* vs. well fluid convection coefficient, for different TEC feed currents. The three different symbols correspond to the three obtained design configurations: ● = *Design* 1, ▲ = *Design* 2, ■ = *Design* 3.

optimized for 4 A and $h = 25\ \mathrm{W\,m^{-2}\,K^{-1}}$, with a maximum mismatch between the performance trends of 6.67 °C.

In an analogue way, the sensitivity of the optimized topologies to the TEC feed current was studied. The electronics unit was initially optimized for a certain value of well fluid convection coefficient and of TEC feed current; the resulting optimized design was then simulated at different values of feed current, while maintaining the value of *h* constant.

Fig. 6 shows that the optimization process is more sensitive to the feed current than to the external convection coefficient. The mismatch between the curves is now larger and can go up to several degrees Celsius. As expected, the lowest T_{HTS}, at a certain TEC feed current, is given by the system that was optimized for it.

An optimal feed current I_{opt}, which minimizes the HTS electronics temperature, can be individuated. Increasing the TEC feed current enhances the thermoelectric effect and the heat transport from the cold to the hot plate. However, that makes the Joule losses within the module larger, in turn causing a larger excessive heat flux that needs to be rejected to the wellbore, and a higher heat backflow to the HTS electronics through the thermal insulation. The optimal current I_{opt} can be defined as the TEC feed current at which the marginal gain in absorbed heat flux from the cold plate, due to an infinitesimal increase of the TEC feed current, becomes smaller than the heat flux that leaks back to the cooled electronics through the insulation. I_{opt} varies slightly for each optimized design, and depends mainly on *h*.

I_{opt} is equal to ~1.2 A for $h = 10\ \mathrm{Wm^2\,K^{-1}}$, to ~1.9 A for $h = 25\ \mathrm{W\,m^{-2}\,K^{-1}}$, to ~2.3 A for $h = 50\ \mathrm{W\,m^{-2}\,K^{-1}}$, to ~2.6 A for $h = 100\ \mathrm{W\,m^{-2}\,K^{-1}}$, and to ~2.9 A for $h = 500\ \mathrm{W\,m^{-2}\,K^{-1}}$. With respect to the considered operations at non-optimal current, working at I_{opt} can reduce the electronics temperature by a maximum ~244 °C at $h = 10\ \mathrm{W\,m^{-2}\,K^{-1}}$, ~59 °C at $h = 25\ \mathrm{W\,m^{-2}\,K^{-1}}$, ~29 °C at $h = 50\ \mathrm{W\,m^{-2}\,K^{-1}}$, ~17 °C at $h = 100\ \mathrm{W\,m^{-2}\,K^{-1}}$, and ~20 °C at $h = 500\ \mathrm{W\,m^{-2}\,K^{-1}}$. The designs that prove to maintain the HTS electronics at the lowest temperature, around the optimal current, are the ones optimized for 2 A and 3 A.

4.3. Design of the actively cooled electronics section

The results from the topology optimization study were used to define the final design of the actively cooled electronics unit (Fig. 7); practical assembly constraints were also taken into account. The heat transfer analysis of the system revealed that the ideal operating condition for the device to work is a combination of high TEC feed current, that guarantees a strong cooling effect, and a high well fluid convection regime, which guarantees an effective removal of the excessive heat. Unfortunately the well fluid convection regime can vary significantly in operation, and therefore the tool needs to be designed for the worst-case design convection coefficient, which was set to $25\ \mathrm{W\,m^{-2}\,K^{-1}}$. *Design* 3 can be immediately discarded from the suitable topologies, as it was optimized for a convection regime that is outside the design conditions and for a TEC feed current that is far from the optimal ones. As mentioned previously, the optimal feed current for $h = 25\ \mathrm{W\,m^{-2}\,K^{-1}}$ is ~1.9 A; the optimized design for these conditions corresponds to the *Design* 1 concept (see Fig. 4). However, *Design* 2 proved to have a very similar performance around the optimal feed current (see Fig. 6), which means that there is some freedom in the design of the aluminum pad and/or layer. The lower mass of aluminum that characterizes *Design* 1 would make the tool lighter, though, which is preferable from a logistic and operational point of view. Furthermore, the aluminum pad, which provides the radial thermal path from the cooler hot plate to the structural chassis, proved to be the fundamental feature for effective operation of the system: an aluminum pad was therefore implemented in the final design. No aluminum layer was included, except for two walls, 10 mm thick, at the two ends of the chassis: they provide mechanical stability, an additional thermal path to better spread the heat in the case of a poor heat rejection rate, and are suitable for the installation of pins for the assembly of the system. The chassis would be in fact split into a top half, where the cooling system and the PCB are installed, and a bottom half, on which the HTNS electronics are mounted. Two smaller pads, with

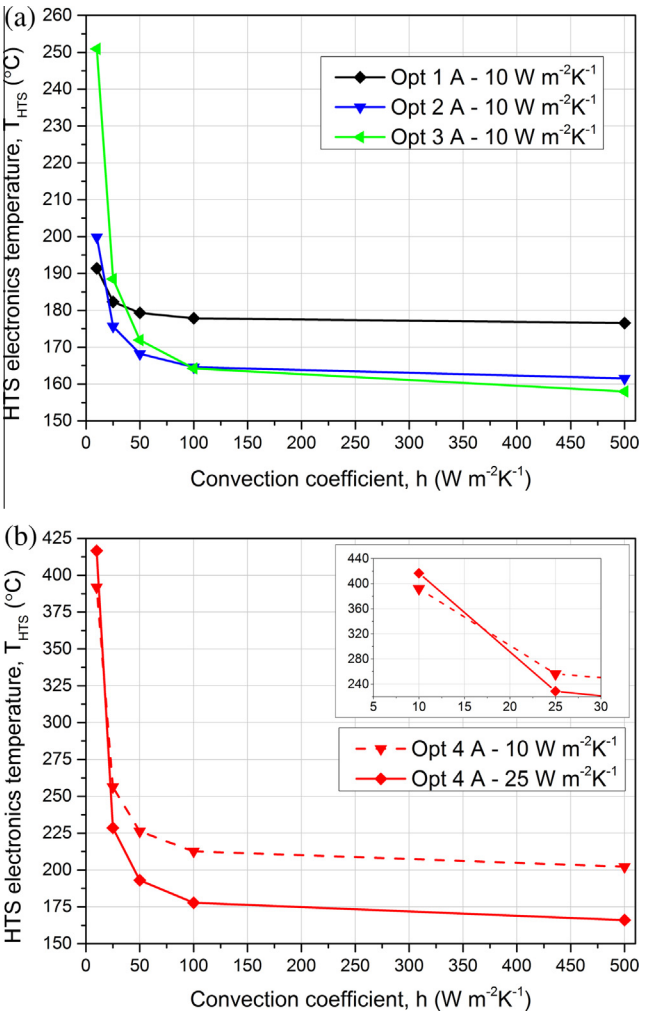

Fig. 5. HTS electronics temperature vs. Convection coefficient for three different systems, optimized for $h = 10$ W m^{-2} K^{-1} and $I_{feed} = 1, 2, 3$ A (a). HTS electronics temperature vs. Convection coefficient for two systems optimized for $h = 10$, 25 W m^{-2} K^{-1} and $I_{feed} = 4$ A (b).

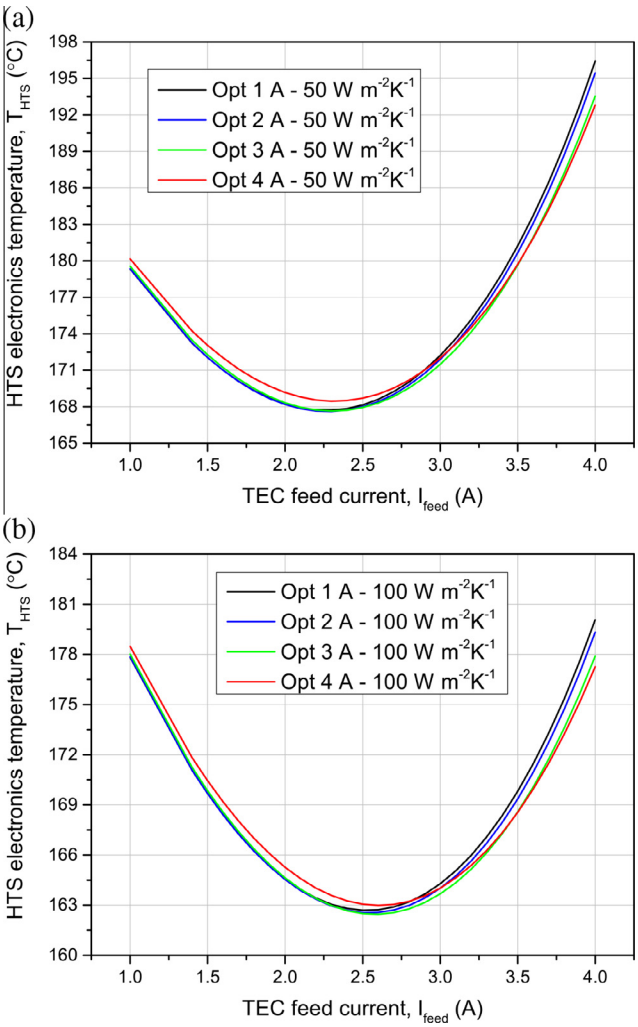

Fig. 6. HTS electronics temperature vs. TEC feed current for four different designs, optimized for $I_{feed} = 1, 2, 3$ and 4 A, and $h = 50$ W m^{-2} K^{-1} (a) and 100 W m^{-2} K^{-1} (b).

threaded holes, were designed in the top part of the chassis: they support a plastic screw system that clamps the cooler between the heat spreader and the chassis, while ensuring effective thermal contacts. The remaining volume was filled with thermal insulation, for thermal protection of the cooled electronics.

Simulations showed the chosen design operates very similarly to the optimized systems (Table 3). The difference in HTS electronics temperature is very small when operating at 1 A or 2 A, as the final design is very similar to the *Design* 1 concept. The HTS electronics are in fact maintained maximum 0.11 °C above the optimized case. When operating at 3 A and 4 A, the mismatch becomes larger, since the *Design* 2 concept would perform better at higher feed currents. However, when operating at 3 A, the HTS components are always maintained less than 1 °C above the optimized system. The mismatch becomes larger than 1 °C for operations at 4 A; that can be considered irrelevant, since $I_{feed} = 4$ A is far from the observed optimal TEC settings and the system would always aim at operating between 2 A and 3 A, close to the optimal conditions.

Table 3 also shows the final system fulfills the design conditions and the electronics can be maintained below 175 °C for every well fluid convection regime, as far as a control system can regulate the TEC feed current around the optimal one. The only exception occurs for the case at $h = 25$ W m^{-2} K^{-1}, where the heat rejection is very poor and the electronics can only be maintained between at an average temperature of 175 °C and 176 °C; this result is still considered acceptable given the small mismatch.

In order to have a clearer overview of the operation of the final design, a characteristic curve that displays the HTS average temperature as a function of the TEC feed current and of the well fluid convection coefficient is illustrated in Fig. 8. As already observed in the previous analyses, the performance of the system is enhanced when high well fluid convection regimes occur. At high TEC feed currents the performance of the system is more sensitive to the convection coefficient than at low I_{feed}, as it can be noticed from the curve slopes on the h-T_{HTS} plane. On the I_{feed}–T_{HTS} plane, instead, it can be observed the HTS electronics temperature reaches a minimum at I_{opt}, which varies for different conditions of well fluid convection. The I_{opt} front is highlighted with red line. The optimal operating current changes more rapidly with h at low convection regimes, where the excessive heat rejection is crucial, and engages a flatter trend while the convection coefficient grows.

4.4. Model validation

The system illustrated in Fig. 7 was manufactured and assembled as shown in Fig. 9. Thermal grease was used to interface the heating components to the chassis, lead wires were installed to

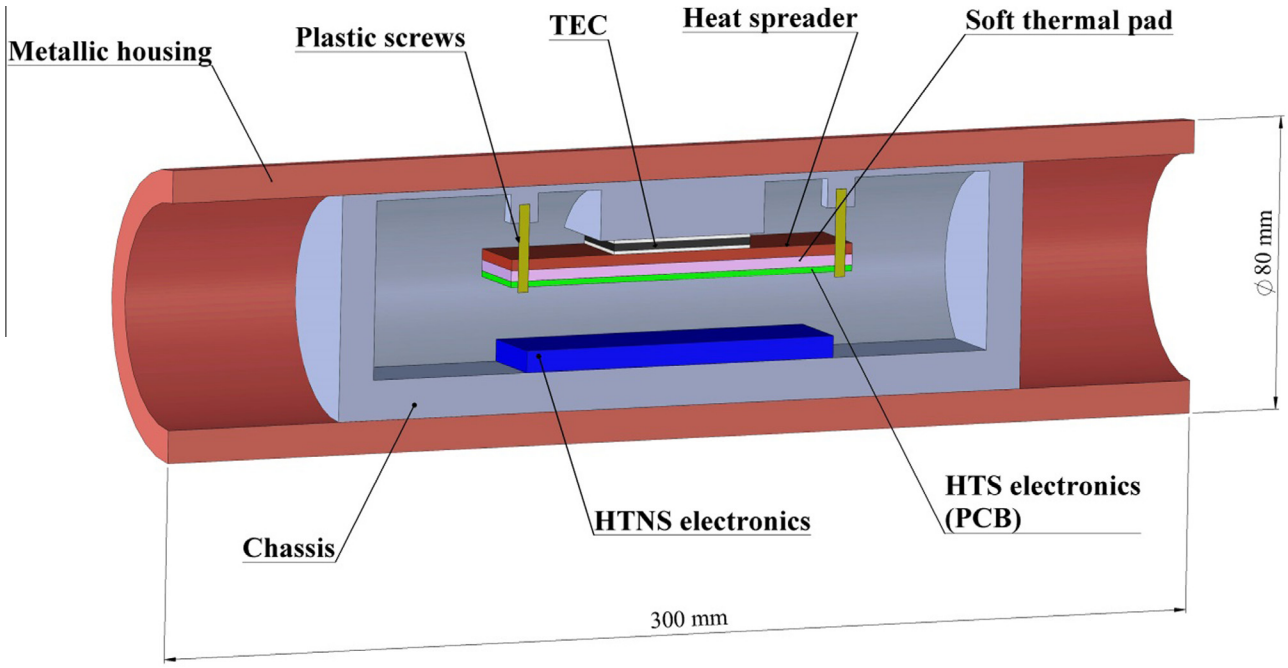

Fig. 7. Illustration of the longitudinal section of the final design. The thermoelectric cooler is clamped between the aluminum pad and the heat spreader through two plastic screws. The remaining volume within the chassis is filled with thermal insulation.

Table 3
Comparison between the performance of the final design (Design) and the optimized systems (Opt). $\Delta T = T_{HTS,design}\ T_{HTS,Opt}$.

h (W m^{-2} K^{-1})	*Opt – 1 A* T_{HTS} (°C)	*Design – 1 A* T_{HTS} (°C)	ΔT (°C)
25	182.31	182.41	0.10
50	179.32	179.43	0.11
100	177.83	177.94	0.11
500	176.56	176.67	0.11
	Opt – 2 A T_{HTS} (°C)	*Design – 2 A* T_{HTS} (°C)	
25	175.63	175.68	0.05
50	168.18	168.23	0.05
100	164.54	164.57	0.03
500	161.46	161.48	0.02
	Opt – 3 A T_{HTS} (°C)	*Design – 3 A* T_{HTS} (°C)	
25	188.22	188.93	0.71
50	171.48	171.87	0.39
100	163.68	163.90	0.22
500	157.12	157.35	0.23
	Opt – 4 A T_{HTS} (°C)	*Design – 4 A* T_{HTS} (°C)	
25	228.62	233.59	4.97
50	192.79	195.71	2.92
100	177.25	179.29	2.04
500	165.23	166.37	1.14

feed the two sets of electronics through external power supplies, and type-K thermocouples were installed to monitor the temperature profile within the tool.

The assembled tool was tested in a dry and ventilated hot environment, where a fan recirculated air at the set-point temperature T_{oven}. *Power Supply* 1 provided the electric power to the TEC, while a voltmeter and a current meter measured the feed voltage and current, respectively. *Power Supply* 2 provided the feed power to the test electronics. A *Data Acquisition System* monitored and recorded the temperature distribution within the tool. The schematic of the experimental setup is reported in Fig. 10.

Two different ovens, in size and air flow capacity, were used to test the tool at 180 °C, 190 °C, and 200 °C. For every oven temperature, the TEC feed current was varied between 1 A and 4 A, and the steady state temperature distribution across the tool was recorded. Furthermore, each test was characterized by the calculation of the average heat transfer coefficient $\bar{h}_{exp}$, which described the heat transfer, mainly driven by convection, occurring at the steady state between the tool housing and the oven environment. Eq (18) was calculated from the balance of the energy fluxes through the control volume shown in Fig. 10, and was used for this purpose. The term $\bar{h}_{exp}$ provides the reference boundary condition for the model validation process.

$$\bar{h}_{exp} = \frac{(P_{TEC} + P_{HTS} + P_{HTNS})}{A_{housing} \cdot (\bar{T}_{housing} - T_{oven})} \tag{18}$$

where $\bar{h}_{exp}$ is the average heat transfer coefficient at the tool housing surface; P_{TEC}, P_{HTS}, and P_{HTNS} are respectively the electric feed powers of the cooler, of the HTS electronics, and of the HTNS electronics; $A_{housing}$ is the outer surface area of the housing; $\bar{T}_{housing}$ is the average of the readings from the four thermocouples installed on the outer surface of the housing (see Fig. 9d); and T_{oven} is the measured oven temperature.

The experimental temperatures were measured with type-K thermocouples and compared with the predictions from the model (see Table 4). An accuracy of ±1.5 °C was used for the thermocouples, according to *IEC 584 Class* 1. Model data points were obtained from the corresponding 1 cm^2 square location within the finite-element geometry; actual measurements were compared with the average temperatures, while lower and higher error bands were introduced according to the model prediction for the maximum and minimum temperatures within the 1 cm^2 square.

Fig. 11 shows the comparison between the experimental and the model temperatures, from the TEC hot plate (probe shown Fig. 9b) and HTS electronics (probe shown in Fig. 9c), which represent the most relevant temperatures for the system operation.

As indicated in Fig. 11, experimental data and model forecasts revealed a good match, and proved the model can reproduce the performance of the real system with a good degree of accuracy. Fig. 11a shows the majority of the data points for the HTS electronics temperature are close to the perfect prediction. Points from the tests at lower convection show a slightly worse match with the

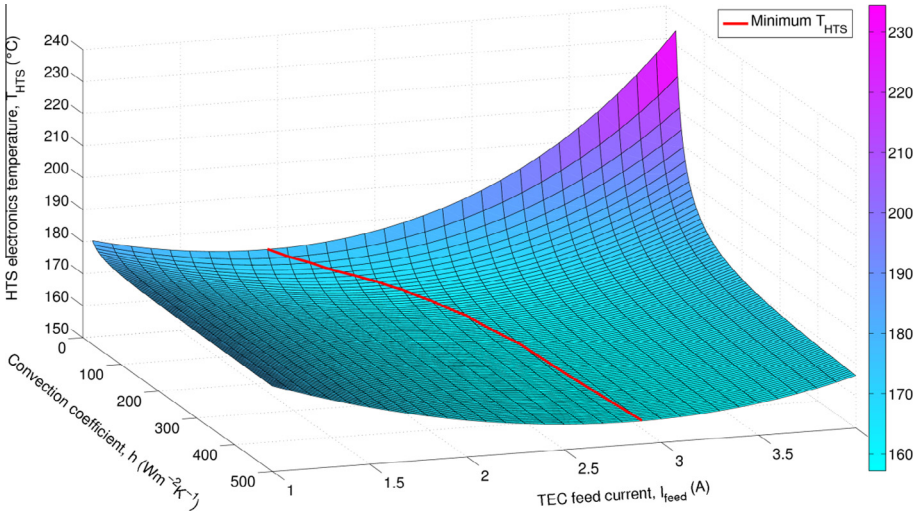

Fig. 8. Characteristic curve of the finally designed TEC integrated system. The plot reports the simulated performance of the cooling system, in a 200 °C environment, as HTS electronics temperature vs. convection coefficient and TEC feed current. The minimum HTS electronics temperature, for each operating condition, is highlighted by a red line. The color bar expresses the HTS electronics temperature in degrees Celsius. (For interpretation of the references to color in this figure legend, the reader is referred to the web version of this article.)

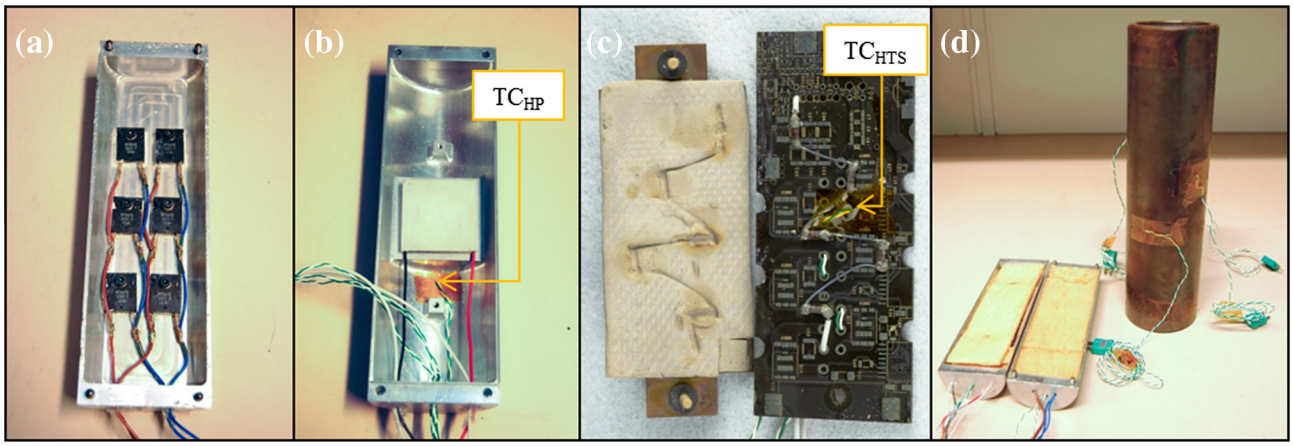

Fig. 9. Illustration of the manufactured components. Six resistors were installed on the chassis bottom half to reproduce the HTNS electronics (a).The TEC was located in the chassis top half, with two threaded holes for implementing the clamping system; the thermocouple TC_{HP} measured the temperature on the hot side of the TEC (b). Five resistors were soldered onto the PCB, to simulate the HTS electronics, and coupled with the soft thermal pad and the heat spreader (c); the thermocouple TC_{HTS} measured the temperature of the PCB. The two halves of the chassis were finally filled with thermally insulating foam and inserted into the metallic housing; the temperature of the housing was monitored by four thermocouples (d).

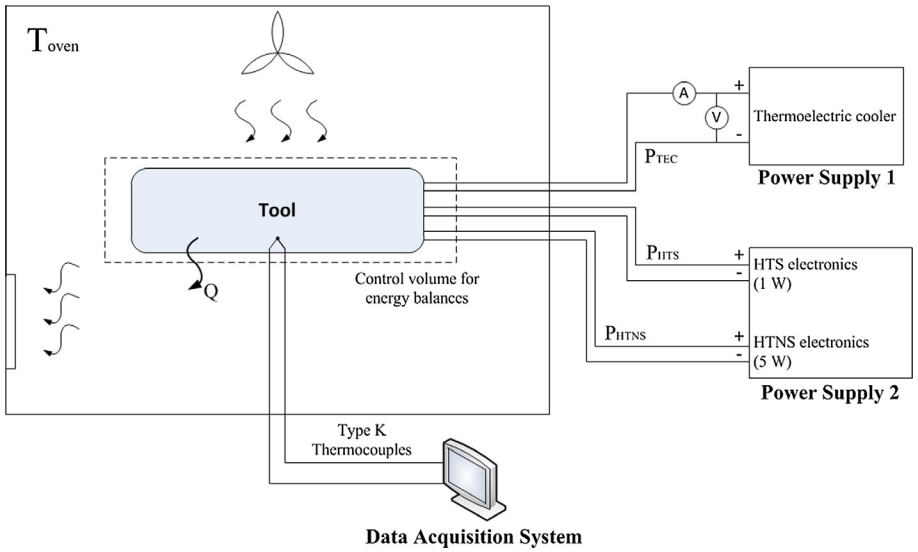

Fig. 10. Schematic of the experimental setup. The main components characterizing the experimental validation of the model are illustrated.

Table 4
Temperatures and parameters characterizing both the experimental procedure and the model validation. The first three columns define the boundary conditions of each test, while the last four columns summarize the TEC hot plate (HP) and HTS electronics temperatures, at stationary operations.

T_{oven} (°C)	I_{feed} (A)	$\bar{h}_{exp}$ (W m^{-2} K^{-1})	$T_{HTS,model}$ (°C)	$T_{HTS,exp}$ (°C)	$T_{HP,model}$ (°C)	$T_{HP,exp}$ (°C)
Lower convection oven						
180.4	1.0	35.1	160.3	161.6	185.3	185.6
180.7	1.5	30.9	154.4	156.4	189.3	190.3
180.5	2.0	29.1	152.0	155.0	194.5	196.0
180.3	2.5	28.2	153.8	157.6	201.3	203.1
190.8	1.0	36.8	170.7	172.5	195.6	195.5
189.9	1.5	31.0	163.9	166.7	198.7	199.3
190.1	2.0	31.1	161.3	164.4	203.5	204.3
190.6	2.5	30.3	163.9	167.8	210.8	211.4
199.3	1.5	35.6	172.7	176.7	207.3	207.3
199.5	2.0	32.3	171.0	175.9	212.9	213.0
199.7	2.3	31.7	172.0	177.4	216.8	216.9
Higher convection oven						
180.7	1.0	65.7	158.7	157.7	183.7	182.6
181.0	2.0	62.4	146.2	145.4	188.7	188.4
180.7	3.0	57.7	147.1	145.8	197.5	197.9
181.1	3.5	59.0	153.7	151.1	203.5	203.1
190.8	1.0	72.9	168.7	168.3	193.6	191.8
191.0	2.0	64.8	156.4	155.7	198.7	197.0
190.2	3.0	60.8	157.0	156.2	206.7	205.7
190.8	3.3	61.1	160.5	158.8	210.1	208.6
200.4	1.5	75.9	170.3	170.7	205.0	203.0
201.8	2.0	73.4	167.1	168.8	209.1	207.4
200.3	2.3	66.3	164.9	166.2	210.1	208.9
200.1	3.0	62.6	167.9	168.1	216.7	214.3

model, which predicts slightly lower HTS electronics temperatures. Based on the thermocouple readings and visual inspection of the system, no degradation at the cold side of the TEC was observed after the tests. No visible breakdown of the thermal interface material, which is rated for a maximum operating temperature of 200 °C, or change in the thermal resistances were detected. The mismatch in the model results can be attributed to the degradation of the TEC itself, which occurred in the ~50 h of testing at high temperature in the higher convection oven, which were carried out first chronologically. The degradation of the module consists of a decrease in the thermoelectric effect and was detected as a drop in the temperature span across the TEC and a decrease of the TEC feed voltage at constant current [58]. The lower heat transport between the plates could therefore have led to higher experimental HTS electronics temperatures. The effects of the degradation are also accentuated when operating in low convection environments and high feed currents.

Fig. 11b, instead, shows a very good match between experiments and model predictions for the hot plate temperatures, both for the lower and higher convection scenarios.

The previously described behavior can also be observed in Fig. 12, where a comparison between model and experiments is reported as a function of the TEC feed current. Experimental results show a good agreement with the model predictions and are able to reproduce the forecast trends with I_{feed}. Furthermore, the experimental data confirm the presence of an optimal operating current I_{opt}, as described in the Section 4.3, and the trend is reproduced by the model. Although Fig. 12c shows a slightly larger mismatch between predictions and experiments, for the lower convection scenario, the convex trend and the value of I_{opt} are reproduced with good approximation. The observed I_{opt} values varied with the outer fluid convection regime, confirming the behavior predicted by the model. As expected and previously shown, lower electronics temperatures were obtained in the higher convection scenario.

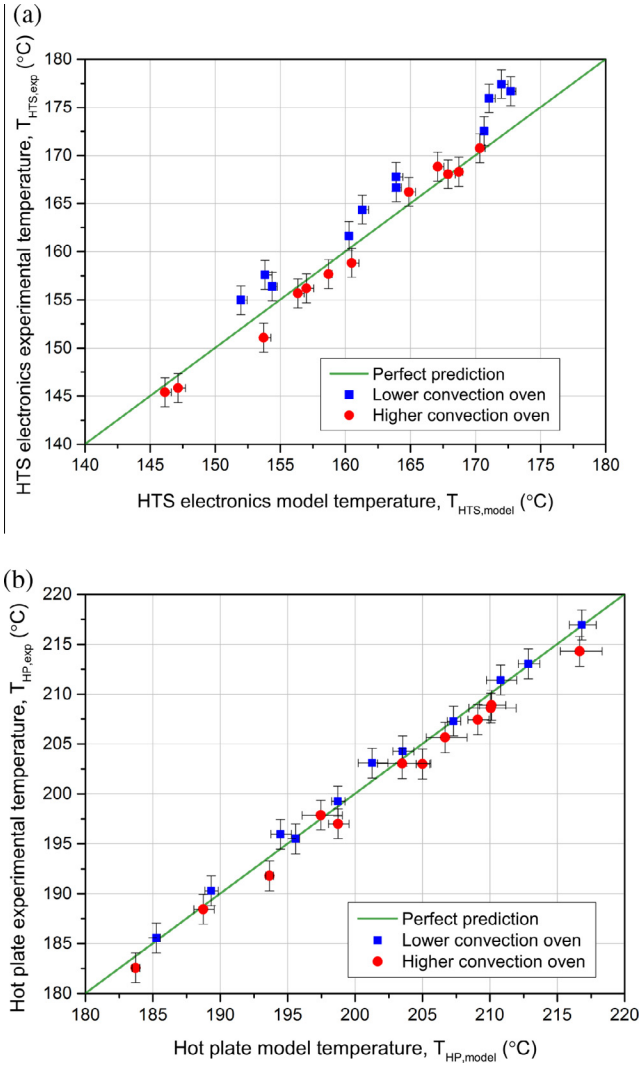

Fig. 11. Comparison between experimental data and model prediction. HTS electronics temperatures are reported in figure (a) and hot plate temperatures are reported in figure (b). Results from all the tests from both the ovens are illustrated, and compared to the perfect prediction scenario.

5. Conclusions

This work presented and demonstrated a method of integrating a TEC into a system with specific design constraints, using topology optimization combined with a 3D finite element model of the system. This technique allows efficient integration of TECs by optimizing how they interact thermally with their surroundings, and is suitable for any TED application where the module must be mounted in a fixed volume. As a specific application, the optimization method was used to aid in the design of an actively cooled electronics unit for a downhole oil well intervention tool, and to optimize the integration setup of a commercial thermoelectric cooler. The geometry to be optimized and the problem-related governing equations were implemented in COMSOL Multiphysics, together with the SIMP topology optimization approach. The model was used to optimize the distribution of aluminum and thermally insulating material within the unit, so the temperature-sensitive electronics could be maintained at a minimum temperature. The system was optimized for several well conditions and for the TEC feed current, and different design concepts

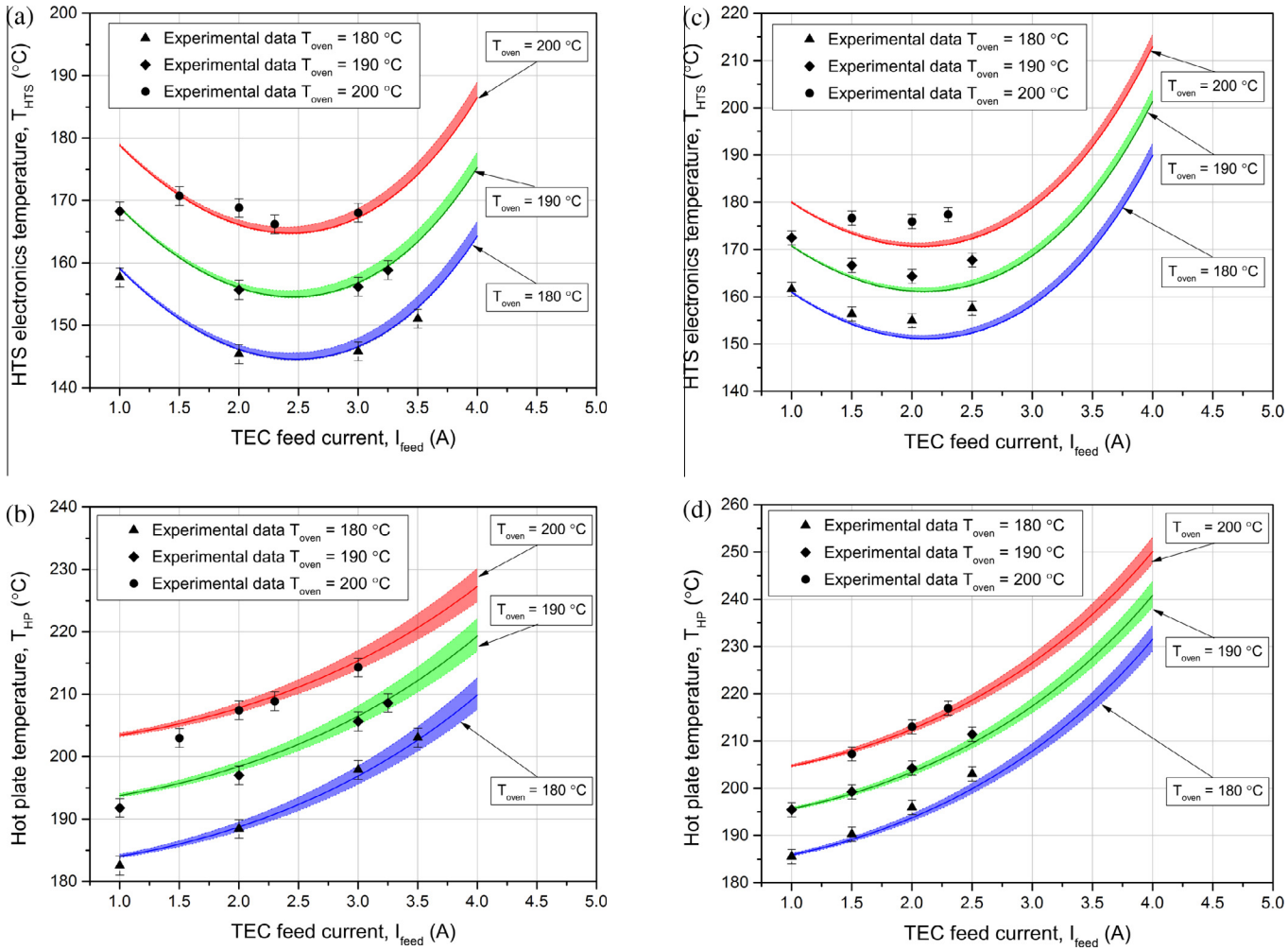

Fig. 12. Comparison between experimental and modeling temperatures vs. TEC feed current, at different oven temperatures. Figures (a) and (b) report respectively the HTS electronics and the hot plate temperatures trends vs. TEC feed current, for the higher convection oven. Figures (c) and (d) report respectively the HTS electronics and the hot plate temperatures vs. TEC feed current, for the lower convection oven. The colored lines show the trends predicted by the model, defined by the maximum and minimum temperatures from the 1 cm^2-square model probe. The single points represent the experimental data. (For interpretation of the references to color in this figure legend, the reader is referred to the web version of this article.)

Fig. 12 (*continued*)

were generated and analyzed. When heat rejection was critical (high TEC feed currents and low convection regimes) the mass of aluminum increased for better conduction out of the tool to the well; when the heat rejection was not critical (low TEC feed currents and high convection regimes) the thermal protection of the cooled electronics was prioritized, and the use of aluminum was significantly lower than the previous cases in favor of the thermal insulator. Optimized systems were found to cool the electronics down to a temperature 37 °C colder than before optimization. Furthermore, the optimization process proved to be not significantly sensitive to the convection range, but highly sensitive to the operating current of the TEC. An optimal operating current, which minimizes the temperature of the HTS components and depends on the well fluid convection regime, was found. This analysis highlighted the importance of a control system that would always seek the best operating conditions for the cooler.

Topology optimization was used to implement the final design of the electronics unit, which simulations predicted to perform very closely to the optimized systems. The final design was manufactured and tested in an experimental setup, at different operating conditions. Model predictions reproduced experimental results with good agreement, replicated the predicted optimal feed currents, and demonstrated the effectiveness of the design method. Topology optimization was shown to be a powerful design tool that can be combined with a TED model to yield optimized designs for thermoelectric integrated systems.

Acknowledgements

S. Soprani and K. Engelbrecht would like to show their gratitude to the Danish Ministry of Technology and Innovation (contract 1355-00051B) and to Welltec A/S for partially funding this work. The authors would also like to acknowledge the TopTEN project, sponsored through the Sapere Aude Program of the Danish Council for Independent Research (DFF–4005-00320), for supporting this study.

Appendix A. Supplementary material

Supplementary data associated with this article can be found, in the online version, at http://dx.doi.org/10.1016/j.apenergy.2016.05.024.

References

[1] Rowe DM. Handbook of thermoelectrics. London: CRC Press Boca Raton; 1995. http://dx.doi.org/10.1201/9781420049718.

[2] Bell LE. Cooling, heating, generating power, and recovering waste heat with thermoelectric systems. Science 2008;321(5895):1457–61. http://dx.doi.org/10.1126/science.1158899.

[3] He W, Zhang G, Zhang X, Ji J, Li G, Zhao X. Recent development and application of thermoelectric generator. Appl Energy 2015;143:1–25. http://dx.doi.org/10.1016/j.apenergy.2014.12.075.

[4] Tritt TM, Subramanian MA. Thermoelectric materials, phenomena, and applications: a bird's eye view. MRS Bull 2006;31(3):188–98. http://dx.doi.org/10.1557/mrs2006.44.

[5] Montecucco A, Knox AR. Accurate simulation of thermoelectric power generating systems. Appl Energy 2014;118(20):166–72. http://dx.doi.org/10.1016/j.apenergy.2013.12.028.

[6] Hermes CJL, Barbosa Jr JR. Thermodynamic comparison of Peltier, stirling, and compression portable coolers. Appl Energy 2012;91(1):51–8. http://dx.doi.org/10.1016/j.apenergy.2011.08.043.

[7] Dresselhaus MS, Chen G, Tang MY, Yang R, Lee H, Wang D, et al. New directions for low-dimensional thermoelectric materials. Adv Mater 2007;19(8):1043–53. http://dx.doi.org/10.1002/adma.200600527.

[8] Snyder GJ, Toberer ES. Complex thermoelectric materials. Nat Mater 2008;7(2):105–14. http://dx.doi.org/10.1038/nmat2090.

[9] Bulusu A, Walker DG. Review of electronic transport models for thermoelectric materials. Superlatt Mictrostuct 2008;44(1):1–36. http://dx.doi.org/10.1016/j.spmi.2008.02.008.

[10] Yang Y, Ma FY, Lei CH, Liu YY, Li JY. Is thermoelectric conversion efficiency of a composite bounded by its constituents? Appl Phys Lett 2013;102(5):053905. http://dx.doi.org/10.1063/1.4791684.

[11] Abramzon B. Numerical optimization of the thermoelectric cooling devices. J Electron Packag 2007;129(3):339–47. http://dx.doi.org/10.1115/1.2753959.

[12] Heghmanns A, Beitelschmidt M. Parameter optimization of thermoelectric modules using a genetic algorithm. Appl Energy 2015;155:447–54. http://dx.doi.org/10.1016/j.apenergy.2015.06.034.

[13] Xiao J, Yang T, Li P, Zhai P, Zhang Q. Thermal design and management for performance optimization of solar thermoelectric generator. Appl Energy 2012;93(20):33–8. http://dx.doi.org/10.1016/j.apenergy.2011.06.006.

[14] Takezawa A, Kitamura M. Geometrical design of thermoelectric generators based on topology optimization. Int J Numer Methods Eng 2012;90(11):1363–92. http://dx.doi.org/10.1002/nme.3375.

[15] Chen L, Li J, Sun F. Performance optimization for a two-stage thermoelectric heat-pump with internal and external irreversibilities. Appl Energy 2008;85(7):641–9. http://dx.doi.org/10.1016/j.apenergy.2007.10.005.

[16] Pan Y, Lin B, Chen J. Performance analysis and parametric optimal design of an irreversible multi-couple thermoelectric refrigerator under various operating conditions. Appl Energy 2007;84(9):882–92. http://dx.doi.org/10.1016/j.apenergy.2007.02.008.

[17] Quan R, Tang X, Quan S, Huang L. A novel optimization method for the electric topology of thermoelectric modules used in an automobile exhaust thermoelectric generator. J Electron Mater 2013;42(7):1469–75. http://dx.doi.org/10.1007/s11664-012-2291-3.

[18] Taylor RA, Solbrekken GL. Comprehensive system-level optimization of thermoelectric devices for electronic cooling applications. IEEE Trans Compon Packag Technol 2008;31(1):23–31. http://dx.doi.org/10.1109/tcapt.2007.906333.

[19] Rezania A, Yazawa K, Rosendahl LA, Shakouri A. Co-optimized design of microchannel heat exchangers and thermoelectric generators. Int J Therm Sci 2013;72:73–81. http://dx.doi.org/10.1016/j.ijthermalsci.2013.05.002.

[20] Gou X, Xiao H, Yang S. Modeling experimental study and optimization on low-temperature waste heat thermoelectric generator system. Appl Energy 2010;87(10):3131–6. http://dx.doi.org/10.1016/j.apenergy.2010.02.013.

[21] David B, Ramousse J, Luo L. Optimization of thermoelectric heat pumps by operating condition management and heat exchanger design. Energy Convers Manage 2012;60:125–33. http://dx.doi.org/10.1016/j.enconman.2012.02.007.

[22] Bendsøe MP, Sigmund O. Topology optimization: theory, methods and applications. Berlin Heidelberg: Springer Verlag; 2004. http://dx.doi.org/10.1007/978-3-662-05086-6.

[23] Sigmund O, Maute K. Topology optimization approaches. Struct Multidiscip Optim 2013;48(6):1031–55. http://dx.doi.org/10.1007/s00158-013-0978-6.

[24] Deaton JD, Grandhi RV. A survey of structural and multidisciplinary continuum topology optimization: post 2000. Struct Multidiscip Optim 2014;49(1):1–38. http://dx.doi.org/10.1007/s00158-013-0956-z.

[25] Dede EM, Lee J, Nomura T. Multiphysics simulation: electromechanical system simulation and optimization studies. London, Heidelberg New York Dordrecht: Springer; 2014. http://dx.doi.org/10.1007/978-1-4471-5640-6_5.

[26] Li Q, Steven GP, Xie YM, Querin OM. Evolutionary topology optimization for temperature reduction of heat conducting fields. Int J Heat Mass Transfer 2004;47(23):5071–83. http://dx.doi.org/10.1016/j.ijheatmasstransfer.2004.06.010.

[27] Gersborg-Hansen A, Sigmund O, Haber RB. Topology optimization of channel flow problems. Struct Multidiscip Optim 2005;30(3):181–92. http://dx.doi.org/10.1007/s00158-004-0508-7.

[28] Sigmund O. Design of multiphysics actuators using topology optimization-Part I: One material structures. Comput Methods Appl Mech Eng 2001;190(49):6577–604. http://dx.doi.org/10.1016/s0045-7825(01)00251-1.

[29] Yin L, Ananthasuresh GK. A novel topology design scheme for the multi-physics problems of electro-thermally actuated compliant micromechanisms. Sens Actuators A 2002;97:599–609. http://dx.doi.org/10.1016/s0924-4247(01)00853-6.

[30] Bruns TE. Topology optimization of convection-dominated, steady-state heat transfer problems. Int J Heat Mass Transfer 2007;50(15):2859–73. http://dx.doi.org/10.1016/j.ijheatmasstransfer.2007.01.039.

[31] Ahn SH, Cho S. Level set-based topological shape optimization of heat conduction problems considering design-dependent convection boundary. Numer Heat Transfer, Part B 2010;58(5):304–22. http://dx.doi.org/10.1080/10407790.2010.522869.

[32] Iga A, Nishiwaki S, Izui K, Yoshimura M. Topology optimization for thermal conductors considering design-dependent effects, including heat conduction and convection. Int J Heat Mass Transfer 2009;52(11):2721–32. http://dx.doi.org/10.1016/j.ijheatmasstransfer.2008.12.013.

[33] Yoon GH. Topological design of heat dissipating structure with forced convective heat transfer. J Mech Sci Technol 2010;24(6):1225–33. http://dx.doi.org/10.1007/s12206-010-0328-1.

[34] McConnell C, Pingen G. Multi-layer, Pseudo 3D thermal topology optimization of heat sinks. In: Proceedings of the ASME 2012 international mechanical engineering congress, Houston, USA; 2012. http://dx.doi.org/10.1115/imece2012-93093.

[35] Marck G, Nemer M, Harion JL. Topology optimization of heat and mass transfer problems: laminar flow. Numer Heat Transfer, Part B 2013;63(6):508–39. http://dx.doi.org/10.1080/10407790.2013.772001.

[36] Matsumori T, Kondoh T, Kawamoto A, Nomura T. Topology optimization for fluid–thermal interaction problems under constant input power. Struct Multidiscip Optim 2013;47(4):571–81. http://dx.doi.org/10.1007/s00158-013-0887-8.

[37] Van Oevelen T, Baelmans M. Numerical topology optimization of heat sinks. In: Proceedings of the 15th international heat transfer conference; 10–15 2014. http://dx.doi.org/10.1615/ihtc15.opt.009168.

[38] Lee J, Nomura T, Dede EM. Heat flow control in thermo-magnetic convective systems using engineered magnetic fields. Appl Phys Lett 2012;101:123507. http://dx.doi.org/10.1063/1.4754119.

[39] Yaji K, Yamada T, Kubo S, Izui K, Nishiwaki S. A topology optimization method for a coupled thermal-fluid problem using level set boundary expressions. Int J Heat Mass Transfer 2015;81:878–88. http://dx.doi.org/10.1016/j.ijheatmasstransfer.2014.11.005.

[40] Alexandersen J, Aage N, Andreasen CS, Sigmund O. Topology optimisation for natural convection problems. Int J Numer Methods Fluids 2014;76(10):699–721. http://dx.doi.org/10.1002/fld.3954.

[41] Castro DA, Kiyono CY, Silva ECN. Design of radiative enclosures by using topology optimization. Int J Heat Mass Transfer 2015;88:880–90. http://dx.doi.org/10.1016/j.ijheatmasstransfer.2015.04.077.

[42] Koga AA, Lopes ECC, Villa Nova H, de Lima CR, Silva E CN. Development of heat sink device by using topology optimization. Int J Heat Mass Transfer 2013;64:759–72. http://dx.doi.org/10.1016/j.ijheatmasstransfer.2013.05.007.

[43] Dede EM, Joshi SN, Zhou F. Topology optimization, additive layer manufacturing, and experimental testing of an air-cooled heat sink. J Mech Des 2015;137(11):111702. http://dx.doi.org/10.1115/1.4030989.

[44] Dede EM. Single-phase microchannel cold plate for hybrid vehicle electronics. Semicond Therm Meas Manage Symp (SEMI-THERM) 2014. http://dx.doi.org/10.1109/semi-therm.2014.6892227.

[45] Soprani S, Haertel JHK, Lazarov BS, Sigmund O, Engelbrecht K. Topology optimization of an actively cooled electronics section for downhole tools. In: Proceedings COMSOL conference 2015, Grenoble, France; 2015.

[46] Bennett GA. Active cooling for downhole instrumentation: preliminary analysis and system selection. Mexico: Los Alamos National Laboratory; 1988.

[47] Flores AG. Active cooling for electronics in a wireline oil-exploration tool Ph.D. Thesis. USA: M.I.T; 1996.

[48] Sinha A, Joshi YK. Downhole electronics cooling using a thermoelectric device and heat exchanger arrangement. J Electron Packag 2011;133(4). http://dx.doi.org/10.1115/1.4005290. 041005-1–041005-12.

[49] Jakaboski JC. Innovative thermal management of electronics in oil well logging. M.Sc. thesis. Georgia Institute of Technology USA; 2004.

[50] Pennewitz E, Kruspeb T, Jungb S, Schillinga M. Evaluation of sorbents at elevated temperatures for downhole application. Chem Eng Trans 2012;29:1543–8. http://dx.doi.org/10.3303/CET1229258.

[51] Soprani S, Engelbrecht K, Nørgaard AJ. Active cooling and thermal management of a downhole tool electronics section. In: Proceedings of the 24th IIR international congress of refrigeration, IIF-IIR, Yokohama, Japan; 2015.

[52] COMSOL Multiphysics 5.0.

[53] Gordon JM, Ng KC, Chua HT, Chakraborty A. The electro-adsorption chiller: a miniaturized cooling cycle with applications to micro-electronics. Int J Refrig 2002;25(8):1025–33. http://dx.doi.org/10.1016/s0140-7007(02)00026-9.

[54] Lazarov BS, Sigmund O. Filters in topology optimization based on helmholtz-type differential equations. Int J Numer Methods Eng 2011;86(6):765–81. http://dx.doi.org/10.1002/nme.3072.

[55] Wang F, Lazarov BS, Sigmund O. On projection methods, convergence and robust formulations in topology optimization. Struct Multidiscip Optim 2011;43(6):767–84. http://dx.doi.org/10.1007/s00158-010-0602-y.
[56] Sigmund O, Petersson J. Numerical instabilities in topology optimization: a survey on procedures dealing with checkerboards, mesh-dependencies and local minima. Struct Optim 1998;16(1):68–75. http://dx.doi.org/10.1007/bf01214002.
[57] Svanberg K. A class of globally convergent optimization methods based on conservative convex separable approximations. SIAM J Optim 2002;12(2):555–73. http://dx.doi.org/10.1137/s1052623499362822.
[58] Barako MT, Park W, Marconnet AM, Asheghi M, Goodson KE. Thermal cycling, mechanical degradation, and the effective figure of merit of a thermoelectric module. J Electron Mater 2012;42(3):372–81.

A.3 P3 - A Fully Developed Flow Thermofluid Model for Topology Optimization of 3D-Printed Air-Cooled Heat Exchangers

J. H. K. Haertel and G. F. Nellis

***Applied Thermal Engineering*, vol. 119, pp. 10-24, 2017.**

Applied Thermal Engineering 119 (2017) 10–24

Contents lists available at ScienceDirect

Applied Thermal Engineering

journal homepage: www.elsevier.com/locate/apthermeng

Research Paper

A fully developed flow thermofluid model for topology optimization of 3D-printed air-cooled heat exchangers

Jan H.K. Haertel [a,*], Gregory F. Nellis [b]

[a] Department of Energy Conversion and Storage, Technical University of Denmark, Frederiksborgvej 399, 4000 Roskilde, Denmark
[b] Department of Mechanical Engineering, University of Wisconsin–Madison, 1500 Engineering Drive, Madison, WI 53706, USA

ARTICLE INFO

Article history:
Received 2 October 2016
Revised 14 February 2017
Accepted 8 March 2017
Available online 10 March 2017

ABSTRACT

In this work, density-based topology optimization is applied to the design of the air-side surface of dry-cooled power plant condensers. A topology optimization model assuming a steady-state, thermally and fluid dynamically fully developed internal flow is developed and used for this application. The conductance of the heat exchanger is maximized for a prescribed pressure drop and prescribed air-side temperature change across the heat exchanger. Polymer with infilled thermally conducting metal filaments is considered as the heat exchanger material which allows cost effective additive manufacturing techniques to be used to fabricate the obtained designs. Parametric studies are presented that analyze the effect of the material thermal conductivity and the heat exchanger unit cell height on the system's performance. The designs obtained from topology optimization are benchmarked against a simple optimized slot channel model in order to demonstrate the superior performance of the topology optimized designs. Thus, this work demonstrates the usefulness of topology optimization to fully exploit the design freedom afforded by additive manufacturing technologies.

1. Introduction

High performance air-side heat transfer surfaces are required by many applications. The work presented here was motivated specifically by the need to transition heat rejection systems for power plants from water-cooled to air-cooled (referred to subsequently as dry-cooled). Dry-cooling of power plants eliminates their water consumption, thus mitigating their environmental impact and providing a higher flexibility for siting options since no large local water source is needed. Currently, water-cooled systems are preferred due to their low cost and compact design; however, power plants are currently the single largest users of fresh water in the US [1] and this is increasingly becoming an issue in several regions of the country. The penalty associated with dry-cooling is lower efficiency due to higher heat rejection temperatures (the dry-bulb vs the wet-bulb temperature) and the lower air-side heat transfer coefficient as well as comparatively high required fan power. These disadvantages have thus far prevented the wide spread use of dry-cooled condensers. Improving the air-side heat transfer surface while keeping the fan power low is crucial for dry-cooled heat exchangers to become economically competitive. In this work, density-based topology optimization is applied to address this optimization challenge.

The application of topology optimization to the design of thermofluid systems is an active area of research. Topology optimization allows a systematic optimization of these nonlinear systems as opposed to classical methods such as trial and error or intuition-based engineering. Therefore, topology optimization can lead to reduced development time and unanticipated and non-intuitive designs can be identified. Nevertheless, the performance increase of the topology optimized designs can result in more complex heat exchanger surfaces than when applying classical design methods. These complex surfaces might not be easily manufactured using conventional manufacturing techniques; however, they can be fabricated using additive manufacturing methods, especially as those methods become increasingly mature. Thus, topology optimization techniques are critical in order to fully exploit the design freedom that these technologies provide. An additive manufacturing or 3D printing method that is being considered for the fabrication of dry-cooled condensers is Fused Layer Modeling (FLM) where polymer material is extruded through a nozzle to build up a structure layer by layer. Using this method, complex surfaces can be fabricated from a relatively cheap polymer in large quantities and with cheap equipment.

* Corresponding author.
E-mail addresses: jhkh@dtu.dk (J.H.K. Haertel), gfnellis@engr.wisc.edu (G.F. Nellis).

http://dx.doi.org/10.1016/j.applthermaleng.2017.03.030
1359-4311/

Nomenclature

a	side length of rectangle for Reynolds number calculation (m)
$A_{\Omega,fl}$	flow area of design domain (m^2)
A_c	cross-sectional area (m^2)
b	side length of rectangle for Reynolds number calculation (m)
b_k	convexity parameter in RAMP interpolation
c	specific heat capacity (J/(kg K))
D	diameter of circular pipe (m)
D_h	hydraulic diameter (m)
F	Brinkman friction term (N/m^3)
$\dot{g}_v'''$	volumetric rate of viscous dissipation (W/m^3)
h	heat transfer coefficient ($W/(m^2 K)$)
height	modeled height of flow between parallel plates problem (m)
k	thermal conductivity (W/(m K))
L	length heat exchanger unit cell (m)
L_{char}	characteristic length (m)
$\mathbf{n}$	normal vector
n_d	number of design variables
Nu	Nusselt number (–)
p	pressure (Pa)
per	perimeter of duct (m)
$\dot{q}$	heat transfer rate (W)
r	residual of the state problem
r_{filter}	filter parameter (m)
Re	Reynolds number
$\boldsymbol{s}$	vector of state variables of the multiphysics problem
T	temperature (°C)
$T_{air,bulk}$	air bulk temperature (°C)
$T^*_{air,bulk}$	prescribed air bulk temperature (°C)
T_{wall}	wall temperature of duct (°C)
UA	heat exchanger's conductance (kW/K)
w	velocity in z-direction (m/s)
$w_{average,\ fl}$	flow area averaged air velocity (m/s)
w_{mean}	mean velocity used for Reynolds number calculation (m/s)
W	wall domain as specified in Fig. 2
x	x-coordinate (m)
y	y-coordinate (m)
z	z-coordinate (m)

Abbreviations

2D	two-dimensional
3D	three-dimensional
ABS	acrylonitrile butadiene styrene
BC	boundary condition
FLM	fused layer modeling
GCMMA	globally convergent version of the Method of Moving Asymptotes
max	maximize
PDE	partial differential equation
s.t.	subject to

Greek symbols

$\bar{\alpha}$	maximum inverse permeability ($Pa\ s/m^2$)
β	projection steepness parameter
γ	design variable
$\boldsymbol{\gamma}$	vector of design variables
Γ_{ij}	boundary of modeled domain as specified in Fig. 2
∂	partial derivative
Δp_{HEX}	air-side pressure drop over the heat exchanger unit cell (Pa)
ΔT	air-to-water temperature difference (°C)
ΔT_{HEX}	air-side temperature increase across the heat exchanger unit cell (°C)
η	projection threshold parameter
μ	dynamic viscosity (Pa s)
∇	nabla operator
ρ	density (kg/m^3)
Ω	design domain as specified in Fig. 2

Indices

air	air
f	fluid
i	counter index
j	counter index
polymer	polymer
s	solid
water	water

High throughput can be obtained using several nozzles in parallel. As a result, the FLM process is fundamentally cost-effective for larger structures such as dry-cooled condensers. The general applicability of polymers as heat exchanger and heat sink material has been demonstrated successfully in different applications [2]. A significant drawback of using polymers as heat exchanger material is the thermal conductivity which is approximately 100 times lower than metal. However, this limitation can be overcome by using fillers such as thermally conductive carbon fibers or metal filaments to increase the effective conductivity of the resulting composite.

Density-based topology optimization [3] determines whether to put solid or void at each point within a design domain in order to maximize a given objective under specified constraints. For this purpose, a density field is introduced that takes the value of 0 for solid and 1 for void which, for this application, corresponds to heat exchanger material (0) or fluid passage (1). Relaxing this optimization problem to density values between 0 and 1 allows for the use of gradient-based optimization methods, which are necessary to efficiently tackle topology optimization problems that typically involve large numbers of design variables. Topology optimization was originally developed for structural mechanics applications and has matured within this field; however it has subsequently been applied to other disciplines such as fluid mechanics [4] and photonics [5].

One application of topology optimization in heat transfer is pure heat conduction problems, as described in[3,6,7]. In addition to pure two dimensional heat conduction, out of plane convection with a constant heat transfer coefficient is considered in various publications: For example Sigmund [8] applied density-based topology optimization to the design of multiphysics actuators. Later works also included in-plane convective heat transfer to an ambient fluid either assuming a constant heat transfer coefficient [9–11] or using a surrogate model for the heat transfer coefficient [12]. This modeling approach was extended to 3D conduction problems with convection to an ambient fluid assuming a constant heat transfer coefficient using density-based [13] and level set topology optimization [14]. Soprani et al. [15,16] applied density-based topology optimization to the thermal integration of a thermoelectric cooler by designing the heat rejection path to convectively cooled boundaries with prescribed heat transfer coefficient. To overcome these simplifications regarding the details of the convective heat transfer process to the ambient fluid, more recent

works included heat conduction in the solid domain and explicit modeling of heat transfer in the fluid within the topology optimization. Different works presented forced convection thermofluid topology optimization models using density-based topology optimization [17–28] and level set boundary expressions [29]. Dede [17] presents 2D and 3D heat conduction problems as well as a 2D thermofluid model with uniform heat production rate in the modeled domain and a fixed Reynolds number of 50 at the fluid inlet. The optimization of different 2D modeled heat dissipating structures is presented by [18] and [19,20] apply 2D topology optimization to the design of water-cooled micro-channel heat sinks where [20] limits the fluid problem to Stokes flow. Marck et al. [21] present pure fluid 2D optimization problems as well as a 2D thermofluid topology optimization model for a pipe with constant wall temperature and report a Reynolds number of 3 in the thermofluid problem. A 2D thermofluid heat exchanger topology optimization model under constant input power is described in [22] where the case of a temperature dependent and temperature independent heat source within the design domain is considered and a maximum Reynolds number of 100 is prescribed. Similar models are used in [23] that model the 2D thermofluid problem using the lattice Boltzmann method and report Reynolds numbers of around 10 as well as in [29] that use level set boundary expressions for the topology optimization and generate 2D and 3D optimized designs with a maximum Reynolds number of 800 for the 2D case. The 2D modeling approach of the above mentioned thermofluid works was extended by [24] and later [25] to a pseudo 3D model where a 2D conductive base layer in which the heat generation occurs interacts with the 2D thermofluid optimization layer. Qian et al. [26] presented topology optimization for a 2D thermofluid system under a tangential thermal gradient constraint generating designs for Reynolds numbers of 50 and 250. The above mentioned works on thermofluid topology optimization treat laminar flow problems. Kontoleontos et al. [27] use a Spalart-Allmaras model to extend the modeling to turbulent flow; however, the temperature distribution in the solid is ignored in their work. Topology optimization for natural convection problems has only recently been addressed and work has been reported applying density-based topology optimization to 2D models [30] as well as 3D- [31] and large-scale 3D systems [32]. Coffin and Maute used level set-based topology optimization to optimize 3D and 2D transient natural convection systems [33]. The design using topology optimization, manufacturing and subsequent experimental testing of optimized heat sinks was presented for a forced convection 2D Stokes flow thermofluid model [28] and a 2D air-cooled heat sink model considering conduction and side surface convection [34]. Castro et al. [35] use the topology optimization method to design enclosures in which radiation is the dominant heat transfer mechanism. For a more detailed description of the literature on thermal and thermofluid topology optimization, the reader is referred to a very recently published review paper on this topic [36]. An extensive body of literature deals with various other optimization approaches applied to heat exchanger design and a detailed presentation of these works lies outside the scope of this study. Therefore, the readers are referred to an exemplary work presenting stochastic optimization of air-cooled heat exchangers where the heat transfer is modeled based on correlations [37] and a review paper on CFD applications in heat exchanger design [38] that also covers literature on optimization in this context.

The 2D models that explicitly consider heat transfer in the fluid [17–30] have in common that the fluid flow is within the plane of the design domain. The model presented in this study presents for the first time an approach where a flow is modeled that is perpendicular to the design domain; this is considered one of the main contributions of this work. One specific benefit of the presented model could be the combination with existing works on thermofluid topology optimization modeling the fluid flow within the design domain plane; hence creating a cross-flow heat exchanger optimization model with explicit modeling of both fluids flowing perpendicular to each other. Another advantage of assuming a fluid dynamically fully developed flow is the simplification of the Navier-Stokes equation to a linear partial differential equation (PDE). This circumvents problems with the increasing nonlinearity of the Navier-Stokes equations that accompany increasing Reynolds number and have so far limited thermofluid density-based topology optimization to Stokes flow or laminar flow with relatively low Reynolds numbers except for [27] that ignore the temperature distribution in the solid. Thus, the approach presented here extends the range of applicability of thermofluid topology optimization since it can be applied to problems with arbitrary Reynolds numbers within in the laminar flow regime provided that one can assume fully developed flow. Extension of the approach to even larger Reynolds number may be possible with a suitable turbulence closure model. Moreover, the above mentioned works, except for [13,15,16] which do not explicitly model the fluid flow, treat rather academic heat sink or heat exchanger problems whereas the optimizations in this study are conducted for specific “real world” operating conditions associated with dry-cooled power plant condensers, even though the optimization is accomplished using some simplifying assumptions. However, it should be noted that the presented modeling approach is by no means limited to the specific application considered in this work but can be applied to arbitrary thermofluid systems in which the fully developed flow assumption is reasonable.

Parametric studies are conducted using the optimization model in order to analyze the influence of the effective conductivity of the filled polymer composite as well as the unit cell height used in the heat exchanger structure on different measures of the system performance. This analysis of the topology optimization results on a system level in the context of a specific heat exchanger design problem is considered another main contribution of this work as current literature on thermofluid topology optimization focuses mainly on the topology optimization implementation and exemplary generation of a few optimized designs. The topology optimized designs generated in this work are compared to a simple, optimized slot channel model in order to demonstrate the improvement in performance afforded by the topology optimization. This study provides some confirmation of the usefulness of topology optimization to exploit the design freedom that is provided by additive manufacturing techniques.

2. Heat exchanger model

2.1. General design and modeling of the heat exchanger

The heat exchanger is configured in a cross-flow arrangement which is typical for gas-to-liquid heat exchangers. This is done to create a relatively large frontal area and short air-channels, which allows a large surface area for heat transfer while keeping the air-side pressure drop low. This arrangement is also convenient for headering the two fluids. The heat exchanger macrostructure consists of a large array of unit cells; the macrostructure and a single unit cell are schematically depicted in Fig. 1. Within the unit cell, there is substantial design freedom relative to the geometry of the air-side heat transfer surface and the use of heat transfer enhancing structures. However, walls with a certain minimal thickness separating the water and air flows are needed to ensure a waterproof design and vertical walls between the unit cells are required periodically in order to ensure mechanical stability of the macrostructure.

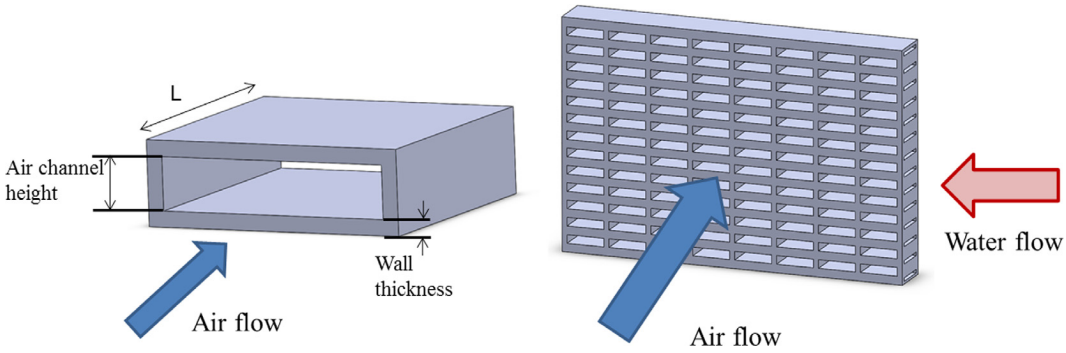

Fig. 1. Air-side heat exchanger unit cell (left) shown without heat transfer enhancing structures and macrostructure (right) consisting of a large array of unit cells.

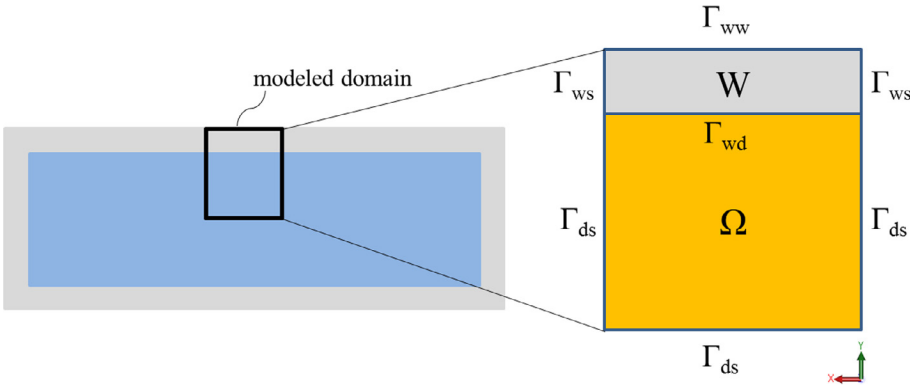

Fig. 2. Illustration of frontal view on heat exchanger unit cell (left) and zoomed in view on the domain modeled for the optimization (right). The domains Ω (design domain) and W (wall) are indicated and the definition of the different domain boundaries Γ_{ij} is given.

Since topology optimization is computationally expensive due to the requirement of typically hundreds of design iterations before convergence to an optimized design, the unit cell is modeled in 2D to reduce the computational complexity. This modeling approach considers the unit cell cross section perpendicular to the air flow, as shown in Fig. 2. Colored in grey are the required walls separating the water and air flow at the top and bottom of the unit cell as well as the required side walls of the unit cell. Within the blue inner area, the distribution of material can be freely chosen in order to shape the air channels using heat transfer enhancing structures. To further reduce the computational resources required, only a part of the unit cell's cross section is modeled, as shown in Fig. 2. By exploiting symmetry on the left, right, and bottom of the modeled domain, a periodic design representative of the entire unit cell can be obtained by optimizing a relatively small fraction of the cell. Only minor adjustments to this periodic design would need to be made in the regions directly adjacent to the side walls of the unit cell to avoid channeling. It should be noted that the water-side heat-transfer is not modeled explicitly in this approach and instead a water temperature is prescribed as the boundary condition on the outer side of the wall. This further reduces the model's computational demand and is justified by the fact that the water-side heat transfer coefficient is typically quite large and the dominant thermal resistance in a dry-cooled condenser will be on the air-side.

2.2. Governing equations

Throughout this study, an incompressible, steady-state, and laminar flow is assumed within the heat exchanger. It is important to note that the laminar flow assumption depends on the geometry of the generated heat exchanger designs. Therefore, this assumption needs to be verified once the optimized designs are generated which is discussed in chapter 4 and Appendix A.

2.2.1. Fluid dynamics modeling

The Navier-Stokes equation for an incompressible, pressure-driven, fully developed internal flow in the z-direction is given by:

$$\mu\left(\frac{\partial^2 w}{\partial x^2}+\frac{\partial^2 w}{\partial y^2}\right)=\frac{dp}{dz} \tag{1}$$

where w is the fluid velocity in z-direction, μ the dynamic viscosity of the fluid, and $\frac{dp}{dz}$ the pressure gradient in z-direction. In fluid flow topology optimization a Brinkman friction term, which is the force exerted on a fluid flowing through an ideal porous medium, is used to penalize fluid flow through the solid area, as described in [4]. The Brinkman friction term is defined as:

$$F(\gamma,w)=\bar{\alpha}(1-\gamma)w \tag{2}$$

where γ is the design variable and $\bar{\alpha}$ is the maximum inverse permeability. The value of $\bar{\alpha}$ should be chosen to be sufficiently large to ensure that the flow through solid area is negligibly small; however, if $\bar{\alpha}$ is set to a value that is too high then numerical instability can occur. Usually, a convex interpolation is used to interpret the Brinkman friction term as presented in [4]. However, since simplified linear Navier-Stokes equations are analyzed in this work, a linear interpolation was found to yield good results. Introducing Eq. (2) into Eq. (1), replacing the axial pressure gradient by the pressure

drop over the heat exchanger and considering air as the fluid provides:

$$\mu_{air}\left(\frac{\partial^2 w}{\partial x^2}+\frac{\partial^2 w}{\partial y^2}\right)=\frac{\Delta p_{HEX}}{L}-\tilde{\alpha}(1-\gamma)w \quad \text{in } \Omega \tag{3}$$

where Δp_{HEX} is the air-side pressure drop over the heat exchanger unit cell, which is set to a fixed value during the optimization, and L is the length of the unit cell in the flow direction. A no-slip condition is assumed at the wall and symmetry is imposed on the remaining boundaries[1] as stated above. This leads to the following set of boundary conditions:

$$\begin{aligned} &w=0 \quad \text{on } \Gamma_{wd} \\ &-\boldsymbol{n}\cdot(-\nabla w)=0 \quad \text{on } \Gamma_{ds} \end{aligned} \tag{4}$$

where $\mathbf{n}$ is the normal vector to the boundary, ∇ is the nabla operator, and Γ_{ij} are the respective domain boundaries, as specified in Fig. 2.

2.2.2. Heat transfer modeling

The two dimensional conductive heat transport in the solid filled polymer can be described as follows:

$$k_s\left(\frac{\partial^2 T_s}{\partial x^2}+\frac{\partial^2 T_s}{\partial y^2}\right)=0 \tag{5}$$

where T_s is the temperature of the solid and k_s is the thermal conductivity of the material. The thermal convection-diffusion equation for thermally and fluid dynamically fully developed internal laminar flow in the z-direction [39] is given by

$$w\rho_f c_f\frac{\partial T_f}{\partial z}=k_f\frac{\partial^2 T_f}{\partial z^2}+k_f\left(\frac{\partial^2 T_f}{\partial x^2}+\frac{\partial^2 T_f}{\partial y^2}\right)+\dot{g}_v''' \tag{6}$$

where T_f is the fluid temperature, ρ_f is the fluid density, c_f is the specific heat capacity of the fluid, k_f is the conductivity of the fluid, and $\dot{g}_v'''$ is the volumetric rate of viscous dissipation. Neglecting axial conduction and viscous dissipation and expressing the axial temperature gradient as the ratio of the air-side temperature increase to the heat exchanger length leads to the following equation

$$w\rho_f c_f\frac{\Delta T_{HEX}}{L}=k_f\left(\frac{\partial^2 T_f}{\partial x^2}+\frac{\partial^2 T_f}{\partial y^2}\right) \tag{7}$$

where ΔT_{HEX} is the air-side temperature increase across the heat exchanger unit cell, which is set to a fixed value during the optimization. To allow for a unified representation of the heat transport in the polymer, Eq. (5), and air, Eq. (7), an interpolation for the thermal conductivity is introduced:

$$\begin{aligned} \gamma w\rho_{air}c_{air}\frac{\Delta T_{HEX}}{L}=k(\gamma)\left(\frac{\partial^2 T}{\partial x^2}+\frac{\partial^2 T}{\partial y^2}\right) \quad &\text{where } \boldsymbol{\gamma} \\ =0 \text{ in } W \quad &\text{and } \boldsymbol{\gamma}\in[0,1] \text{ in } \Omega \end{aligned} \tag{8}$$

The axial energy transport term on the left hand side of Eq. (8) can be interpreted as a velocity dependent heat sink. Through this term, the thermal modeling is coupled to the fluid velocity field which implicitly depends on the density field of the design variable. The convective energy transport term is additionally penalized with a linear interpolation as presented in [22,26]. This ensures that the small amount of fluid leakage through the solid domain, which is to some degree unavoidable in density-based topology optimization, does not interact with the thermal modeling. To interpolate between the thermal conductivity of solid and fluid during the optimization process, a RAMP-style function [40] as presented in [30] is used which leads to:

$$k(\gamma)=k_{air}\frac{\gamma\left(\frac{k_{polymer}}{k_{air}}(1+b_k)-1\right)+1}{\frac{k_{polymer}}{k_{air}}(1+b_k\gamma)} \tag{9}$$

where k_{air} and $k_{polymer}$ are the respective thermal conductivities of air and polymer and b_k is a parameter that controls the convexity of the interpolation. Since the water-side heat transfer is not explicitly modeled, the temperature at the outer boundary of the wall is set to a fixed value. The remaining boundaries are modeled with a symmetry condition as described in Section 2.1. This leads to the following set of boundary conditions for Eq. (8):

$$\begin{aligned} &T=T_{water} \quad &&\text{on } \Gamma_{ww} \\ &-\boldsymbol{n}\cdot(-\nabla T)=0 \quad &&\text{on } \Gamma_{ds} \text{ and } \Gamma_{ws} \end{aligned} \tag{10}$$

where T_{water} is the prescribed water temperature.

Thus, the thermofluid problem solved in this work is stated by Eqs. (3) and (8) as well as the respective boundary conditions given by Eqs. (4) and (10). As mentioned above, the thermal problem is coupled to the fluid velocity field through the convective energy transport term in z-direction. However, it should be noted that there is no back coupling from the thermal to the fluid model since constant material properties are used throughout the optimization.

3. Topology optimization implementation

3.1. Optimization problem

The optimization objective is to maximize the heat exchanger's conductance UA which is the inverse of the total thermal resistance between water and air. UA is defined in the context of the 2D model according to

$$UA=\frac{\dot{q}}{(T_{water}-T_{air,bulk})}=\frac{\dot{q}}{\Delta T} \tag{11}$$

where $\dot{q}$ is the heat transfer rate from the water to the air within the modeled domain, T_{water} is the prescribed boundary condition, and $T_{air,\ bulk}$ is the velocity weighted average air temperature (i.e., the bulk temperature). As described in chapter 2, the water-side heat transfer is not explicitly modeled in this work, which is why T_{water} is used as an approximation for $T_{water,\ bulk}$ in Eq. (11). Thus, the water-side heat transfer resistance is not considered in the optimization which is justified by the fact that the air-side heat transfer resistance is dominant in air-to-water heat exchangers. Moreover, the water-side geometry is not changing during the optimization as the design domain is only on the air side of the heat exchanger. $T_{air,\ bulk}$ can be computed by

$$T_{air,bulk}=\frac{1}{A_{\Omega,fl}w_{average,fl}}\int_{\Omega}\gamma w T\,d\Omega \tag{12}$$

where $A_{\Omega,fl}$ is the flow area of the design domain and $w_{average,\ fl}$ is the flow area averaged air velocity within the design domain. However, maximizing the conductance can lead to local optima associated with situations where the temperature difference in the denominator of Eq. (11) approaches 0. Therefore, a slightly modified optimization formulation is used in which the heat transfer rate is maximized and the difference between the air bulk temperature and the water temperature is set as a constraint. This approach corresponds to maximizing the conductance for a fixed value of air-to-water temperature difference, ΔT, and leads to the following optimization problem:

[1] Both symmetry boundary conditions (BCs) and periodic BCs could be used for this design problem. However, the constraints on the design are less restrictive when using a symmetry BC. E.g., for a very narrow modeled domain only half of a fin (fluid at left side of modeled domain and solid on right side) could be formed using a symmetry BC which would not be possible using a periodic BC. Due to this added flexibility, symmetry BCs where chosen in this work.

$$\begin{aligned} &\max \quad \dot{q}(\boldsymbol{\gamma}, \boldsymbol{s}) \\ &s.t. \quad (T_{water} - T_{air,bulk}(\boldsymbol{\gamma}, \boldsymbol{s})) < (T_{water} - T^{*}_{air,bulk}) \\ &\qquad r(\boldsymbol{\gamma}, \boldsymbol{s}) = 0 \\ &\qquad 0 \leqslant \gamma_i \leqslant 1 \quad for\ i = 1, \ldots, n_d \end{aligned} \tag{13}$$

where $\boldsymbol{\gamma}$ is the vector of the design variables, $\boldsymbol{s}$ is the vector of the state variables of the multiphysics problem described in Section 2, $T^{*}_{air,bulk}$ is the prescribed bulk air temperature, $r(\boldsymbol{\gamma}, \boldsymbol{s})$ is the residual of the finite element formulation of the multiphysics problem, and n_d is the number of design variables.

3.2. Density filtering and projection

Density filtering is used to solve issues with ill-posedness of thermofluid topology optimization problems [41]. In this work, a Helmholtz-type PDE-filter [42] is applied since it can be easily implemented in the utilized FEM software and allows for computationally efficient filtering. The filter PDE is stated by:

$$-r^2_{filter}\left(\frac{\partial^2 \tilde{\gamma}}{\partial x^2} + \frac{\partial^2 \tilde{\gamma}}{\partial y^2}\right) + \tilde{\gamma} = \gamma \tag{14}$$

where r_{filter} is the filter parameter and $\tilde{\gamma}$ is the filtered design variable. A symmetry boundary condition is applied at the left, right, and bottom of the design domain and $\tilde{\gamma}$ is prescribed to be solid at the boundary to the wall. This leads to the following set of boundary conditions:

$$\begin{aligned} &-\boldsymbol{n} \cdot (-\nabla \tilde{\gamma}) = 0 \quad &&\text{on } \Gamma_{ds} \\ &\tilde{\gamma} = 0 &&\text{on } \Gamma_{wd} \end{aligned} \tag{15}$$

The density filter inherently introduces a band of intermediate densities between the solid and fluid region which is physically not meaningful and adds an artificial heat transfer resistance between the solid and fluid domains in this specific modeling approach[2]. To obtain a sharper solid-fluid transition, a smooth Heaviside projection [43] is used, which is given by:

$$\bar{\tilde{\gamma}} = \frac{\tanh(\beta\eta) + \tanh(\beta(\tilde{\gamma} - \eta)}{\tanh(\beta\eta) + \tanh(\beta(1 - \eta))} \tag{16}$$

where $\bar{\tilde{\gamma}}$ is the projected design variable, η is a threshold parameter and β determines the steepness of the projection. The reader should note that $\bar{\tilde{\gamma}}$ becomes the physically meaningful design variable in the interpolations stated in Section 2.

3.3. Computational implementation

The topology optimization model is implemented in the commercial simulation software COMSOL Multiphysics [44]. COMSOL's *heat transfer module* is used to solve the energy equation (Eq. (8)). The Navier-Stokes equation and filter PDE are implemented in COMSOL's *coefficient form PDE interface* in which the PDEs can be stated as indicated in Eq. (3) and Eq. (14). A first order discretization is used to solve the state equations of the thermofluid problem and the filter PDE. The optimization is conducted with COMSOL's *optimization module* using the globally convergent version of the Method of Moving Asymptotes (GCMMA) [45] where the constraint for the air bulk temperature is implemented as a global constraint. The adjoint problem is solved automatically in COMSOL to obtain the sensitivities for the objective and constraint functional. COMSOL is interfaced with MATLAB to allow for automatized parameter changes during the optimization. Changing parameter values during the optimization is necessary because a continuation approach [41] is applied to the convexity parameter b_k of the conductivity interpolation. This is done to ensure a relatively convex optimization problem at the beginning of the process and to increasingly penalize the thermal conductivity of intermediate densities. The sequence of values $b_k = \{0, 2, 10, 10\}$ is used for all optimizations presented in this study. During the ramping of b_k, the projection steepness parameter β is held constant at a value of 5 in order to reduce the grey band between solid and fluid areas. After ramping b_k, β is set to a value of 10 to obtain final designs with a sharp solid-fluid transition which correspond to the sequence of values $\beta = \{5, 5, 5, 10\}$. The projection threshold parameter η is held at a constant value of 0.5 throughout the optimization and an initial design variable density of 0.5 is set in the entire design domain in all optimizations. Other model parameters that are kept constant during the optimization are stated in Table 1.

[2] The artificial heat transfer resistance occurs because the fluid flow is already penalized and close to zero in the grey area due to a relatively high maximum friction force. At the same time is the thermal conductivity in the grey area significantly lower than pure filled polymer; especially with increasing convexity of the conductivity interpolation.

4. Results

The topology optimization model is used to generate optimized structures for different unit cell heights and effective composite conductivities. Air channel heights between 2 mm and 14 mm are considered, where the thickness of the wall between the air and the water channel is held constant at 1.5 mm. The thermal conductivities are varied between 0.1 W/(m K), which is in the range of unfilled plastics such as acrylonitrile butadiene styrene (ABS), and 300 W/(m K) which is on the order of metallic heat sink materials. The parameters defining the operating conditions of the heat exchanger are selected to be similar to actual operating conditions anticipated in dry-cooled power plant condensers [46]. Heat capacity, thermal conductivity, viscosity, and density of air are considered constant in this work and are evaluated at a temperature of 45 °C. The values of the constant, unless explicitly stated otherwise, heat exchanger operating parameters and thermophysical properties of air used in the parameter studies are given in Table 2.

An optimized design and the corresponding fluid velocity field and temperature distribution is shown in Fig. 3 for an air channel height of 6 mm and thermal conductivity of 5 W/(m K) in order to illustrate a typical result. The optimized design consists of three fins connected to the wall separating water and air flow. The three fins are roughly of the same size and have smaller secondary

Table 1
Model and optimization parameter values.

Parameter	Value
$\bar{\alpha}$	2×10^5 Pa s m^{-2}
Design domain width	4 mm
Maximum element size in mesh	3.25×10^{-5} m
r_{filter}	4.3×10^{-5} m

Table 2
Values of the constant, unless explicitly stated otherwise, heat exchanger operating parameters and thermophysical properties of air used in this work.

Operating parameter	Value	Thermophysical properties of air	Value
$\frac{\Delta p_{HEX}}{L}$	4000 (Pa/m)	c_{air}	1006 (J/(kg K))
$\frac{\Delta T_{HEX}}{L}$	1200 (K/m)	k_{air}	0.027 (W/(m K))
T_{water}	70 (°C)	μ_{air}	1.941×10^{-5} (Pa s)
$T^{*}_{air,\ bulk}$	45 (°C)	ρ_{air}	1.112 (kg/m^3)

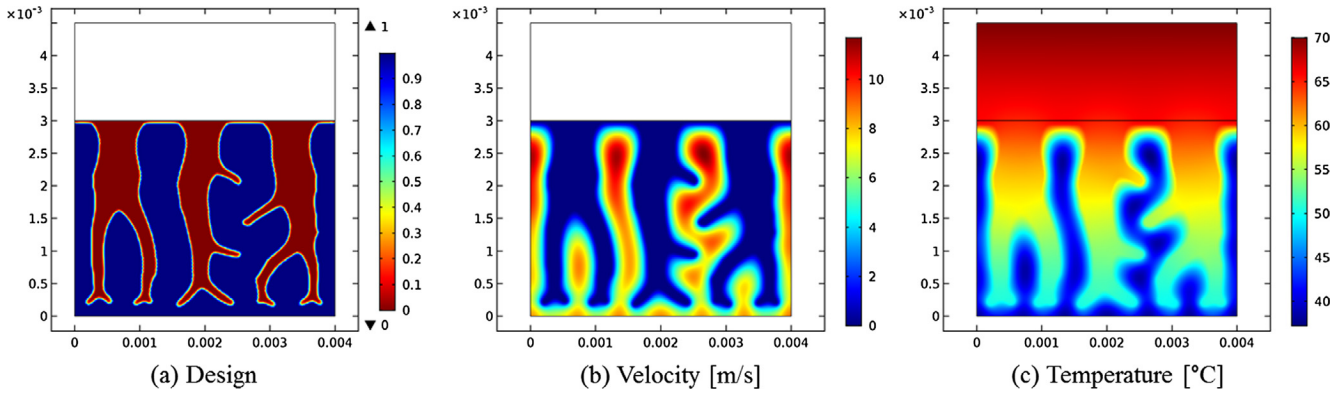

Fig. 3. Optimized design for 5 W/(m K) and an air channel height of 6 mm. (a) shows the geometry (red is solid, blue is air, and white is the wall between the air and water passages, which is not part of the optimization design domain) as well as the corresponding velocity field (b) and temperature distribution (c). (For interpretation of the references to color in this figure legend, the reader is referred to the web version of this article.)

branches. The fluid channels tend to become slightly larger closer to the top boundary of the design domain. Consequently, the fluid flow is increasing closer to the hot water boundary which allows heat transfer between the (not explicitly modeled) water and air flow to take place with minimal heat transfer resistance in the polymer. The temperature distribution shown in Fig. 3(c) shows the cool air channels in the design and the warmer heat exchanger material. It can be seen how the dendritic structures conduct the heat relatively evenly in all parts of the design domain. The Reynolds number of the air flow in the optimized design is of interest to verify the laminar flow assumption that was used for the thermofluid modeling. However, this Reynolds number cannot be determined in a straightforward way due to the unconventional channel geometry. For this reason, it is estimated based on a pipe flow and flow between parallel plates assumption. The computation of the air flow Reynolds number of the design from Fig. 3 and another exemplary design is described in Appendix A. The Reynolds number of the design from Fig. 3 is 271 assuming pipe flow and 318 assuming flow between parallel plates which is significantly lower than the critical Reynolds number for laminar-turbulent transition which is for pipe flow reported to be between 2040 [47] and 2100 [48] and for flow between parallel plates slightly below 2300 [48]. Similar results with the estimated air flow Reynolds number being well below the critical Reynolds number are obtained for all designs generated in this work with maximal values of around 650 which justifies the laminar flow assumption that was used in the presented modeling approach. Nevertheless, thermofluid topology optimization including a turbulence closure model could result in different optimized geometries than the designs obtained in this study due to the differences in the heat transfer modeling. For example broader air channels in which turbulent flow occurs might be formed. However, including a turbulence closure model in the topology optimization and benchmarking the results against those of the current study will be left for future works as research on turbulent flow topology optimization is still in its very beginnings.

4.1. Parametric study of system performance

Optimized designs for a composite thermal conductivity of 5 W/(m K) with several different air channel/unit cell heights are depicted in Fig. 4. For an air channel height of 2 mm, four small fins

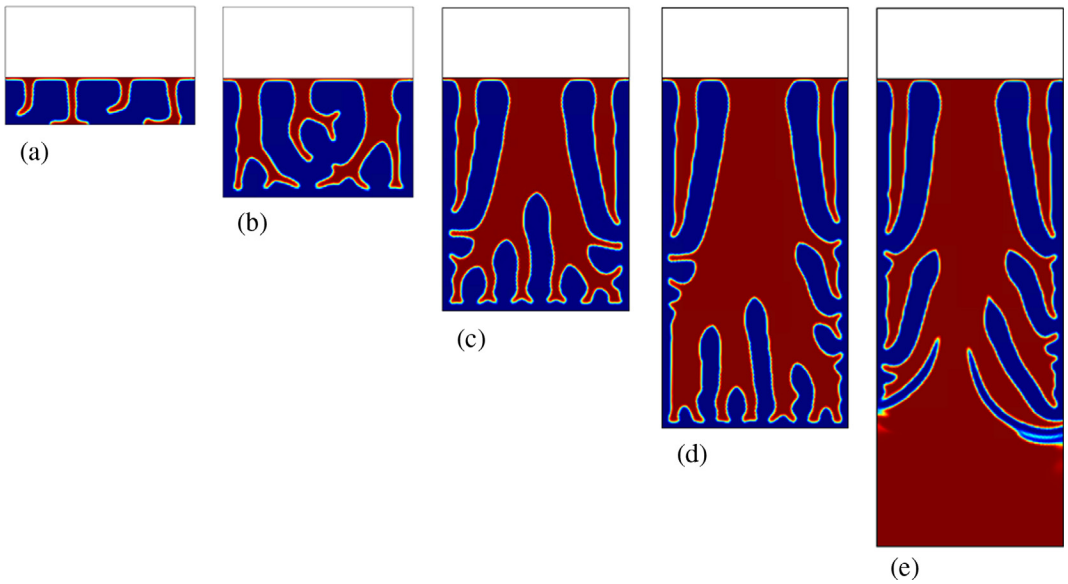

Fig. 4. Optimized designs for 5 W/(m K). The air channel height is taking the values of 2 mm (a), 5 mm (b), 10 mm (c), 15 mm (d), and 20 mm (e). Red corresponds to polymer and blue to fluid passages. White is the unit cell wall (polymer) which is not part of the design domain. (For interpretation of the references to color in this figure legend, the reader is referred to the web version of this article.)

evolve whereas for the larger air channel heights three fins evolve in each case. Again, the dendritic shape of the fins and slightly larger fluid channels close to the top boundary of the design domain can be seen. Furthermore, it is interesting to note that in the 20 mm air channel height design, the fluid channels are placed only in the top 75% of the design domain and the bottom region is filled entirely with solid. This shows that the composite conductivity is, for this unit cell height, not high enough to make it attractive to distribute the air channels within the entire design domain. There is wasted polymer material placed in the regions far from the water just to prevent air from flowing so far from the water. Slight grey areas occur in this design at the transition from the dendritic fin to the polymer material without fluid channels.

Fig. 5 shows optimized designs for an air channel height of 6 mm for different effective composite thermal conductivities. Design (a), which corresponds to a conductivity of 0.1 W/(m K), has only one horizontal fluid channel directly next to the wall that separates the air flow from the water. The rest of the design domain is filled with polymer to prevent air flow. Design (b) consists of four fins: two smaller fins in the middle and a larger dendritic one at each side of the design domain. The larger fins are quite thick in order to prevent too much air flow at the bottom of the design domain. The designs (c), (d), and (e) consist each of three fins with secondary branches from the main fin. An increasingly finer feature size can be observed with increasing thermal conductivity. The fact that smaller feature sizes become increasingly advantageous leads to grey regions in the secondary branches in design (f) and to a smaller extent in design (e). However, a black and white design could be obtained using a finer mesh and smaller filter radius allowing a finer design resolution or by implementing robust topology optimization approaches [43,49] that guarantee a minimum length scale in the solid which is left for future works. Similar findings regarding the design's conductivity dependence are obtained for other unit cell heights. It is interesting to observe that design (c) is nearly symmetric with respect to a vertical line in the center of the modeled domain which is not enforced by the boundary conditions that only enforce symmetry with respect to the left, right, and bottom boundary of the design domain. This additional symmetry line in the center of the modeled domain seems to be advantageous from a design point of view in this specific case; however, the other optimized designs are asymmetric with regards to this line.

As stated above, the operating parameters pressure drop over heat exchanger flow length and temperature drop over heat exchanger flow length are selected to be consistent with a specific application in this work. Still, it is interesting to examine the effect of varying these parameters on the optimization and the resulting optimized designs. Fig. 6 shows the effect of either halving or doubling one of these operating parameters while keeping the other parameter at the reference value for a constant air channel height of 4 mm and effective composite conductivity of 5 W/(m K). Design (a) is optimized for the reference values of pressure drop and temperature increase over the heat exchanger which are used throughout this work and stated in Table 2. Two larger fins at the side of the design domain with secondary and small tertiary branches and a smaller fin in the middle of the design domain are generated. Halving either the pressure drop or the temperature increase over the heat exchanger results in relatively similar designs ((b) and (c)). However, the air channels between the fins are slightly larger in these designs compared to design (a) which is due to the lower pressure drop (b) or lower axial temperature increase (c). Doubling either the pressure drop or temperature increase over the heat exchanger results in designs with four main fins ((d) and (e)) and significantly smaller air channels between the fins as in the other cases. This is due to the fact that more heat can be transported away by the air flow per unit flow area due to higher flow velocities (increased pressure drop) or higher axial temperature gradient (increased temperature increase over the heat exchanger).

4.1.1. Parameter studies

In the subsequent section, the influence of the composite thermal conductivity on the optimal air channel height will be dis-

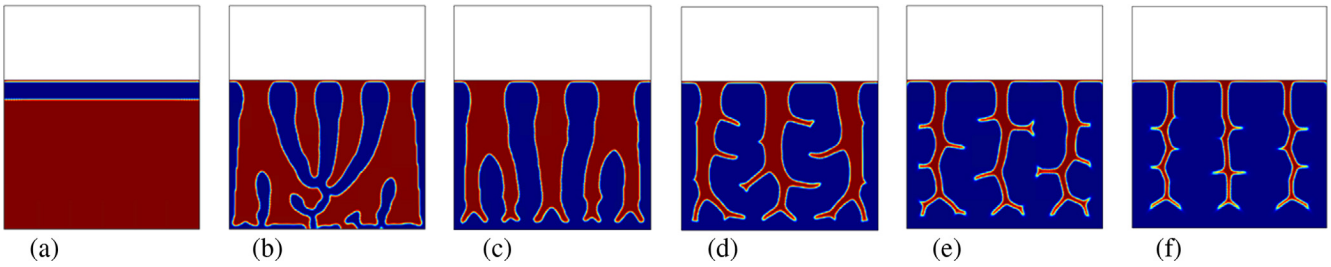

Fig. 5. Optimized designs for different conductivities for an air channel height of 6 mm. The polymer composite conductivity is increasing from left to right taking the values of 0.1 (a), 0.5 (b), 2 (c), 10 (d), 50 (e), and 300 (f) W/(m K) respectively. Red corresponds to polymer and blue to fluid. White is the unit cell wall (polymer) which is not part of the optimizable domain. (For interpretation of the references to color in this figure legend, the reader is referred to the web version of this article.)

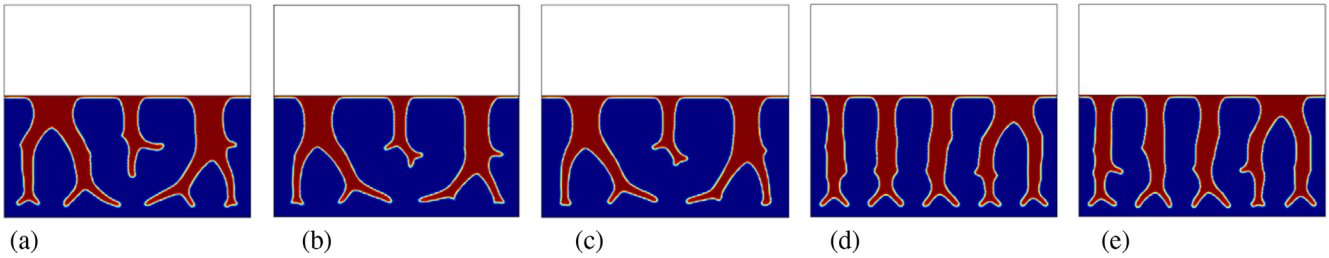

Fig. 6. Influence of the operating parameters pressure drop over heat exchanger flow length and temperature increase over heat exchanger flow length on the optimized designs for 5 W/(m K) and an air channel height of 4 mm. Design (a) corresponds to the standard case of a 4000 Pa/m pressure drop and 1200 K/m temperature increase. In the other cases the pressure drop and temperature increase take the values of 2000 Pa/m and 1200 K/m (b), 4000 Pa/m and 600 K/m (c), 8000 Pa/m and 1200 K/m (d), 4000 Pa/m and 2400 K/m (e), respectively.

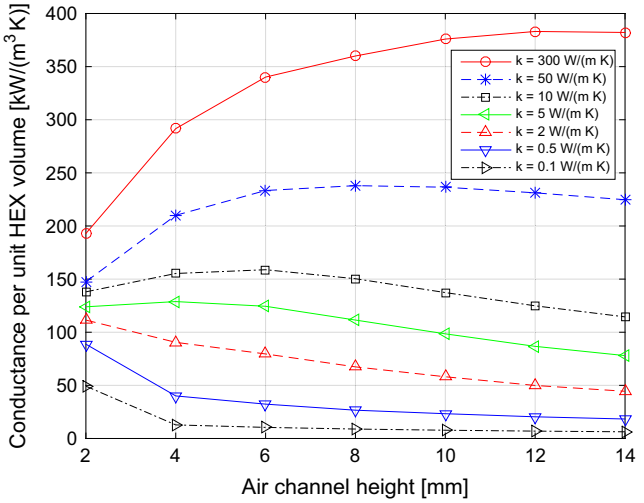

Fig. 7. Heat exchanger's conductance per heat exchanger unit volume plotted against the air channel height for different thermal conductivities of the polymer.

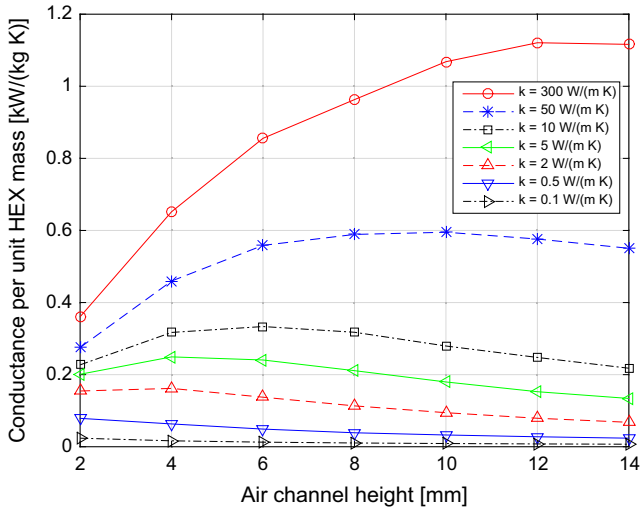

Fig. 8. Heat exchanger's conductance per unit heat exchanger mass plotted against the air channel height for different values of thermal conductivity.

cussed for different measures of the heat exchanger's performance. Fig. 7 shows the heat exchanger conductance per volume (total volume of polymer composite, air, and water channels) plotted against the air channel height for different polymer thermal conductivities. To calculate the heat exchanger volume, a constant water channel height of 1 mm is assumed to exist between the unit cells. It can be seen that both the effective thermal conductivity and the air channel height have a significant influence on the system performance. The optimal air channel height increases with increasing thermal conductivity. For conductivities of 0.1, 0.5, and 2 W/(m K), a 2 mm air channel height (the smallest value considered) is found optimal. The optimal air channel height increases to approximately 4, 6, 8, and 12 mm for the thermal conductivities of 5, 10, 50, and 300 W/(m K) respectively. The increase of the optimal air channel height with increasing thermal conductivity can be explained by the reduced thermal resistance in the heat transfer enhancing structures that can therefore productively extend further away from the water cooled wall.

Another metric that can be used to examine the heat exchanger performance is conductance per unit heat exchanger mass since the amount of polymer needed significantly influences in additive manufacturing the manufacturing time and cost. The heat exchanger conductance per polymer mass vs. the air channel height is depicted for different thermal conductivities in Fig. 8. For these studies, a composite density of 1000 kg/m^3 which corresponds to the density of ABS is assumed. It should be noted that this is an approximation for higher effective thermal conductivities of the composite as the conductive filler density can differ from the polymer density. The optimal air channel heights, when considering conductance per mass, behave similarly to conductance per volume. For conductivities of 0.1 and 0.5 W/(m K) an air channel height of 2 mm is optimal. For conductivities of 2, 5, 10, 50, and 300 W/(m K) the optimal heights are approximately 4, 4, 6, 10, and 12 mm, respectively. For lower thermal conductivities, the dependence of conductance per mass on the air channel height is less pronounced than when considering conductance per unit volume.

The effect of varying the operating parameters pressure drop over heat exchanger flow length and temperature increase over heat exchanger flow length on the heat exchanger conductance per volume and conductance per mass for a constant effective composite conductivity of 5 W/(m K) and constant air channel height of 4 mm is shown in Table 3. Halving the pressure drop results in a decrease of heat exchanger conductance per volume and conductance per mass of around 18% compared to the reference case. Doubling the pressure drop yields a conductance per volume increase of 25% and a conductance per mass increase of 20%. Varying the temperature increase over the heat exchanger has a similar effect, halving the axial temperature increase results in a conductance decrease of 23% on a per volume basis and 19% on a per mass basis. Doubling the axial temperature increase yields a conductance per volume increase of 30% and a conductance per mass increase of 25%.

It should be kept in mind that the presented studies are conducted using the assumption of a 2D fully developed flow to obtain a stable and not too computationally expensive optimization model as stated in chapter 2. Even though assuming a fully developed flow is a mature technique in thermofluid modeling, an experimental validation of the designs' performance would be beneficial to quantify the influence of the assumptions that are made. This is left for a future work as this paper focuses on the theoretical aspects of the fully developed flow model and its application to the presented specific heat exchanger design problem. To assess the influence of the mesh resolution on the modeling of the thermofluid problem, three representative optimized designs (0.5 W/(m K) and 2 mm air channel height; 5 W/(m K) and 4 mm; 10 W/(m K) and 6 mm) are re-evaluated using a maximum element size in the mesh of 50% and 25% of the value used throughout this work which is stated in Table 1. The maximum deviation between the meshes in terms of predicted conductance per volume is found to be 2.17% and 2.16% in terms of conductance per mass for the case 0.5 W/(m K) and air channel height of 2 mm. The maximum conductance deviation between the meshes for the other two optimized designs is around 1.5% both on a per volume basis and per mass basis. This suggests that the accuracy of the computations can still be slightly increased when using a finer mesh than the one used in this work which is chosen as a trade-off between accuracy and computational demand. Nevertheless, the uncertainty due to the mesh resolution seems acceptable compared to the uncertainty that is associated with the assumptions on which the presented optimization model relies.

To provide some validation of the fluid-side fully developed flow thermofluid model used in this work, a comparison to analytical solutions for fully developed flow Nusselt numbers in simple geometries, i.e. flow between parallel plates and flow in a circular pipe, is conducted. The 2D thermofluid problem in these geome-

Table 3
Effect of varying the operating parameters pressure drop over heat exchanger flow length and temperature increase over heat exchanger flow length on the heat exchanger conductance per unit volume and conductance per unit mass. The effective composite conductivity is 5 W/(m K) and the air channel height is 4 mm.

Design in Fig. 6	$\frac{\Delta p_{HEX}}{L}$ (Pa/m)	$\frac{\Delta T_{HEX}}{L}$ (Pa/m)	*Conductance/unit HEX volume* (kW/(m^3 K))	*Conductance/unit HEX mass* (kW/(kg K))
(a)	4000	1200	128.9	0.249
(b)	2000	1200	103.4	0.208
(c)	4000	600	99.7	0.201
(d)	8000	1200	160.8	0.299
(e)	4000	2400	167.4	0.312

tries is modeled with a prescribed temperature at the boundary to the, in this validation model not explicitly considered, solid, while constraining the difference between the prescribed temperature at the solid boundary (T_{wall}) and the air bulk temperature. This corresponds to a 3D problem with in axial (or z) direction constant heat flux from the wall to the duct as the mass flow in the duct, the fluid properties, the duct geometry, and the driving force for the heat transfer ($T_{wall}(z)$-$T_{air,bulk}(z)$) are constant along the axial coordinate. Hence, the Nusselt number obtained from this numerical model can be compared to analytical solutions for fully developed flow Nusselt numbers for constant heat flux from the wall in axial direction which are stated in [50] for flow between parallel plates and in [51] for flow in a circular tube. A relative deviation between numerical model and correlations of around 0.1% was found for the same maximum element size in the mesh as used in the optimization model which confirms the validity of the utilized modeling approach. The calculations done for this comparison are presented in Appendix B. It is interesting to note that the deviation of numerical validation model and analytical solution in terms of Nusselt number is lower than the deviation of conductance in the optimized geometries when refining the mesh. This is probably due to the simpler geometries used in the validation model compared to the topology optimized geometries.

It is important to state that the chosen modeling approach provides a conservative estimate for the heat transfer in the geometries as the local heat transfer in the entrance region of a duct or similar geometry is always higher than in the fully developed region [52]. A comparison to experiments done within the ARPA-E ARID project [53] within which also this study was conducted indicates an increased performance of the topology optimized geometries compared to conventionally designed 3D-printed heat exchangers in terms of conductance per heat exchanger mass. However, it is not possible to reliably quantify this improvement based on the currently available experimental data. For this reason, it was decided to consistently compare the topology optimized designs to designs generated by a simpler optimization model in this study. This benchmarking to size optimized slot channel designs that represent a simpler but established heat exchanger geometry is presented in the following section.

4.2. Comparison to size optimized slot channel model

To validate the improved performance of the topology optimized designs, the results are compared to a model that is mathematically similar to the topology optimization model but consists of an arbitrary number of vertical slots for air flow. The slot width of this model is adjusted to maximize the conductance per unit heat exchanger volume for a given number of slots subject to the same bulk temperature constraint that is applied to the topology optimization model. The width of the modeled domain is 4 mm as it is when conducting the topology optimization. This allows for a fair comparison between a conventional, simple heat exchanger geometry that is optimized in a straightforward way and the less intuitive and more complex structures that are obtained using the topology optimization approach. Symmetry boundary conditions are applied at the left, right, and bottom boundaries of the modeled domain as in the topology optimization model to obtain results which are representative of the entire unit cell. The slot width is optimized for air channel heights of 2, 5, and 10 mm and thermal conductivities of 0.5, 2, 5, 10, 50, and 300 W/(m K). For each conductivity, an optimal number of slots and optimal air channel height is determined. For example, for a conductivity of 5 W/(m K), 5 fins with a width of 0.24 mm and an air channel height of 5 mm are found to be optimal. The resulting design and the corresponding air velocity and temperature distribution are depicted in Fig. 9. A summary of the optimal air channel height, optimal number of fins, and optimal fin width for all thermal conductivities is given in Table 4.

The slot channel designs with optimal number of slots, slot width and air channel height for the respective conductivity are shown in Fig. 10. The topology optimized designs for each thermal conductivity at the optimal height (out of 2, 5, and 10 mm air chan-

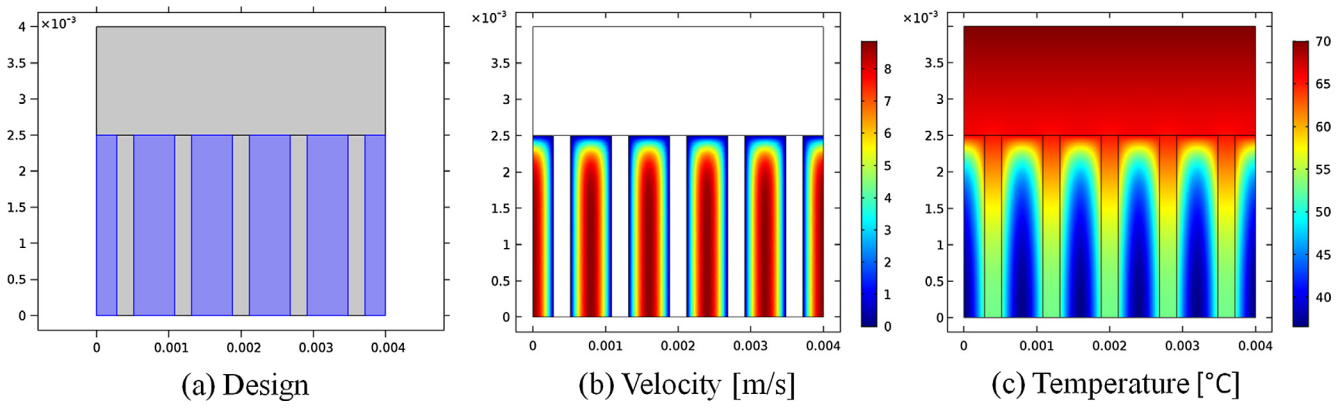

Fig. 9. The optimal slot channel model design for 5 W/(m K) (a) where the fins are depicted in grey and fluid slots are shown in blue as well as the corresponding velocity field (b) and temperature distribution (c). (For interpretation of the references to color in this figure legend, the reader is referred to the web version of this article.)

Table 4
Optimal air channel height, optimal number of fins, and optimal fin width for the analyzed composite effective thermal conductivities in the slot channel model.

Conductivity (W/(m K))	Optimal air channel height (mm)	Optimal number of fins	Optimal fin width (mm)
0.5	2	5	0.31
2	2	5	0.17
5	5	5	0.25
10	5	5	0.19
50	10	6	0.08
300	10	6	0.03

nel heights) are added to the figure to allow a qualitative comparison between the two optimization techniques. It can be seen that the optimal air channel height is approximately the same in the slot channel and topology optimization model for the same conductivity: for conductivities of 0.5 and 2 W/(m K) a 2 mm height is optimal, for 5 and 10 W/(m K) a 5 mm height is optimal, and for 50 and 300 W/(m K) a 10 mm air channel height yields the highest conductance. The largest optimal fin width is 0.31 mm for 0.5 W/(m K) and the smallest optimal fin width is 0.03 mm and occurs for 300 W/(m K). Five fins are optimal for all slot channel model designs except for conductivities of 50 and 300 W/(m K) where six fins are optimal. Compared to this, fewer, thicker fins are generated by the topology optimization: Four fins occur for 0.5 and 2 W/(m K), three fins for 5 and 10 W/(m K) and 2 fins for 50 and 300 W/(m K). These fins, however, have finer secondary and in some cases tertiary branches that conduct the heat evenly in the air flow; hence allowing for a lower total number of fins. These thicker fins with finer branches are more suited for additive manufacturing, if necessary with minor post processing after the topology optimization, than the very thin fins in the slot channel model that occur for higher composite conductivities. As for the topology optimized designs, the air flow Reynolds number in the slot channel model is determined to verify the laminar flow assumption. This is straightforward since the flow in each slot can be considered as a flow between two parallel plates. The highest Reynolds number is obtained for the design in Fig. 10(f). The determined value of 257 is significantly below the critical Reynolds number for laminar-turbulent transition in flow between two parallel plates that is reported to be slightly below 2300 [48] which justifies the laminar flow assumption used in the slot channel model. The air bulk velocity and characteristic length used to determine the Reynolds number of the slot channel design from Fig. 10(f) are stated in Table A.1 in Appendix A.

To assess the manufacturability of the topology optimization and slot channel model designs in a more quantitative way, the aspect ratio, i.e. length over width of fins, is compared. However, defining the aspect ratio in the topology optimized designs is not straightforward since the fins in the same design have different lengths and widths and the fin width might vary along the length. Moreover, there are thinner secondary branches which are each characterized by their own aspect ratio. To still be able to approximatively assess the aspect ratio in the topology optimized designs, the following procedure was conducted: For each fin in the respective design, the aspect ratio is determined for the main structure of the fin using an average width. Shorter secondary branches are not considered since they are much shorter than the main fin, thus having a lower aspect ratio even though their width is smaller than the width of the main branch. Then for each design the maximum aspect ratio among all fins is chosen as representative aspect ratio for the entire design. This aspect ratio of the topology optimized designs and the aspect ratio of the slot channel plotted against the effective composite conductivity are shown in Fig. 11. In addition, the aspect ratio of a slot channel model having a minimum fin width constraint of 0.3 mm is also shown in the figure for comparison.

It can be seen that the aspect ratio of the topology optimized designs and the fin width constraint slot channel model are on the same order for all thermal conductivities. The aspect ratio of the unconstrained slot channel model is higher than the value associated with the other two models for all thermal conductivities

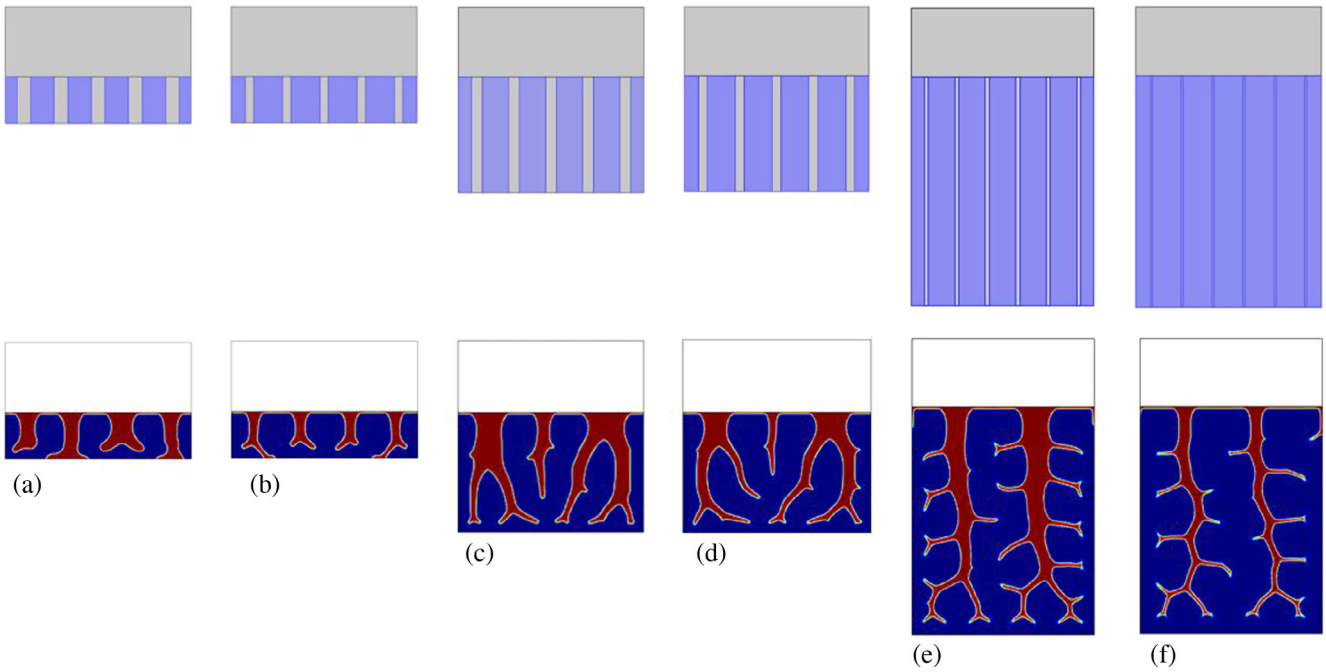

Fig. 10. Slot channel designs with optimal air channel height, number of fins, and fin width for thermal conductivities of 0.5 (a), 2 (b), 5 (c), 10 (d), 50 (e), and 300 (f) W/(m K). Fins and wall to water are depicted in grey and air channels in blue. The topology optimized designs for the same respective conductivity are added for comparison below where red corresponds to fins and blue to void passages for air flow. (For interpretation of the references to color in this figure legend, the reader is referred to the web version of this article.)

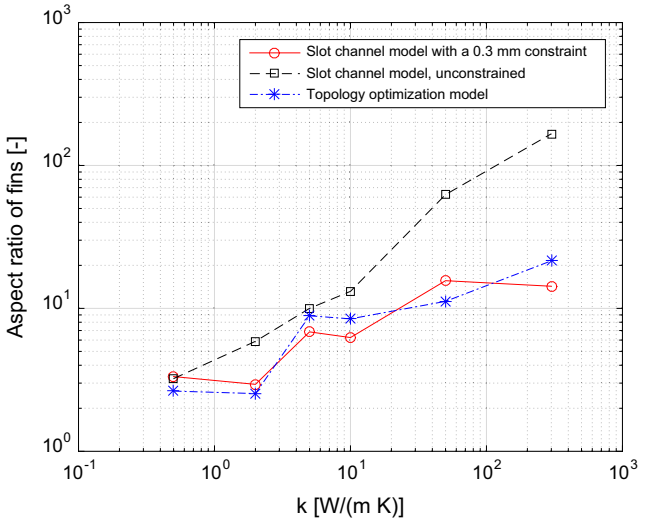

Fig. 11. Aspect ratio defined as fin length over fin width of the slot channel model with a 0.3 mm minimum fin width constraint, of the unconstrained slot channel model, and of the topology optimization model.

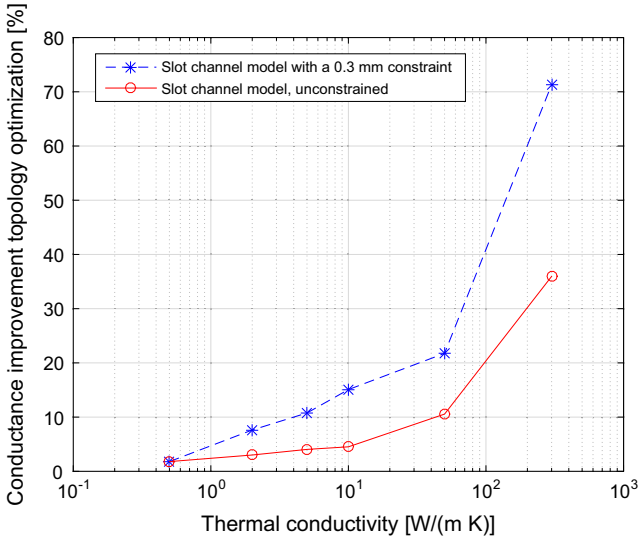

Fig. 12. Improvement of conductance per unit heat exchanger volume achieved with the topology optimized designs compared to the simple slot channel model plotted against the composite effective thermal conductivity. The cases of no minimum fin width in the slot channel model and a 0.3 mm minimum fin width in the slot channel model are considered.

except for 0.5 W/(m K). However, for lower conductivities the aspect ratio is still in the same order of magnitude – only for 50 and 300 W/(m K) is the aspect ratio of the unconstrained model much larger (around one order of magnitude higher) than for the constrained slot channel and the topology optimization model. Observing the trend of the aspect ratio with increasing conductivity, one can see that the aspect ratio of the unconstrained slot channel model is continuously increasing with increasing conductivity. Compared to this, the constrained slot channel model and the topology optimization model also show a general trend of increasing aspect ratio with increasing conductivity but have relatively similar aspect ratios for the same optimal air channel heights and significant increase of the aspect ratio when the optimal air channel height changes from 2 to 5 mm and from 5 to 10 mm which corresponds to conductivities changing from 2 to 5 W/(m K) and from 10 to 50 W/(m K).

A quantitative comparison between the performance of the slot channel designs and the topology optimized designs can be seen in Fig. 12, where the improvement in conductance per unit heat exchanger volume of the topology optimized designs compared to the slot channel model is plotted against the composite effective thermal conductivity. This comparison is conducted with no constraint on the fin width and a 0.3 mm minimum fin width constraint in the slot channel model. However, it should be noted that comparing the width constrained slot channel model to the topology optimized model is not entirely fair since no robust length scale control is implemented in the topology optimization even though the density filter mostly prevents very thin features from appearing in the final designs as can be seen in Fig. 10. Fig. 12 shows that for 0.5 W/(m K) the constrained and unconstrained slot channel model yield the same result relative to the topology optimization model since the optimal fin width in the slot channel model is 0.31 mm. For higher conductivities, the optimal fin width in the slot channel model is below 0.3 mm which is why the topology optimization improvement compared to the constrained case is higher than compared to the unconstrained case. The conductance improvement achieved by topology optimization is increasing with increasing effective thermal conductivity: a 1.7% conductance increase is observed for 0.5 W/(m K) and a 71% increase with the fin width constraint and 36% increase without fin width constraint occurs for 300 W/(m K). The increasing conductance improvement achieved with the topology optimized designs with increasing conductivity is due to the fact that designs with secondary branches from the main fins which differ more from the standard slot channel designs become more advantageous at higher conductivities than at low conductivities. Summarizing, it can be stated that the topology optimized designs afford a significant conductance improvement over the constraint slot channel model for roughly the same fin aspect ratio which can be used as a measure to estimate the printability of the designs. Also, relative to the unconstrained slot channel model the topology optimized designs show improved conductance. However, this is achieved with significantly lower aspect ratios of the fins; hence with topology optimized designs that are easier to print. Both observations in terms of conductance improvement and printability are most dramatic for higher effective polymer conductivities (above 10 W/(m K)).

5. Conclusions

This work addresses the air-side surface optimization of dry-cooled power plant condensers that are additively manufactured with polymers containing thermally conducting metal filaments. To tackle this design challenge, a fully developed flow thermofluid topology optimization model is developed and used to maximize the heat exchanger conductance. The fully developed flow assumption leads to simplified linear Navier-Stokes equations yielding a thermofluid topology optimization model that is stable for arbitrary Reynolds numbers within the laminar flow regime. This work demonstrates the applicability of thermofluid topology optimization to a real world heat exchanger design problem by using appropriate simplifications. Reynolds numbers of the flow in the optimized geometries are determined and the computed values are found to be significantly below the values of critical Reynolds numbers for laminar-turbulent transition reported in the literature. This confirms the laminar flow assumption that was used for the thermofluid modeling. Parametric studies are conducted to analyze the interplay of the heat exchanger material thermal conductivity and unit cell height on the system performance. The thermal conductivity is varied over three orders of magnitude and the influence of doubling and halving the pressure drop and

temperature increase over the heat exchanger is studied using the same set of optimization parameters which demonstrates the robustness of the developed topology optimization model.

Apart from the obvious finding that higher filled polymer conductivities significantly increase the heat exchanger conductance, it is also shown that the optimal unit cell height increases with increasing conductivity of the filled polymer. Furthermore, it was found that the optimized designs tend to require finer feature sizes with increasing polymer conductivities. Hence, research should be conducted regarding the cost-efficient printability of small features in parallel with the development of 3D printable filled polymers with higher thermal conductivities. In future works, robust topology optimization approaches could be used to tailor the optimized designs to manufacturing constraints regarding the minimum printable solid feature size of the additive manufacturing process. To verify the developed topology optimization methodology, a comparison to a model using simple, slot-type air channels is conducted. It is shown that in terms of conductance per unit heat exchanger volume, the topology optimized designs outperform the simple slot geometry by up to 71% when the minimum fin width of the slot geometry is set to 0.3 mm and by up to 36% when an unconstrained slot geometry is considered. The conductance improvement through topology optimization increases with increasing effective polymer conductivity. To assess the printability of topology optimized designs and the slot channel designs, the fin aspect ratio, i.e. length over width of fins, is compared. The topology optimized designs show similar aspect ratios as the constraint slot-type geometry and, especially for higher conductivities, smaller aspect ratios, hence a better printability, than the unconstrained slot channel designs.

This work demonstrates that a significant performance improvement over simpler heat exchanger geometries can be obtained with the presented 2D optimization approach, thus confirming the usefulness of topology optimization to exploit the design freedom that additive manufacturing techniques provide. An experimental quantification of the impact of the fully developed flow assumption on the performance of the heat exchanger is planned in a future work; nevertheless, it should be noted that assuming a fully developed flow is a mature technique in thermofluid modeling. An interesting and industrially relevant extension of the presented modeling approach is the combination with existing thermofluid topology optimization models to allow for cross-flow heat exchanger design with explicit modeling of both fluids flowing perpendicular to each other.

Acknowledgements

This work was supported by the TOpTEn project sponsored through the Sapere Aude Program of the Danish Council for Independent Research (DFF – 4005-00320). Moreover, Jan Haertel would like to thank the Direktør, Professor H.I. Hannovers Legat for a travel grant that partially supported the research stay at UW-Madison during which the presented work was conducted. Professor Nellis gratefully acknowledges support from the Department of Energy Advanced Research Projects Agency through their ARID program (DE-FOA-0001197). Furthermore, the authors wish to thank Sanford Klein and Kurt Engelbrecht for the helpful discussions with regard to this work.

Appendix A. Computation of Reynolds number in optimized designs

It is customary to use the area mean velocity to characterize internal flow [47,48] which is given by:

$$w_{mean} = \frac{1}{A_c}\int_{A_c} w\, dA_c \tag{A.1}$$

where A_c is the cross-sectional area of the flow. With w_{mean} as characteristic velocity and using the thermophysical properties of air stated in Table 2, the Reynolds number in the optimized designs can be computed as follows:

$$Re = \frac{\rho_{air} w_{mean} L_{char}}{\mu_{air}} \tag{A.2}$$

where L_{char} is a characteristic length of the geometry. However, it is not straightforward to define a characteristic length for the unconventional geometries of the topology optimized designs. Therefore, parts of the whole design are considered representatively for the entire design and compared to standard geometries for which the critical Reynolds number for laminar-turbulent transition is reported in the literature, i.e. pipe flow and flow between two parallel plates. This procedure is shown in the following exemplarily for the designs shown in Fig. A1: In both designs the largest flow area is identified that can be approximated by a rectangular duct

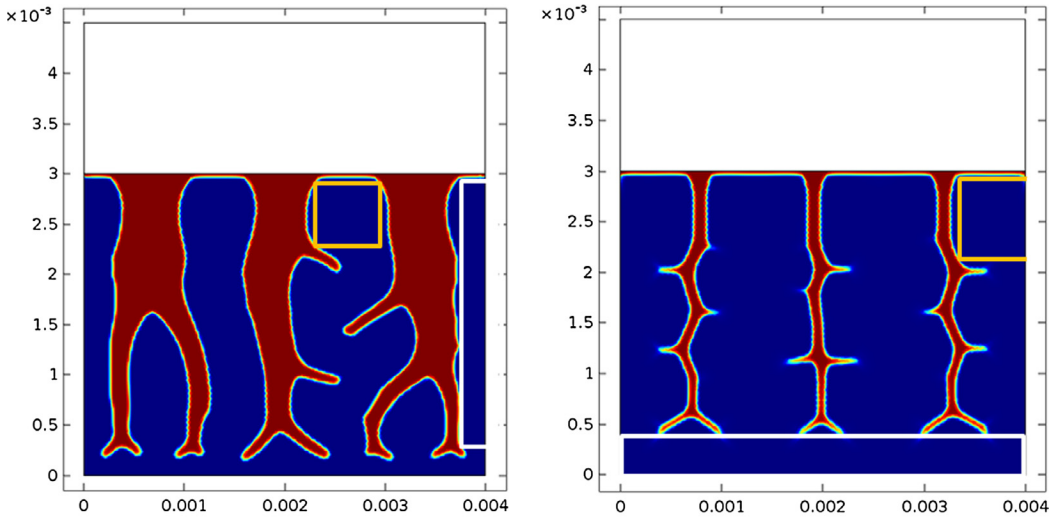

Fig. A1. Topology optimized designs from Figs. 3 and 5(f). The areas in which the Reynolds number was determined assuming a pipe flow (orange) and flow between two parallel plates (white) are indicated. (For interpretation of the references to color in this figure legend, the reader is referred to the web version of this article.)

Table A.1
Approximation of the Reynolds number in the topology optimized designs shown in Fig. A1 and the slot channel design from Fig. 9(f). The flow conditions in the topology optimized designs are approximated assuming a pipe flow in a rectangular duct as well as a flow between two parallel plates.

Design	*Considered flow*	w_{mean} (m/s)	L_{char} (mm)	*Re* (–)
Topology optimized design	Pipe flow	7.4	0.64	271
From Fig. 3	Parallel plates	7.6	0.73	318
Topology optimized design	Pipe flow	10.7	1.00	614
From Fig. 5(f)	Parallel plates	14.0	0.80	643
Slot channel design from Fig. 10(f)	Parallel plates	7.0	0.64	257

(marked as orange rectangle) or by a flow between parallel plates (marked in white). It should be noted that the area used for the pipe flow approximation in Fig. 5(f) is mirrored over the right boundary of the modeled domain which is not shown in the depiction. Similarly, the area used for the flow between two plates approximation is mirrored over the right boundary of the modeled domain in the design from Fig. 3 and mirrored over the bottom part of the modeled domain in the design from Fig. 5(f). The characteristic length for the pipe flow approximation is the hydraulic diameter given by:

$$D_h = \frac{2ab}{a+b} \tag{A.3}$$

where a and b are the respective length of the rectangle's sides. The characteristic length for the flow between two plates is the distance between the plates, i.e. two times the distance from the vertical white line to the right symmetry boundary in the design from Fig. 3 and two times the distance from the horizontal white line to the bottom boundary in the design from Fig. 5(f). The mean velocity in the marked areas is computed in COMSOL according to Eq. (A.1). The results of these calculations are summarized in Table A.1. Table A.1. contains additionally the mean velocity, characteristic length (i.e. width of air slots), and Reynolds number of the slot channel design from Fig. 10(f).

Appendix B. Nusselt number comparison to analytical solution

For two simple geometries, i.e. flow between two parallel plates and flow in a circular pipe, the Nusselt number obtained from the numerical validation model is compared to the respective analytical solution. As stated in Section 4.1, only the heat transfer problem in the air flow is modeled for these geometries and the temperature at the boundary to the solid is set to the fixed value T_{wall}. The same values as in the optimization model are used for the pressure drop and temperature increase over the heat exchanger (stated in Table 2) and T_{wall} is set to the same value as T_{water} in the optimization model since the heat conduction in the solid is not considered in the validation model. The characteristic dimension of the validation model, i.e. the distance between the parallel plates or the diameter of the circular pipe, is adjusted so that $T_{air,bulk}$ takes the value of $T^{*}_{air,bulk}$ stated in Table 2. Thus, the problem modeled in the validation model is similar to the original problem of the optimization model.

The mean Nusselt number in the context of the considered internal flow problems is defined as:

$$Nu = \frac{hD_h}{k_{air}} \tag{B.1}$$

where h is the average heat transfer coefficient within the duct. The hydraulic diameter D_h corresponds to the pipe diameter in the case of flow inside a circular pipe and two times the distance of the plates in the case of flow between parallel plates. The heat transfer coefficient in the 2D fully developed flow model is given by

$$h = \frac{\dot{q}}{per(T_{wall} - T_{air,bulk})} \tag{B.2}$$

Table B.1
Thermally and fluid dynamically fully developed flow Nusselt number and hydraulic diameter for flow between parallel plates and flow in a circular pipe obtained from the numerical model and from analytical solutions in the literature.

Geometry	*Case*	D_h (mm)	*Nu* (–)
Flow between parallel plates	Analytical solution [50]	–	8.235
	Numerical model	0.67	8.241
Flow in a circular pipe	Analytical solution [51]	–	4.364
	Numerical model	0.52	4.367

where *per* is the perimeter of the duct which can be computed by:

$$\begin{aligned} per &= 2\ height\ L \quad \text{for flow between parallel plates} \\ per &= \pi\ D\ L \quad \text{for flow in a circular pipe} \end{aligned} \tag{B.3}$$

where D is the pipe diameter and *height* is the modeled height of the flow between parallel plates problem. The height modeled is set to 4 mm and symmetry conditions are applied at the top and bottom of the modeled domain to represent an infinitely extended duct perpendicular to the air flow direction. Using the above equations, the Nusselt number in the numerical fully developed flow model can be computed. This Nusselt number is equivalent to the Nusselt number in a fully developed flow problem with constant wall heat flux in the axial direction, for which analytical solutions exist, as described in Section 4.1. The comparison between the Nusselt number computed using the numerical model according to Eq. (B.1) and the respective analytical solution for the case of flow between parallel plates [50] and flow in a circular pipe [51] is shown in Table B.1.

References

[1] J. Macknick, R. Newmark, G. Heath, K.C. Hallett, A review of operational water consumption and withdrawal factors for electricity generating technologies. Technical report NREL/TP-6A20-50900, National Renewable Energy Laboratory, 2011. http://dx.doi.org/10.2172/1219149.

[2] C. T'Joen, Y. Park, Q. Wang, A. Sommers, X. Han, A. Jacobi, A review on polymer heat exchangers for HVAC&R applications, Int. J. Refrig. 32 (5) (2009) 763–779, http://dx.doi.org/10.1016/j.ijrefrig.2008.11.008.

[3] M.P. Bendsøe, O. Sigmund, Topology Optimization: Theory, Methods, and Applications, Springer Science & Business Media, 2013, http://dx.doi.org/10.1007/978-3-662-05086-6.

[4] T. Borrvall, J. Petersson, Topology optimization of fluids in Stokes flow, Int. J. Numer. Meth. Fluids 41 (1) (2003) 77–107, http://dx.doi.org/10.1002/fld.426.

[5] J.S. Jensen, O. Sigmund, Topology optimization for nano-photonics, Laser Photonics Rev. 5 (2) (2011) 308–321, http://dx.doi.org/10.1002/lpor.201000014.

[6] Q. Li, G.P. Steven, Y.M. Xie, O.M. Querin, Evolutionary topology optimization for temperature reduction of heat conducting fields, Int. J. Heat Mass Transf. 47 (23) (2004) 5071–5083, http://dx.doi.org/10.1016/j.ijheatmasstransfer.2004.06.010.

[7] A. Gersborg-Hansen, M.P. Bendsøe, O. Sigmund, Topology optimization of heat conduction problems using the finite volume method, Struct. Multidiscip. Optimiz. 31 (4) (2006) 251–259, http://dx.doi.org/10.1007/s00158-005-0584-3.

[8] O. Sigmund, Design of multiphysics actuators using topology optimization–Part I: One-material structures, Comput. Methods Appl. Mech. Eng. 190 (49) (2001) 6577–6604, http://dx.doi.org/10.1016/s0045-7825(01)00251-1.

[9] L. Yin, G.K. Ananthasuresh, A novel topology design scheme for the multiphysics problems of electro-thermally actuated compliant micromechanisms, Sens. Actuators A: Phys. 97 (2002) 599–609, http://dx.doi.org/10.1007/978-3-642-59497-7_59.

[10] T.E. Bruns, Topology optimization of convection-dominated, steady-state heat transfer problems, Int. J. Heat Mass Transf. 50 (15) (2007) 2859–2873, http://dx.doi.org/10.1016/j.ijheatmasstransfer.2007.01.039.
[11] S.H. Ahn, S. Cho, Level set–based topological shape optimization of heat conduction problems considering design-dependent convection boundary, Num. Heat Transfer, Part B: Fund. 58 (5) (2010) 304–322, http://dx.doi.org/10.1080/10407790.2010.522869.
[12] A. Iga, S. Nishiwaki, K. Izui, M. Yoshimura, Topology optimization for thermal conductors considering design-dependent effects, including heat conduction and convection, Int. J. Heat Mass Transf. 52 (11) (2009) 2721–2732, http://dx.doi.org/10.1016/j.ijheatmasstransfer.2008.12.013.
[13] M. Zhou, J. Alexandersen, O. Sigmund, C.B. Pedersen, Industrial application of topology optimization for combined conductive and convective heat transfer problems, Struct. Multidiscip. Optimiz. 1–16 (2016), http://dx.doi.org/10.1007/s00158-016-1433-2.
[14] P. Coffin, K. Maute, Level set topology optimization of cooling and heating devices using a simplified convection model, Struct. Multidiscip. Optimiz. 53 (5) (2016) 985–1003, http://dx.doi.org/10.1007/s00158-015-1343-8.
[15] S. Soprani, J.H.K. Haertel, K. Engelbrecht, B.S. Lazarov, O. Sigmund, Topology optimization of an actively cooled electronics section for downhole tools, in: Proceedings. Comsol Conference 2015, 2015.
[16] S. Soprani, J.H.K. Haertel, B.S. Lazarov, O. Sigmund, K. Engelbrecht, A design approach for integrating thermoelectric devices using topology optimization, Appl. Energy 176 (2016) 49–64, http://dx.doi.org/10.1016/j.apenergy.2016.05.024.
[17] E.M. Dede, Multiphysics topology optimization of heat transfer and fluid flow systems, in: Proceedings of the COMSOL Users Conference, 2009.
[18] G.H. Yoon, Topological design of heat dissipating structure with forced convective heat transfer, J. Mech. Sci. Technol. 24 (6) (2010) 1225–1233, http://dx.doi.org/10.1007/s12206-010-0328-1.
[19] E.M. Dede, Optimization and design of a multipass branching microchannel heat sink for electronics cooling, J. Electron. Packag. 134 (4) (2012) 041001, http://dx.doi.org/10.1115/1.4007159.
[20] T. Van Oevelen, M. Baelmans, Numerical topology optimization of heat sinks, in: Proceedings of the 15th International Heat Transfer Conference, Begell House Publishers, 2014, pp. 10–15, http://dx.doi.org/10.1615/ihtc15.opt.009168.
[21] G. Marck, M. Nemer, J.L. Harion, Topology optimization of heat and mass transfer problems: laminar flow, Num. Heat Transfer, Part B: Fund. 63 (6) (2013) 508–539, http://dx.doi.org/10.1080/10407790.2013.772001.
[22] T. Matsumori, T. Kondoh, A. Kawamoto, T. Nomura, Topology optimization for fluid–thermal interaction problems under constant input power, Struct. Multidiscip. Optimiz. 47 (4) (2013) 571–581, http://dx.doi.org/10.1007/s00158-013-0887-8.
[23] K. Yaji, T. Yamada, M. Yoshino, T. Matsumoto, K. Izui, S. Nishiwaki, Topology optimization in thermal-fluid flow using the lattice Boltzmann method, J. Comput. Phys. 307 (2016) 355–377, http://dx.doi.org/10.1016/j.jcp.2015.12.008.
[24] C. McConnell, G. Pingen, Multi-Layer, Pseudo 3D thermal topology optimization of heat sinks, ASME 2012 International Mechanical Engineering Congress and Exposition, Houston, Texas, USA, 2012. http://dx.doi.org/10.1115/imece2012-93093.
[25] J.H.K. Haertel, K. Engelbrecht, B.S. Lazarov, O. Sigmund, Topology optimization of thermal heat sinks, in: Proceedings. Comsol Conference 2015, 2015.
[26] X. Qian, E.M. Dede, Topology optimization of a coupled thermal-fluid system under a tangential thermal gradient constraint, Struct. Multidiscip. Optimiz. 1–21 (2015), http://dx.doi.org/10.1007/s00158-016-1421-6.
[27] E.A. Kontoleontos, E.M. Papoutsis-Kiachagias, A.S. Zymaris, D.I. Papadimitriou, K.C. Giannakoglou, Adjoint-based constrained topology optimization for viscous flows, including heat transfer, Eng. Optimiz. 45 (8) (2013) 941–961, http://dx.doi.org/10.1080/0305215x.2012.717074.
[28] A.A. Koga, E.C.C. Lopes, H.F.V. Nova, C.R. de Lima, E.C.N. Silva, Development of heat sink device by using topology optimization, Int. J. Heat Mass Transf. 64 (2013) 759–772, http://dx.doi.org/10.1016/j.ijheatmasstransfer.2013.05.007.
[29] K. Yaji, T. Yamada, S. Kubo, K. Izui, S. Nishiwaki, A topology optimization method for a coupled thermal–fluid problem using level set boundary expressions, Int. J. Heat Mass Transf. 81 (2015) 878–888, http://dx.doi.org/10.1016/j.ijheatmasstransfer.2014.11.005.
[30] J. Alexandersen, N. Aage, C.S. Andreasen, O. Sigmund, Topology optimisation for natural convection problems, Int. J. Numer. Meth. Fluids 76 (10) (2014) 699–721, http://dx.doi.org/10.1002/fld.3954.
[31] J. Alexandersen, Topology optimisation of passive coolers for light-emitting diode lamps, in: 11th World Congress of Structural and Multidisciplinary Optimisation, 2015.
[32] J. Alexandersen, O. Sigmund, N. Aage, Large scale three-dimensional topology optimisation of heat sinks cooled by natural convection, Int. J. Heat Mass Transf. 100 (2016) 876–891, http://dx.doi.org/10.1016/j.ijheatmasstransfer.2016.05.013.
[33] P. Coffin, K. Maute, A level-set method for steady-state and transient natural convection problems, Struct. Multidiscip. Optimiz. 53 (5) (2016) 1047–1067, http://dx.doi.org/10.1007/s00158-015-1377-y.
[34] E.M. Dede, S.N. Joshi, F. Zhou, Topology optimization, additive layer manufacturing, and experimental testing of an air-cooled heat sink, J. Mech. Des. 137 (11) (2015) 111403, http://dx.doi.org/10.1115/1.4030989.
[35] D.A. Castro, C.Y. Kiyono, E.C.N. Silva, Design of radiative enclosures by using topology optimization, Int. J. Heat Mass Transf. 88 (2015) 880–890, http://dx.doi.org/10.1016/j.ijheatmasstransfer.2015.04.077.
[36] T. Dbouk, A review about the engineering design of optimal heat transfer systems using topology optimization, Appl. Therm. Eng. 112 (2017) 841–854, http://dx.doi.org/10.1016/j.applthermaleng.2016.10.134.
[37] A.R. Doodman, M. Fesanghary, R. Hosseini, A robust stochastic approach for design optimization of air cooled heat exchangers, Appl. Energy 86 (7) (2009) 1240–1245, http://dx.doi.org/10.1016/j.apenergy.2008.08.021.
[38] M.M.A. Bhutta, N. Hayat, M.H. Bashir, A.R. Khan, K.N. Ahmad, S. Khan, CFD applications in various heat exchangers design: a review, Appl. Therm. Eng. 32 (2012) 1–12, http://dx.doi.org/10.1016/j.applthermaleng.2011.09.001.
[39] G. Nellis, S. Klein, Heat Transfer, Cambridge University Press, New York, 2008, http://dx.doi.org/10.1017/cbo9780511841606.
[40] M. Stolpe, K. Svanberg, An alternative interpolation scheme for minimum compliance topology optimization, Struct. Multidiscip. Optimiz. 22 (2) (2001) 116–124, http://dx.doi.org/10.1007/s001580100129.
[41] O. Sigmund, J. Petersson, Numerical instabilities in topology optimization: a survey on procedures dealing with checkerboards, mesh-dependencies and local minima, Struct. Optimiz. 16 (1) (1998) 68–75, http://dx.doi.org/10.1007/bf01214002.
[42] B.S. Lazarov, O. Sigmund, Filters in topology optimization based on Helmholtz-type differential equations, Int. J. Numer. Meth. Eng. 86 (6) (2011) 765–781, http://dx.doi.org/10.1002/nme.3072.
[43] F. Wang, B.S. Lazarov, O. Sigmund, On projection methods, convergence and robust formulations in topology optimization, Struct. Multidiscip. Optimiz. 43 (6) (2011) 767–784, http://dx.doi.org/10.1007/s00158-010-0602-y.
[44] COMSOL Multiphysics 5.2.
[45] K. Svanberg, A class of globally convergent optimization methods based on conservative convex separable approximations, SIAM J. Optim. 12 (2) (2002) 555–573, http://dx.doi.org/10.1137/s1052623499362822.
[46] R. Felber, G. Nellis, N. Rudolph, Design and modeling of 3D printed air-cooled heat exchangers, in: Proceedings of the 16th International Refrigeration and Air Conditioning Conference at Purdue, 2016.
[47] K. Avila, D. Moxey, A. de Lozar, M. Avila, D. Barkley, B. Hof, The onset of turbulence in pipe flow, Science 333 (6039) (2011) 192–196, http://dx.doi.org/10.1126/science.1203223.
[48] R.W. Hanks, The laminar-turbulent transition for flow in pipes, concentric annuli, and parallel plates, AIChE J. 9 (1) (1963) 45–48, http://dx.doi.org/10.1002/aic.690090110.
[49] B.S. Lazarov, F. Wang, O. Sigmund, Length scale and manufacturability in density-based topology optimization, Arch. Appl. Mech. 86 (1–2) (2016) 189–218, http://dx.doi.org/10.1007/s00419-015-1106-4.
[50] R.D. Cess, E.C. Shaffer, Heat transfer to laminar flow between parallel plates with a prescribed wall heat flux, Appl. Sci. Res., Section A 8 (1) (1959) 339–344, http://dx.doi.org/10.1007/bf00411758.
[51] R. Siegel, E.M. Sparrow, T.M. Hallman, Steady laminar heat transfer in a circular tube with prescribed wall heat flux, Appl. Sci. Res., Section A 7 (5) (1958) 386–392.
[52] T.L. Bergman, F.P. Incropera, D.P. DeWitt, A.S. Lavine, Fundamentals of Heat and Mass Transfer, John Wiley & Sons, 2011.
[53] P.J. Hruska, Exploring Dry Air Cooling Heat Exchanger Technologies and Applications Master thesis, University of Wisconsin, Madison, 2016.

A.4 P4 - Topology Optimization of Thermal Heat Sinks

J. H. K. Haertel, K. Engelbrecht, B. S. Lazarov and O. Sigmund

***Proceedings of the COMSOL Conference 2015*, 2015.**

Topology Optimization of Thermal Heat Sinks

J. H. K. Haertel[1]*, K. Engelbrecht[1], B. S. Lazarov[2] and O. Sigmund[2]
[1] Department of Energy Conversion and Storage, Technical University of Denmark
[2] Department of Mechanical Engineering, Technical University of Denmark
*Corresponding author: Frederiksborgvej 399, Building 779, 4000 Roskilde, Denmark, jhkh@dtu.dk

Abstract: In this paper, topology optimization is applied to optimize the cooling performance of thermal heat sinks. The coupled two-dimensional thermofluid model of a heat sink cooled with forced convection and a density-based topology optimization including density filtering and projection are implemented in COMSOL Multiphysics. The optimization objective is to minimize the heat sink's temperature for a prescribed pressure drop and fixed heat generation. To conduct the optimization, COMSOL's Optimization Module with GCMMA as the optimization method is used. The implementation of this topology optimization approach in COMSOL Multiphysics is described in this paper and results for optimized two-dimensional heat sinks are presented. Furthermore, parameter studies regarding the effect of the prescribed pressure drop of the system on Reynolds number and realized heat sink temperature are presented and discussed.

Keywords: Topology optimization, thermofluid modeling, heat sink, forced convection, PDE filter.

1. Introduction

Topology optimization is becoming increasingly popular as a design method for multiphysics systems in general and thermofluid systems in particular [1,2]. Traditional designs are based either on engineering intuition or on trial and error approaches. In contrast, topology optimization [3] provides a systematic way to account for the complex environment in the design process and therefore can yield unintuitive designs.

The focus of the work is to describe the implementation of the three-field density-based topology optimization model [4] in COMSOL Multiphysics. The three-field model resembles many micro- and nano- scale production processes [5,6] and provides a base for considering manufacturing uncertainties [4] in the optimization.

In density-based topology optimization, the algorithm determines the optimal distribution of a material in a given design domain. In the specific case considered in this paper, solid heat sink material is distributed in order to minimize a selected objective. The rest of the domain is occupied with a cooling fluid. The material distribution is modeled with the help of a density field which takes the value 1 if a point is occupied with fluid and 0 if a point is occupied with solid. In order to utilize gradient-based optimization methods, the material distribution problem is relaxed to take values between zero and one.

Topology optimization of thermofluid systems has been presented for example in [7,8,9,10] for forced convective heat transfer, and in [11] for natural convection problems. In this paper, the topology optimization of heat sinks cooled with forced convection is presented. The heat sink is used to cool a surface with a constant heat production and the pressure drop in the fluid is constrained. The optimization objective is the minimization of the solid plate temperature of the heat sink. This objective combined with the pressure drop constraint yields an interesting optimization problem from an engineering point of view.

The thermofluid modeling is described in section 2 and a brief introduction to the applied topology optimization method including density filtering and projection is given is section 3. Section 4 is concerned with the model and optimization implementation in COMSOL Multiphysics. The optimization results are presented in section 5. Optimized heat sink structures and the corresponding temperature and fluid velocity distributions are depicted as well as parameter studies regarding the cooling effect and the system's Reynolds number dependency of the prescribed pressure drop.

2. Thermofluid Modeling and Governing Equations

In the following sections, the thermofluid modeling of the system is presented. The basic

idea of the 2D modeling of the forced convection heat sink is shown in (Figure 1). Details about the COMSOL Multiphysics implementation of the model are described in section 4.

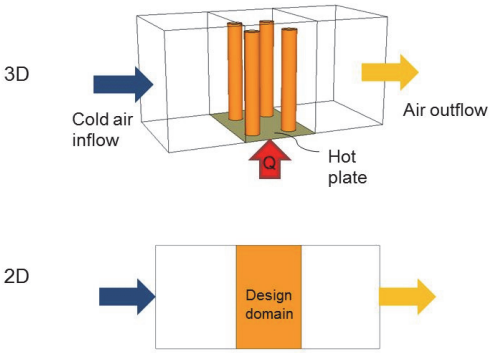

Figure 1. Sketch of the modeled forced convection heat sink in 3D and 2D.

2.1 Fluid Dynamics Modeling

The fluid dynamics are modeled under the assumption of a stationary laminar flow with an incompressible fluid. Furthermore, a 2D fluid flow is assumed which can be motivated by stating that the heat sink fins are much longer than the solid base plate. This leads to the 2D Navier-Stokes equation (1) and continuity equation (2).

$$\rho_{fl} \cdot (\boldsymbol{u} \cdot \nabla)\boldsymbol{u} = -\nabla p + \mu(\nabla^2 \boldsymbol{u}) + \boldsymbol{F} \quad (1)$$

$$\rho_{fl}(\nabla \cdot \boldsymbol{u}) = 0 \quad (2)$$

In the Navier stokes equation a Brinkman friction term (equation (3)) is introduced to penalize fluid velocities inside the solid material in the design domain. Outside the design domain this term is omitted so that the Navier-Stokes equation describes normal fluid flow.

$$\boldsymbol{F}(\gamma) = -\overline{\alpha}\frac{1-\gamma}{1+b_\alpha \gamma}\boldsymbol{u} \quad (3)$$

Where γ is the design variable and the used interpolation is given in [11] which is a slightly modified version of the original interpolation used in [12]. The parameter b_α determines the convexity of the interpolation. In all interpolations used in this work γ=0 corresponds to solid and γ=1 corresponds to fluid.

2.2 Heat Transfer Modeling

The heat transfer in the fluid outside the design domain is modeled according to equation (4). Equation (5) describes the modeling of the heat transfer within the design space which includes an interpolation of the thermal conductivity based on γ. The conductive heat transfer in the solid plate is stated in equation (6).

$$\rho_{fl} c_{fl} \boldsymbol{u} \cdot \nabla T_{fl} - \nabla \cdot (k_{fl} \nabla T_{fl}) = 0 \quad (4)$$

$$\rho_{fl} c_{fl} \boldsymbol{u} \cdot \nabla T_{fl} - \nabla \cdot (\mathrm{k}_{fl} I_k(\gamma) \nabla T_{fl}) = \frac{q_{conv}(\gamma)}{dz_{fl}} \quad (5)$$

$$\nabla \cdot (k_s \nabla T_s) + \frac{q_{prod}}{dz_s} - \frac{q_{conv}(\gamma)}{dz_s} = 0 \quad (6)$$

Where the parameters dz_{fl} and dz_s describe the respective thickness of the fluid layer and the solid plate.

The heat transfer between the design domain layer and the solid plate base layer is modeled by a heat flow having the mathematical structure of convective heat transport with a variable heat transfer coefficient. This allows to model high heat flow into the design domains in case of solid, low heat flow in the case of fluid, and interpolations in between. The case of solid represents high conductive heat flow from the base plate layer into the heat sink's fins and the low heat flow for fluid represents a purely convective heat transfer from the solid base layer into the fluid layer. A similar idea of a thermal base layer and a fluid-thermal design layer with heat transfer in between, however implemented in a different way than in this work, was presented in [13]. The heat transfer term utilized in this model is defined as follows:

$$q_{conv}(\gamma) = \mathrm{h}_{min} I_h(\gamma)\,(\mathrm{T_s} - \mathrm{T_{fl}}) \quad (7)$$

The interpolation function for the thermal conductivity and the heat transfer is a RAMP-style function as used in [11] and originally presented in [14]. The formula is stated in equation (8).

$$\mathrm{I}_i(\gamma) = \frac{\gamma(C_i(1+b_i)-1)+1}{C_i(1+b_i\gamma)} \tag{8}$$

$$C_k = \frac{k_{fl}}{k_s} \tag{9}$$

$$C_h = \frac{h_{min}}{h_{max}} \tag{10}$$

For both thermal conductivity and heat transfer interpolations respective parameters b_k and b_h determine the convexity of the interpolation function in equation (8). The parameter C_i in equation (8) is defined by equation (9) for the conductivity interpolation and by equation (10) for the heat transfer interpolation.

3. Topology Optimization

3.1 Problem Formulation

The considered optimization objective is to minimize the average temperature of the solid plate with heat production which depends implicitly on the design variable field $\boldsymbol{\gamma}$ and the system's state variables $\boldsymbol{s}$. Thus, the topology optimization problem can be defined in the following way:

$$\begin{aligned} &\text{min.:} && T_{s,average}(\boldsymbol{\gamma}, \boldsymbol{s}) \\ &\text{s.t.:} && \boldsymbol{r}(\boldsymbol{\gamma}, \boldsymbol{s}) = \mathbf{0} \\ & && 0 \leq \gamma_i \leq 1 \quad \text{i=1,…,n} \end{aligned} \tag{11}$$

Where $\mathbf{r}(\mathbf{y},\mathbf{s})$ is the residual of the discretized system of state equations that are described in section 2. Apart from the indicated constraints, no additional constraints need to be imposed since system constraints such as the prescribed pressure drop are already considered in the thermofluid model.

3.2 Filter and Projection

A density filter should be used in fluid-thermal topology optimization to avoid problems with ill-posedness of the optimization problem and to introduce a minimum length-scale into the design. In this work, a Helmholtz-type PDE filter [15] is used since it allows for a computationally efficient density filtering and can be easily implemented in COMSOL Multiphysics. The filter PDE is given by

$$-{r_f}^2\nabla^2\tilde{\gamma} + \tilde{\gamma} = \gamma \tag{12}$$

where r_f is the filter parameter. A drawback of density filtering is the inherent introduction of a band with intermediate densities between the solid and fluid regions. This band can be reduced by projecting the filtered design variable field towards 0 and 1, thus obtaining a design with sharper transitions from fluid to solid. For this purpose, a smoothed Heaviside projection [4] is used which is defined as:

$$\bar{\tilde{\gamma}}_i = \frac{\tanh(\beta\eta) + \tanh(\beta(\tilde{\gamma}_i - \eta)}{\tanh(\beta\eta) + \tanh\big(\beta(1-\eta)\big)} \tag{13}$$

Where η is a threshold parameter and β determines the steepness of the projection. It should be stated that the projected $\bar{\tilde{\gamma}}$ field becomes the physically meaningful one that is used in the interpolation functions which are presented in chapter 2.

4. Use of COMSOL Multiphysics

Within the presented studies, air is used as fluid and copper as heat sink material. COMSOL's Material Library is used to define the material properties. A symmetry condition is imposed along the axial center line so that the problem size is halved. The basic dimensions of the topology optimization model are indicated in Table 1.

Table 1: Basic dimensions of the topology optimization model.

Length channel	5.5 mm
Length design domain and solid plate	1.5 mm
Width channel and solid plate	4 mm
Height channel	10 mm

4.1 Multiphysics Implementation

Systems with Reynolds numbers up to 150 are considered in the analysis, thus the fluid flow is laminar. Therefore, COMSOL's Laminar Flow physics interface is used to solve the fluid mechanical system stated in equation (1) and

equation (2). The pressure difference between inlet and outlet is fixed and a no slip condition is imposed at the channel side. A first order discretization is used for the velocity and pressure field and pseudo-time stepping is enabled to increase the robustness of the solver.

The heat transport problem which is stated by equation (4), (5), and (6) is implemented in the Heat Transfer Module. The fluid's temperature at the inlet is fixed to 290 K and a total heat production of either 0.025 W or 0.05 Watt is set in the solid plate. Thermal insulation is modeled on the channel wall. For both the fluid and the solid temperature field, a linear discretization is used. To reduce the computational complexity, the fluid mechanics solution was decoupled from the heat transfer equations. Therefore, only the heat transfer solution depends on the fluid velocity field but the velocity field is determined under the assumption of a constant fluid temperature. This assumption should be a legitimate approximation since the changes of the fluid temperature are smaller than 20 K in the analyzed system.

4.2 Implementation of Topology Optimization

The topology optimization is implemented within the Optimization Module using an element-wise constant design variable field. The interpolation functions for the friction force, thermal conductivity, and out-of-plane heat transfer being stated in equation (3) and (8) are implemented in COMSOL as variables depending on the design variable field.

COMSOL's Coefficient Form PDE interface is used to implement the PDE filter described in equation (12) and a linear discretization is chosen for the filtered design variable field. The threshold parameter is set as 0.5 and the filter parameter is set as 1.5 times the minimum mesh size to avoid numerical instabilities which can occur with smaller filter radii. Zero flux boundaries are set for the filter PDE at the symmetry line and the outside border of the channel. At the remaining boundaries, a design variable value of one which corresponds to pure fluid is enforced which prevents solid from being "glued" to the design domain boundaries. The projection of the filtered field stated in equation (13) is realized with an analytical function in COMSOL.

The optimization is conducted using the GCMMA optimization method [16]. During the optimization, the convexity parameters of the interpolation functions and the steepness parameter of the projection are ramped as needed. This continuation approach [17] is conducted to obtain a more convex optimization problem at the beginning and to subsequently increase the penalization of intermediate densities during the optimization. COMSOL's LiveLink for MATLAB is used to automate the parameter ramping within a MATLAB script.

5. Results and Discussion

The design variable field of the optimized heat sink is shown in (Figure 2) for a prescribed pressure drop of 0.75 Pa and a total heat production of 0.05 W in the solid plate (corresponding to a heat flux of 8333 W/m^2). It can be seen that the topology optimization generated a structure with four fins and three fluid channels. Moreover, it should be noted that the fins have small bumps which presumably enhance the heat transfer into the fluid. The corresponding velocity magnitude distribution and streamlines of the velocity field are depicted in (Figure 3). (Figure 4) shows the corresponding temperature distribution in the fluid design layer.

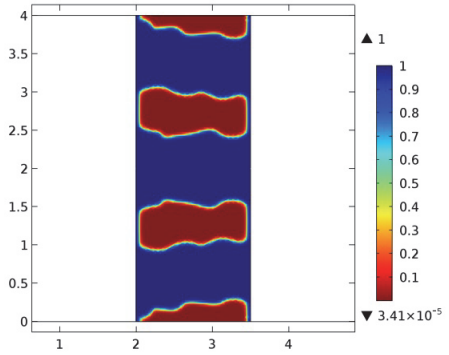

Figure 2. Design variable field of optimized heat sink. A density of 0 indicates solid material and 1 indicates flow passages.

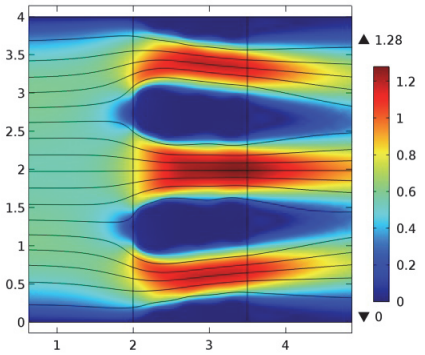

Figure 3. Fluid velocity magnitude (m/s) and streamlines for optimized heat sink.

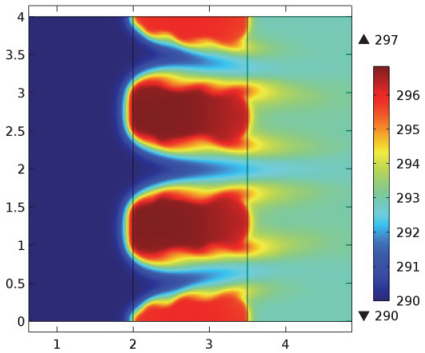

Figure 4. Temperature distribution (K) for optimized heat sink.

A parameter study showing the optimized heat sink's solid plate temperature plotted against the prescribed system pressure drop is shown in (Figure 5). Two heat production rates of 0.025 W and 0.05 W are included in the study. For both heat production rates, the solid plate's temperature decreases monotonously with increasing pressure drop. (Figure 6) depicts the dependency of the optimized system's Reynolds number of the prescribed pressure drop. The channel width was used as the characteristic length for the Reynolds number, and the average velocity at the inlet was used as the characteristic velocity. The Reynolds number increases with increasing pressure drop and maximum Reynolds numbers of around 140 are reached. The Reynolds number decrease between the pressure drop of 1 Pa and 1.25 Pa for a heat production of 0.025 W and between the pressure drop of 0.75 Pa and 1 Pa for a heat production of 0.05 W is explained by the addition of a new fin to the system. Thereby, the cooling performance is increased but the system operates with a lower volume flow and thus a lower Reynolds number.

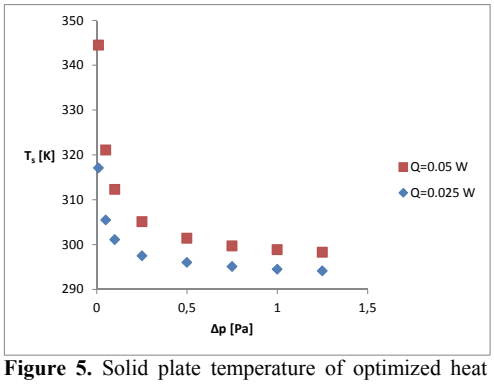

Figure 5. Solid plate temperature of optimized heat sink plotted against prescribed system pressure drop.

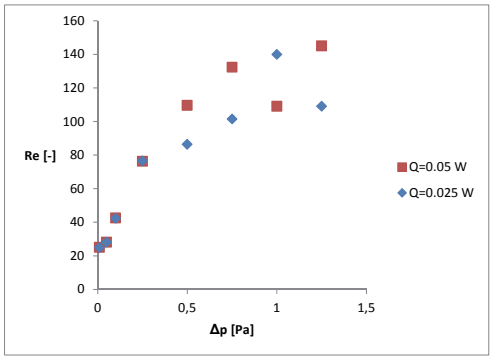

Figure 6. Reynolds number of optimized structures plotted against prescribed system pressure drop.

6. Conclusions

A 2D heat sink model with constant heat production and a three-field density-based topology optimization were implemented in COMSOL Multiphysics. The topology optimization was used to minimize the heat sink's temperature for a prescribed pressure drop and given heat production. Therefore, this work demonstrates that topology optimization of complex multiphysics systems can be implemented with comparatively little effort in COMSOL.

In a future work, transient and 3D validation simulations without symmetry condition will be

conducted with the optimized geometries to judge the physical validity of the obtained 2D optimization results.

7. References

1. J.D. Deaton, R.V. Grandhi, A survey of structural and multidisciplinary continuum topology optimization: post 2000, *Structural and Multidisciplinary Optimization*, **49**, 1-38 (2014)
2. E.M. Dede, T. Nomura, J. Lee, *Multiphysics Simulation*, Springer (2014)
3. M.P. Bendsøe, O. Sigmund, *Topology Optimization - Theory, Methods and Applications*, Springer Verlag, Berlin Heidelberg, 2003
4. F. Wang, B.S. Lazarov, O. Sigmund, On projection methods, convergence and robust formulations in topology optimization, *Structural and Multidisciplinary Optimization*, **43**, 767-784 (2011)
5. M. Jansen, B.S. Lazarov, M. Schevenels, O. Sigmund, On the similarities between micro/nano lithography and topology optimization projection methods, *Structural and Multidisciplinary Optimization*, **48**, 717 – 730 (2013)
6. M. Zhou, B.S. Lazarov, O. Sigmund, Topology optimization for optical projection lithography with manufacturing uncertainties, *Applied optics*, **53**, 2720-2729 (2014)
7. E.M. Dede, Multiphysics topology optimization of heat transfer and fluid flow systems, *Proceedings of the COMSOL Users Conference 2009 Boston, (2009)*
8. G.H. Yoon, Topological design of heat dissipating structure with forced convective heat transfer, *Journal of Mechanical Science and Technology*, **24** , 1225-1233 (2010)
9. T. Matsumori, T. Kondoh, A. Kawamoto, T. Nomura, Topology optimization for fluid-thermal interaction problems under constant input power, *Structural and Multidisciplinary Optimization*, **47**, 571-581 (2013)
10. G. Marck, M. Nemer, J.L.Harion, Topology optimization of heat and mass transfer problems: laminar flow, *Numerical Heat Transfer, Part B: Fundamentals,* **63**, 508-539 (2013)
11. J. Alexandersen, N. Aage, C.S. Andreasen, O. Sigmund, Topology optimisation for natural convection problems, International Journal for Numerical Methods in Fluids, **76**, 699-721 (2014)
12. T. Borrvall, J. Petersson, Topology optimization of fluids in Stokes flow, *International journal for numerical methods in fluids*, **41**, 77-107 (2003)
13. C. McConnell, G. Pingen, Multi-layer, pseudo 3D thermal topology optimization of heat sinks, *Proceedings of the ASME 2012 International Mechanical Engineering Congress, Houston, (2012)*
14. M. Stolpe, K. Svanberg, An alternative interpolation scheme for minimum compliance topology optimization, *Structural and Multidisciplinary Optimization*, **22**, 116-124, 2001
15. B.S. Lazarov, O. Sigmund, Filters in topology optimization based on Helmholtz-type differential equations, *International Journal for Numerical Methods in Engineering*, **86**, 765-781 (2011)
16. K. Svanberg, A class of globally convergent optimization methods based on conservative convex separable approximations, *SIAM journal on optimization*, **12**, 555-573 (2002)
17. O. Sigmund, J. Petersson, Numerical instabilities in topology optimization: a survey on procedures dealing with checkerboards, mesh-dependencies and local minima, *Structural optimization*, **16**, 68-75, (1998)

8. Acknowledgments

This work was supported by the TOpTEn project sponsored through the Sapere Aude Program of the Danish Council for Independent Research (DFF – 4005-00320).

Moreover, the authors wish to thank Niels Aage for help and advice regarding the topology optimization implementation in COMSOL Multiphysics.

A.5 P5 - Topology Optimization of a Pseudo 3D Thermofluid Heat Sink Model

J. H. K. Haertel, K. Engelbrecht, B. S. Lazarov and O. Sigmund

International Journal of Heat and Mass Transfer, **vol. 121C, pp. 1073-1088, 2018.**

Topology Optimization of a Pseudo 3D Thermofluid Heat Sink Model

Jan H. K. Haertel[1a], Kurt Engelbrecht[a], Boyan S. Lazarov[b], Ole Sigmund[b]

[a] *Department of Energy Conversion and Storage, Technical University of Denmark, Frederiksborgvej 399, 4000 Roskilde, Denmark*

[b] *Department of Mechanical Engineering, Technical University of Denmark, Nils Koppels Allé Building 404, 2800 Kgs. Lyngby, Denmark*

Abstract

This paper investigates the application of density-based topology optimization to the design of air-cooled forced convection heat sinks. To reduce the computational burden that is associated with a full 3D optimization, a pseudo 3D optimization model comprising a 2D modeled conducting metal base layer and a thermally coupled 2D modeled thermofluid design layer is used. Symmetry conditions perpendicular to the flow direction are applied to generate periodic heat sink designs. The optimization objective is to minimize the heat sink heat transfer resistance for a fixed pressure drop over the heat sink and a fixed heat production rate in the base plate. Optimized designs are presented and the resulting fin geometry is discussed from a thermal engineering point of view and compared to fin shapes resulting from a pressure drop minimization objective. Parametric studies are conducted to analyze the influence of the pressure drop on the heat sink heat transfer resistance. To quantify the influence of the assumptions made in the pseudo 3D optimization model, validation simulations with a body-fitted mesh in 2D and 3D are conducted. A good agreement between optimization model and validation simulations is found, confirming the physical validity of the utilized optimization model. Two topology optimized designs are exemplarily benchmarked against a size optimized parallel fin heat sink and an up to 13.6% lower thermal resistance is found to be realized by the topology optimization.

Keywords: Topology optimization, Heat sink design, Thermofluid modeling, Forced convection

1. Introduction

Forced convection heat sinks are used in a wide range of applications. This paper focuses on the design of air-cooled heat sinks as used for micro-electronics cooling since thermal management is increasingly becoming a bottleneck for advancement in the design of these systems [1]. Moreover, better heat management allows electronics to operate at higher performance for longer periods of time [2]. Classical heat sink designs applied to electronics cooling are mainly pin fin and parallel

[1] Corresponding author: jhkh@dtu.dk (Jan H. K. Haertel)

Nomenclature

A_{Ω_d}	design domain area	*Abbreviations*	
b_j	convexity parameter in interpolation function	2D	two-dimensional
		3D	three-dimensional
c	heat capacity	min.	minimize
C_j	parameter in RAMP interpolation	PDE	partial differential equation
Da	Darcy number	s.t.	subject to
$\mathbf{F}$	volumetric force		
f	fin volume fraction	*Greek symbols*	
h	heat transfer coefficient	$\overline{\alpha}$	maximum inverse permeability
I_α	friction interpolation function	β	projection steepness parameter
I_h	heat transfer interpolation function	γ	design variable
I_k	conductivity interpolation function	$\tilde{\gamma}$	filtered design variable
k	thermal conductivity	$\overline{\tilde{\gamma}}$	projected design variable
L_c	characteristic length	Γ_j	domain boundary j
$\mathbf{n}$	normal vector	η	projection threshold parameter
n_{eval}	number of model evaluations	μ_f	dynamic fluid viscosity
p	pressure	ρ_f	fluid density
$\dot{q}_{inter}$	transferred heat between base plate and design layer	Ω_j	domain j
$\dot{Q}_{prod}$	produced heat in base plate	*Subscripts*	
$\mathbf{r}$	residual of discretized multiphysics problem	air	air
		av	average
r_{filter}	filter parameter	d	design domain
R_{th}	thermal resistance	f	fluid
$\mathbf{s}$	state vector of multiphysics problem	i	counter subscript
T	temperature	in	inlet
$\mathbf{u}$	velocity vector	j	counter subscript
$V_{base\ plate}$	volume base plate	max	maximum
$\mathbf{x}$	xy-coordinate vector	out	outlet
$\Delta z_{base\ plate}$	thickness base plate	s	solid
$\Delta z_{channel}$	thickness channel	$symm$	symmetry
		w	wall

plate fin designs often with air as the coolant due to availability, simplicity of operation and low cost. Also microchannel heat sinks cooled by liquids such as water and oil have been investigated in various works as they allow for the rejection of higher specific power rates than air-cooled heat sinks. A comprehensive review of microchannel heat sinks considering channel geometry, flow conditions, and utilized coolants is given in [3]. The heat transfer and fluid dynamics in heat sinks are for example described in [4]. Various later works deal with the design and optimization of forced convection heat sinks: for instance Lee et al. [5] apply a simulation model based on analytical equations to the prediction and optimization of the thermal performance of fin heat sinks. Park et al. [6] use the results of 3D CFD simulations to create a Kriging metamodel which is used for shape optimization of a plate fin heat sink. With the above mentioned methods significant improvements in the thermal design of heat sinks can be achieved; however, they are limited in the sense that an

a priori design parametrization is needed both for the fin shape and the position of the fins relative to each other. In contrast, topology optimization allows for almost unlimited design freedom which makes it possible to identify also unintuitive and complex optimized structures without relying on the design engineer's intuition. This aspect becomes even more important with the increasing maturing of additive manufacturing technologies as these methods provide unprecedented design freedom.

Topology optimization [7] was developed in the context of structural engineering but has since then been applied to a wide range of engineering disciplines such as acoustics, photonics, and fluid flow [8]. It is a means to optimize the material distribution in a given design domain subject to certain constraints. In density-based topology optimization, which is used in this work, a density-field is introduced that can take the value of 0 (solid) or 1 (void) in each point of a design domain. This binary optimization problem is relaxed to continuous values between 0 and 1 to allow for the use of efficient gradient-based optimization techniques. In the presented thermofluid design problem 0 corresponds to heat sink material and 1 to fluid passage, thus allowing for a flexible representation of arbitrary heat sink fin geometries during the optimization. Topology optimization applied to the design of thermal systems such as heat sinks and heat exchangers is an active field of research [9]. Early applications of topology optimization to heat transfer problems consider 2D heat conduction problems with convective heat transfer to an ambient fluid in the out-of-plane direction by assuming a constant heat transfer coefficient as e.g. [10]. When treating 2D conduction problems with convective heat transfer within the modeled plane, the design dependent convective boundary to the fluid needs to be captured which can be done by using an interpolation scheme [11, 12, 13], by applying level set based topology optimization to track the boundary [14], or by comparing the density of adjacent elements in the finite element mesh [15]. A constant heat transfer coefficient is assumed in [11, 12, 14] whereas [13] and [15] use a surrogate model for the heat transfer coefficient to capture the dependence of the local convective heat transfer on the geometry of the optimized structure to some degree. More recently published works present also 3D optimization models with diffusive heat transport in the solid and design dependent convective boundaries with a constant heat transfer coefficient using density-based [16, 17] and level set [18] topology optimization. Dede and coworkers [16] use additive layer manufacturing to fabricate and subsequently experimentally evaluate an optimized heat sink design. The thermal integration of a thermoelectric cooler in a robotic downhole intervention tool using topology optimization to distribute conducting and insulating material in a 3D domain as well as fabrication and experimental validation of the prototype is presented in [19]. Pizzolato et al. [20] apply density-based topology optimization to the design of conducting fins in a phase change material (PCM) storage tank modeling the solidification of the PCM as transient thermal diffusion problem both in 2D and 3D.

The topology optimization works presented above simplify the heat transfer to the ambient fluid to Newtons law of cooling, i.e. assuming a constant heat transfer coefficient or a surrogate model for it. This limiting assumption can be avoided when using thermofluid, or conjugate heat transfer, topology optimization models which also explicitly consider the heat transfer in the fluid during the optimization. First fairly academic applications of topology optimization to 2D forced convection conjugate heat transfer problems are given in [21, 22]. 2D topology optimization of water-cooled microchannel heat sinks is presented in [23] solving the Navier-Stokes equations and [24] assuming Stokes flow where [24] fabricate and experimentally evaluate an optimized heat sink prototype. Matsumori et al. [25] apply topology optimization to a 2D thermofluid heat exchanger model; however, assuming the same thermal conductivity in solid and fluid. Similar heat exchanger models are treated in [26] that apply 2D lattice Boltzmann modeling and [27] who use a level set topology optimization approach to generate optimized designs in 2D and 3D. Qian and Dede [28] present a thermofluid model for topology optimization under tangential thermal gradients. The abovementioned works on thermofluid topology optimization, except for [27] that also conduct 3D optimizations, rely on 2D optimization models. This approach was extended by [29] and later [30] to a pseudo 3D model with a heat sink base plate thermally interacting with a thermofluid design layer that represents the heat sink fins and fluid flow. The extension of the presented work which also deals with a pseudo 3D heat sink model compared to [29, 30] is discussed later in this section. A fully developed flow heat exchanger model is given in [31] where the fluid flow is perpendicular to the design domain. All above presented works on thermofluid topology optimization treat laminar flow problems. Turbulent flow topology optimization is still in its very beginnings and, to the authors' best knowledge, only Kontoleontos et al. [32] have applied turbulent flow topology optimization to a conjugate heat transfer problem, albeit with the simplification of not considering the temperature field in the solid. Natural convection problems have only more recently been investigated due to the complex coupling of fluid and temperature problem. Alexandersen et al. [33] pioneered this area presenting a 2D natural convection heat sink topology optimization model that was later extended to 3D [34] and large-scale 3D [35]. Level set based topology optimization applied to 3D and 2D transient natural convection problems is treated in [36].

Full 3D optimization models allow to exploit 3D design freedom; however, at the cost of high computational demand. Conducting such optimizations is currently only possible using a computer cluster and parallelizable optimization models [35]. The computational effort is significantly reduced when using a pseudo 3D heat sink model comprised of the 2D modeled base plate and 2D thermofluid design layer while it allows for more detailed modeling than pure 2D heat sink topology optimization models. Such pseudo 3D models can be optimized on a powerful desktop computer and, therefore, be applied by a broader range of users than models which require access

to high performance computing tools. Steady state laminar flow pseudo 3D heat sink models, as analyzed in this study, have been treated before in conference papers [29, 30]; however, without detailed discussion of the results. Furthermore, full 3D validation simulations that can be used to assess assumptions regarding the heat transfer between base plate and thermofluid design layer and other simplifications have not yet been conducted. This is done in the presented study and considered one of the main contributions of this work. Moreover, the validation simulations are conducted using a body-fitted mesh and explicit representation of the solid-fluid boundary to assess the accuracy of the implicit solid-fluid representation based on a density field which inherently has some grey area at the solid-fluid interface. This has previously been done in [25] for forced convection conjugate heat transfer topology optimization; nevertheless, only for one exemplary design in 2D and assuming equal thermal conductivity in the solid and fluid. In this work, 2D and 3D validation simulations are conducted over the entire range of analyzed pressure drops to assess the difference between the optimization model, 2D body-fitted mesh validation model, and 3D body-fitted mesh validation model separately. A novelty for thermofluid topology optimization in this work is the application of symmetry conditions at the boundaries perpendicular to the flow direction to generate periodic heat sink designs. Furthermore, this is the first forced convection thermofluid topology optimization study to use air as a coolant, which is challenging for the optimization due to the large conductivity difference between air and metal, apart from [31] that rely on a simplified fully developed flow model. Also, analyzing differences in fin shapes between thermal resistance and pressure drop minimization, as done in this study, is a novelty in works on topology optimization. Two exemplary topology optimized designs are compared to size optimized parallel fin designs to provide a quantitative benchmarking against a simpler established heat sink geometry. A comparable benchmarking has so far in studies on thermofluid topology optimization only been conducted for the simplified fully developed flow model treated in [31].

2. Heat sink model

2.1. General model description

A 3D sketch of a forced convection heat sink as treated in this work can be seen in Fig. 1 (left). Heat is generated in the heat sink base plate and transferred to the fluid flowing between the fins. Since topology optimization typically requires several hundred iterations until convergence to a final design, a full 3D optimization is computationally expensive. Hence, a pseudo 3D heat sink optimization model, as shown in Fig. 1 (right), which approximates the original 3D heat sink model as two 2D thermally coupled problems is used in this work. The simplified model consists of a 2D thermofluid design layer that represents the original 3D thermofluid problem in the fluid flow and heat sink fins and of a 2D conductive base plate layer that represents the original 3D thermal

diffusion problem in the heat sink base plate. The modeling of the heat transfer between the two coupled layers is described in section 2.2.2. Two different thermofluid design layer geometries, corresponding to heat sink *model a* and *model b*, are shown in Fig. 2. The respective design layer consists of the design domain, Ω_d, and non-optimizable pure fluid area, Ω_f. As mentioned above, the design variable field can represent either heat sink fin material or fluid passage at each point of the design domain; thus, allowing for a flexible optimization of the fin topology. The heat sink base plate is below the design domain and has the same fixed area as Ω_d. The modeling of the thermal coupling between the base plate and thermofluid design layer is described in section 2.2.2. Figure 2 states additionally the boundary conditions and dimensions of *model a* and *model b*. For both 2D models and the corresponding 3D validation models, a channel height, $\Delta z_{channel}$, of 8 mm and a thickness of the metal base plate, $\Delta z_{base\,plate}$, of 0.2 mm are assumed. However, in section 5.2.5, a reduced base plate thickness of 0.005 mm is analyzed in order to emphasize hotspots. Symmetry conditions are applied at the top and bottom boundary of *model a* which leads to a periodic heat sink design perpendicular to the air flow direction. In *model b*, symmetry is assumed only at the top boundary of the design domain so that the modeled area corresponds to the bottom half of the entire heat sink. This second non-periodic heat sink geometry with inlet and outlet width smaller than the design domain width represents a design problem where the best design is less intuitive, although it does not necessarily represent a practical application. This case is optimized to demonstrate the potential of the topology optimization method to generate more complex designs and to show a case where the optimal number of fins of the design changes for different pressure drops over the heat sink.

2.2. Thermofluid modeling

Throughout this work, an incompressible, laminar, and steady-state flow is assumed. Furthermore, as described in the previous section, the fluid and heat transfer problems in the thermofluid design layer are modeled two-dimensionally. This 2D assumption is motivated by the fact that the fin height is significantly larger than the xy-dimensions. Also the original 3D thermal diffusion problem in the base plate is simplified to a 2D problem as the xy-dimensions of the base plate are much larger than its height. The validity of these simplifications is assessed in section 5.2.2.

2.2.1. Fluid dynamics modeling

Assuming an incompressible fluid and two-dimensional flow in the xy-plane, the continuity equation and Navier-Stokes equation are defined as:

$$\rho_f \left(\nabla \cdot \mathbf{u}\right) = 0 \tag{1}$$

$$\rho_f \cdot \left(\mathbf{u} \cdot \nabla\right) \mathbf{u} = -\nabla p + \mu_f \left(\nabla^2 \mathbf{u}\right) + \mathbf{F} \tag{2}$$

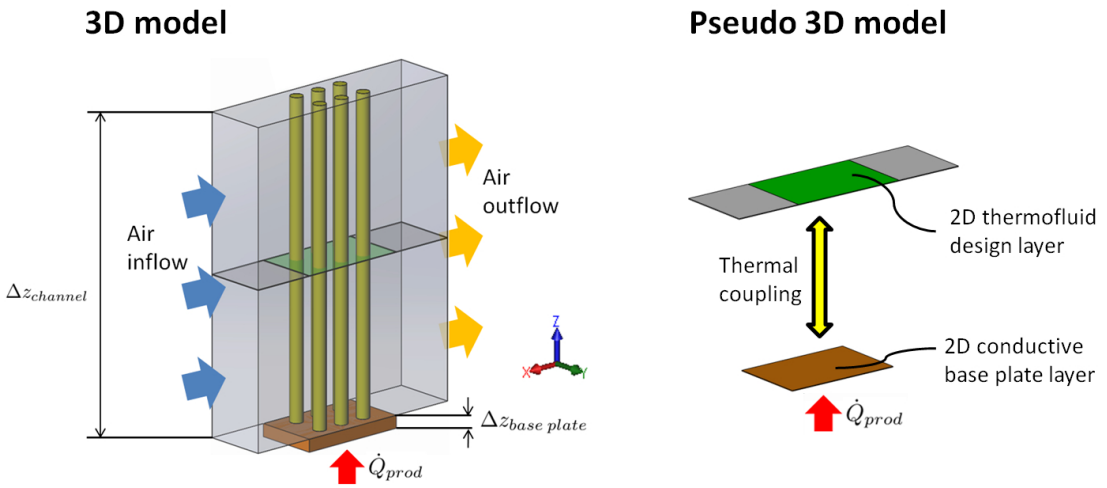

Figure 1: Left: 3D sketch of a forced convection heat sink as treated in this work including base plate (brown), fins (yellow) and modeled domain for air flow (grey). Exemplarily, pin fins are depicted in yellow. Right: Simplified pseudo 3D model consisting of a 2D thermofluid design layer where green corresponds to the design domain and grey to non-optimizable fluid area as well as the 2D modeled base plate (brown). The thermofluid design layer is also shown in the 3D model for illustrative purposes.

where ρ_f is the fluid density, $\mathbf{u}$ is the fluid velocity vector, p is the pressure field, μ_f is the dynamic viscosity of the fluid, and $\mathbf{F}$ is the Brinkman friction term. The Brinkman friction term is used in fluid flow topology optimization to penalize flow through solid areas within the design domain and corresponds to the force exerted on a fluid flowing through an ideal porous medium [37]. It is defined as:

$$\mathbf{F}(\gamma) = -\overline{\alpha}\,\mathbf{u}\,I_\alpha(\gamma) \qquad \text{in } \Omega_d \tag{3}$$

where $\overline{\alpha}$ is the maximum inverse permeability of the porous medium and $I_1(\gamma)$ a suitable function for the inverse permeability interpolation which is stated and discussed in section 3.1. The
155 maximum inverse permeability is computed by:

$$\overline{\alpha} = \mu_f/(Da\,L_c^2) \tag{4}$$

where Da is the Darcy number and L_c a characteristic length which corresponds to the design domain width within this work. Ideally, the value of $\overline{\alpha}$ would be set to infinity to prevent any fluid from flowing through solid areas. However, very high values of $\overline{\alpha}$ can cause numerical problems and issues with convergence to poor local optima. Therefore, the choice of $\overline{\alpha}$, or Da from which $\overline{\alpha}$ follows, needs to be a tradeoff that ensures negligible fluid flow through the solid while avoiding problems with numerical stability and the optimization trajectory. Outside the design domain, no Brinkman friction is exerted on the fluid; hence:

$$\mathbf{F} = \mathbf{0} \qquad \text{in } \Omega_f \tag{5}$$

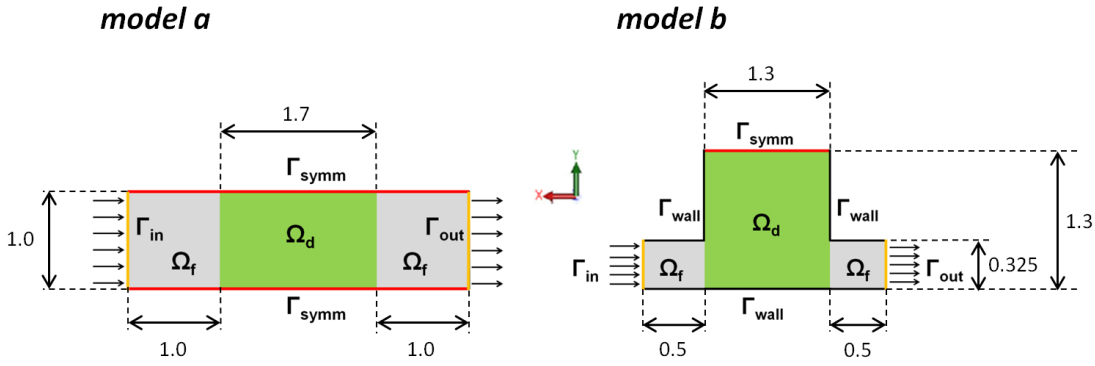

Figure 2: Schematic illustration of the domains Ω_i and boundaries Γ_j as well as dimensions in mm of heat sink *model a* and *model b*. The design domain is highlighted in green, the non-optimizable fluid area in grey, the symmetry boundaries are marked with a red line, the inlet and outlet boundaries with an orange line, and the wall boundaries with a black line. Please note that the models are not true to scale relative to each other.

The pressure drop between inlet and outlet, Δp, is prescribed in both *model a* and *model b*:

$$p|_{\Gamma_{in}} - p|_{\Gamma_{out}} = \Delta p \tag{6}$$

where $p|_{\Gamma_{in}}$ and $p|_{\Gamma_{out}}$ is the respective pressure at the inlet and outlet of the modeled domain as specified in Fig. 2. Additionally, a normal laminar inflow is set at the inlet boundary, Γ_{in}. The symmetry boundary condition for the fluid flow is given by the following two equations:

$$\mathbf{u} \cdot \mathbf{n} = 0 \qquad \text{on } \Gamma_{symm} \tag{7}$$

$$\mathbf{K} - (\mathbf{K} \cdot \mathbf{n})\,\mathbf{n} = \mathbf{0} \qquad \text{on } \Gamma_{symm} \tag{8}$$

where $\mathbf{n}$ is the vector normal to the respective boundary and $\mathbf{K}$ is defined as:

$$\mathbf{K} = [\mu_f\,(\nabla \mathbf{u} + (\nabla \mathbf{u})^T)]\,\mathbf{n} \tag{9}$$

In *model b*, a no slip condition is imposed on the wall boundaries, Γ_{wall}.

2.2.2. Heat transfer modeling

In the thermofluid design layer outside the design domain, the 2D thermal convection-diffusion equation without heat source or heat sink is solved which is given by:

$$\rho_f\, c_f\, \mathbf{u}\, \nabla T_f - \nabla \cdot (k_f\, \nabla T_f) = 0 \qquad \text{in } \Omega_f \tag{10}$$

where T_f is the temperature field in the thermofluid design layer, c_f the specific fluid heat capacity, and k_f the thermal conductivity of the fluid. Within the design domain, the following 2D thermal convection-diffusion equation is solved:

$$\gamma\, \rho_f\, c_f\, \mathbf{u}\, \nabla T_f - \nabla \cdot (k_f\, I_k(\gamma)\, \nabla T_f) = \frac{\dot{q}_{inter}(\gamma)}{\Delta z_{channel}} \qquad \text{in } \Omega_d \tag{11}$$

where $I_k(\gamma)$ is a function that interpolates between the thermal conductivity of the fluid, k_f, and that of the heat sink material, k_s. The interpolation function used for $I_k(\gamma)$ is stated in section 3.1. The term $\dot{q}_{inter}(\gamma)$ represents the heat transferred from the solid base plate to the thermofluid design layer and $\Delta z_{channel}$ is the height of the air channel and fins. By multiplying the advective energy transport term in equation (11) with γ, a linear penalization of the advective energy transport through solid areas is added, as it was done in [25, 28, 31] . This ensures that slight fluid leakage through solid areas, which is to some degree unavoidable in density-based topology optimization, does not result in advective energy transport through these regions. It should be noted that the temperature problem is coupled to the fluid problem through the velocity field $\mathbf{u}$; nevertheless, there is no back coupling from the temperature problem to the fluid problem since constant thermophysical properties for air are assumed throughout this work. The thermophysical properties of air used in this study are stated in section 5.1. In the metal base plate, a 2D heat conduction problem is solved:

$$\nabla \cdot (k_s \, \nabla T_s) = -\frac{\dot{Q}_{prod}}{V_{base\ plate}} + \frac{\dot{q}_{inter}(\gamma)}{\Delta z_{base\ plate}} \qquad \text{in } \Omega_d \tag{12}$$

where k_s is the base plate thermal conductivity, T_s is the temperature field in the base plate, $\dot{Q}_{prod}$ is the prescribed heat production rate, $V_{base\ plate}$ is the volume of the base plate, and $\Delta z_{base\ plate}$ is the height of the base plate. In all studies presented in this work, apart from section 5.2.5, a uniform heat production rate is assumed in the base plate. The out-of-plane heat transfer between base plate and thermofluid design layer, $\dot{q}_{inter}(\gamma)$, needs to flexibly represent both the conductive heat transfer from the base plate into the heat sink fins as well as the convective heat transfer from the base plate to the fluid. This is achieved by using a heat transfer coefficient which is interpolated between a high conductive heat transfer into the fins and a lower convective heat transfer to the fluid:

$$\dot{q}_{inter}(\gamma) = h_f \, I_h(\gamma) \, (T_s - T_f) \tag{13}$$

where h_f is the heat transfer coefficient describing the convective heat transfer to the fluid and $I_h(\gamma)$ is a function interpolating between h_f and the heat transfer coefficient from the base plate into the heat sink fins, h_s. The parameter h_s represents the conductive heat transfer resistance in the z-direction in the fins and is empirically determined.

The fluid inlet temperature is set to the fixed value T_{in}:

$$T_f = T_{in} \qquad \text{on } \Gamma_{in} \tag{14}$$

The outlet, symmetry, and adiabatic wall boundary condition for the temperature field in the thermofluid design layer is given by:

$$\mathbf{n} \cdot \nabla T_f = 0 \qquad \text{on } \Gamma_{out} \cup \Gamma_{symm} \cup \Gamma_{wall} \tag{15}$$

Perfect thermal insulation is moreover assumed on all boundaries of the heat sink base plate:

$$\mathbf{n} \cdot \nabla T_s = 0 \qquad \text{on } \partial\Omega_d \tag{16}$$

3. Topology optimization

3.1. Interpolation functions

A continuous design field, $\gamma(\mathbf{x})$, taking values between 0 and 1 is introduced in density-based topology optimization. In the given design problem, 1 corresponds to fluid passage, 0 to heat sink fin material, and interpolation functions are used to represent intermediate values. For the Brinkman friction term, an interpolation function as stated in [33] and first introduced in [37] is used in this work:

$$I_\alpha(\gamma) = \frac{1-\gamma}{1+b_\alpha\,\gamma} \tag{17}$$

where b_α is a parameter determining the convexity of the interpolation. For the interpolation of the thermal conductivity within the design layer and the heat transfer between heat sink base plate and thermofluid design layer, a RAMP-style interpolation as used in [33] and originally presented in [38] is applied:

$$I_j(\gamma) = \frac{\gamma\,(C_j(1+b_j)-1)+1}{C_j\,(1+b_j\,\gamma)} \qquad \text{j=k,h} \tag{18}$$

where b_j is the interpolation convexity parameter and C_j is defined in the respective case by:

$$C_k = \frac{k_f}{k_s} \tag{19}$$

$$C_h = \frac{h_f}{h_s} \tag{20}$$

3.2. Problem formulation

The optimization objective considered in this work is to minimize the heat sink thermal resistance for a prescribed pressure drop over the heat sink and prescribed heat production rate. The thermal resistance of the heat sink, R_{th}, is defined as:

$$R_{th}(\gamma,\mathbf{s}) = \frac{T_{s,av}(\gamma,\mathbf{s}) - T_{in}}{\dot{Q}_{prod}} \tag{21}$$

where $T_{s,av}$ is the average temperature in the base plate and $\mathbf{s}$ is the state vector of the thermofluid problem stated in section 2.2. Thus, the topology optimization problem can be stated as follows:

$$\begin{aligned} \min_{\gamma}.: \quad & R_{th}(\gamma,\mathbf{s}) \\ \text{s.t.:} \quad & r(\gamma,\mathbf{s}) = 0 \\ & \iint_{\Omega_d} (1-\gamma)\; dx\,dy - f\;A_{\Omega_d} \le 0 \\ & 0 \le \gamma(\mathbf{x}) \le 1 \qquad\qquad \forall\,\mathbf{x} \in \Omega_d \end{aligned} \tag{22}$$

where $r(\gamma, \mathbf{s})$ is the residual of the finite element formulation of the thermofluid problem stated in section 2.2, A_{Ω_d} is the design domain area, and f is the prescribed maximum fin volume fraction or fin cross-sectional area fraction. The pressure drop over the heat sink does not appear explicitly as constraint in this statement since it is prescribed as boundary condition in the thermofluid model. The fin volume fraction constraint is set in parentheses since it is omitted in this work except for section 5.2.4. In general, this volume fraction constraint is not needed in the optimization formulation (22) unless constraining the total fin volume would be desired for some design reason. If the entire cross-section is occupied by fins ($f = 1$), no fluid flows over the heat sink which would be fairly detrimental to the heat sink thermal performance. If there is no fin material at all in the cross-section ($f = 0$), the heat can only be transferred directly from the base plate to the fluid which is also ineffective as the fins provide much more contact area between heat sink and fluid than the base plate. Hence, due to the physics of the optimization problem, the optimal value of f will always be in between these two extreme cases. In section 5.2.4, also the pressure drop over the heat sink is minimized for a fixed fluid inlet velocity that is prescribed as boundary condition in the thermofluid model and subject to a constraint on the fin volume fraction. This optimization problem is given by:

$$\begin{aligned} \min_{\gamma}.: \quad & \Delta p(\gamma, \mathbf{s}) \\ \text{s.t.:} \quad & r(\gamma, \mathbf{s}) = 0 \\ & \iint_{\Omega_d} (1 - \gamma) \; dx \, dy - f \; A_{\Omega_d} \geq 0 \\ & 0 \leq \gamma(\mathbf{x}) \leq 1 \qquad\qquad \forall \, \mathbf{x} \in \Omega_d \end{aligned} \tag{23}$$

In the case of pressure drop minimization, a minimum cross-sectional area fraction constraint is needed since the lowest pressure drop for a prescribed fluid inlet velocity will always be obtained by a design with no fin material in the cross section ($f = 0$). It should be noted that in the thermal resistance minimization problem, in contrast, a maximum cross-sectional area fraction constraint is applied as the values of f analyzed in section 5.2.4 are below the f value that minimizes the heat sink thermal resistance in that specific case.

3.3. PDE filter and projection

Density filtering is needed in thermofluid topology optimization to avoid problems with ill-posedness of the optimization problem [39]. A Helmholtz-type partial differential equation (PDE) filter [40] is used in this study which is defined as follows:

$$-r_{filter}^2 \, \nabla^2 \, \tilde{\gamma} + \tilde{\gamma} = \gamma \qquad\qquad \text{in } \Omega_d \tag{24}$$

where $\tilde{\gamma}$ is the filtered design field and r_{filter} is the filter parameter. The following boundary conditions are used for the filter PDE:

$$\tilde{\gamma} = 1 \qquad \text{on } \partial\Omega_d \setminus (\Gamma_{symm} \cup \Gamma_{wall}) \tag{25}$$

$$\mathbf{n} \cdot \nabla\tilde{\gamma} = 0 \qquad \text{on } \Gamma_{symm} \cup \Gamma_{wall} \tag{26}$$

To reduce the gray area between solid and fluid which is inherently introduced by the filtering process, a smoothed heaviside projection [41] is applied on the filtered design field:

$$\bar{\tilde{\gamma}} = \frac{\tanh(\beta\,\eta) + \tanh(\beta\,(\tilde{\gamma} - \eta))}{\tanh(\beta\,\eta) + \tanh(\beta\,(1 - \eta))} \tag{27}$$

where $\bar{\tilde{\gamma}}$ is the projected design field, β is a parameter controlling the projection steepness, and η is the projection threshold parameter. It should be noted that the projected design field becomes the physical meaningful one in the interpolation functions (Eq. (17) and (18)) and the thermal convection-diffusion equation (Eq. (11)).

4. Implementation

The heat sink topology optimization models are implemented in the commercial finite element software COMSOL Multiphysics [42]. The fluid problem (Eq. (1) and (2)) is solved with COMSOL's *CFD Module* using a second order discretization for the velocity field and first order discretization for the pressure. COMSOL's *Heat Transfer Module* is used to solve the thermal convection-diffusion equation (Eq. (10) and (11)) and the thermal diffusion problem in the base plate (Eq. (12)) using second order elements for T_f due to the steep temperature gradients in the thermofluid design layer and first order elements for T_s. The filter PDE (Eq. (24)) is implemented in the *Coefficient Form PDE Interface* using a linear discretization and the filter parameter is set to 1.5 times the maximum element size in the design domain. Triangular elements are used for all PDEs and no stabilization scheme is applied as it was found to slightly blur the sensitivities within COMSOL's optimizer when compared to a finite difference check. The parallel sparse direct solver PARDISO [43] that is available in COMSOL is used to solve the system of discretized finite element equations and segregated solver steps are used for the fluid problem, thermal problem, and filter PDE. The optimization is conducted within COMSOL's *Optimization Module* which automatically solves the adjoint problem to provide sensitivities for the objective and constraint functionals and the globally convergent version of the Method of Moving Asymptotes (GCMMA) [44] is used as the optimization method. A continuation approach [39, 45] is applied on the convexity parameters of the interpolation functions, b_α, b_h, b_k, and the steepness parameter of the design projection, β. This is done to ensure a more convex optimization problem in the beginning and to consequently gradually increase the penalization of intermediate densities

as well as to increase the sharpness of the solid-fluid interface. The choice of the final values of the conductivity and Brinkman interpolation convexity parameters, b_k and b_α, is particularly important as they mainly determine whether there will be areas with unphysical intermediate densities in the final design. This is due to the high conductivity difference between heat sink metal and air which is used as coolant in this work. This high conductivity difference can make thin features with intermediate densities that have increased thermal conductivity compared to air but do not effectively prevent the fluid from flowing through them advantageous. Thus, the values of b_k and b_α need to ensure a strong penalization of intermediate densities through fairly nonlinear interpolation functions. However, highly nonlinear interpolation functions caused problems with numerical stability during test optimizations. To mitigate this issue, the solid conductivity in the xy-plane in the thermofluid layer of the optimization model is set to a value lower than in reality as stated in section 5.1. Further discussions regarding these aspects are provided in section 5.1 and 5.2. The heuristically chosen continuation strategies used to optimize *model a* and *model b* are indicated in Table 1. These continuation strategies are conservative both in terms of number of continuation steps and number of model evaluations in each step. A less conservative continuation strategy could be used as well; however, with an increased risk of converging to poor local optima. Values of constant optimization parameters and mesh parameters of the optimization models are provided in Table 2. The corresponding finite element mesh has around $34,000$ elements in the case of *model a* and around $66,000$ elements in the case of *model b*. The choice to implement this model in COMSOL has limited several modelling parameters such as the problem size and filtering techniques, which has led to a limitation in the range of Reynolds numbers that could be modeled. However, the COMSOL framework allows for faster implementation of various modeling scenarios and materials and is therefore a useful tool for topology optimization. Dedicated models for specific conditions would allow for higher fluid velocities, larger model dimensions, and higher resolution of the problem at the cost of longer development time.

Table 1: Values of optimization parameters and number of model evaluations during the continuation approach for *model a* and *model b*.

Continuation step	$n_{eval,model\ a}$	$n_{eval,model\ b}$	b_α	b_k	b_h	β
1	500	600	8	0.1	0.1	1
2	250	300	4	5	2	1.5
3	150	150	2	20	8	2
4	100	100	1	50	8	2.5
5, 6, 7, 8, 9	80	80	1	50	8	3, 4, 5, 6, 7
10	80	80	1	50	8	7

Table 2: Values of constant optimization and mesh parameters for *model a* and *model b*.

Parameter	*Model a* value	*Model b* value
Da [-]	10^{-5}	10^{-5}
max. element size in Ω_d [mm]	1.33×10^{-2}	8.66×10^{-3}
max. element size in Ω_a [mm]	2.86×10^{-2}	1.63×10^{-2}
r_{filter} [mm]	2.00×10^{-2}	1.30×10^{-2}

5. Results and discussion

5.1. Problem setup

Within this work, the thermophysical properties of air are assumed constant and evaluated at 20 °C. The resulting values are given in Table 3. A thermal conductivity of 400 W/(m K), which corresponds to the conductivity of copper, is assumed in the heat sink base plate. The high conductivity difference between copper and air can cause issues with regards to grey area in the final design and numerical stability during the optimization as discussed in section 4. For this reason, the value of C_k, which determines the solid conductivity in the xy-plane in the thermofluid design layer, is in both models set to lower thermal conductivities than the thermal conductivity assumed in the heat sink base plate. The chosen C_k value corresponds to a solid thermal conductivity of 24 W/(m K) in *model a* and 0.072 W/(m K) in *model b* which makes the latter a more academic model. It should be noted that the C_k value chosen in *model b*, which is lower than the value used in *model a* is not chosen due to problems with grey area or numerical stability during the optimization but because of convergence to only locally optimal topologies that were observed during preliminary *model b* optimizations. This issue is further discussed in section 5.3 In the *model a* pseudo 3D and full 3D validation models, the thermal conductivity of the heat sink base plate is used in all solid domains to assess the influence of the chosen lower value of C_k in the optimization model. The abovementioned and other constant model parameters used within this work are stated in Table 4. As already stated in section 2.2.2, a uniform heat production rate is assumed in the heat sink base plate in all studies presented in this work apart from the model presented in section 5.2.5 where hotspots are studied. Moreover, the base plate thickness differs in section 5.2.5 from the value given in Table 4.

5.2. Results model a

Thermofluid topology optimization problems are quite non-convex and can easily converge to only locally optimal topologies depending on the starting guess or initial design. Therefore, several initial designs are used for each optimization in this work and only the respective best performing design is presented. The initial designs used for the optimization of *model a* are shown in Fig. 3.

Table 3: Constant thermophysical properties of air used in this work.

Thermophysical property	Value
c_{air} [J/(kg K)]	1006
k_{air} [W/(m K)]	0.024
μ_{air} [Pa s]	1.94×10^{-5}
ρ_{air} [kg/m^3]	1.204

Table 4: Constant parameters used in the heat sink *model a* and *model b*.

Parameter	*Model a* value	*Model b* value
C_k [-]	1/1000	1/3
h_f [W/(m^2 K)]	50	50
h_s [W/(m^2 K)]	2×10^5	2×10^5
$k_{s,base\,plate}$ [W/(m K)]	400	400
$\dot{Q}_{prod}$ [W]	0.175	0.25
T_{in} [°C]	20	20
$\Delta z_{base\,plate}$ [mm]	0.2	0.2
$\Delta z_{channel}$ [mm]	8	8

For all *model a* optimizations presented in this work, the initial designs (a) - (k) and a uniform initial density field of value 0.8 are used. The initial designs (a) - (c) can be interpreted as parallel fin heat sink when the periodic structure is considered. The asymmetry of the designs (d) - (k) with regards to a horizontal line in the center of the design domain is intended as this was found to yield improved optimization results compared to designs that are symmetric with regards to this line. Note that only the initial designs (g), (h), and (i) led to best performing final designs in all optimizations conducted for this work; all other initial guesses led to only locally optimal designs. Still, it is important to test various initial topologies as it is not known a priori which one will yield the best performing final design in the different optimizations.

5.2.1. Analysis and discussion of optimized designs

An exemplary *model a* optimization result for a pressure drop over the heat sink of 3 Pa with corresponding velocity magnitude field, temperature field in the thermofluid design layer, and temperature field in the metal base plate is shown in Fig. 4. Four fins are formed within the design domain where the bottom left and top right fin are halved by the symmetry boundary. The two fins in the bottom part of the design domain reach the left boundary and the two fins in the upper part of the design domain reach the right boundary so that the fins are almost arranged diagonally from the bottom left to the top right of the design domain. All fins have to some degree

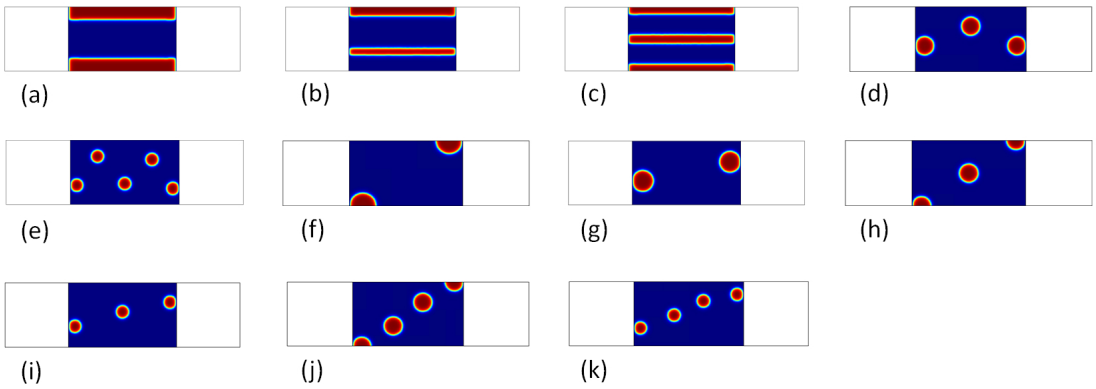

Figure 3: Initial designs used for *model a* (red is solid and blue is fluid). The designs (a) - (k) as well as a uniform initial density field of value 0.8 are used to generate the *model a* results presented in this study.

a streamlined shape except for the bottom left fin which is almost triangular. This fin is probably shaped in this way to fit closely to the left boundary of the design domain and a more streamlined fin shape would probably occur if the design domain reached further left. Maximum air velocities between the fins of around 2.5 m/s are reached and the majority of the air flows through the upper part of the design domain. The somewhat diagonal arrangement of the fins results in a to some degree diagonal air flow from the top left to the bottom right of the design domain. Moreover, it can be seen that the Brinkman penalization effectively prevents air from flowing through the fins. The fins are nearly isothermal within the modeled plane which provides some justification for assuming a lower solid conductivity in the thermofluid plane compared to the original value in the metal base plate. A very uniform temperature can be seen in the base plate with a maximum temperature difference in the plate of slightly less than 0.4 K.

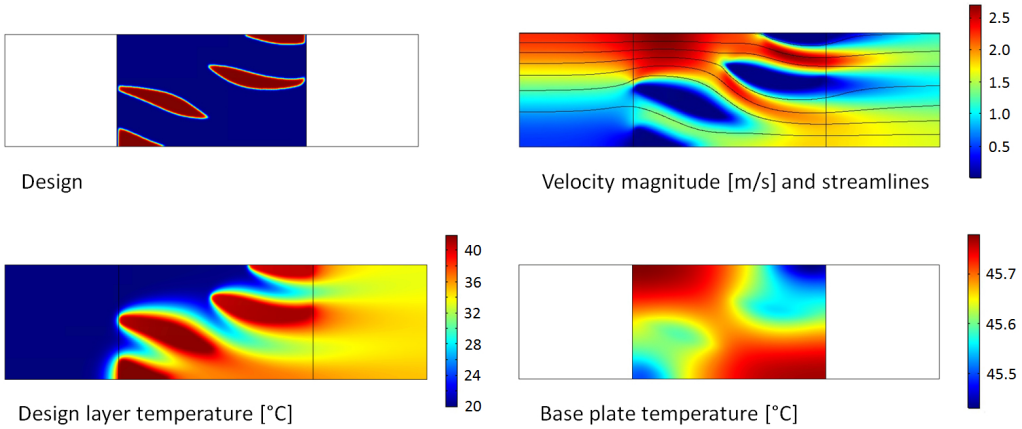

Figure 4: Exemplary *model a* design obtained for a pressure drop over the heat sink of 3 Pa where red corresponds to solid and blue to fluid. Additionally, the corresponding velocity field, temperature field in the thermofluid design layer, and temperature field in the metal base plate are shown.

Figure 5 shows the influence of the prescribed pressure drop over the heat sink on the optimized designs. The pressure drop ranges from 0.5 to 7 Pa so that the influence of increasing convection-domination on the optimized topologies can be studied. Design (a) consists of one fin in the bottom left and a second fin in the top right of the design domain. Increasing the pressure drop to 1 Pa results in a changed topology with four fins in a diagonal arrangement similar to the one described above in the discussion of Fig. 4. Compared to design (a), a smaller fin at the bottom left and a smaller fin at the top right of the design domain are added. Both smaller fins are halved by the symmetry boundary. Increasing the pressure drop further leads to the same topology; however, the length and thickness of the fins increases. The fins in all presented designs have streamlined shapes apart from the triangularly shaped bottom left fin in the designs (c) - (f). The shapes of the individual fins differ within the same design and between the designs at different pressure drops. It is not possible to classify the fin shapes according to classical heat sink fin shapes such as NACA airfoil [46], dropform, ellipse or plate fin as e.g. analyzed in [47, 48] but the topology optimized fins show a similarity to these designs. In general, the optimized structures tend to reduce overall pressure drop by forming streamlined shapes and to increase contact distance between the fluid and solid by forcing the fluid to take a slightly diagonal path across the heat sink. All designs have clearly defined solid features without intermediate density areas apart from the thin band at the solid-fluid interface which results from the density filtering. This means that the chosen values of interpolation convexity parameters and solid conductivity in the thermofluid design layer work well in preventing unphysical intermediate density features in the analyzed pressure drop range. Also the applied density filter mitigates problems with very thin unpractical fin features in the final designs. However, only robust topology optimization approaches [41, 49] may prevent such features reliably, but these are not considered in this study and have not yet been applied to thermofluid topology optimization.

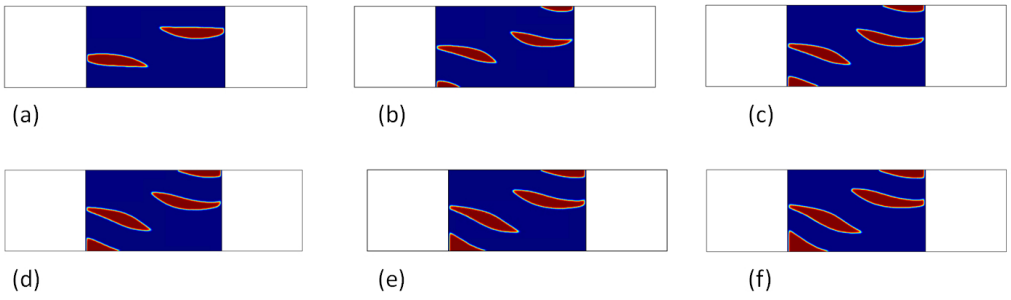

Figure 5: Influence of prescribed pressure drop over heat sink on the optimized topology for *model a*. The pressure drop takes the values 0.5 (a), 1 (b), 2 (c), 3 (d), 5 (e), and 7 Pa (f).

5.2.2. Model validation and parametric studies

It is important to verify the topology optimization model for several reasons: The accuracy of the solid fluid representation using a density field with Brinkman penalization should be assessed which can be done by replacing this modeling approach with an explicit separate modeling of solid and fluid domains and a body-fitted mesh resolving the physics in the thermal boundary layer with high accuracy. Moreover, the threshold value for the explicit solid fluid boundary representation, $\bar{\tilde{\gamma}} = 0.8$, and the assumption of a lower solid conductivity in the thermofluid design layer plane, i.e. the choice of C_k, should be validated. The influence of these factors can be checked in a pseudo 3D validation model which will subsequently be referred to as the 2D validation model. Moreover, a full 3D validation model is used to quantify the influence of the assumptions inherent to the pseudo 3D modeling approach. These are the simplification of a 3D thermofluid problem to the 2D thermofluid design layer and the interpolation of the simplified heat transfer coupling between the 2D base plate model and the thermofluid design layer, i.e. the choice of the parameters h_f and h_s. These effects are captured explicitly in the 3D model as convective heat transfer from the base plate to the fluid and conductive heat transport from the base plate into the heat sink fins. Furthermore, the drag force from the top and bottom model boundary on the air flow is captured in the 3D model while it is not considered in the 2D approach.

Figure 6 shows the 3D boundary layer mesh for the optimized design shown in Fig. 4 and the corresponding 3D velocity magnitude field and temperature field. The mesh consists of approximately 403,000 elements in total and is shown on the fin and base plate surface as well as on the bottom wall and left symmetry boundary of the channel. The 2D assumption in the optimization model seems to be well justified for the fluid problem as the flow shows very little variation along the z-coordinate apart from a small hydraulic boundary layer near the top and bottom walls. The z-dependency of the temperature field is slightly more pronounced as there is a temperature drop of around 8 °C along the fins in addition to a thermal boundary layer above the base plate. Nevertheless, the 2D thermofluid design layer assumption seems to be justified as an approximation. The temperature drop in the fins of around 8 °C predicted by the 3D model agrees well with the around 4 °C temperature difference between the fins in the thermofluid design layer and the base plate which can be seen in the corresponding pseudo 3D model results shown in Fig. 4 as the fin temperature in the pseudo 3D model can be interpreted as an averaged temperature along the height of the fins. Hence, the value of the pseudo 3D model parameter h_s, which represents the conductive thermal resistance along the z-coordinate in the fins, yields good results for the presented case.

To provide a more quantitative means of evaluating the agreement between the optimization model and the 2D and 3D validation model, the heat sink thermal resistance and Reynolds number are compared over a pressure drop range from 0.5 Pa to 7 Pa which is shown in Fig. 7. Note

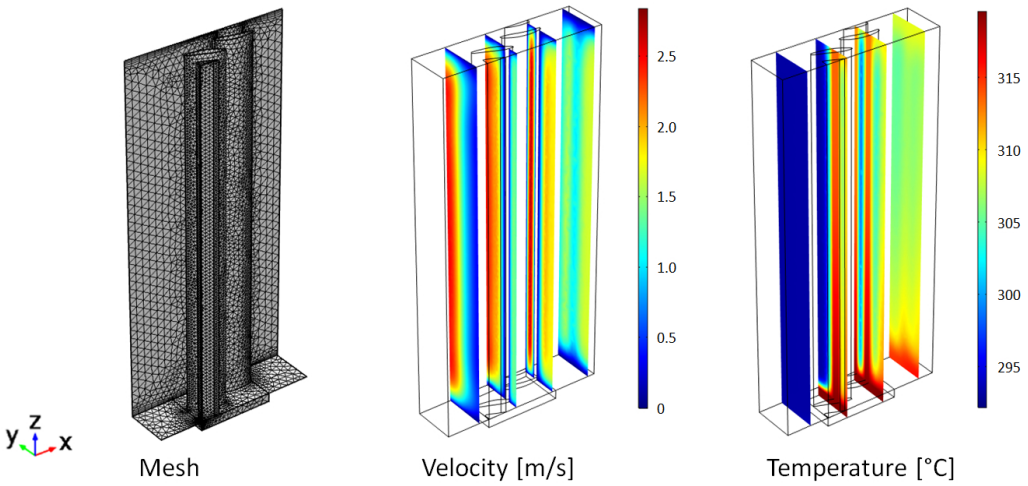

Figure 6: Mesh used in the 3D body-fitted mesh validation model of the optimized *model a* geometry shown in Fig. 4 with corresponding velocity and temperature field.

that all quantitative *model a* results presented in the following are obtained by evaluating the model with a projection steepness parameter of $\beta = 15$ even though β is only ramped up to a value of 7 during the optimization as shown in Table 1. The higher β value used for the final model evaluation yields a better solid-fluid thresholding and hence minimizes the effect of grey area in the design. To be consistent, also the contours of the *model a* 2D and 3D validation models are generated using a projection steepness parameter value of 15. Furthermore, it should be noted that the value of the thermal resistance in this model is more of a relative measure as it depends on the heat input into the base plate which is proportional to the size of the modeled area within the periodic heat sink structure. The Reynolds number is computed with the average velocity at the inlet as characteristic velocity and inlet width as characteristic length since a characteristic length based on the fin geometry can differ significantly between the different designs. The Reynolds number increases almost linearly with increasing pressure drop over the heat sink. At a 0.5 Pa pressure drop, the Reynolds number is around 30 and the highest Reynolds number at 7 Pa pressure drop is around 200 both in the optimization model and the 2D validation model and around 170 in the 3D validation model. These values are well below the critical Reynolds number for laminar turbulent transition that is for flow between parallel plates, which can be used as simplified reference geometry for the flow between the fins, reported to be slightly below 2300 [50]. Hence, assuming a laminar flow seems to be valid even though an additional experimental validation of the flow conditions should be conducted which is left for future works [2]. The optimization model and 2D validation model show good agreement in terms of predicted

[2]As mentioned in the introduction and shown in [16], fabrication of topology optimized designs using additive manufacturing techniques may have great potential due to the design freedom that these methods provide. How-

Reynolds number where the 2D validation model consistently predicts slightly lower values. This deviation is assumed to be mainly due to the implicit boundary representation between solid and fluid used in the optimization and slight fluid leakages through the solid domains in the optimization model. The 3D validation model consistently predicts the lowest Reynolds numbers which is owed to the wall friction at the top and bottom boundaries of the modeled domain which is not considered in the 2D optimization and 2D validation model. The relative offset in terms of Reynolds number between the optimization model and the 3D validation model increases with increasing pressure drop from around 12% at $\Delta p = 0.5$ Pa to around 17% at $\Delta p = 7$ Pa. A decrease of thermal resistance with increasing pressure drop over the heat sink can be observed as expected. This effect is significantly more pronounced for lower pressure drops; for higher pressure drops, an increase of pressure drop leads to a small further decrease in thermal resistance. A good agreement between the optimization model and both validation models can be seen over the entire pressure drop range which provides some justification for the validity of the assumptions made in the optimization model. Over the entire pressure drop range, the optimization model consistently predicts the lowest and the 3D validation model the highest thermal resistance. The main reason for this is presumably the difference in Reynolds numbers between the models. A higher Reynolds number is equivalent to a higher coolant flow rate and hence better cooling performance. Thus, the 3D validation model, which predicts the lowest Reynolds numbers, yields the highest thermal resistance and the optimization model, which predicts the highest Reynolds numbers, yields the lowest thermal resistance.

A cross-check of the *model a* optimized geometries based on the 2D validation model is stated in Table 5. Each design optimized for a respective pressure drop of 0.5, 1, 2, 3, 4, and 5 Pa is tested at each of the other pressure drop values. Ideally, each design should perform best at the pressure drop for which it is optimized, and this is the case as can be seen from Table 5. Furthermore, it can be seen that the performance differs for lower pressure drops considerably more between the designs than for higher pressure drops.

5.2.3. Benchmarking to size optimized parallel fin designs

Cross-checking the optimization results is important as poor local optima within the generated designs can be identified. Nevertheless, it is limited in the sense that the designs are only compared

ever, it should be noted that the dimensions of the design domains treated in this work are in the millimeter to submillimeter range which are presently more suited to micromachining or conventional chemical etching techniques than most mature additive manufacturing techniques. These dimensions were chosen due to the limitation to low Reynolds numbers of the COMSOL modeling framework. Achieving low Reynolds numbers in models with larger model dimensions would have only been possible at the trade-off of unrealistically low fluid velocities. Generally, treatment of higher Reynolds number problems and larger model dimensions is possible in more customizable and computationally efficient frameworks than COMSOL.

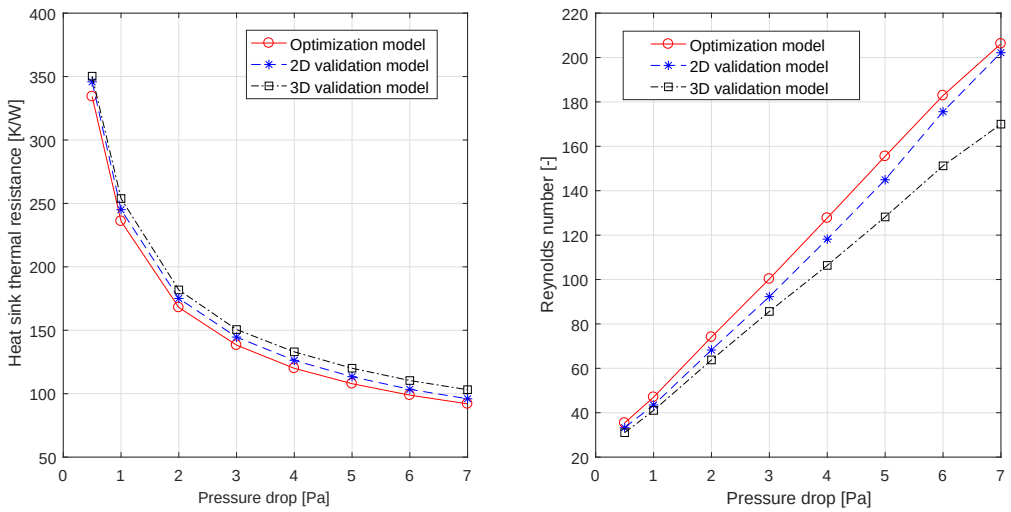

Figure 7: Influence of pressure drop over the heat sink on the heat sink heat transfer resistance as defined in equation (21) (left) and the Reynolds number of the optimized designs (right). Results are shown for the *model a* optimization model, the corresponding 2D body-fitted mesh validation model, and 3D body-fitted mesh validation model.

Table 5: Cross-check of *model a* optimized designs heat transfer resistance [K/W] based on the 2D body-fitted mesh validation model.

Design for Δp [Pa] \ Δp [Pa] tested for	0.5	1	2	3	4	5
0.5	**345.8**	260.3	205.3	180.5	165.1	154.3
1	375.5	**245.1**	180.8	155.9	141.2	131.0
2	439.2	257.8	**175.1**	146.4	130.3	119.4
3	494.1	277.0	177.6	**144.6**	126.8	115.0
4	538.5	294.7	182.2	145.5	**126.2**	113.7
5	595.9	319.8	191.1	149.1	127.5	**113.6**

within the optimized set and, therefore, it is of interest to benchmark the performance of the topology optimized designs to a conventional heat sink geometry. In this case, a size-optimized parallel fin design is chosen as the reference geometry. All fins have the same thickness, th_{fin}, which is the optimization variable. Optimal fin thicknesses are determined exemplarily for a pressure drop of 2 Pa and for 1, 1.5, 2, and 2.5 fins within the design domain. The fins are spaced relative to each other such that the resulting periodic structure has a uniform distance between the fins. The size optimization is conducted for a projection steepness parameter $\beta = 7$ to allow for a fair comparison to the topology optimization as $beta = 7$ is the last value of the continuation

scheme used in this work. Table 6 shows the optimal fin thickness for the different numbers of fins within the design domain and the respective thermal resistance. Moreover, the thermal resistance of the corresponding topology optimized design is shown. It can be seen that the optimal fin thickness decreases with increasing number of fins within the modeled domain as expected. The design with two fins performs best among the size optimized designs having a thermal resistance of 184.5 K/W for the optimal fin thickness of 0.06 mm. Still, the topology optimized design for the same pressure drop has a lower thermal resistance of 168.0 K/W which is a relative improvement of 9.8% compared to the best size optimized design.

Table 6: Thermal resistance of the size optimized parallel fin heat sink designs and topology optimized (TO) design for a pressure drop of 2 Pa. Furthermore, the optimal fin thickness is stated for the parallel fin designs.

Design	optimal th_{fin} [mm]	R_{th} [K/W]
1 fin	0.23	250.6
1.5 fin	0.11	189.6
2 fin	0.06	**184.5**
2.5 fin	0.05	218.3
TO design	-	**168.0**

Figure 8 shows the best performing size optimized design and the topology optimized design to which it is compared. It can be seen that the fins of the topology optimized design are not as thin as the fins of the size optimized design which is advantageous for mechanical stability. Moreover, the topology optimized design may be more robust with regards to manufacturing uncertainty as the performance of parallel fin heat sinks and heat exchangers is sensitive to flow maldistribution caused by small differences of geometry between the channels [51]. However, these aspects need to be assessed and quantified in future works. A second exemplary benchmarking of a topology optimized design to a size optimized parallel fin design is presented in section 5.2.5 for a non-uniform heat generation rate in the base plate.

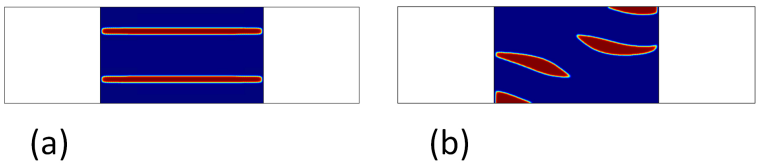

Figure 8: Size optimized 2 fin design (a) and topology optimized design (b) for a pressure drop of 2 Pa.

5.2.4. Comparison to pressure drop minimization

The optimized heat sink fins depicted in Fig. 5 have a relatively streamlined shape as already mentioned above. Therefore, it is of interest to compare the shape of fins optimized with regard to

thermal resistance minimization and fins of the same cross-sectional area optimized with regard to pressure drop minimization. For a better comparison of the shapes, the same initial design which is generated with thermal resistance minimization objective without volume constraint is used for all optimizations within this section. This design is then used to initialize thermal resistance and pressure drop optimizations with active volume constraint that can be directly compared to each other. Moreover, the air inlet velocity in all pressure drop minimizations is set such that the Reynolds number is the same as in the thermal resistance minimization design without a volume constraint. This initial design and the designs optimized with volume constraints between 19.3% and 5% are shown in Fig. 9. The design obtained by thermal resistance minimization without volume constraint consists of a single thin fin stretching across the entire length of the design domain which could be interpreted as a plate fin heat exchanger when considering the periodic structure. The fin is slightly streamlined with a blunt front and rear end where the fin reaches the respective end of the design domain. A similarly shaped fin stretching over the entire length of the design domain is generated for $f = 15\%$ and $f = 10\%$; however, it is becoming increasingly thinner. For $f = 5\%$, two very thin fins with slightly streamlined front and rear end are formed at the position of the single longer fin in the previous designs. The design obtained by pressure drop minimization for $f = 19.3\%$ stretches over the entire length of the design domain as the thermal resistance minimized design at the same f value. However, the pressure drop minimized design resembles more a mix of flat ellipse and NACA shape apart from the blunt front and rear end where the fin reaches the respective end of the design domain. The fin shape is the same for decreasing f values but its length decreases with decreasing f so that the fins do not have a blunt ends for $f = 15\%$ and lower. The comparable problem of optimal 2D cross-sections for drag minimization in laminar Navier-Stokes flow has been treated in the literature by using variational methods of optimal control [52], by numerical solution of the 2D Navier-Stokes and adjoint problem where the latter provides first and second order necessary conditions for a shape with minimal drag [53], and using density-based topology optimization in a finite element framework [54]. Pironneau [52] concludes that the optimal shape has a 90° wedge shape at the front end and [53] present slender, close to ellipsoid optimal profiles with wedge shaped front and rear end for Reynolds numbers between 1 and 40. Kondoh et al. [54] study the problem for Reynolds numbers of up to 2000 finding similar optimized profiles as [53] for lower Reynolds numbers and, for higher laminar Reynolds numbers, shapes very similar to the pressure drop minimized designs with $f \leq 15\%$ depicted in Fig. 9. A smoother front and rear end of the profiles is the main difference to the more wedge shaped front and rear ends presented in [54]. The smoother shapes obtained in this study are most probably due to the density filtering that smears out fine features which was not applied in [54].

The objective function values for thermal resistance and pressure drop minimization of the

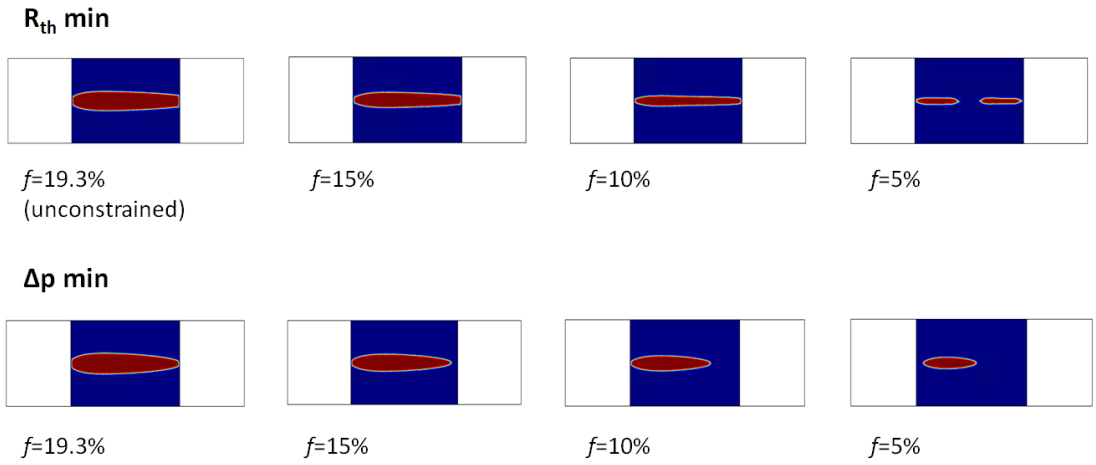

Figure 9: Comparison of thermal resistance minimization and pressure drop minimization for *model a*. The top left design is generated without volume constraint and used as initial design for all other optimizations shown in this figure which are conducted with active constraint on the fraction of solid volume in the design domain.

designs shown in Fig. 9 are given in Table 7. Considering the thermal resistance objective, it can be seen that the thermal resistance increases with decreasing volume constraint values from 225 K/W at $f = 19.3\%$ to 282 K/W at $f = 5\%$ as the cross-sectional area for heat transfer from the base plate into the fin and the contact area between fin and airflow decrease. An even stronger increase in thermal resistance with decreasing volume constraint values from 226 K/W at $f = 19.3\%$ to 387 K/W at $f = 5\%$ occurs for the pressure drop minimization objective as these designs have less contact area between fin and fluid as those of the thermal resistance minimization for the same f value. The pressure drop decreases significantly with decreasing f for the pressure drop minimization from 2.95 Pa at $f = 19.3\%$ to 1.28 Pa at $f = 5\%$. Comparing both optimization objectives for the same f, it can be seen that the differences both in thermal resistance and pressure drop increase with decreasing f. For $f = 19.3\%$, the relative difference in thermal resistance is 0.3% and the relative difference in pressure drop 1.7%. However, much larger differences would be observed when comparing designs where several fins are advantageous from a thermal point of view as a single fin is always advantageous for the pressure drop minimization objective.

5.2.5. Non-uniform heat production rate in the base plate

In the studies presented above, a uniform heat production rate in the heat sink base plate is considered and a thermal conductivity of 400 W/(m K) is assumed in the base plate which is at the higher side of the thermal conductivities of metals and alloys commonly used in heat sinks. Moreover, air is considered as the coolant which limits the heat flux magnitude that can be rejected by the heat sink compared to other coolants as, for example, water. These factors lead to relatively uniform base plate temperatures that could be well approximated using a lumped model for the base plate, i.e. relying on a pure 2D optimization model instead of the presented

Table 7: Comparison of thermal resistance minimization and pressure drop minimization objective function values for different volume constraints using *model a*.

	R_{th} min. objective			**Δp min. objective**		
f [%]	R_{th} [K/W]	Δp [Pa]	Re [-]	R_{th} [K/W]	Δp [Pa]	Re [-]
19.3	225.4	3.00	115	226.1	2.95	115
15	226.5	3.00	131	244.0	2.45	115
10	234.6	3.00	152	289.3	1.87	115
5	282.0	3.00	173	387.3	1.28	115

pseudo 3D approach which captures the thermal diffusion problem in the base plate. Therefore, a model with non-uniform heat production rate in the base plate and reduced base plate thickness that leads to thermal hotspots is introduced in this section to demonstrate the added value of the pseudo 3D optimization model. The base plate thickness considered in this section is 0.005 mm and the same total heat production in the base plate as in the studies above is assumed; however, the heat is only released in one circular area in the bottom left and one circular area in the top right part of the design domain. An exemplary topology optimization using this model is conducted for a pressure drop of 2 Pa and the optimized design and the corresponding velocity magnitude, design layer temperature, and base plate temperature are shown in Fig. 10. The areas where the heat generation in the base plate occurs are marked with yellow circles. The resulting design consists of three fins which is a different topology than the corresponding 2 Pa design for a uniform base plate heat production rate (see Fig. 5c) that comprises 4 fins. Moreover, an optimization for this pressure drop is conducted for comparison using an optimization model with a lumped model for the heat sink base plate, i.e. assuming a spatially non-varying base plate temperature. This optimization results in a topology comprising 4 fins similar to the design shown in Fig. 5c which is not surprising as the base plate temperature only varies by around 0.4 °C in the case of uniform heat generation. In the case of non-uniform heat generation in the base plate, the topology with three fins is advantageous since the top and bottom fins can be placed directly on the respective area of heat generation and hence effectively dissipate the heat from there. For this reason, the bottom and top fin have an around 10 °C higher temperature than the middle fin. The highest temperatures in the base plate occur around the areas of heat generation even though fins are placed above these areas to remove the heat. A temperature difference of 15 °C occurs between the hotspots and the coldest part of the base plate which is below the middle fin. Comparing the heat sink thermal resistances realized by the different optimization models, it is interesting to note that the non-uniform heat generation design has a thermal resistance of 164.6 K/W which is slightly lower than the thermal resistance of 168.0 K/W realized by the uniform

heat generation model and 167.3 K/W realized by the lumped base plate model. This shows that the topology optimization can make use of the increased hotspot temperatures and remove the heat more efficiently than in the case of an isothermal or almost isothermal base plate which provides some confirmation of the usefulness of explicitly modeling the thermal diffusion in the base plate in the optimization model.

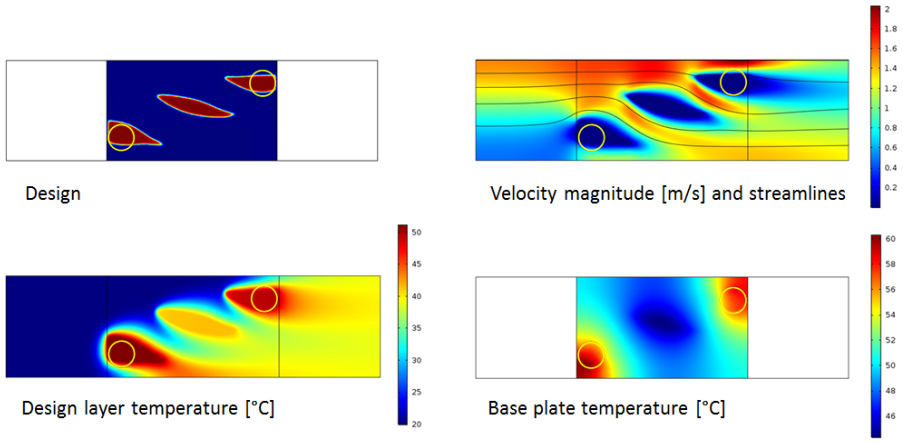

Figure 10: Topology optimized *model a* design obtained for a non-uniform heat production rate in the base plate and a pressure drop over the heat sink of 2 Pa. Red corresponds to solid, blue to fluid and the areas where the heat input into the base plate occurs are marked by yellow circles. Additionally, the corresponding velocity field, temperature field in the thermofluid design layer, and temperature field in the metal base plate are shown.

As presented in section 5.2.3 for the case of uniform heat generation in the base plate, a comparison to a size optimized parallel heat sink is conducted. Also in this case 1 fin, 1.5 fins, 2 fins, and 2.5 fins within the design domain, spaced such that the fins have a uniform distance in the periodic structure, are considered. Furthermore, a design with with 2 fins is optimized where the fins are spaced such that the fin center coincides with the center of the circular areas of heat input which results in a slightly irregular fin pattern when considering the periodic fin structure. For each of these cases, the optimal fin thickness is determined and the resulting fin thickness and thermal resistances of these size optimized designs and the topology optimized design are provided in Table 8. The design *2 fin (a)* refers to the design with 2 fins and a uniform fin spacing in the periodic structure and the design *2 fin (b)* refers to the design with 2 fins where the center of the respective fin coincides with the center of the respective circular area of heat input. As in the case of uniform heat production rate in the base plate, the design with 2 fins and uniform fin spacing in the periodic structure has the lowest thermal resistance. A slightly higher thermal resistance is realized by the design *2 fin (b)* which shows that equal flow distribution between the parallel fins is more important for the overall thermal performance than an exact placing of the fins above the areas of heat input. The topology optimized design has a lower thermal resistance than the best

size optimized design. In this case, a relative thermal resistance reduction of 13.6% is afforded by the topology optimization.

Table 8: Thermal resistance of size optimized parallel fin heat sink designs and the topology optimized design for a pressure drop of 2 Pa and a non-uniform heat flux in the base plate. Furthermore, the optimal fin thickness is stated for the parallel fin designs.

Design	optimal th_{fin} [mm]	R_{th} [K/W]
1 fin	0.25	267.6
1.5 fin	0.11	197.3
2 fin (a)	0.07	**187.0**
2 fin (b)	0.07	190.1
2.5 fin	0.05	220.6
TO design	-	**164.6**

5.3. Results model b

As mentioned in section 2.1, the *model b* geometry is included in this work to generate more complex topologies than those obtained for *model a* and to demonstrate a case where the number of fins in the optimized designs varies for different pressure drops over the heat sink. Only a uniform heat production rate in the base plate is considered for the *model b* optimizations. A uniform design field with $\gamma = 0.8$ and a straight fluid channel between inlet and outlet are used as initial designs for *model b* of which the boundary conditions and dimensions are shown in Fig. 2. Hence, fewer initial guesses are used as in the *model a* optimizations. For this reason, a design continuation approach between the different pressure drops optimized for is applied in the *model b* optimizations. This means that the optimal design at a certain pressure drop is used as an additional initial design for the next higher and lower pressure drops. As stated in section 5.1, a lower solid conductivity in the xy-plane in the thermofluid design layer, i.e. C_k value, was chosen in *model b* compared to *model a*. This is done to avoid problems with convergence to poor local optima that were observed during preliminary *model b* optimizations. More specifically, convergence to designs with fewer fins than optimal were observed when using the same C_k value as in *model a*. This issue can be avoided when using the presented approach with a lowered C_k value and design continuation between different pressure drops; however, the lowered C_k value leads to a more academic optimization model. The effect of this assumption can be quantified by comparing the predicted thermal resistance of a pseudo 3D body-fitted mesh validation model with a solid conductivity in the fins corresponding to the conductivity of copper to the thermal resistance of the optimization model as done for *model a*. However, this comparison is omitted for *model b* as this model serves mainly to demonstrate the capabilities of the topology optimization method to

generate more complex designs. The unphysically low C_k value in the optimization model may possibly also be avoided by other means such as ramping the C_k value during the optimization or using different initial designs with several fins as presented for *model a* but both of these approaches are not considered for *model b* in this work. An exemplary optimized *model b* design for $\Delta p = 20\ Pa$ with the corresponding fluid velocity magnitude and streamlines, thermofluid design layer temperature, and base plate temperature is depicted in Fig. 11. The design consists of three fins at the bottom, left, and right boundary of the design domain, where a no slip condition is imposed. Four more fins are formed in the middle of the design domain with small channels between them and one larger channel between the uppermost fin and the symmetry boundary at the top of the design domain. The maximum temperature in the fins is around 51 °C, and it can be seen that the fins are not entirely isothermal in the modeled plane due to the relatively low solid conductivity assumed in *model b* within the thermofluid design layer. The metal base plate is fairly isothermal with the temperature ranging between 51.9 °C and almost 52.4 °C.

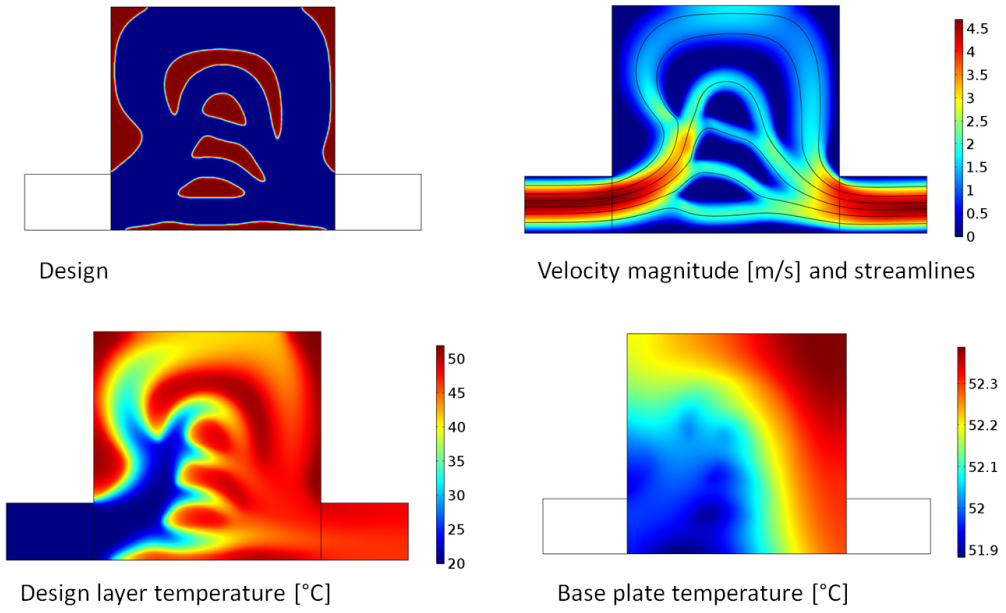

Figure 11: Exemplary *model b* design obtained for a pressure drop over the heat sink of 20 Pa where red corresponds to solid and blue to fluid. Moreover, the corresponding velocity field, temperature field in the thermofluid design layer, and temperature field in the metal base plate are shown.

Figure 12 shows optimized *model b* topologies with respect to the pressure drop over the heat sink where pressure drops between 1 and 20 Pa are considered. The general design is the same in all cases. Three fins are formed at the bottom, left, and right side of the design domain where a no slip condition is imposed. Additionally, a number of fins are formed in the middle of the design domain: One fin for $\Delta p = 1$ Pa, two fins for 2.5 Pa, 3 fins for 7.5 Pa, and 4 fins for 20 Pa. The Reynolds number of the optimized designs defined with regards to the average inlet velocity and

inlet width as characteristic length range between 7.2 for $\Delta p = 1$ Pa and 67.0 for $\Delta p = 20$ Pa. Hence, the laminar flow assumption seems to be also well justified for *model b*.

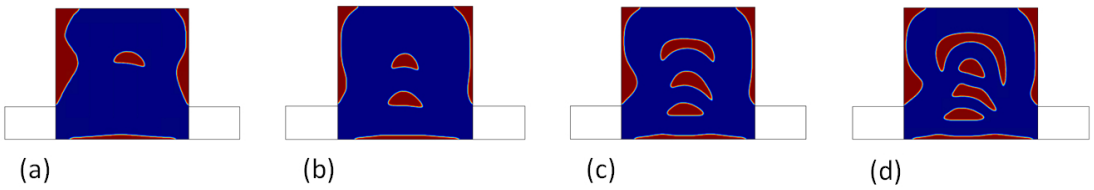

Figure 12: Influence of pressure drop over *model b* heat sink on optimized designs. Red corresponds to solid and blue to fluid. The pressure drop takes the values 1 (a), 2.5 (b), 7.5 (c), and 20 Pa (d).

A cross-check of the objective function values of the optimized designs shown in Fig. 12 based on a pseudo 3D body-fitted mesh validation model is stated in Table 9. The solid-fluid interface is thresholded at $\bar{\tilde{\gamma}} = 0.8$ as it is done in *model a* and the heat sink thermal resistance is computed with two times the heat production rate stated in Table 4 to represent the entire heat sink of which only the bottom half is optimized due to the assumed symmetry boundary condition at the top of the design domain. Moreover, the conductivity of copper is set in the solid domains of the thermofluid design layer to provide a more realistic validation model. Each design performs best at the pressure drop for which it is optimized, which provides some confirmation of the validity of these results from an optimization point of view. It also shows that the presented optimization with lowered C_k value may be interpreted as a more heuristic optimization that still yields useful designs when evaluated under more realistic conditions.

Table 9: Discrete cross-check of *model b* optimized designs heat transfer resistance [K/W] based on the pseudo 3D body-fitted mesh validation model.

Design for Δp [Pa] \ Δp [Pa] tested for	1	2.5	7.5	20
1	**751.4**	317.8	203.1	151.4
2.5	871.5	**288.5**	129.6	98.2
7.5	1216.7	360.0	**119.9**	64.9
20	1909.9	525.0	150.5	**64.1**

6. Conclusions

In this work, a thermofluid topology optimization model assuming steady state laminar flow is applied to the design of forced convection air-cooled heat sinks. To reduce the computational effort that is associated with a 3D optimization model, a pseudo 3D heat sink model comprised

of a 2D modeled heat sink base plate and 2D modeled thermofluid design layer that are thermally coupled is used. Heat sink designs being periodic perpendicular to the flow direction are generated using symmetry conditions at the sides of the modeled domain. The optimization objective is to minimize the heat sink heat transfer resistance for a prescribed pressure drop over the heat sink and prescribed heat production rate in the base plate. Optimized designs are presented and discussed from a thermal engineering point of view. Parametric studies are conducted to analyze the influence of the prescribed pressure drop on the optimized topologies as well as on Reynolds number and thermal resistance of the system. To assess the influence of the implicit solid-fluid boundary representation in density-based topology optimization, 2D and 3D validation simulations with explicit representation of the solid-fluid boundary and a body-fitted mesh are conducted. Moreover, the 3D validation model is used to check the validity of the heat sink representation in the presented pseudo 3D model. A good agreement between the models in terms of predicted thermal resistance and Reynolds number is found over the entire analyzed pressure drop range and reasons for deviations between the models are discussed. It is found that the 3D thermofluid problem of the airflow around the heat sink fins can be approximated as a 2D problem in the analyzed case. Still, the pseudo 3D optimization model can also be useful in cases of more pronounced three-dimensional physical phenomena to provide promising starting guesses for a subsequent full 3D optimization. Another means to deal with more pronounced 3D physical phenomena is to add further thermofluid layers to the pseudo 3D model. However, this is non-trivial even if only fin cross-sections being constant in z-direction are considered. This is mainly because assumptions for the heat exchange between the layers, both for fluid-fluid and fin-fin heat transfer, need to be made. Further assumptions would be needed if also momentum transfer between the layers was considered. Moreover, the computational burden increases significantly with each added thermofluid layer. The complexity increases even more if the fin cross-sections are allowed to differ between the layers since a different 2D design variable field is then needed to be introduced for each thermofluid layer. For these reasons, the analysis of pseudo 3D heat sink models with several thermofluid layers is left for future works. A cross-check based on the 2D validation model shows that each design performs best at the pressure drop optimized for. Furthermore, two exemplary topology optimized designs are benchmarked to a size optimized parallel fin heat sink to provide a comparison to a conventional heat sink geometry. A thermal resistance reduction of up to 13.6% is found to be afforded by the topology optimization which provides some confirmation for the added benefit of topology optimization. Fins generated with thermal resistance minimization as optimization objective are compared to pressure drop minimized fins for given volume constraints in terms of resulting fin shape, thermal resistance, and pressure drop. Moreover, an exemplary topology optimization is conducted for a model with heat generation in two local thermal hotspots in the base plate. This optimization results in a different topology and

slightly lower thermal resistance than in the case of a uniform or an almost uniform base plate temperature which demonstrates the usefulness of including the thermal diffusion problem in the base plate in the optimization model. A second non-periodic and more academic, heat sink model with inlet and outlet width smaller than the design domain width is optimized to generate more complex and topologically more interesting fin designs. Optimization results for different pressure drops are presented and discussed and a cross-check based on a 2D body-fitted mesh validation model confirms the optimization technique.

Acknowledgements

This work was supported by the TOpTEn project sponsored through the Sapere Aude Program of the Danish Council for Independent Research (DFF 4005-00320).
Moreover, the authors wish to thank Rasmus Bjørk for helping to run COMSOL/MATLAB on a computer cluster and Niels Aage and Casper Schousboe Andreasen for their helpful advice with regards to the topology optimization implementation in COMSOL.

References

[1] S. V. Garimella, A. S. Fleischer, J. Y. Murthy, A. Keshavarzi, R. Prasher, C. Patel, S. H. Bhavnani, R. Venkatasubramanian, R. Mahajan, Y. Joshi, et al., Thermal challenges in next-generation electronic systems, Components and Packaging Technologies, IEEE Transactions on 31 (4) (2008) 801–815. doi:10.1109/TCAPT.2008.2001197.

[2] A. Vassighi, M. Sachdev, Thermal and power management of integrated circuits, Springer Science & Business Media, 2006. doi:10.1007/0-387-29749-9.

[3] A. M. Adham, N. Mohd-Ghazali, R. Ahmad, Thermal and hydrodynamic analysis of microchannel heat sinks: A review, Renewable and Sustainable Energy Reviews 21 (2013) 614–622. doi:10.1016/j.rser.2013.01.022.

[4] A. D. Kraus, A. Bar-Cohen, Thermal analysis and control of electronic equipment, Washington, DC, Hemisphere Publishing Corp., 1983, 633 p.

[5] S. Lee, Optimum design and selection of heat sinks, in: Semiconductor Thermal Measurement and Management Symposium, 1995. SEMI-THERM XI., Eleventh Annual IEEE, IEEE, 1995, pp. 48–54. doi:10.1109/STHERM.1995.512051.

[6] K. Park, P.-K. Oh, H.-J. Lim, The application of the cfd and kriging method to an optimization of heat sink, International journal of heat and mass transfer 49 (19) (2006) 3439–3447. doi:10.1016/j.ijheatmasstransfer.2006.03.009.

[7] M. P. Bendsoe, O. Sigmund, Topology Optimization: Theory, Methods, and Applications, Springer, 2003. doi:10.1007/978-3-662-05086-6.

[8] J. D. Deaton, R. V. Grandhi, A survey of structural and multidisciplinary continuum topology optimization: post 2000, Structural and Multidisciplinary Optimization 49 (1) (2014) 1–38. doi:10.1007/s00158-013-0956-z.

[9] T. Dbouk, A review about the engineering design of optimal heat transfer systems using topology optimization, Applied Thermal Engineering 112 (2016) 841–854. doi:10.1016/j.applthermaleng.2016.10.134.

[10] O. Sigmund, Design of multiphysics actuators using topology optimization–part i: One-material structures, Computer methods in applied mechanics and engineering 190 (49) (2001) 6577–6604. doi:10.1016/s0045-7825(01)00251-1.

[11] L. Yin, G. K. Ananthasuresh, A novel topology design scheme for the multi-physics problems of electro-thermally actuated compliant micromechanisms, Sensors and Actuators A: Physical 97 (2002) 599–609. doi:10.1007/978-3-642-59497-7_59.

[12] T. E. Bruns, Topology optimization of convection-dominated, steady-state heat transfer problems, International Journal of Heat and Mass Transfer 50 (15) (2007) 2859–2873. doi:10.1016/j.ijheatmasstransfer.2007.01.039.

[13] A. Iga, S. Nishiwaki, K. Izui, M. Yoshimura, Topology optimization for thermal conductors considering design-dependent effects, including heat conduction and convection, International Journal of Heat and Mass Transfer 52 (11) (2009) 2721–2732. doi:10.1016/j.ijheatmasstransfer.2008.12.013.

[14] S.-H. Ahn, S. Cho, Level set–based topological shape optimization of heat conduction problems considering design-dependent convection boundary, Numerical Heat Transfer, Part B: Fundamentals 58 (5) (2010) 304–322. doi:10.1080/10407790.2010.522869.

[15] Y. Joo, I. Lee, S. J. Kim, Topology optimization of heat sinks in natural convection considering the effect of shape-dependent heat transfer coefficient, International Journal of Heat and Mass Transfer 109 (2017) 123–133. doi:10.1016/j.ijheatmasstransfer.2017.01.099.

[16] E. M. Dede, S. N. Joshi, F. Zhou, Topology optimization, additive layer manufacturing, and experimental testing of an air-cooled heat sink, Journal of Mechanical Design 137 (11) (2015) 111702. doi:10.1115/1.4030989.

[17] M. Zhou, J. Alexandersen, O. Sigmund, C. B. Pedersen, Industrial application of topology optimization for combined conductive and convective heat transfer problems, Structural and Multidisciplinary Optimization 54 (4) (2016) 1045–1060. doi:10.1007/s00158-016-1433-2.

[18] P. Coffin, K. Maute, Level set topology optimization of cooling and heating devices using a simplified convection model, Structural and multidisciplinary optimization 53 (5) (2016) 985–1003. doi:10.1007/s00158-015-1343-8.

[19] S. Soprani, J. H. K. Haertel, B. Lazarov, O. Sigmund, K. Engelbrecht, A design approach for integrating thermoelectric devices using topology optimization, Applied Energy 176 (2016) 49–64. doi:10.1016/j.apenergy.2016.05.024.

[20] A. Pizzolato, A. Sharma, K. Maute, A. Sciacovelli, V. Verda, Topology optimization for heat transfer enhancement in latent heat thermal energy storage, International Journal of Heat and Mass Transfer 113 (2017) 875–888. doi:10.1016/j.ijheatmasstransfer.2017.05.098.

[21] E. M. Dede, Multiphysics topology optimization of heat transfer and fluid flow systems, in: Proceedings of the COMSOL Users Conference, 2009.

[22] G. H. Yoon, Topological design of heat dissipating structure with forced convective heat transfer, Journal of Mechanical Science and Technology 24 (6) (2010) 1225–1233. doi:10.1007/s12206-010-0328-1.

[23] E. M. Dede, Optimization and design of a multipass branching microchannel heat sink for electronics cooling, Journal of Electronic Packaging 134 (4) (2012) 041001. doi:10.1115/1.4007159.

[24] A. A. Koga, E. C. C. Lopes, H. F. V. Nova, C. R. de Lima, E. C. N. Silva, Development of heat sink device by using topology optimization, International Journal of Heat and Mass Transfer 64 (2013) 759–772. doi:10.1016/j.ijheatmasstransfer.2013.05.007.

[25] T. Matsumori, T. Kondoh, A. Kawamoto, T. Nomura, Topology optimization for fluid–thermal interaction problems under constant input power, Structural and Multidisciplinary Optimization 47 (4) (2013) 571–581. doi:10.1007/s00158-013-0887-8.

[26] K. Yaji, T. Yamada, M. Yoshino, T. Matsumoto, K. Izui, S. Nishiwaki, Topology optimization in thermal-fluid flow using the lattice boltzmann method, Journal of Computational Physics 307 (2016) 355–377. doi:10.1016/j.jcp.2015.12.008.

[27] K. Yaji, T. Yamada, S. Kubo, K. Izui, S. Nishiwaki, A topology optimization method for a coupled thermal–fluid problem using level set boundary expressions, International Journal of Heat and Mass Transfer 81 (2015) 878–888. doi:10.1016/j.ijheatmasstransfer.2014.11.005.

[28] X. Qian, E. M. Dede, Topology optimization of a coupled thermal-fluid system under a tangential thermal gradient constraint, Structural and Multidisciplinary Optimizationdoi:10.1007/s00158-016-1421-6.

[29] C. McConnell, G. Pingen, Multi-layer, pseudo 3d thermal topology optimization of heat sinks, in: Volume 7: Fluids and Heat Transfer, Parts A, B, C, and D, ASME International, 2012. doi:10.1115/imece2012-93093.

[30] J. H. K. Haertel, K. Engelbrecht, B. S. Lazarov, O. Sigmund, Topology optimization of thermal heat sinks, in: Proceedings of the COMSOL Conference 2015, 2015.

[31] J. H. K. Haertel, G. F. Nellis, A fully developed flow thermofluid model for topology optimization of 3d-printed air-cooled heat exchangers, Applied Thermal Engineering 119 (2017) 10–24. doi:10.1016/j.applthermaleng.2017.03.030.

[32] E. Kontoleontos, E. Papoutsis-Kiachagias, A. Zymaris, D. Papadimitriou, K. Giannakoglou, Adjoint-based constrained topology optimization for viscous flows, including heat transfer, Engineering Optimization 45 (8) (2013) 941–961. doi:10.1080/0305215x.2012.717074.

[33] J. Alexandersen, N. Aage, C. S. Andreasen, O. Sigmund, Topology optimisation for natural convection problems, International Journal for Numerical Methods in Fluids 76 (10) (2014) 699–721. doi:10.1002/fld.3954.

[34] J. Alexandersen, O. Sigmund, N. Aage, Topology optimisation of passive coolers for light-emitting diode lamps, in: Proceedings of the 11th World Congress of Structural and Multidisciplinary Optimisation, 2015.

[35] J. Alexandersen, O. Sigmund, N. Aage, Large scale three-dimensional topology optimisation of heat sinks cooled by natural convection, International Journal of Heat and Mass Transfer 100 (2016) 876–891. doi:10.1016/j.ijheatmasstransfer.2016.05.013.

[36] P. Coffin, K. Maute, A level-set method for steady-state and transient natural convection problems, Structural and Multidisciplinary Optimization 53 (5) (2016) 1047–1067. doi:10.1007/s00158-015-1377-y.

[37] T. Borrvall, J. Petersson, Topology optimization of fluids in stokes flow, International journal for numerical methods in fluids 41 (1) (2003) 77–107. doi:10.1002/fld.426.

[38] M. Stolpe, K. Svanberg, An alternative interpolation scheme for minimum compliance topology optimization, Structural and Multidisciplinary Optimization 22 (2) (2001) 116–124. doi:10.1007/s001580100129.

[39] O. Sigmund, J. Petersson, Numerical instabilities in topology optimization: a survey on procedures dealing with checkerboards, mesh-dependencies and local minima, Structural optimization 16 (1) (1998) 68–75. doi:10.1007/bf01214002.

[40] B. S. Lazarov, O. Sigmund, Filters in topology optimization based on helmholtz-type differential equations, International Journal for Numerical Methods in Engineering 86 (6) (2011) 765–781. doi:10.1002/nme.3072.

[41] F. Wang, B. S. Lazarov, O. Sigmund, On projection methods, convergence and robust formulations in topology optimization, Structural and Multidisciplinary Optimization 43 (6) (2011) 767–784. doi:10.1007/s00158-010-0602-y.

[42] Comsol multiphysics 5.2.

[43] O. Schenk, K. Gärtner, Solving unsymmetric sparse systems of linear equations with pardiso, Future Generation Computer Systems 20 (3) (2004) 475–487. doi:10.1016/s0167-739x(03)00188-2.

[44] K. Svanberg, A class of globally convergent optimization methods based on conservative convex separable approximations, SIAM journal on optimization 12 (2) (2002) 555–573. doi:10.1137/s1052623499362822.

[45] M. Stolpe, K. Svanberg, On the trajectories of penalization methods for topology optimization, Structural and Multidisciplinary Optimization 21 (2) (2001) 128–139. doi:10.1007/s001580050177.

[46] E. N. Jacobs, K. E. Ward, R. M. Pinkerton, The characteristics of 78 related airfoil sections from tests in the variable-density wind tunnel, Tech. rep., National Advisory Committee for Aeronautics; Washington, DC, United States (1933).

[47] N. Sahiti, A. Lemouedda, D. Stojkovic, F. Durst, E. Franz, Performance comparison of pin fin in-duct flow arrays with various pin cross-sections, Applied Thermal Engineering 26 (11) (2006) 1176–1192. doi:10.1016/j.applthermaleng.2005.10.042.

[48] F. Zhou, I. Catton, Numerical evaluation of flow and heat transfer in plate-pin fin heat sinks with various pin cross-sections, Numerical Heat Transfer, Part A: Applications 60 (2) (2011) 107–128. doi:10.1080/10407782.2011.588574.

[49] B. S. Lazarov, F. Wang, O. Sigmund, Length scale and manufacturability in density-based topology optimization, Archive of Applied Mechanics 86 (1-2) (2016) 189–218. doi:10.1007/s00419-015-1106-4.

[50] R. W. Hanks, The laminar-turbulent transition for flow in pipes, concentric annuli, and parallel plates, AIChE Journal 9 (1) (1963) 45–48. doi:10.1002/aic.690090110.

[51] K. K. Nielsen, K. Engelbrecht, C. R. Bahl, The influence of flow maldistribution on the performance of inhomogeneous parallel plate heat exchangers, International Journal of heat and Mass transfer 60 (2013) 432–439. doi:10.1016/j.ijheatmasstransfer.2013.01.018.

[52] O. Pironneau, On optimum design in fluid mechanics, Journal of Fluid Mechanics 64 (1) (1974) 97–110. doi:10.1017/s0022112074002023.

[53] D. W. Kim, M.-u. Kim, Minimum drag shape in two-dimensional viscous flow, International journal for numerical methods in fluids 21 (2) (1995) 93–111. doi:10.1002/fld.1650210202.

[54] T. Kondoh, T. Matsumori, A. Kawamoto, Drag minimization and lift maximization in laminar flows via topology optimization employing simple objective function expressions based on body force integration, Structural and Multidisciplinary Optimization 45 (5) (2012) 693–701. doi:10.1007/s00158-011-0730-z.

A.6 P6 - Investment casting and experimental test of heat sinks designed by topology optimization

T. Lei, J. Alexandersen, B. S. Lazarov, F. Wang, J. H. K. Haertel, O. Sigmund and K. Engelbrecht

[Under review in ***International Journal of Heat and Mass Transfer***]

.

Investment casting and experimental test of heat sinks designed by topology optimization

Tian Lei[1], Joe Alexandersen[2], Boyan S. Lazarov[2], Fengwen Wang[2], Jan H. K. Haertel[1], O. Sigmund[2], Kurt Engelbrecht[1]*

[1]*Department of Energy Conversion and Storage, Technical University of Denmark, 4000 Roskilde, Denmark*

[2]*Department of Mechanical Engineering, Technical University of Denmark, 2800 Lyngby, Denmark*

*corresponding author: kuen@dtu.dk

Abstract. Topology optimization (TO) is an attractive numerical tool to obtain optimized engineering designs, which has been originally developed for mechanical optimization and extended to the area of conjugate heat transfer. With rapid developments in topology optimization models, promising designs have been proposed and presented recently for conjugate heat transfer problems. However, only a very small number of experimental validations of TO heat transfer devices have been reported. In this paper, investment casting (IC) using 3D stereolithography (SLA) printed patterns, for the first time to our knowledge, is proposed to fabricate 3D metal heat transfer devices designed by TO. Three heat sinks for natural convection are designed by a known topology optimization model and five reference pin-fin heat sinks are constructed for comparison. From those designs six heat sinks are cast in Britannia metal, fully reproducing the complex 3D optimized designs. It shows that SLA-assisted IC is a very promising technology with low cost and high accuracy for fabricating TO metal parts, which is not limited to heat transfer devices and can be extended to other areas such as structural optimization. A natural convection experimental setup is used to experimentally study the performance of the fabricated heat sinks. The results show that the tested TO heat sinks can always realize the best heat dissipation performance compared to pin-fin heat sinks, when operating under the conditions used for the optimization. Moreover, validation simulations have been conducted to investigate the temperature distribution, fluid flow pattern and local heat transfer coefficient for the TO and pin-fin designs, further evidencing that TO designs always perform better under the design conditions. In addition, the impact of the heat sink orientation and radiation are presented.

Keywords. topology optimization, heat sink, natural convection, investment casting, stereolithography printing, experimental test

Nomenclature

Variables			
A	area	*Greek letters*	

$\mathbf{A_m}$	Convective heat transfer area	α	Brinkman penalization coefficient, orientation angle of the heat sink with respect to gravity (polar angle)
c_p	Specific heat	β	Coefficient of thermal expansion, rotation angle of the heat sink (azimuthal angle)
g	gravity	γ	Density field for topology optimization (0 represents solid and 1 represents fluid)
h	Convective heat transfer coefficient	ϵ	Emissivity
I	current	μ	Kinematic viscosity
k	Thermal conductivity	ρ_0	Density of the fluid
p	pressure	ρ	Density
Q	Heat transfer power	σ	Stefan-Boltzmann constant
$q'''(x)$	Volumetric heat generation	*Subscripts*	
		a	Air
T	temperature	conv	convection
		eff	effective
T_m	Metal surface temperature	f	fluid
T_0	Ambient temperature	m	metal
u	Fluid velocity vector	rad	radiation
V	voltage	s	Solid
x_{cond}	Thermal conduction distance		

1. Introduction

Topology optimization is a method that optimizes material distribution within a design domain for maximizing a desired objective under given constraints. TO was originally developed for structural mechanics but has since been applied to different areas such as acoustics, fluid mechanics, conjugate heat transfer, and several others [1, 2]. To set up the optimization, boundary conditions, constraints and an objective function are defined first and the finite element method is usually used to solve the equations describing the physical problem. The design is updated gradually to approach the optima using a variety of algorithms and there exist different TO approaches such as density, level set, topological derivative, phase field, and evolutionary approaches [3].

During the last two decades, several studies have been presented to optimize flow, conduction, convection and conjugate heat transfer problems, which were reviewed in Refs. [4]. Bruns [5] used topology optimization to study steady-state convection-dominated heat transfer problems. Yoon [6] presented a study of 2D thermofluid topology optimization of heat dissipating structures with forced convective heat transfer. Topology optimization of heat and mass transfer problems was investigated by Marck et al. [7] and the authors presented three examples of conjugate heat transfer, including a full bi-objective optimization. Coffin and Maute [8] showed 2D and 3D topology optimization of convective heat transfer problems, using the level set method. In their study, the convection coefficient was assumed constant, but a diffusive model was introduced for the fluid temperature to avoid internal cavities. Koga et al. [9] used topology optimization to design a heat sink system for minimizing the pressure drop in the fluid flow and maximizing the heat dissipation effect. They were viewed in [5] as the first to present an experimental test of a channel heat system designed by TO. Dede [10] presented topology optimization of steady state convection-diffusion heat transfer problems using the commercial simulation software COMSOL Multiphysics [11]. An example of the channel topology was given for minimizing the mean temperature and total dissipated fluid power. Dede et al. [12] further fabricated a

TO heat sink using metal additive manufacturing and experimentally compared its performance with convectional fin / pin-fin heat sinks. Haertel and Nellis [13] applied density-based topology optimization to heat exchanger design assuming a fully developed internal flow. The pressure drop and air-side temperature change were prescribed and the conductance of the heat exchanger was maximized. Alexandersen et al. [14] developed 2D topology optimization of heat sinks for natural convection using the steady-state incompressible Navier–Stokes equations coupled to the thermal convection–diffusion equation through the Boussinesq approximation. This work was further extended to 3D by using a large scale TO framework to design heat sinks with an order of 20-330 million state degrees of freedom in Ref. [15]. In addition, this TO tool was applied to design heat sinks for light-emitting diode lamps [16]. This paper presents a continuing study based on Refs. [14], [15] and [16], in which we design passive heat sinks for natural convection, cast them using the lower cost lost wax method, and implement related experimental tests.

As mentioned above, the experimental validation of TO conjugate heat transfer devices has rarely been done and only two related studies, Refs. [9] and [12], can be referenced to our knowledge, although a large number of topological designs of conjugate heat transfer problems have been presented. This is partly due to the fact that most presented topology optimization works treat rather academic problems with e.g. artificial material properties or unrealistic operating conditions, which cannot be easily converted to a prototype that can be used for experiments. Another issue is that topology optimized heat transfer devices often exhibit complex shapes with fine features, which cannot be fabricated using traditional machining techniques. New developing technologies such as metal additive manufacturing (AM), typically selective laser melting, thus becomes very attractive to fabricate 3D topology-optimized designs. A good example is the work presented by Dede et al. [12], showing that combining metal AM and TO designs is a promising path to develop new heat transfer devices. Although metal AM is becoming a mature technology and has been applied in specific areas including aeronautical and medical industries, there are still some limits to fabricate TO thermal devices using metal AM, such as high cost, limited material selection, potential reduction in thermal properties due to porosity between layers in the structure and difficult post-processing. Therefore, this paper proposes investment casting assisted with stereolithography 3D printing, SLA-assisted IC for short, to fabricate metal devices designed by topology optimization as an alternative.

Investment casting is one of the oldest manufacturing processes, which is still widely used for fabricating jewelry and industrial metal products [17]. In the traditional IC process, the wax pattern is shaped into the desired pattern by hand or injection, which is surrounded with a refractory (the investment) and hardens into the mold. By heating the mold, the wax pattern melts and flows out, forming a continuous cavity inside the mold. Then molten metal at the proper casting temperature is poured into to the mold. After cooling down, the mold is broken and the solidified metal part is removed and post-processed. Due to the usage of wax, this process is often referred to as lost wax casting, especially for jewelry production. However, shaping wax directly into a complicated TO geometry is very difficult with conventional methods. Modern 3D printing technology provides a new approach to fabricate complicated patterns precisely based on wax or castable resin [18]. The latter is a photochemically solidified material and melts out like wax during heating. As both SLA printing and investment casting exhibit high accuracy [17, 18], this process can precisely produce the desired topology optimized metal parts.

Compared with 3D metal AM, SLA-assisted IC has lower cost based on the authors' prototyping experience. The initial cost of the SLA printer and the casting equipment is about 5,000 USD and the casting cost of a 50 cm^3 part is about 30 USD including printing and casting. As a lax comparison, a

typical direct metal laser sintering (DMLS) device costs at least 100,000 USD and the printing cost is beyond 500 USD to prototype the same part [19]. It is anticipated that the cost of SLA assisted IC is still competitive in the mass production level. In addition, IC is a sophisticated technology and offers a wide choice of commonly used high conductive metals and alloys for heat transfer applications [17]. In contrast, 3D metal AM is limited to a few steels, aluminum and titanium alloys [20], and the maximum thermal conductivity is less than 200 W/(m·K). Although significant development in the metal AM has been made recently and part densities above 99% can be achieved by optimizing the process parameters [21], the reduction in heat transfer properties of AM parts is still a concern and more studies are needed, as even 1% porosity can reduce the effective thermal conductivity significantly. Wong [22] reported selective laser melting of heat transfer devices in stainless steel 316L and aluminium 6061. The bulk material of aluminium 6061 has a relatively high thermal conductivity of 170 W/(m·K), while the maximum part density is about 90% after fine tuning of the process, which reduced the overall thermal conductivity to 70 W/(m·K). In comparison, the porosity of IC parts can be precisely controlled depending on the material and process, making it suitable to fabricate fully dense metal products. Another practical concern is post-processing. There may be some avoidable supporting structures left after the DMLS process and removing them can be difficult. In the IC process, the resin supporting structures from the SLA process are removed more easily before casting, which simplifies the post processing and increases the accuracy of the final part. All these characteristics make SLA-assisted IC a promising technique to manufacture complicated TO designs in metals.

This paper applies a known TO solver to design passive heat sinks for natural convection applications and validates them against reference pin-fin heat sinks by both experiment and simulation. It is structured as follows: Section 2 introduces the TO solver and summarizes the topological designs. For the comparison, five reference pin-fin heat sinks are designed using the same available volume and metal volume. Section 3 proposes and applies the SLA assisted IC process to fabricate six heat sinks; Section 4 describes the natural convection test apparatus and the validation model based on COMSOL Multiphysics; Section 5 presents the experimental and simulation results, and compares TO designs with reference heat sinks, and Section 6 gives brief conclusions.

2. Topology optimization of heat sinks

Topology optimization [1] is an iterative design process of distributing a specified volume of material in a given domain by optimizing an objective function and fulfilling a set of constraints. Initially developed for structural mechanics, nowadays the method is applied in a wide range of disciplines like photonics and electromagnetics, fluid mechanics, heat transfer, etc. The design problem considered in this article is inspired by the optimization of heat sinks for LED lamps [14, 15, 16] where the goal is to distribute conductive material by minimizing the volumetric thermal compliance of the system. A detailed formulation of the optimization problem is presented in [15]. Thus, for brevity, only the most important parts are included in the presentation here. A heat source stacked between an aluminum plate and an insulation foam layer form the non-design heat supply part of the optimization setup. A highly conductive material is distributed in a cylindrical design domain attached to the heat source. The numerical modeling of the physical response is based on the Navier-Stokes and convection-diffusion equations where the Boussinesq approximation is introduced to take density-differences due to temperature-variations into account.

$$\rho_0 u_j \frac{\partial u_i}{\partial x_j} - \mu \frac{\partial}{\partial x_j}\left(\frac{\partial u_i}{\partial x_j} + \frac{\partial u_j}{\partial x_i}\right) + \frac{\partial p}{\partial x_i} = -\alpha(x) u_i - \rho_0 \beta (T - T_0) g_i \quad (1)$$

$$\frac{\partial u_j}{\partial x_j} = 0 \quad (2)$$

$$\rho_0 c_p \frac{\partial T}{\partial x_j} - \frac{\partial}{\partial x_j}\left(k(x)\frac{\partial T}{\partial x_j}\right) = q'''(x) \quad (3)$$

where $\alpha(x)$ is the spatially-varying Brinkman penalization coefficient taking values *0* for fluid and ∞ for solid, *k(x)* is the spatially-varying thermal conductivity and $q'''(x)$ is a volumetric heat source term. The equations are defined in the domain $\Omega = \Omega_s \cup \Omega_f$, where Ω_s denotes the part of the domain occupied by solid and Ω_f the part occupied by fluid. The penalization, $\alpha(x)$, ensures zero velocities in the solid, however, for numerical simulations the penalization is relaxed and α takes finite value in the part occupied with solid [15]. Similar to the Brinkman penalization, the conductive coefficient takes the value k_f in the fluid and k_s in the solid. The volumetric heat source $q'''(x)$ is only active within a predefined domain coinciding with the actual heat source.

The above PDEs are discretized using the finite element method, presented in [15, 16], on a regular grid occupying a parallelepiped with dimensions 150 mm × 150 mm × 250 mm connected to a 1 W heat source. The optimization process is iterative and requires a new state solution for each design update. A density field $\gamma(x)$ is utilized to represent the design. The field takes values between zero and one, where $\gamma = 1$ represents the fluid and $\gamma = 0$ represents the solid. With the help of the density, the Brinkman penalization, α, and the conductivity coefficient, *k*, are interpolated between their values for solid and fluid. The gradients of the objective function are obtained by adjoint sensitivity analysis as described in [14, 15].

The optimization problem is regularized using PDE filtering [23, 24]. The computational time is controlled by parallelizing the state solution process and the design updates [25]. For the results presented here runtimes vary from a day on 2000-4000 CPUs to a week on lower computational resources. The density distribution is updated in parallel [26] using the Method of Moving Asymptotes (MMA) [27].

Figure 1 shows three heat sinks designed by TO with different boundary conditions. The first two heat sinks in Figure 1 (a) and (b) are optimized when the heating surface is perpendicular to the horizontal direction, and they are named “horiz1” and “horiz2”, respectively. The optimization domains are chosen as 1/4 and 1/8 of the full size domain for the two designs respectively. Based on this constraint, “horiz1” is bilateral symmetric, while “horiz2” has an 8-fold mirror symmetry geometry. For the heat sink “horiz1”, two wide thin structures grow from the base and bend toward the center near the boundary of the design space, which separate the air flow into three streams. Two tree-like structures are located at the top and bottom positions from the side view, and they fully contact the main flow stream in the middle. The cross sections of these four branches are streamlined in the flow direction, which helps to reduce the flow resistance. Many smaller sub-branches are generated on the crown of the four main trunks, which could dissipate heat in an efficient way. The heat sink "horiz2" consist of two sets of 4 branches: one set of tall branches with elongated cross-sections to guide the flow in and out of the heat sink; and one set of shorter tree-like branches to utilise the central flow as for "horiz1". The performance of "horiz2" is expected to be below that of "horiz1" due to the reduced design freedom imposed by the additional symmetry requirements. Due to the required repetition, the branches cannot be designed as would be optimal, but rather optimal in an averaged sense with respect to the rotation of the design. A more detailed analysis of the design features and their effect can be found in Reference [14] for similar heat sink designs in aluminium

In addition, the third heat sink “vert” in Figure 1 (c) is designed for orientation in the vertical direction and the heating surface is perpendicular to the gravitational direction. The optimization domain is 1/8 of

the full domain, which generates an 8-fold symmetry design. As seen in Figure 1 (c), there are many tiny branches growing from the eight main trunks, and the upper sections of these branches are connected with each other, forming a thin barrel structure, yielding a chimney-effect that increases the mass flow into the heat sink. In the middle of "vert", eight small arrow-like branches grow up from the base of the main trunks, which help to dissipate heat in the center of the heat sink. All the TO heat sinks have a base plate with a thickness of approximately 3 mm.

Five pin-fin heat sinks as seen in Figure 2 are also designed for comparison in both experiment and simulation validations. To allow for a reasonable comparison, the overall size is held the same as the TO designs, which has a diameter D of 65 mm and a height H of 60 mm. All reference heat sinks have 3 mm thick base plates, which is the same value as for the TO heat sinks. In addition, the metal volume V_m for each reference heat sink is controlled to be close to 48.2 cm^3, which is the average volume of the TO designs. A variation of less than 2.5% in the volume exists due to the choice of the pin diameter and pin distribution. The void fraction, or so-called porosity, is defined as $\varepsilon = 1 - V_m/\pi D^2 H$, which is about 0.76 for each heat sink. The pins are 60 mm long for each pin-fin heat sink, giving a total heat sink height of 63 mm, and the pin diameter ranges from 2.7 to 8.7 mm with a step of 1.5 mm, corresponding to a length-to-diameter ratio from 22.2 to 6.9. The details of the heat sinks are listed in Table 1. In general, the pins are distributed evenly. The fin number and fin distance are determined by the constrained volume and porosity. Some outer pins are cut smaller to fit the profile of the design space. Although many studies have been implemented to optimize the pin diameter, length-to-diameter ratio and the porosity, this paper is not intended to optimize all the parameters and only the pin diameter varies for comparison. The TO heat sinks have a similar surface area of about 261-283 cm^2 as seen in Table 1, while the surface area of the reference heat sinks ranges from 255 to 677 cm^2 depending on the pin diameters. Although the surface area of TO heat sinks is lower than that of most of the reference groups, it is anticipated that TO designs will give superior performance, as the optimized flow management contributes significantly to the heat dissipation.

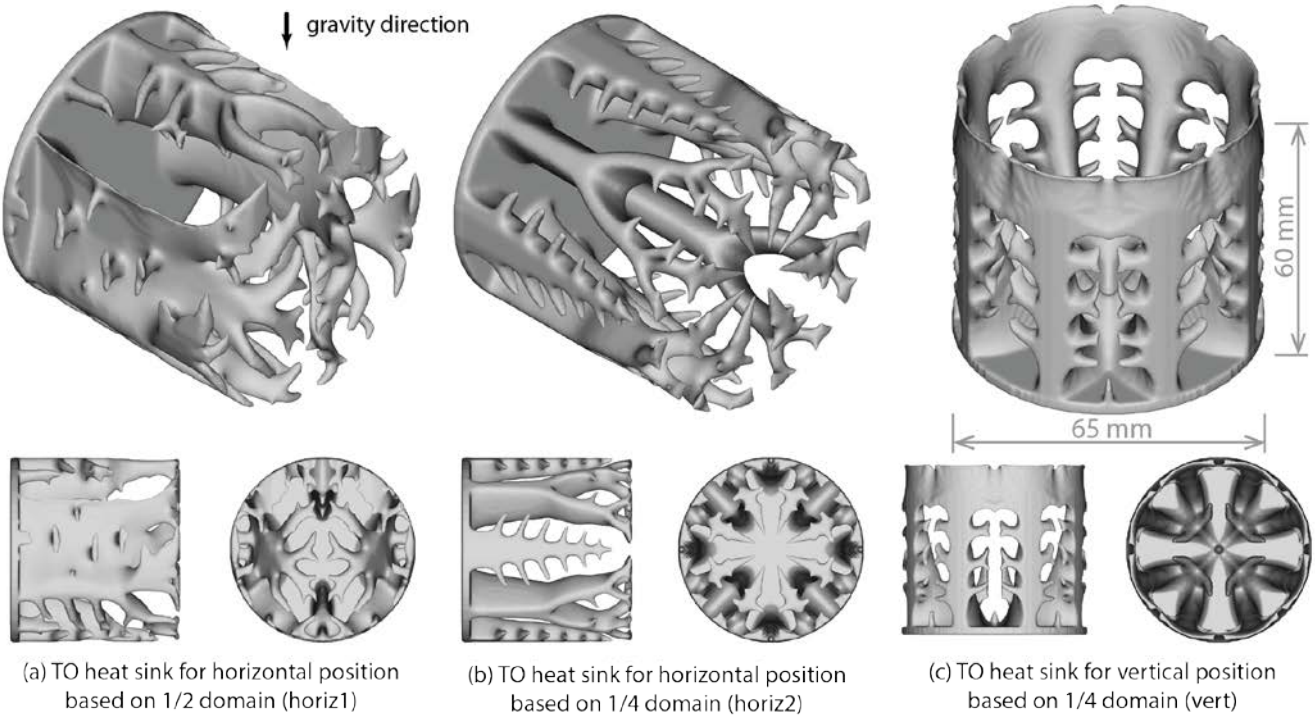

Figure 1. Heat sinks designed by topology optimization

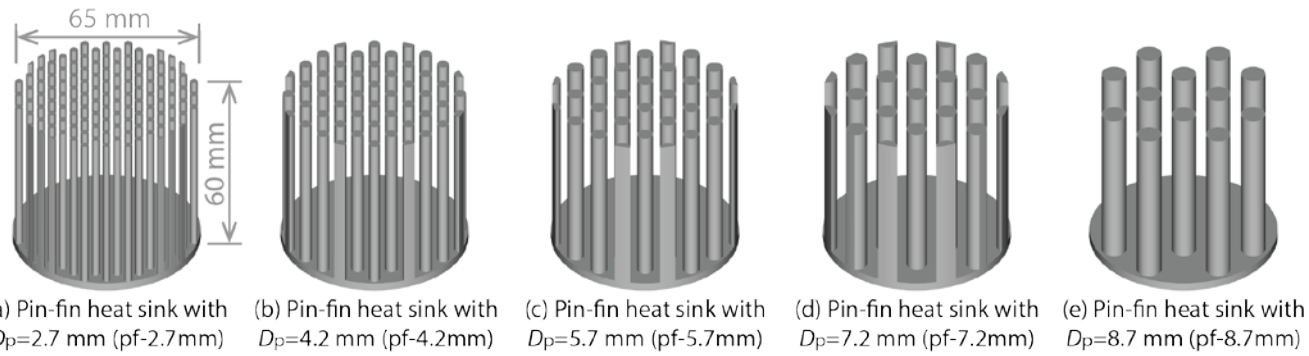

Figure 2. Reference pin-fin heat sinks

Table 1. Characteristics of TO and reference heat sinks

	horiz1	horiz2	vert	pf-2.7mm	pf-4.2mm	pf-5.7mm	pf-7.2mm	pf-8.7mm
Design volume [cm^3]	48.3	47.7	48.6	47.6	48.8	48.8	49.4	48.7
Design mass* [g]	362.3	357.8	364.5	357.0	366.0	366.0	370.5	365.3
Design surface area [cm^2]	265.9	261.4	283.4	677.5	456.2	456.2	378.5	255.1
Design pin number [-]	-	-	-	121	52	32	21	12
Measured mass [g]	364	367	385	-	366	371	358	-

*Calculated based on the design volume and an estimated density of 7.5 g/cm^3

3. Fabrication of TO heat sinks using SLA-assisted investment casting

The process of investment casting used in this study is derived from jewelry fabrication, which is suitable for fast prototyping. It consists of the five steps as seen in Figure 3. The process starts with the 3D SLA printing of the castable resin pattern in step (a), which is an alternative to the traditional wax injection molding or manual sculpting. In the molding process, the resin part that constitutes the heat sink pattern is glued to a wax gating system that controls the metal flow into the mold. The whole pattern is then fixed inside a steel flask. A plaster slurry is poured into the flask to form the mold in step (b) and it is degassed to remove bubbles before hardening. In step (c), the mold is placed in a furnace and the temperature is increased in steps for melting and burning out the castable resin and wax. The mold is then slowly cooled, and when it reaches the required casting temperature, the molten metal is poured into the cavity through the gating system, forming the desired metal part in step (d). Finally, the metal part is demolded after cooling down (step (e)) and it is post-processed, including removing the gating structures, cleaning and polishing, etc.

We design and cast the heat sinks based on the Britannia metal (Sn-Sb-Cu alloy), which is a tin-based alloy consisting of 92% tin, 6% antimony and 2% copper. The thermal diffusivity of Britannia metal is measured using a Netzsch 457 Laser Flash Apparatus, which is about 27.3 mm^2/s at room temperature. The thermal conductivity is estimated as 47 W/(m·K) using an estimated density of 7500 kg/m^3 and heat capacity of 230 J/(kg·K). It has a low casting temperature of about 260 °C and it is relatively easy to avoid casting voids that can increase the porosity of the finished part.

Figure 4 (a) and (b) show the TO design "horiz2" and the resin pattern printed by a Formlabs SLA printer, i.e. FORM2. To avoid deformation in the casting procedure, two rings with guiding channels are added onto the top of the heat sink branches. Without these constrained rings, the branches trended to contract toward the center and the thin base plate bent in a preliminary test. The finished plaster mold is presented in Figure 4 (c), and there is a spout in the middle guiding the liquid metal flow. After casting,

the TO heat sink in Figure 4 (d) shows a yellow/golden appearance and all the details from the TO design are captured accurately. The sprue structure is removed and the bottom plate is milled flat. In total, three TO and three reference heat sinks are fabricated as showed in Figure 5. The heat sink is partly polished, showing a silvery surface. The fabricated heat sinks show that SLA assisted IC has a high accuracy, making this technique suitable for prototyping TO designs. The mass of the fabricated heat sinks is measured and listed in Table 1. The mass of the heat sink "vert" is about 4% larger than the prediction due to fabrication error, and the others have similar mass with a variation smaller than 3%.

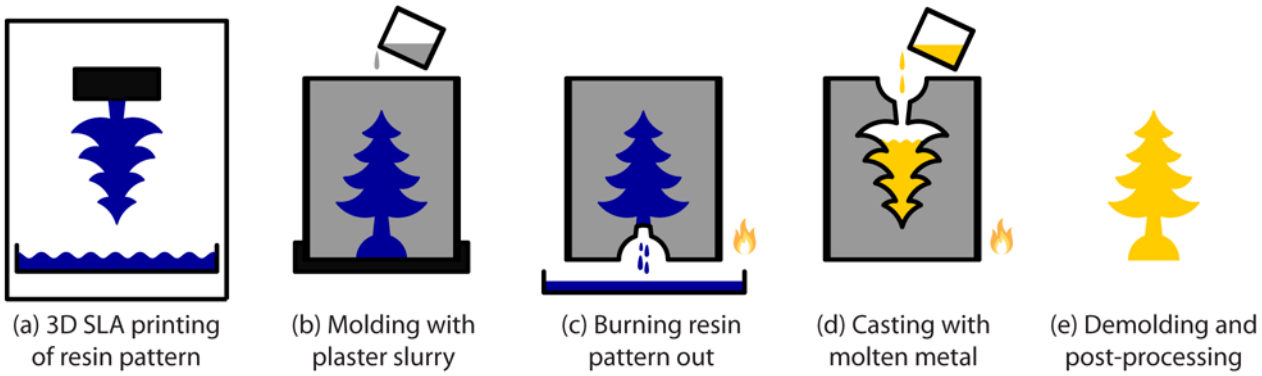

Figure 3. Process of SLA assisted investment casting

(a) TO design (b) Resin pattern (c) Plaster mold (d) Metal heat sink

Figure 4. TO design of "horiz2", resin pattern by SLA printing, plaster mold, and heat sink in the Britannia metal (Sn-Sb-Cu alloy) before gates are removed.

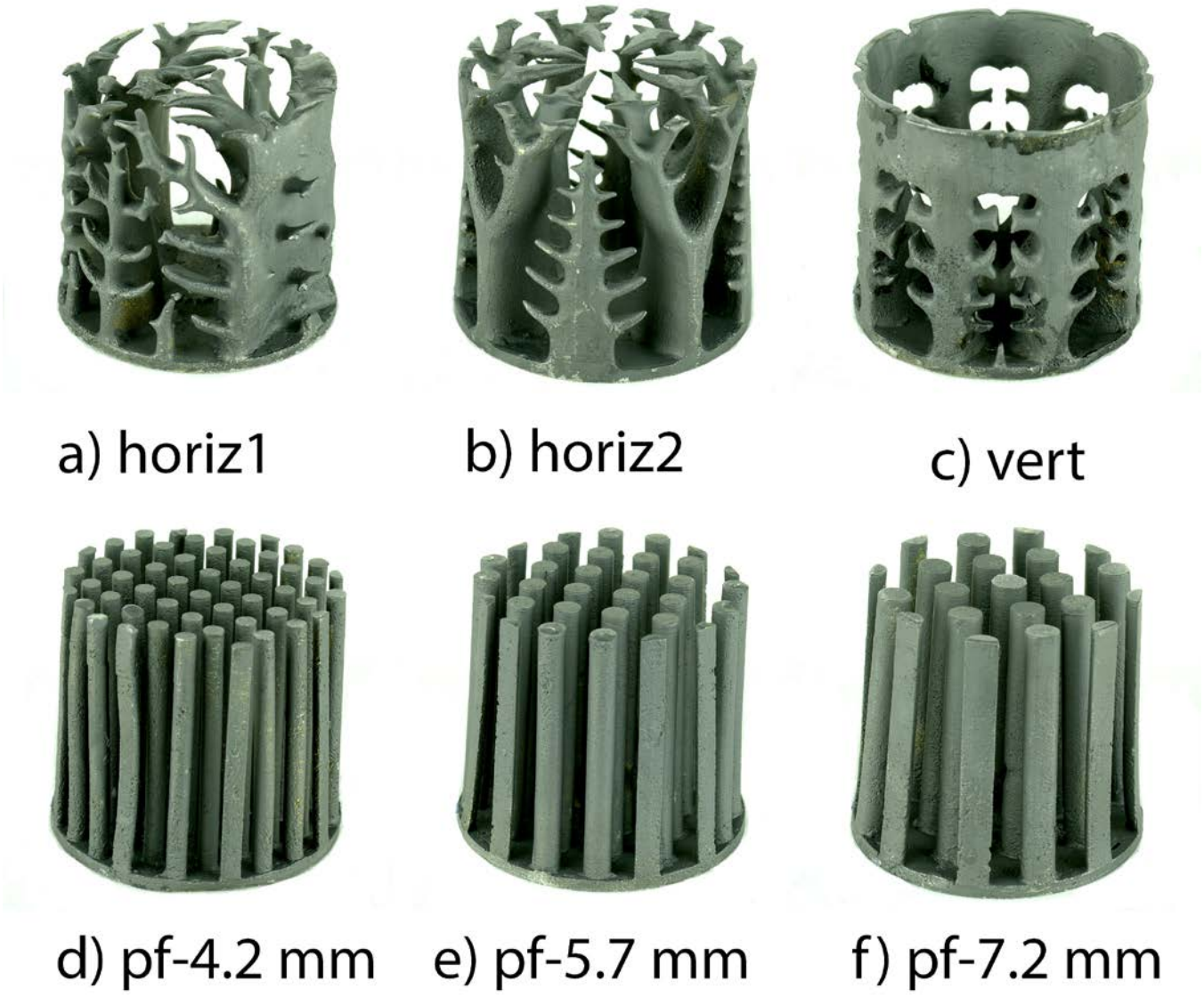

Figure 5. TO and reference heat sinks fabricated by SLA-assisted investment casting. All heat sinks are coated with graphite paint for IR measurements.

4. Experimental apparatus and validation simulation model

This section introduces the methodology for validating the TO heat sinks based on both experiment and simulation. In both methods, the heat sinks are set in an open environment for natural convection test as the TO model does. A heat source is applied on the aluminum heating plate attached to the bottom of heat sinks to impel the natural convection flow. The bottom of the heating plate is insulated and a vast majority of the heat is conducted through the conductive metal and then to the environment by convection. Based on this concept, a natural convection test apparatus is constructed and a validation simulation model based on COMSOL Multiphysics is built as described below.

4.1. Experimental setup

As seen in Figure 6, the test apparatus consists of two main parts: the outer shield and the test section supported by a tripod. The outer shield is a round cylinder with an open top and bottom with a diameter

of about 1 m, which is about 15 times larger than the heat sink diameter. A preliminary experimental test shows the outer shield can effectively reduce the flow interruption from the devices and human activity. It is also noted that the test results do not change with or without the outer shield, if the open environment is held calm and stable. Still, the outer shield is used although we reduce the interruption to the lowest level. Another reason for using the shield is that it can largely reduce reflections disturbing infrared thermal imaging conducted in the test. As seen in Figure 6 (a), a 200 mm long rod is made of fiberglass reinforced plastic and fixed to the tripod for supporting the test section, which is also used to reduce the flow disruption by the tripod. The orientation and position of the heat sink are changed by adjusting the tripod platform. An Omega KHLV 101-10 thin film heater is pressed and attached to an aluminum heating plate as the heat source. The 52 mm round aluminum plate is mounted to the bottom of the heat sink. Thermal paste is applied on contacting surfaces to reduce thermal resistance. The whole heat system is installed on the insulation housing based on a four-point supporting structure using small nylon screws. There is a gap between the heat section and the base, forming an air insulation to reduce the heat loss. The insulation housing is made of fiberglass reinforced plastic and Armaflex insulation foam is filled inside. The insulation housing and the insulation foam have a thermal conductivity of about 0.5 and 0.037 W/(m·K), respectively.

Resistance temperature detectors (RTDs) PT100 from Measurement Specialties, Inc. are used to acquire the temperature on the aluminum heating plate and the heat sink surface, as seen in Figure 6. These micro RTD sensors have a dimension of 2×2 mm and the measurement error is ±0.3 ºC. The temperature data is recorded by a National Instruments (NI) 9216 PT100 RTD module with a NI cDAQ 9181 acquisition device. The thin film heater is power by a TTi EL302P power supply unit, which has meter accuracies of 0.1% in voltage and 0.3 % in current. Figure 6 (d) shows that an infrared FLIR SC5000 thermal imaging camera is set up for capturing the temperature distribution on the heat sink surface.

In the test, the power input Q and the temperatures on the heating plate and the branches are measured. Heat is dissipated from the heat sink to the open environment by convection (Q_{conv}), radiation (Q_{rad}) and conduction through the insulation, which is also the loss (Q_{loss}). Therefore, we have

$$Q = IV = Q_{\mathrm{conv}} + Q_{\mathrm{rad}} + Q_{\mathrm{loss}} \quad (4)$$

where V and I are the voltage and current applied to the thin film heater.

The convection term Q_{conv} is:

$$Q_{\mathrm{conv}} = \int h_{\mathrm{local}}(T_{\mathrm{m}} - T_{\mathrm{a}})\mathrm{d}A_{\mathrm{m}} \quad (5)$$

where h_{local}, T_{m}, T_{a} and A_{m} are the local heat transfer coefficient, metal surface temperature, air temperature and surface area for convection.

Using the method presented in Ref. [23], the heat transfer by radiation between the heat sink and the imaginary air enclosure surface is:

$$Q_{\mathrm{rad}} = \frac{A_{\mathrm{a}}\sigma\left({T_{\mathrm{m}}}^4 - {T_{\mathrm{a}}}^4\right)}{\frac{A_{\mathrm{a}}}{A_{\mathrm{m}}}\left(\frac{1-\epsilon_{\mathrm{m}}}{\epsilon_{\mathrm{m}}}\right)+1} \quad (6)$$

where σ, ϵ_{m}, A_{m} and A_{a} are the Stefan–Boltzmann constant, emissivity of the metal surface, surface area of the heat sink and surface area of the imaginary air enclosure, respectively. The imaginary air enclosure here is the domain with a diameter of 65 mm and height of 60 mm.

The loss is mainly the conduction through the insulation housing. Thus Q_{loss} becomes:

$$Q_{\mathrm{loss}} = \int k_{\mathrm{eff}} \frac{T_{\mathrm{m}} - T_{\mathrm{a}}}{x_{cond}} \, \mathrm{d}A \qquad (7)$$

where k_{eff}, x_{cond} and A are the effective thermal conductivity, distance and surface area for conduction.

In this study, Q_{rad} and Q_{loss} are estimated at about a total of 0.19 W (0.075 W for Q_{rad} and 0.115 W for Q_{loss}) out of the total 1.08 W of the experimental heating power. For different heat sinks, these ratios do not change much, as the temperature T_{m} is at the same level. Therefore, a direct way of evaluating the heat sinks is to compare the temperature at the heating plate, T_{h}. Lower T_{h} represents lower thermal resistance which corresponds to better heat dissipation performance. In principle, the overall heat transfer coefficient and the dimensionless Nusselt number can be deduced from the measured surface temperatures. However, the temperature distribution on TO heat sinks is unique and the measurement at different positions is difficult, due to the complicated geometry. Therefore, we mainly compare the temperatures at the heating plate and the overall heat resistance in the experiments. In addition, simulations could provide more details including the local heat transfer coefficient and the average heat flux, which will be discussed in Section 5.

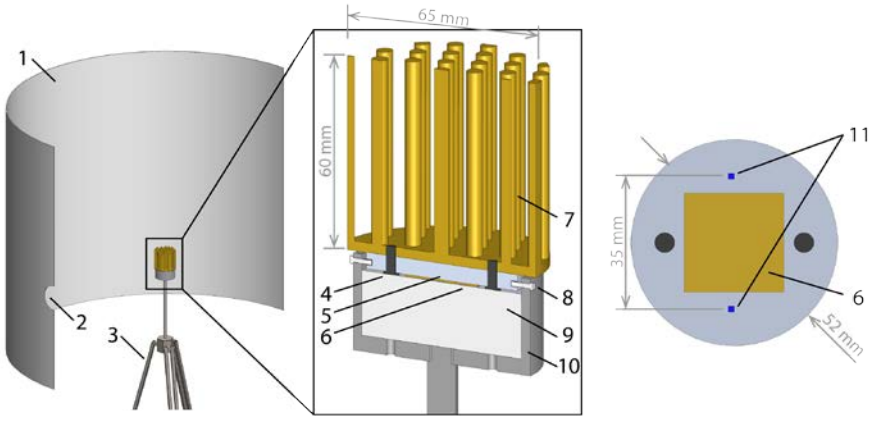

(a) Schematic of the test apparatus (b) Schematic of the heating system with insulations (c) Schematic of the aluminum plate and RTD sensors

(d) Photograph of the test apparatus (e) Photograph of the heating system

Figure 6. Schematic diagrams (a)-(c) and photographs (d)-(e) of the heat sink test apparatus (1, outer shield; 2, viewport for IR camera; 3, tripod; 4, steel screw; 5, aluminum heating plate; 6, thin film heater; 7, heat sink; 8, nylon screw; 9, insulation foam; 10, fiberglass housing; 11, RTD temperature sensors)

4.2. Simulation model

As mentioned above, 3D models of the analyzed heat sinks are implemented in COMSOL Multiphysics, as seen in Figure 7. The modeling in COMSOL performed with the same approach as described in section 2. However, solid and fluid domains are modeled separately with explicit representation of the solid-fluid boundary in the validation model [29]. That is, we set the buoyancy force to $\rho_a \beta (T - T_0) g$ in the *y*-direction, where ρ_a is the density of ambient air and g is gravity. The air domain is separated into two subdomains, which are concentric cylinders of different heights: one is the inner domain surrounding the heat sink which is resolved with finer mesh; the other domain is further away from the heat sink and is resolved with a coarser mesh. The inner domain has a diameter and height of 200 mm. The outer domain has a diameter of 600 mm and height of 800 mm. The bottom of the inner domain is 200 mm above the bottom of outer domain. The lateral surface of the outer air domain is set as an open boundary; the bottom of both domains is set as an open boundary as well; the top is set as outflow boundary. The test section is set inside the inner air domain. As in the experimental setup, the heater, aluminum plate and heat sink are mounted together and the heat section is insulated by the housing and foam inside. Two copper wires that lead to the heater are also considered as shown in Figure 7(b) and the air gap is simulated using a thin film boundary. In the simulation, user-defined material properties are used to capture more details.

A tetrahedral mesh with a linear shape function is used and the total number of elements is approximately 0.6-1.5×10^6 depending on the complexity of the heat sink geometry. Four different mesh densities have been applied to discretize the domain and the mesh resolution increases from the outer air domain to the inner heat sink. A mesh independence study is implemented, showing that the predicted temperatures change insignificantly when further refining the mesh. A transient solver is used and a time period of 3000 s is simulated, which allows the heat sink to reach a steady state. In this study, we only address the comparison study at the steady state.

As mentioned above, three TO heat sinks are designed based on two different orientations, and the unique geometry guides the flow in different ways. Therefore, we investigate the effect of the orientation on the heat sinks in both experiment and simulation, where the orientation angle α is defined as seen in Figure 7 (d). In addition, the heat sink “horiz1” has the two airplane flap-like branches and the flow pattern will be significantly affected by the rotation angle β as seen in Figure 7 (e). Therefore, the impact of the rotation angle is also studied for “horiz1”.

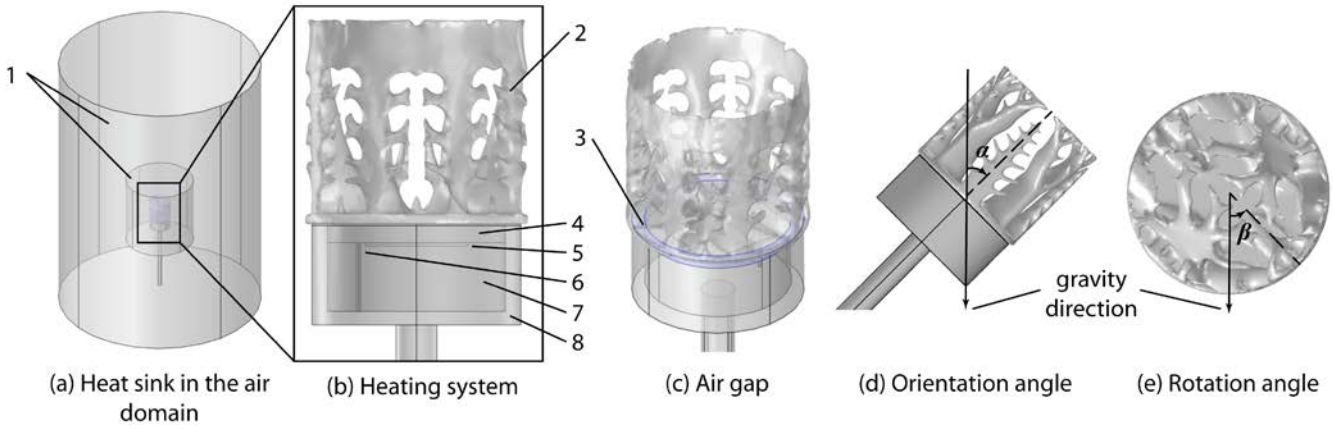

Figure 7. Heat sink validation model using the Boussinesq approximation based on COMSOL Multiphysics® (1, air domains; 2, heat sink; 3, air gap; 4, aluminum heating plate; 5, thin film heater; 6, copper cables; 7, insulation foam; 8, insulation housing)

5. Results and discussion

For each experimental test, a constant heating power is applied and the heat sink is heated up to drive the natural convection flow. Until the heat sink reaches a steady state, the temperatures at the aluminum heating plate are recorded for comparison. The temperature difference between two measured points on the heating plate as seen in Figure 6(c) is less than 0.3 ºC, as the aluminum is highly conductive. Therefore, only the average value of the two measured temperatures is presented below. Simulations also predict small temperature variations across the aluminum plate, indicating that using the average of the measured temperatures is sensible.

5.1. Comparison between TO and pin fin heat sinks

5.1.1. Temperature span for TO and pin fin heat sinks

In total, all eight heat sinks listed in Table 1 are simulated and six are tested experimentally with two orientation angles α=0º and 90º. The largest and smallest diameter pin-fin heat sinks listed in Table 1 were not fabricated because their predicted performance was lower than the others. Although the TO heat sinks are designed based on a heating power of 1.0 W, higher heating power up to 7.9 W is applied for testing. Figure 8 presents the temperature spans, ΔT, between the aluminum plate and the open air predicted by simulation and experimentally measured. The respective values are plotted in bars and dots. The air temperature T_a in the simulation is 16.5 ºC and it ranges from 15-23 ºC in the measurements as they were conducted over several days. In each experimental test, T_a is stable. Multiple dots for the same heat sink represent repeated experiments. The dashed lines represent the average value of measured ΔT for "vert" at α=0º and "horiz1" at α=90º, respectively, which are expected to be the best heat sinks for the two different orientation angles.

The simulations in Figure 8 (a) show that "vert" realizes the lowest ΔT of about 6.1 ºC compared to all other tested heat sinks. For the two TO heat sinks optimized for α=90º ("horiz1" and "horiz2"), ΔT is significantly higher. Within the five reference heat sinks, the best performance is obtained with either "pf-4.2 mm" or "pf-5.7 mm" for different heating powers. Too small or too large pin diameter increases ΔT and the overall thermal resistance, which is defined as $\Delta T/Q$. The simulations show that too small pins with a dense distribution increase the flow resistance of "pf-2.7 mm". Thus, the velocity between

pins in the middle is much smaller than that for the other heat sinks, which also increases the temperature and forms a hot spot in the center of the heat sink. As a result, the overall heat resistance increases. For the heat sink "pf-8.7 mm" with large pins and a sparse pin distribution, the heat transfer area is largely reduced as seen in Table 1. Although the air flows freely through the pins, the thermal resistance of "pf-8.7 mm" is still high, reflected by the large temperature span. This indicates that the TO design "vert" guides the air flow in a better pattern with the same heat transfer area, realizing better heat transfer coefficient. With increasing heater power, the optimal pin diameter changes from 5.7 to 4.2 mm, showing that smaller pins and a denser distribution are preferable for high heating powers. The simulations verify that "vert" performs best compared to the reference heat sinks when the heating power is 1.1 W or 3.0 W. The performance of "vert" is slightly lower than the optimal reference design for Q= 5.0 and 7.9 W; however, the applied input power is much higher than the 1 W for which "vert" is optimized.

The experimental data shown in Figure 8 (a) further verifies that "vert" is a superior design within all the heat sinks when the heating power is 1.1 W. The average ΔT of "vert" is also the lowest for higher heating powers, although the measured ΔT varies with a variation less than 4%. In general, the experimental data follows the trends predicted by simulations well, and the average variation is within 8%. Possible reasons for the deviation may be the estimated radiation emissivity, material properties, fabrication variation and measurement error, etc.

The simulation and experimental results for α=90º are presented in Figure 8 (b). In both simulations and experiments, "horiz1" is always the best design for different heating powers up to 5.0 W. For Q=7.9 W, the modelled and measured ΔT of "horiz1" and "pf-5.7 mm" are similar, showing a similar heat dissipation performance. In contrast, "horiz2" exhibits a ΔT slightly higher than that of "horiz1", which is the second best. Although both "horiz1" and "horiz2" are designed by TO, "horiz1" is always better due to its unique design and larger freedom based on 1/2 of the full domain as seen in Figure 5. Because "vert" was optimized for α=0º, it does not perform well with α=90º, neither in experiments nor simulations. This is the same for "horiz1" and "horiz2" with α=0º. This experimental cross validation shows that the TO heat sinks do give the best performance under the conditions for which they are optimized. For the reference heat sinks, the optimal design changes from "pf-7.2 mm" to "pf-5.7 mm" with increasing heating power, when the orientation angle is 90º.

It can be concluded from the presented data that the TO designs always perform better than the reference heat sinks in both experiments and simulations at the working conditions for which they are optimized. Their superior performance can also extend to higher values of heating power. The following section will present a detailed analysis of the TO and reference designs.

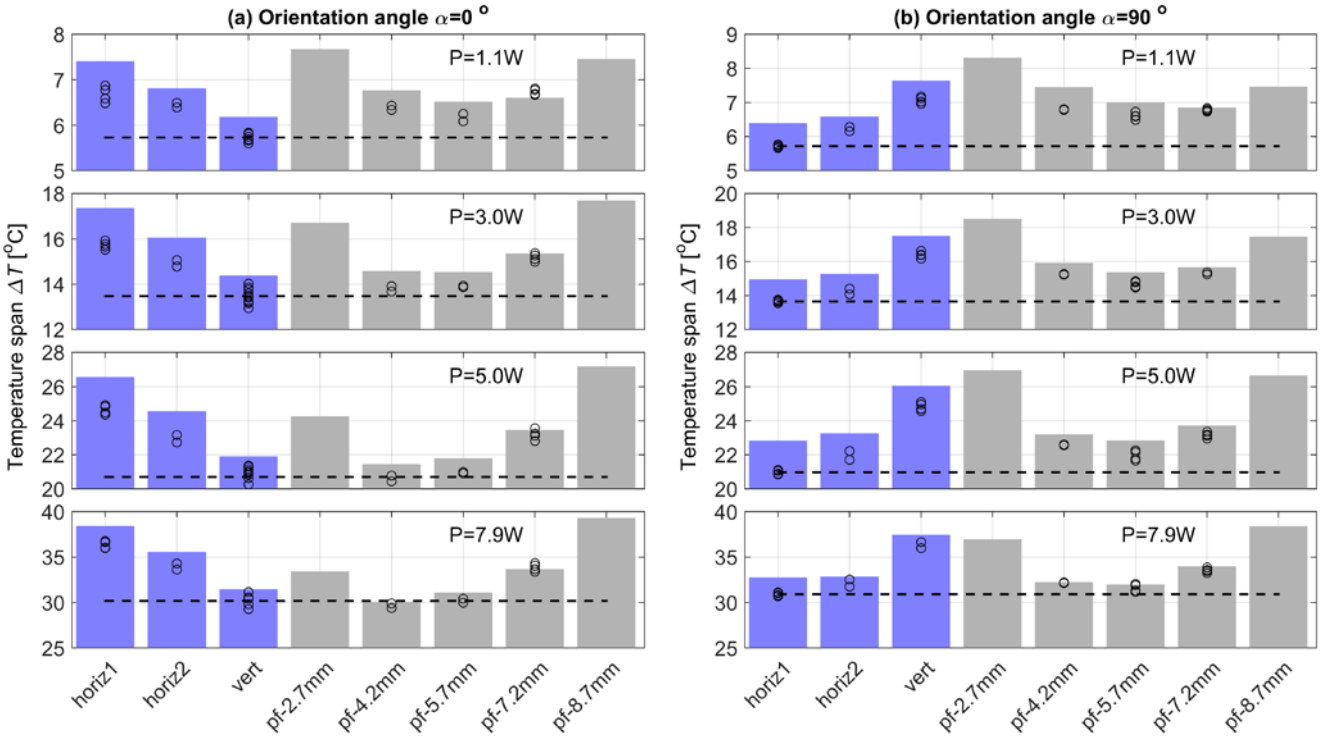

Figure 8. Temperature spans between the aluminum heating plate and the ambient for TO and pin fin heat sinks. Blue bars represent simulation results of TO heat sinks; grey bars represent simulation results of pin fin heat sinks; dots represent experimental results; a dashed line represents the average value of repeated experiments for "vert" with α=0º or for "horiz1" with α=90º.

5.1.2. Analysis of TO and pin fin heat sinks with α=0º

For this analysis, we present the temperature distribution predicted by simulation for a 1 W power dissipation (corresponding to the conditions for optimization), experimentally measured temperature distribution, velocity field and local heat transfer coefficient predicted by simulation of "vert" and "pf-5.7 mm" as seen in Figure 9 and Figure 10. The "pf-5.7 mm" is chosen as a benchmark because it gives the best pin fin performance at 1.1 W. As the heat sink has a metallic and reflective surface, the reflection causes difficulties to capture a good thermograph using the infrared thermal imaging camera. Therefore, we paint the heat sink using graphite spray. This unavoidably increases the emissivity to approach 1.0 which increases the percentage of heat dissipation by radiation. Therefore, the maximum ΔT presented in the following thermographs is lower than the simulation results and those results presented in Figure 8. Another reason for a lower ΔT is that the outer profile shown in the thermographs generally has a lower temperature than the inner. This effect caused by the graphite painting is studied in Section 5.3. Figure 9 (a) shows model prediction for the temperature of the heat sink surface and the air in the central cross sectional panel. The surface temperature exhibits a gradient from the base plate to the top ring structure. The air temperature distribution in the middle looks like a torch, showing that the air carrying the heat in the middle flows upward through the central part of the heat sink. The thermograph captured by the infrared camera in Figure 9 (b) shows a similar temperature distribution as the simulation. It also shows that the insulation performs as expected, based on the temperature profile of the support structure below the heat sink. The air from the open environment flows through the gaps between branches into the middle, exchanging heat with the metal as seen in Figure 9 (c). The hot air concentrates in the middle and flows upward, forming a similar torch-shape distribution as the air

temperature. Figure 9 (d) presents the local heat transfer coefficient at the heat sink surface, which is $\delta Q_{\mathrm{conv}}/(\Delta T \delta A)$ at a local position. It is seen that the local heat transfer coefficient of the outer surface is higher than that at the inner surface, and the highest h_{local} is found on the tips of the sub-branches. The average h_{local} for the heat sink "vert" is 6.27 W/(m^2·K). We also summarize the information of the total heat transfer rate via convection and average energy flux via convection in Table 2, which is about 0.89 W and 35.5 W/m^2, respectively. The radiation dissipates about 0.08 W and the conduction through the insulation housing is about 0.11 W.

.

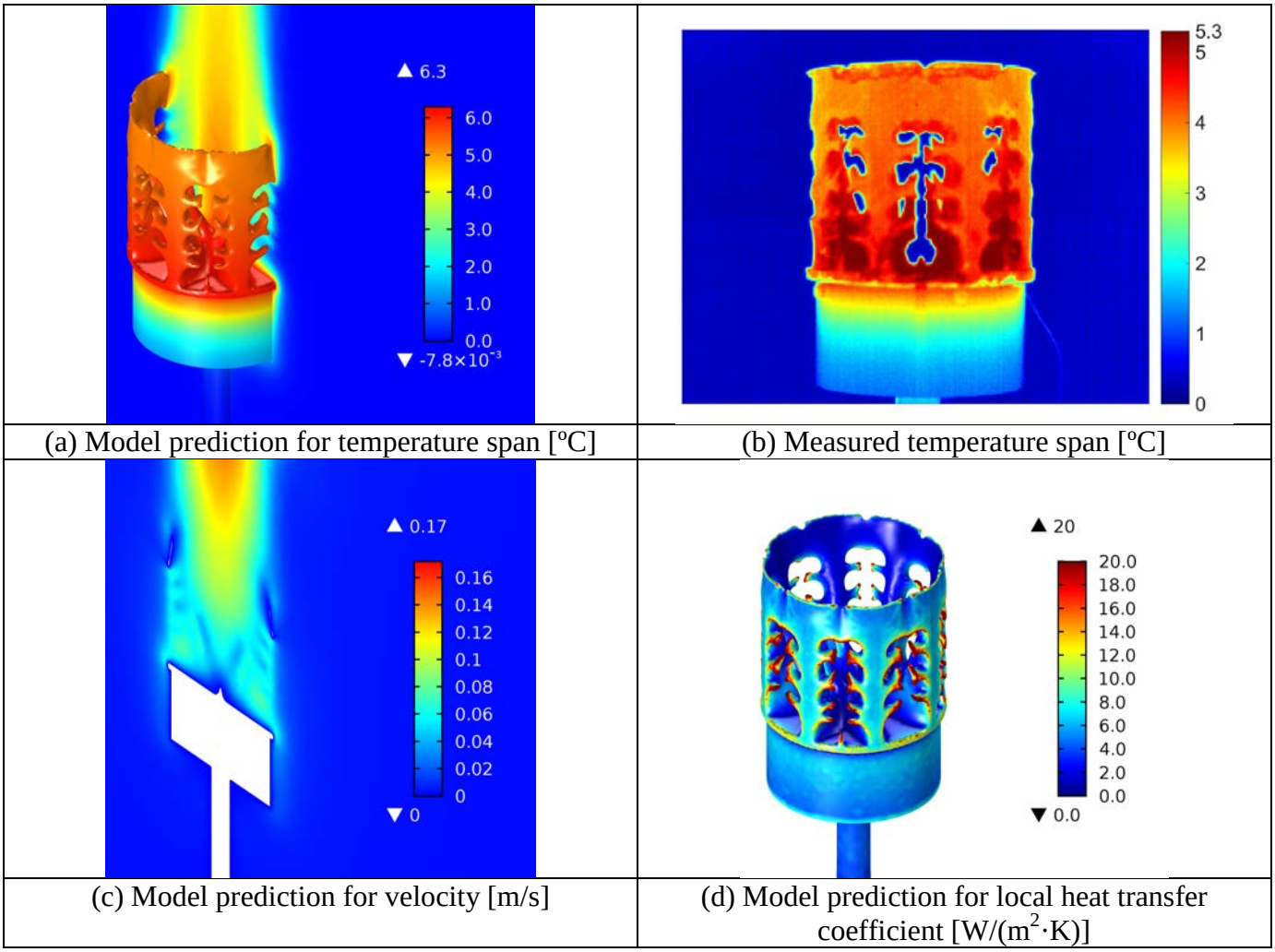

(a) Model prediction for temperature span [ºC]

(b) Measured temperature span [ºC]

(c) Model prediction for velocity [m/s]

(d) Model prediction for local heat transfer coefficient [W/(m^2·K)]

Figure 9. (a) - (b) modelled and measured temperature span, (c) modelled flow velocity and (d) modelled local heat transfer coefficient of the heat sink "vert" with α=0º

Table 2. Parameters of the heat sink surface in the validation simulation

	α=0°		α=90°		
	vert	pf-5.7mm	horiz1	horiz2	pf-5.7mm
Total heat transfer rate by convection [W]	0.89	0.88	0.90	0.90	0.88
Average energy flux [W/m^2]	35.5	25.2	38.7	39.1	25.4
Average h_{local} [W/(m^2·K)]	6.27	4.47	6.86	6.65	4.24
Designed surface area [cm^2]	283	456	266	261	456

For the heat sink “pf-5.7 mm”, both modelled and measured temperatures in Figure 10(a) and (b) show that the inner pins have a higher temperature than those located further toward the outer edge. The cut pins on the edge have a much lower temperature than those in the middle. From Figure 10(a) and (c), it is observed that the air carrying the heat flows upward like “vert” does. In contrast, the flow velocity at the bottom of “pf-5.7 mm” is very small, meaning the air here flows slowly and it does not transfer heat well with the pins through convection. Figure 10 (a) shows that the surface of the outer pins has a higher h_{local} than the inner ones, and the average h_{local} is about 4.47 W/(m^2·K), which is lower than 6.27 W/(m^2·K) for “vert”. In addition, the total heat transfer rate of “pf-5.7 mm” is the same as “vert”, meaning that the radiation and the conduction loss are almost the same but “pf-5.7 mm” needs a larger temperature span to transfer the same amount of heat. With a larger surface area, the average energy flux of “pf-5.7 mm” is also lower that “vert”. The comparison shows the flow guided by the optimized geometry contributes largely to the heat dissipation and the TO design gives a good optimized structure for maximizing performance.

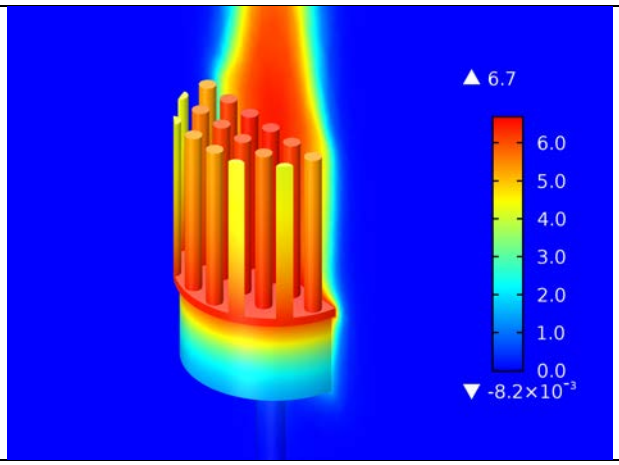

(a) Model prediction for temperature span [K]

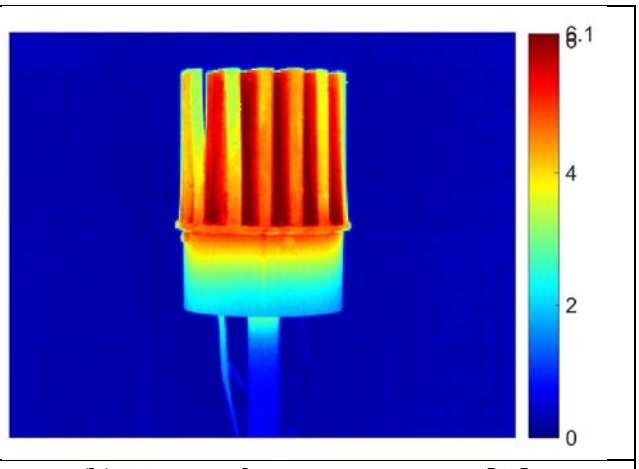

(b) Measured temperature span [K]

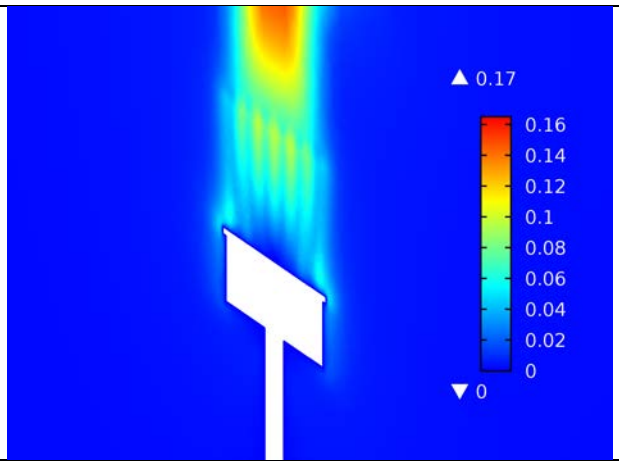

(c) Model prediction for velocity [m/s]

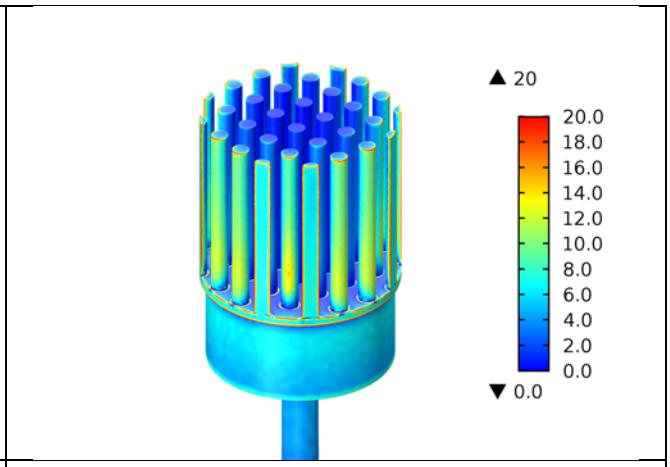

(d) Model prediction for local heat transfer coefficient [W/(m^2·K)]

Figure 10. (a) - (b) modelled and measured temperature span, (c) modelled flow velocity and (d) modelled local heat transfer coefficient of the heat sink "pf-5.7mm" with α=0º

5.1.3. Analysis of TO and pin fin heat sinks with α=90º

For the orientation angle α=90º, the three heat sinks "horiz1", "horiz2" and "pf-5.7 mm" are presented in detail. The modelled surface temperature distribution in "horiz1" is presented in Figure 11(a). There is a temperature gradient from the base plate to the crown in the heat flux direction. At the same time, the branches at the lower position have a lower temperature than those on the top, as the cold air first contacts and exchanges heat with the branches at the bottom. This behavior is also observed in the measured thermograph in Figure 11(b), although the measured value is lower than the modelled temperature span. As seen in Figure 11(c), the two main branches have a cross section similar to an airplane flap. These branches gather the airflow into the center and the air accelerates due to the buoyancy effect, showing a very efficient geometry for transferring heat by natural convection. The crown of "horiz1" has more sub-branches which dissipate the heat efficiently (see h_{local} in Figure 11 (d)). A large local heat transfer coefficient is also seen at the lower position. The average h_{local} is about 6.86 W/(m^2·K). The energy flux is close to that for the heat sinks tested with α=0º, indicating that the radiation and the conduction loss for different heat sinks are similar.

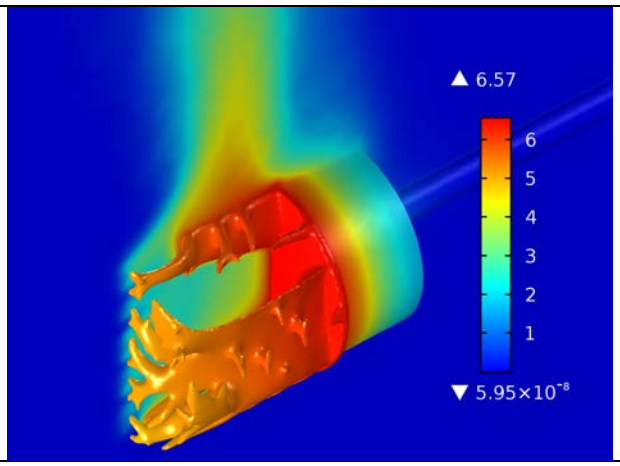

(a) Model prediction for temperature span [K]

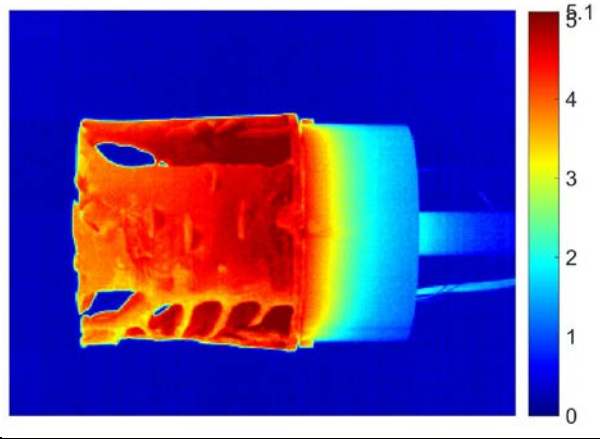

(b) Measured temperature span [K]

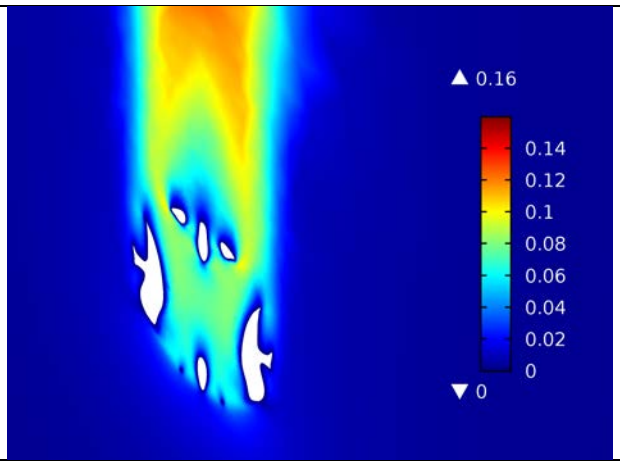

(c) Model prediction for velocity [m/s]

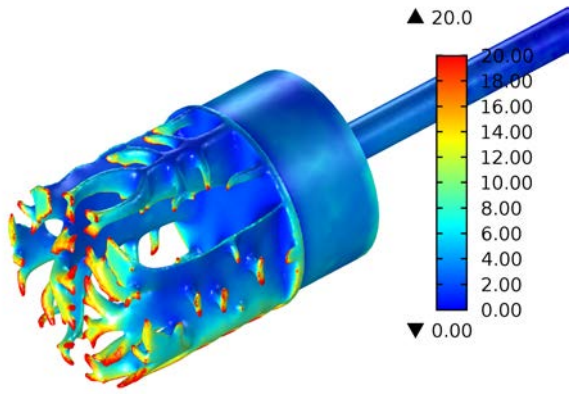

(d) Model prediction for local heat transfer coefficient [W/(m^2·K)]

Figure 11. (a) - (b) modelled and measured temperature span, (c) modelled flow velocity and (d) modelled local heat transfer coefficient of the heat sink "horiz1" with α=90^o

Simulation and experimental results of the heat sink "horiz2" are given in Figure 12. As mentioned before, this heat sink is optimized based on a smaller domain, which is 1/4 of the full size. Therefore, the vertical flow is not guided to be fully optimal for heat transfer resulting in a slightly poorer performance than that of "horiz1", as shown in Figure 8(b). Both the temperature distribution predicted by simulation and experimentally measured show that the gradient develops from the base plate to the crown and from lower to higher positions. The flow velocity as shown in Figure 12 (c) explains why this design performs worse than "horiz1". The lee side of the branches in "horiz2" is significantly larger than that of "horiz1", and many branches are not streamlined in the flow direction for this orientation, which blocks natural convection flow paths. This results in a lower air flow through the heat sink compared to "horiz1" which again lowers the overall heat transfer performance of this design. Due to the additional symmetry requirements, not all branches are streamlined in the flow direction, but instead are a form of averaged designs for multiple rotations, as discussed in Section 5.2. Although the measured temperature span of "horiz2" is slightly higher than "horiz1", it still shows how the boundary conditions affect the topological design and how the TO designs reflect the physics principles incorporated in the model.

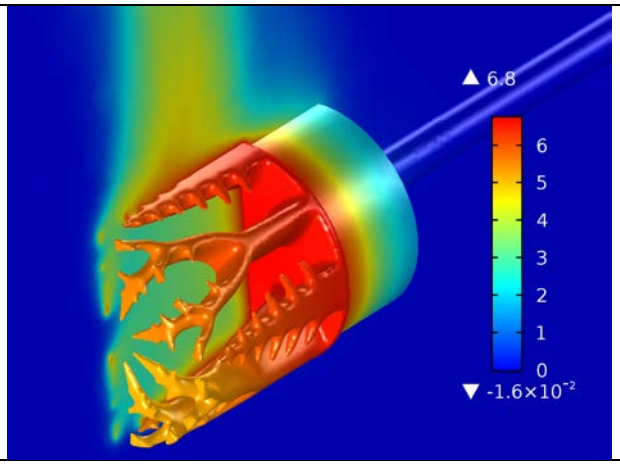

(a) Model prediction for temperature span [K]

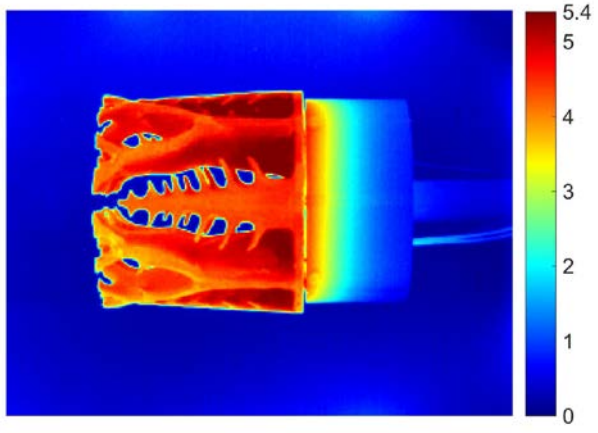

(b) Measured temperature span [K]

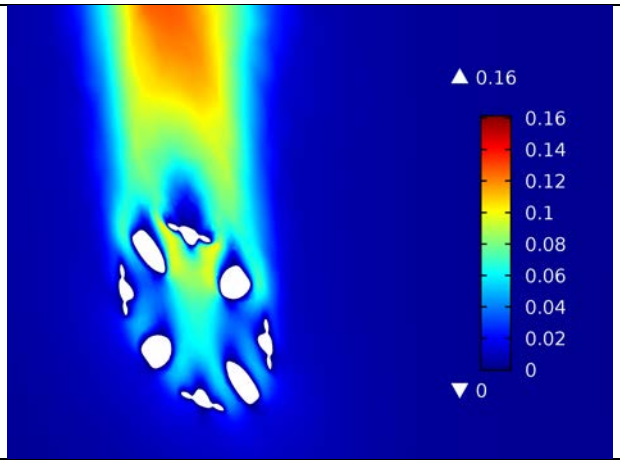

(c) Model prediction for velocity [m/s]

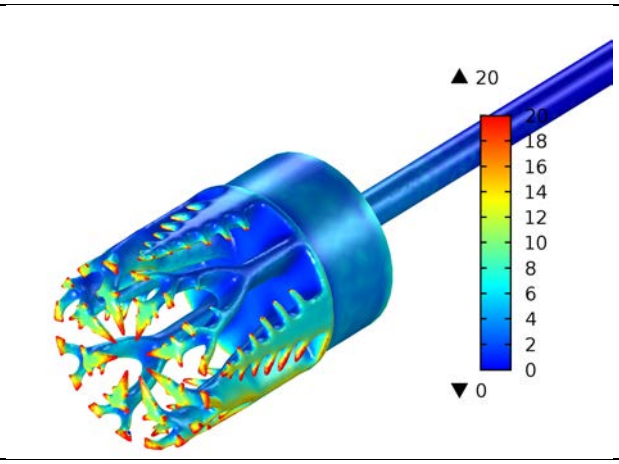

(d) Model prediction for local heat transfer coefficient [W/(m^2·K)]

Figure 12. (a) - (b) modelled and measured temperature span, (c) modelled flow velocity and (d) modelled local heat transfer coefficient of the heat sink "horiz2" with α=90º

To compare the TO designs to one of the reference heat sinks, simulation and experimental results of the heat sink "pf-5.7 mm" are provided in Figure 13. It can be seen that the behavior of the temperature distribution is similar to that in "horiz1" or "horiz2". Since the experimentally measured temperature span is shown in the side view, the maximum value is much lower than that in the simulation. The flow distribution depicted in Figure 13(c) indicates why this design presents lower performance than the TO designs. Most of the air flows through the gap without good contact with the pins and the velocity inside the heat sink is about 0.06 m/s, which is much lower than "horiz1" or "horiz2". The local heat transfer coefficient in Figure 13(d) also shows that the pins locating at the bottom and outer contact with air well and exhibits a higher local heat transfer coefficient, but many inside do not transfer heat with the air in an efficient way, which is partly due to the high local air temperature. The average local heat transfer coefficient is about 4.24 W/(m^2·K), which is much lower than those for "horiz1" and "horiz2", although the total heat transfer rate is the same.

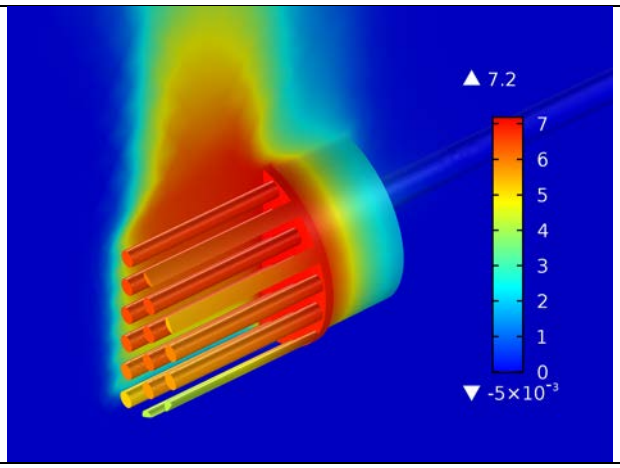

(a) Model prediction for Temperature span [K]

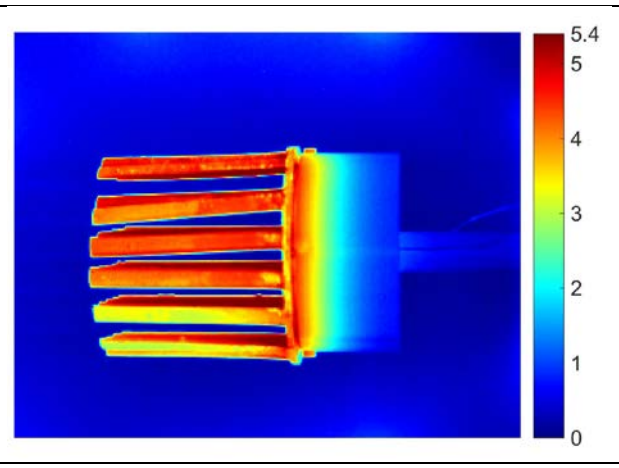

(b) Measured temperature span [K]

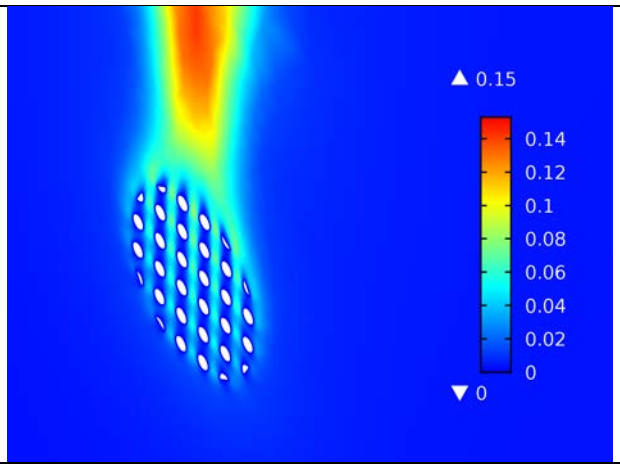

(c) Model prediction for velocity [m/s]

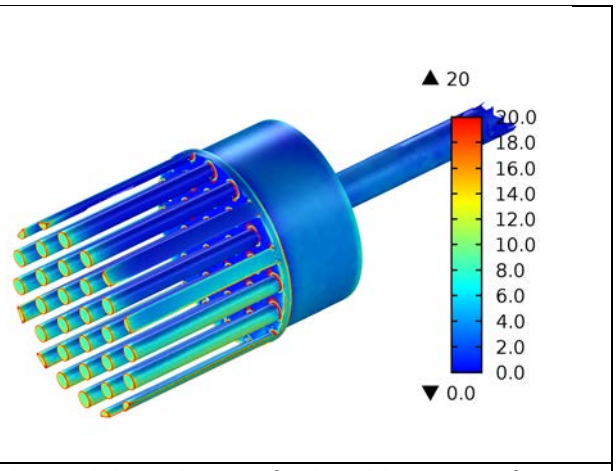

(d) Model prediction for local heat transfer coefficient [W/(m^2·K)]

Figure 13. (a) - (b) modelled and measured temperature span, (c) modelled flow velocity and (d) modelled local heat transfer coefficient of the heat sink "pf-5.7mm" with α=90º

5.2. Impact of orientation

The orientation effect with respect to gravity of TO designs is interesting as they are designed based on different orientation angles, which results in significantly different optimized geometries as shown above. They are supposed to perform best under exactly the working conditions optimized for, but some degradation of performance is expected when the orientation is changed. Therefore, a study on the orientation effect of three heat sinks, "vert", "horiz1" and "pf-5.7mm" is performed and presented in Figure 14. The simulation results are indicated as lines and the experimental results are represented by dots. Repeated experiments generate multiple dots. The simulation shows that the best and the worst designs are "vert" and "horiz1" for the orientation angle α=0º, and the "pf-5.7mm" is in the middle. When the orientation angle changes to 45º and 90º, the situation reverses: "horiz1" turns to be the best and "vert" is the worst. This shows the orientation angle has a large impact on the TO designs and the results reflect the preset constraints as predicted. A more robust TO design could be generated using a multiobjective optimization to give a heat sink that performs well at both α =0 º and α =90 º, but this is not considered here.

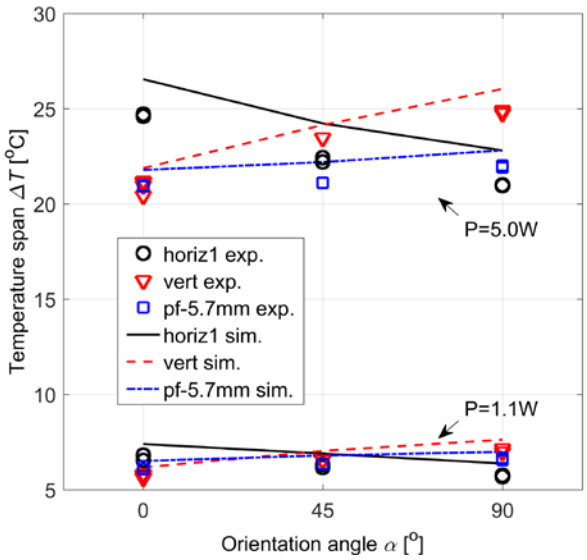

Figure 14. Impact of the orientation angle,α, on the temperature span for the three heat sinks "horiz1", "vert" and "pf-5.7mm"

A more detailed study is implemented to further investigate the impact of the rotation angle, or azimuthal angle. Design "horiz1" is chosen, as it was shown to have the best performance at $\alpha = 90°$, see Figure 8, and because it has two big flap-like branches as seen in Figure 11(c), which could largely affect the flow through the heat sink as it is rotated about its axis. Both simulation and experiment tests start from β=0°, which is the designed rotation angle for "horiz1", and the results are shown in Figure 15. With increasing angle, the streamlined branches turn from the vertical to a more horizontal position, which begins to block the flow. Therefore, the temperature at the aluminum heating plate increases immediately due to decreased air flow through the heat sink. The flap-like branches turn to be horizontal when β=90°, which drives the temperature to reach the maximum temperature. Further increases of β turns the branches back to the vertical direction, which lowers the temperature and realizes better heat dissipation performance again. When the angle is 180°, the performance is very close to that for 0°, although the branches are optimized for the reversed direction. The TO heat sinks have been modelled in detail in Ref [30] with regard to orientation and rotation angles, and it was shown that "horiz1" is more sensitive to "horiz2" due to the higher symmetry requirements on optimization of "horiz1".

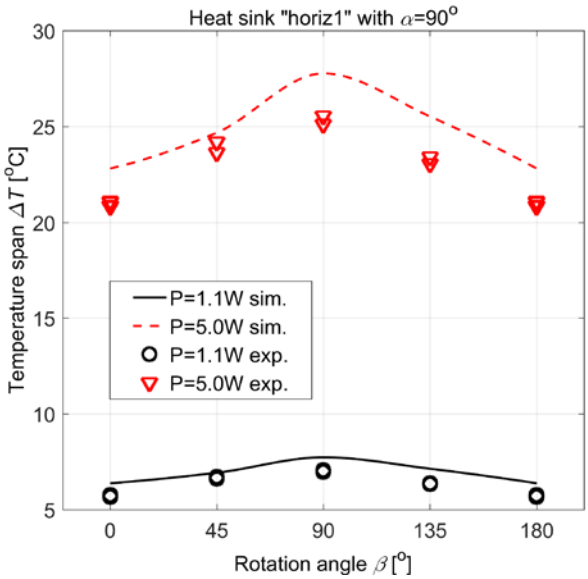

Figure 15. Impact of rotation angle, β, on temperature span for "horiz1" when the orientation angle, α, is 90°

5.3. Impact of radiation

As discussed in Section 4.1 and 5.1, the heat sink is painted with graphite spray and the resulting dark black surface gives a radiative emissivity close to 1, which is preferable for heat dissipation. Although the effect of radiation is not included in the TO model, we present the effect brought by the graphite painting for the TO design "vert" as an exemplarily case in Figure 16. With the graphite paint the temperature at the aluminum plate is lower as for an unpainted surface, as expected. The difference increases as the heating power and temperature span increase, showing a nonlinear behavior. This confirms that such a surface treatment, which has been applied widely in electronics cooling applications, can further improve the heating dissipation performance..

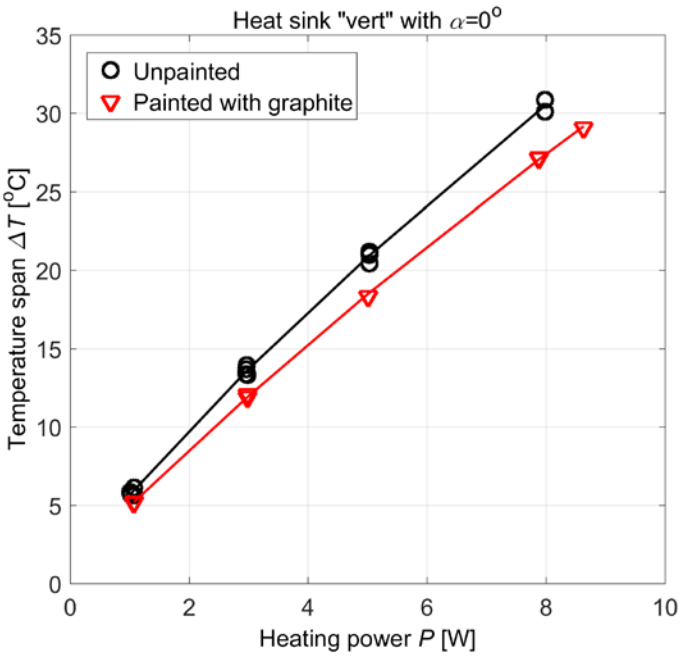

Figure 16. Impact of radiation for the heat sink “vert”

6. Conclusions

Stereolithography-assisted investment casting is developed and applied to fabricate metal heat transfer devices designed by topology optimization. A comparison with metal additive manufacturing shows that the SLA-assisted IC technique is a promising alternative, which has a low cost and is flexible with regards to part size and metals that can be used. Note the pattern size is dependent on the capacity of the 3D printing device, but gluing with wax can increase the maximum cast size.

Building on optimization studies in Refs. [14], [15] and [16], we present a validation of TO heat sinks by both simulation and experiment. The heat sink “vert” is designed for vertical operation and two more designs, “horiz1” and “horiz2”, are generated based on the horizontal directions. Five reference pin-fin heat sinks are also conceived for comparison. Six heat sinks are fabricated based on the SLA-assisted IC technique in Britannia metal and the resulting heat sinks capture structural details with high accuracy. These results successfully demonstrate the capabilities of this combined fabrication process.

A natural convection test apparatus is constructed and simulation models are built in COMSOL Multiphysics for validating the TO heat sink performance. The simulation results fit the experiments well with a variation of less than 8%. Both validation tests show that the TO heat sinks can always realize the best heat dissipation performance at the working conditions optimized for; and even for a higher heating power in some cases. A detailed analysis of the temperature distribution, velocity and local heat transfer coefficients further verifies the high performance of the topological designs, showing the branches generated by TO guide the flow in optimized ways for maximizing the overall heat dissipation performance. Although the heat transfer area is lower compared to the reference heat sinks, optimized geometries still realize lower thermal resistance. Moreover, an orientation study is conducted which shows that the performance of TO heat sinks strongly depends on the design conditions, as predicted. Lastly, the impact of radiation is presented for an exemplarily case.

As the Britannia metal is less conductive than most metals used in heat transfer devices, future studies will emphasize the fabrication and testing of TO designs based on aluminum or copper alloys. A bronze heat sink has been fabricated successfully, which is not presented here, and it shows this process can be applied to different metals and alloys. With developments in the TO solvers, more designs can be tested based on this fast prototyping technique with low cost. Please note that this technique is not limited to the heat transfer devices but can as well be applied to other areas such as structural optimization.

Acknowledgements

This work was financed by the TopTEn project sponsored through the Sapere Aude Program of the Danish Council for Independent Research (DFF – 4005-00320). The authors would like to thank Dr. W. R. Kiebach, Dr. K. B. Andersen and Mr. J. Geyti from the Department of Energy Conversion and Storage, Technical University of Denmark, for technical support.

References

1. M. P. Bendsøe, O. Sigmund, Topology Optimization: Theory, Methods and Applications, Springer, 2003. DOI: http://doi.org/10.1007/978-3-662-05086-6
2. J. D. Deaton, R. V. Grandhi, A survey of structural and multidisciplinary continuum topology optimization: post 2000, Structural and Multidisciplinary Optimization, 2014, 49(1): 1-38. DOI: https://doi.org/10.1007/s00158-013-0956-z
3. O. Sigmund, and K. Maute, Topology optimization approaches A comparative review, Structural and Multidisciplinary Optimization, 2013, 48(6): 1031-1055. DOI: http://doi.org/10.1007/s00158-013-0978-6
4. X. Y. Chen, Topology optimization of microfluidics - A review, Microchemical Journal, 2016, 127: 52-61. DOI: https://doi.org/10.1016/j.microc.2016.02.005
5. T. E. Bruns, Topology optimization of convection-dominated steady-state heat transfer problems, International Journal of Heat and Mass Transfer, 2007, 50: 2859–2873. DOI: https://doi.org/10.1016/j.ijheatmasstransfer.2007.01.039
6. G. H. Yoon, Topological design of heat dissipating structure with forced convective heat transfer, Journal of Mechanical Science and Technology, 2010, 24 (6): 1225-1233. DOI: https://doi.org/10.1007/s12206-010-0328-1
7. G. Marck, M. Nemer and J. L. Harion, Topology optimization of heat and mass transfer problems: laminar flow, *Numerical Heat Transfer Part B: Fundamentals*, 2013, 63 (6): 508-539. DOI: http://dx.doi.org/10.1080/10407790.2013.772001
8. P. Coffin, and K. Maute, Level set topology optimization of cooling and heating devices using a simplified convection model, Structural and Multidisciplinary Optimization, 2016, 53(5): 985-1003. DOI: https://doi.org/10.1007/s00158-015-1343-8
9. A. A. Koga, E. C. C. Lopes, H. F. V. Nova, et al., Development of heat sink device by using topology optimization. International Journal of Heat and Mass Transfer, 2013, 64: 759-772. DOI: http://doi.org/10.1016/j.ijheatmasstransfer.2013.05.007
10. E. M. Dede, Multiphysics topology optimization of heat transfer and fluid flow systems, Proceedings of the COMSOL Conference, Boston, USA, 2009.
11. COMSOL Multiphysics® Modeling Software, https://www.comsol.com/, September 19, 2017.
12. E. M. Dede, S. N. Joshi and F. Zhou, Topology optimization, additive layer manufacturing, and experimental testing of an air-cooled heat sink, J. Mech. Des. 2015, 137 (111702): 1-9. DOI: https://doi.org/10.1115/1.4030989

13. J. H. K. Haertel and G. F. Nellis, A fully developed flow thermofluid model for topology optimization of 3D-printed air-cooled heat exchangers, Applied Thermal Engineering, 119: 10-24. DOI: https://doi.org/10.1016/j.applthermaleng.2017.03.030
14. J. Alexandersen, N. Aage, C. S. Andreasen, et al., Topology optimisation for natural convection problems, International Journal for Numerical Methods in Fluids, 2014, 76 (10): 699-721. DOI: http://dx.doi.org/10.1002/fld.3954
15. J. Alexandersen, O. Sigmund and N. Aage, Large scale three-dimensional topology optimisation of heat sinks cooled by natural convection. International Journal of Heat and Mass Transfer, 2016, 100: 876-891. DOI: http://doi.org/10.1016/j.ijheatmasstransfer.2016.05.013
16. J. Alexandersen, O. Sigmund and N. Aage, Topology optimisation of passive coolers for light-emitting diode lamps, The 11th World Congress on Structural and Multidisciplinary Optimization, Sydney, Australia, 2015.
17. S. Singh and R. Singh, Precision investment casting: A state of art review and future trends. Proceedings of the Institution of Mechanical Engineers Part B: Journal of Engineering Manufacture, 2016, 230 (12): 2143-2164. DOI: http://dx.doi.org/10.1177/0954405415597844
18. Jewelry Resins for Superb Detail, https://formlabs.com/materials/jewelry/, September 19, 2017.
19. 3D Hubs, https://www.3dhubs.com/, September 19, 2017.
20. E. O. Olakanmi, R. F. Cochrane and K. W. Dalgarno, A review on selective laser sintering/melting (SLS/SLM) of aluminium alloy powders: Processing, microstructure, and properties. Progress in Materials Science, 2015, 74: 401-477. http://doi.org/10.1016/j.pmatsci.2015.03.002
21. N. T. Aboulkhair, N. M. Everitt, I. Ashcroft, et al., Reducing porosity in AlSi10Mg parts processed by selective laser melting. Additive Manufacturing, 2014, 1-4: 77-86. DOI: http://doi.org/10.1016/j.addma.2014.08.001.
22. M. Wong, S. Tsopanos, C. J. Sutcliffe, et al., Selective laser melting of heat transfer devices, Rapid Prototyping Journal, 2007, 13 (5): 291-297. DOI: http://doi.org/10.1108/13552540710824797
23. B. S. Lazarov and O. Sigmund, Filters in topology optimization based on Helmholtz-type differential equations, International Journal for Numerical Methods in Engineering, 2011, 86(6): 765–781. DOI: 10.1002/nme.3072
24. B. S. Lazarov, F. Wang, and O. Sigmund, Length scale and manufacturability in density-based topology optimization, Archive of Applied Mechanics, 2016, 86(1): 189–218. DOI: https://doi.org/10.1007/s00419-015-1106-4
25. N. Aage, E. Andreassen, and B. Lazarov, Topology optimization using petsc: An easy-to-use, fully parallel, open source topology optimization framework, Structural and Multidisciplinary Optimization, 2015, 51(3): 565–572. DOI: https://doi.org/10.1007/s00158-014-1157-0
26. N. Aage and B. Lazarov, Parallel framework for topology optimization using the method of moving symptotes, Structural and Multidisciplinary Optimization, 2013, 47(4): 493–505. DOI: https://doi.org/10.1007/s00158-012-0869-2
27. K. Svanberg, The method of moving asymptotes - a new method for structural optimization, International Journal for Numerical Methods in Engineering, 1987, 24: 359–373. DOI: 10.1002/nme.1620240207
28. A. I. Zografos and J. E. Sunderland, Natural convection from pin fin arrays, Experimental Thermal and Fluid Science, 1990, 3 (4): 440-449. DOI: https://doi.org/10.1016/0894-1777(90)90042-6
29. Using the Boussinesq Approximation for Natural Convection, https://www.comsol.com/blogs/using-the-boussinesq-approximation-for-natural-convection/, September 19, 2017.
30. J. Alexandersen, O. Sigmund, K. E. Meyer, B. S. Lazorov, Design of passive coolers for light-emitting diode lamps using topology optimisation, International Journal of Heat and Mass Transfer, 2017, under review.

A.7 P7 - Cross-flow heat exchanger design using thermofluid topology optimization

J. H. K. Haertel, K. Engelbrecht, B. S. Lazarov and O. Sigmund

Extended abstract, *10th International Conference on Computational Heat, Mass and Momentum Transfer (ICCHM^{2}T 2017)*, 2017.

Proceedings of ICCHM²T2017
May 28-June 1, 2017, Seoul, Korea ***Paper Number 160006***

CROSS-FLOW HEAT EXCHANGER DESIGN USING THERMOFLUID TOPOLOGY OPTIMIZATION

Jan H. K. Haertel[*†], Kurt Engelbrecht[*], Boyan S. Lazarov[**], and Ole Sigmund[**]

[*] Department of Energy Conversion and Storage, Technical University of Denmark
[†] Corresponding author, Email: jhkh@dtu.dk
[**]Department of Mechanical Engineering, Technical University of Denmark

ABSTRACT
In this work, density-based topology optimization is applied to the design of a gas-to-gas cross-flow heat exchanger. The thermofluid problem is modeled as one fluid flowing within the two dimensionally modeled domain (*fluid 1*) and a second fluid flow perpendicular to this plane (*fluid 2*); hence, the heat transfer in both fluids is explicitly captured in the optimization model. The heat transfer rate between the fluids is maximized subject to a bulk temperature constraint on the flow perpendicular to the modeled domain. An optimized cross-flow heat exchanger design is presented and discussed.

INTRODUCTION
Topology optimization [1] deals with the optimization of a material distribution within a design domain under given constraints. This allows for the systematic design of engineering systems with the possible advantages of reduced development time and identification of unintuitive and novel optimized geometries. The topology optimization method originated in structural mechanics but has subsequently been applied to a wide range of fields such as fluidics, acoustics, and heat transfer [2]. Topology optimization of thermofluid systems is an active area of research and work has been reported for forced convection [3, 4] and natural convection problems [5]. In this study, topology-optimization is applied for the first time to the design of a cross-flow heat exchanger with explicit modeling of both fluids. For this purpose, a density-field is introduced in the design domain which takes the value 0 in areas where *fluid 2* flows perpendicular to the modeled domain and 1 in areas where *fluid 1* flows within the modeled plane. This binary optimization problem is relaxed to continuous design variable values between 0 and 1 to allow for the use of efficient gradient-based optimization methods.

THEORY AND METHODS
The two fluid flows are assumed to be laminar and pressure-driven and modeled in 2D to reduce the computational complexity of the problem. Air is considered as the fluid in both flows. *Fluid 1* flows within the plane of the modeled domain. Within the design domain, the design density field interpolates between the flow of *fluid 1* and *fluid 2* where *fluid 2* flows perpendicular to the modeled plane. The heat exchanger material separating the two fluid flows is not explicitly represented in the current model. It is planned to implement an interface identification method [6] to explicitly include the properties of the heat exchanger material in the thermofluid model during optimization. The Navier-Stokes equations and continuity equation are solved for *flow 1*. *Flow 2* is modeled assuming a thermally and fluid dynamically fully developed internal flow in the out-of-plane direction as presented in [7]. Therefore, it is sufficient to solve a simplified linear Navier-Stokes equation for that flow. A Brinkman friction term [8] is introduced to the Navier-Stokes equations of both *flow 1* and *flow 2* to prevent *fluid 1* from flowing in areas of *fluid 2* and vice versa. A single thermal equation that is coupled with the fluid mechanics is solved to obtain the temperature distribution in *fluid 1* and *2*. It represents the standard convection-diffusion equation in *fluid 1* and an out-of-plane fully developed internal flow convection-diffusion equation in *fluid 2*. An interpolation between both equations is conducted within the design domain during the optimization. The inlet temperature of *fluid 1* is prescribed and *fluid 2* acts as a heat sink in the 2D modeled domain as it transports energy in the out-of-plane direction while heating up. Symmetry boundary conditions are set at both sides of the modeled domain. The optimization objective is to maximize the heat transfer between the fluids subject to a minimum bulk temperature constraint in *fluid 2* which allows the specification of a desired temperature difference between the fluids. The optimization model is implemented in the commercial finite element software COMSOL Multiphysics [9] that is interfaced with MATLAB to automate the optimization. The globally convergent version of the Method of Moving Asymptotes (GCMMA) [10] is used as optimization method.

RESULTS AND DISCUSSION
An exemplary optimization result is depicted in Figure 1 showing the optimized design field (a), the corresponding temperature distribution in *fluid 1* and *fluid 2* (b), the flow field of fluid 1 (c), and the fully developed flow field of *fluid 2* flowing perpendicular to the modeled plane. Three separate flow passages for

fluid 2 (red) are formed within the design domain. Channels for *fluid 1* (blue) are generated between these flow passages to allow for an efficient heat transfer between the two fluids. A clear 0/1 design field is obtained, meaning that the optimized design represents a practical geometry.

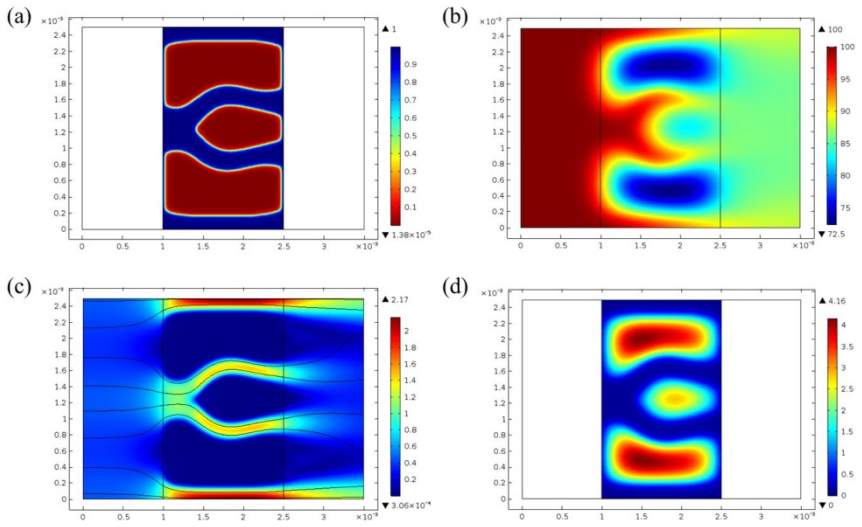

Figure 1. Optimized design (a), where blue indicates flow passages of *fluid 1* and red indicates flow passages of *fluid 2*, with corresponding temperature field [°C] (b) and respective velocity distribution [m/s] in *fluid 1* (c) and *fluid 2* (d).

ACKNOWLEDGMENTS

This work was supported by the TOpTEn project sponsored through the Sapere Aude Program of the Danish Council for Independent Research (DFF – 4005-00320).

REFERENCES

1. Bendsøe, M. P., and Sigmund, O., 2003, *Topology Optimization: Theory, Methods, and Applications*, Springer Verlag, Berlin Heidelberg
2. Deaton, J. D., and Grandhi, R. V., 2014, A survey of structural and multidisciplinary continuum topology optimization: post 2000, Structural and Multidisciplinary Optimization, ***49***(1), pp. 1-38.
3. Yoon, G. H., 2010, Topological design of heat dissipating structure with forced convective heat transfer, Journal of Mechanical Science and Technology, **24**(6), pp. 1225-1233.
4. Matsumori, T., Kondoh, T., Kawamoto, A., and Nomura, T., 2013, Topology optimization for fluid–thermal interaction problems under constant input power, Structural and Multidisciplinary Optimization, 47(4), pp. 571-581.
5. Alexandersen, J., Aage, N., Andreasen, C. S., and Sigmund, O., 2014, Topology optimisation for natural convection problems, International Journal for Numerical Methods in Fluids, **76**(10), pp. 699-721.
6. Clausen, A., Aage, N., and Sigmund, O., 2015, Topology optimization of coated structures and material interface problems, Computer Methods in Applied Mechanics and Engineering, **290**, pp. 524-541.
7. Nellis, G. F., & Klein, S. A., 2009, *Heat Transfer*, Cambridge University Press, New York.
8. Borrvall, T., and Petersson, J., 2003, Topology optimization of fluids in Stokes flow, International journal for numerical methods in fluids, **41**(1), pp. 77-107.
9. COMSOL 5.2
10. Svanberg, K., 2002, A class of globally convergent optimization methods based on conservative convex separable approximations, SIAM journal on optimization, **12**(2), pp. 555-573.